Doctoral Dissertations

Student Theses and Dissertations

Spring 2011

One pot synthesis of metal, carbides and polymeric aerogels

Naveen K. Chandrasekaran

Recommended Citation

ONE POT SYNTHESIS OF METAL, CARBIDES AND POLYMERIC AEROGELS

by

NAVEEN K. CHANDRASEKARAN

A DISSERTATION

Presented to the Faculty of the Graduate School of the

MISSOURI UNIVERSITY OF SCIENCE AND TECHNOLOGY

In Partial Fulfillment of the Requirements for the Degree

DOCTOR OF PHILOSOPHY

in

CHEMISTRY

2011

Approved

Dr. Nicholas Leventis, Advisor
Dr. Chariklia Sotiriou-Leventis, Co-Advisor
Dr. Klauss Woelk
Dr. Jeffrey Winiarz
Dr. Isaac Kakkatukuzhy

PUBLICATION DISSERTATION OPTION

This dissertation consists of the following four manuscripts for publication:

Pages 17-102 have been published in *Chemistry of Materials* **2010**, *22*, 6692-6710.

Pages 103-131 have been published in *Journal of Materials Chemistry* **2009**, 19, 63-65.

Pages 132-147 have been published in *Journal of American Chemical Society* **2009**, 131, 4576-4577.

Pages 148-203 have been published in *Journal of Materials Chemistry* **2010**, 131, 20, 7456-7471.

ABSTRACT

Ultra-low density, three-dimensional assemblies of nanoparticles are referred to as aerogels, and typically are derived from supercritical fluid (SCF) drying of wet-gels. Aerogels are generally fragile materials, but that issue has been addressed successfully by X-aerogels, in which the inorganic nanoparticle framework plays the role of the template for the accumulation of polymer that connects covalently and crosslinks the nanoparticles. The resulting materials can be 300× stronger than the native network, for a nominal increase in density by a factor of 3×. Since the exceptional mechanical properties of X-aerogels are traced to the conformal polymer coating, it was reasonable to seek organic aerogels of the crosslinker itself. Thus, here we demonstrate a new efficient method for the synthesis of polyurea (PUA) aerogels by reaction of di or triisocyanates with controlled amounts of water, resulting in *in-situ* amine formation, which reacts further with yet-unreacted isocyanate to form polyurea. PUA aerogels prepared by this method have variable nanomorphology (from fibrous to particulate, depending on the chemical identity and the concentration of the monomer), extremely high mechanical strength and they are flame retardant.

Smelting dates to 3000 B.C. and is used to produce metal from the ore via chemical reduction with carbon. Carbon aerogels are produced by pyrolysis of purely organic resorcinol-formaldehyde (RF) aerogels. Here we have developed interpenetrating networks of RF and metal oxide (MOx) aerogels that upon pyrolysis undergo smelting yielding metal, or carbide aerogels, depending on the chemical identity of M: oxides of Fe, Co, Ni, Sn, Cu yield metal aerogels, refractory Cr, Ti, Hf, oxides yield carbides. By casting a conformal polymer coating on the RF-MOx interpenetrating nanoparticle networks, or by controlling the drying process and thus the compactness of the network.

ACKNOWLEDGMENTS

First and foremost, I would like to thank my advisor, Professor Nicholas Leventis and co-advisor, Professor Chariklia Sotiriou-Leventis for their guidance and support throughout the completion of my research and dissertation. I would like to express my deepest gratitude and appreciation to them for their advice and encouragement. They were very kind, supportive and patient and have always helped me think, express my thoughts and explore areas within and outside my research. Over the years, I have learned a lot for which I would always remain indebted to them.

I would like to thank my advisory committee members, Dr. Klaus Woelk, Dr. Jeffrey Winiarz and Dr. Isaac Kakkatukuzhy for serving in my committee and advising me throughout the completion of my dissertation. I want to express my appreciation and gratitude to Professor Hongbing Lu of the Mechanical Engineering Department of The University of Texas - Dallas and to Professor Arif Mumtaz of the Physics Department of the Quaid-i-Azam University, Islamabad, Pakistan for their help in characterizing our materials. I would like to thank the Chemistry Department of MS&T for Teaching Assistantships, Mr. Joe Counsil for training and helping me to maintain our lab equipment and Mr. Mike Myers and Mr. Dean Lenz for their help with the lab facilities. I would also like to thank all the past and recent members of the Leventis Group. Especially,want to express my gratitude to Dr. Amala Dass and Dr. Sudhir Mulik also for their support and guidance to start my research at MS&T, and Mr. Anand Sadekar, for his friendship and help all these years. Finally, I would like to express my love and affection to my parents, Mr. A. Chandrasekaran and Mrs. D. B. Hemalatha, my grandparents, Mr. A. D. Balakrishnan and Mrs. Sarojini Balakrishnan, my uncle, Mr. Ravi Kumar and my aunt, Mrs. D. B. Usha Rani.

TABLE OF CONTENTS

LIST OF ILLUSTRATIONS

Supporting Information

PAPER II

Supporting Information

LIST OF SCHEMES

LIST OF TABLES

1. INTRODUCTION

1.1   AEROGELS

Ultra-low density, three-dimensional assemblies of nanoparticles are referred to as aerogels, which are typically derived from supercritical fluid (SCF) drying of wet gels made through a sol-gel process. Their large internal void space is responsible for low dielectric constants, low thermal conductivities, and high acoustic impedance. Aerogels are classified as open cell foams with mesoporous structure and large internal empty space. They can be either purely organic materials (such as resorcinol-formaldehyde, phenol-formaldehyde, and polyurea aerogels) or inorganic materials such as metal and semimetal oxide aerogels.

Aerogels are derived by SCF drying of wet gels in a process that replaces entrained liquid phase with air. Aerogels have been considered for thermal and acoustic insulation, as dielectrics, supports for catalysts, and hosts of functional guests for chemical, electronic, and optical applications.[1,2]

Aerogels were initially prepared by Kistler in 1931.[3] He reported gelation of sodium silicate by acid catalysis. With this process gelation took a few days. It was followed by extensive washing with water, then methanol, which was removed by SCF drying. However, rapid development of aerogels did not start for almost 40 years, until Stanislaus Teichner at Universite Claud Bernard, Lyon, sought a method to store oxygen and rocket fuels in porous materials.[1] In the early 1980s, particle physics researchers realized that silica aerogels would be an ideal medium for the production and detection of Cherenkov radiation.[2] Their experiments required large transparent tiles of silica aerogel.

Using the tetramethoxysilane method, they fabricated two large detectors, one using 1700 liters of silica aerogel in the TASSO detector at the Deutsches Elektronen Synchrotron (DESY) in Hamburg, Germany,[1] and another at CERN using 1000 liters of silica aerogel prepared at the University of Lund in Sweden.[3] BASF in Germany simultaneously developed CO_2 substitution methods for the preparation of silica aerogel beads from sodium silicate.[2] This material was in production until 1996, marketed as "Basogel".[1] In the late 1980s, researchers at Lawrence Livermore National Laboratory (LLNL), led by Larry Hrubesh, prepared the world's lowest density silica aerogel.[4] This aerogel had a density of 0.003 g cm^{-3}, only three times that of air. Shortly thereafter, Rick Pekala, also of LLNL, extended the techniques used to prepare inorganic aerogels to the preparation of aerogels of organic polymers.[5,6] These polymers included resorcinol-formaldehyde and melamine-formaldehyde aerogels. Resorcinol-formaldehyde aerogels could be pyrolyzed to yield aerogels of pure carbon.[5,6] Their development opened a completely new area in aerogel research.

Carbon aerogels are comprised of particles with sizes measured in nanometers, which are covalently bonded.[5-8] Since carbon aerogels combine electrical conductivity with typical aerogel properties such as high mesoporosity (2-40 nm),[6,7] low density (~ 0.25 g cm^{-3}),[6,7] and high surface area (~ 1000 m^{2}g^{-1}),[6,7] they are considered for a wide variety of applications from separations,[8] to non reflective panels,[8-10] materials for hydrogen storage,[11] and anodes in lithium ion batteries or electrodes for supercapacitors.[11]

1.2   THE SOL-GEL PROCESS

The most investigated aerogels are of the inorganic type and they are based on silica. Silica aerogels are prepared via a sol-gel process, which typically involves acid- or base- catalyzed hydrolysis, followed by condensation of silicon alkoxides (Figure 1.1).[12-15] Those wet-gels can be dried either supercritically to aerogels, thus retaining most of their volume, but they can also be dried under ambient pressure and temperature to obtain xerogels resulting in extensive shrinkage.

A.
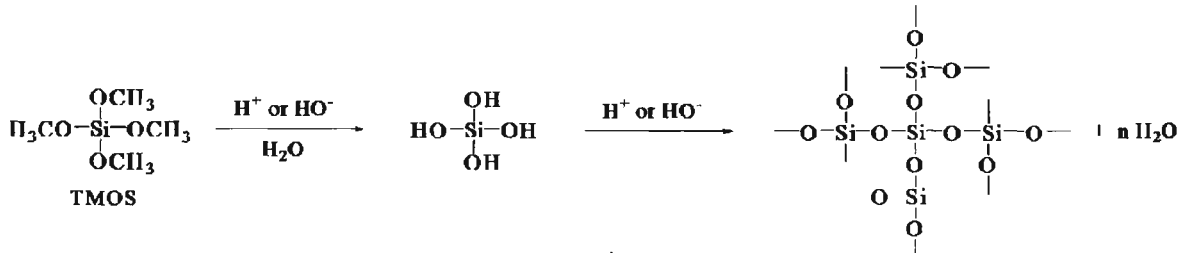
B.

Figure 1.1   Preparation of a silica gel by the sol-gel process: (A) Chemically.
(B) Experimentally.

Typically, SCF drying involves replacing gelation solvents with liquid CO_2 in an autoclave, the temperature is then increased above the critical point of CO_2 (31 °C, 1072 psi) and CO_2 is vented off at constant temperature (e.g., at 40 °C). This process prevents formation of a liquid-gas interface retracting through the volume of the wet-gel (as during drying under ambient pressure) and prevents capillary forces from being exerted on the delicate skeletal framework, thus retaining the pore structure of the wet-gel into the final dry object (aerogel). Silica aerogels have actually been used as Cerenkov radiation detectors,[1,2,14] aboard spacecraft as collectors for cosmic particles,[1,2,14] and for thermal insulation in planetary vehicles.[1,2,14] Commercialization has been slow because silica aerogels are fragile and hygroscopic and they require supercritical drying. The last two issues can be tolerated, but the fragility problem is fatal.

1.3   POLYMER-CROSSLINKED AEROGELS

Our solution to the fragility problem has been polymer crosslinked aerogels. Since silica aerogels have surface terminated hydroxyl groups, it is reasonable to borrow and apply polyurethane chemistry, in which diols react with isocyanate groups to form carbamates (urethanes). The crosslinking process involves not only formation of carbamates with surface silanols, but also ureas by hydrolysis of dangling isocyanates into amines. These amines in turn react with more isocyanate in the mesopores.[16] In other words; the polymer not only forms conformal coating on the surface of silica aerogels, but also reinforces the interparticle necks that are the weak points on the aerogel framework. The aerogels obtained by this method have been called X-aerogels (Figure 1.2).
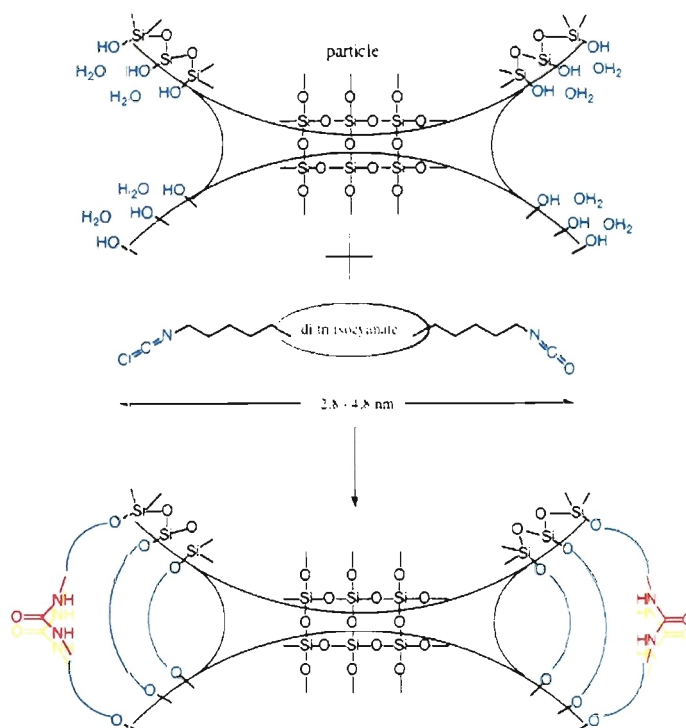
Figure 1.2 The structure of a polymer crosslinked aerogel: Polymeric tethers connect interparticle necks, which are the weak points in the aerogel skeletal framework.

As a result of crosslinking, the bulk density of X-aerogels increases by a minimal factor of ~2.5, but the flexural strength obtained through a short beam three-point bent test method increases by a factor of 300.[16-18] The increase in bulk density is attributes to the widening of the interparticle necks due to the accumulation of polymer (Figure 1.3). Thus, a typical native aerogel fails with less than 100 g of vertical force, whereas a crosslinked sample, can withstand in excess of 30 kg.[13-16] This technology has been extended to several metal oxide and rare earth oxide aerogels.[15] There are three degrees of freedom in the design of polymer crosslinked aerogels: the chemical identity of the framework, the chemical identity of the polymer and the surface functionality of the nanoparticle. The latter was determined to be a versatile parameter by careful choice of the reactive group on the surface of silica. This process was studied and demonstrated

with amine functionality decorated on the surface of silica for attachment of polyurea, epoxy resins or polystyrene.[16-26]
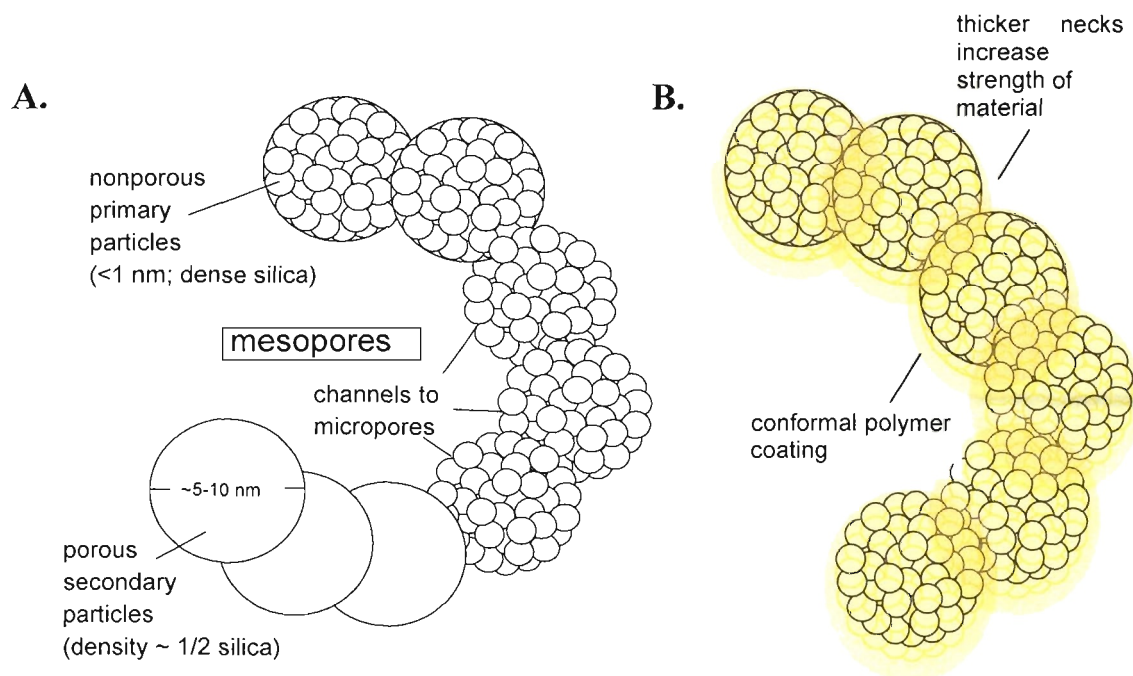
Figure 1.3 Nanostructure of mesoporous silica: (A) before crosslinking (B) after crosslinking

In X-aerogels the inorganic polymer framework plays the role of the template for the accumulation of polymer. Since the exceptional mechanical properties of X-aerogels are attributed to the conformal polymer coating, it is reasonable to prepare polymeric (organic) aerogels of the crosslinker itself, with morphology and interparticle connectivity similar to those of X-aerogels.

1.4   ORGANIC AEROGELS

We prepare organic aerogels by a bottom-up approach, whereas we mix suitable monomers, or monomers with an initiator, followed by an incubation period under heat or light. The reaction yields either a soluble polymer or a colloid. Soluble polymers form high molecular weight gels, which are supported by Van der Waals forces and collapse to dense polymers upon drying (even with SCF CO_2). On the other hand, a colloidal solution with interparticle crosslinking forms a three dimensional network of covalently bonded particles. This network forms a colloidal gel that can be SCF-dried to form monolithic aerogels. Colloidal solutions with no interparticle crosslinking form precipitates, which is the classical case of suspension polymerization. Those possible pathways are summarized in Scheme 1.

Most of the work in organic aerogels has been concentrated on resorcinol-formaldehyde (RF) aerogels which, upon pyrolysis, yield carbon aerogels. Nevertheless, a few reports have been published on other classes of organic aerogels, including polyimide, polyacrylonitrile, polydicyclopentadiene, polyurethane, and polyurea aerogels.[27-31]

The isocyanate (-N=C=O) is a very reactive functional group that reacts with many other functional groups such as alcohols to form urethanes, amines to form ureas and carboxylic acids to form amides. It can also react with itself to form dimers, or trimers (isocyanurates) in the presence of suitable catalysts.
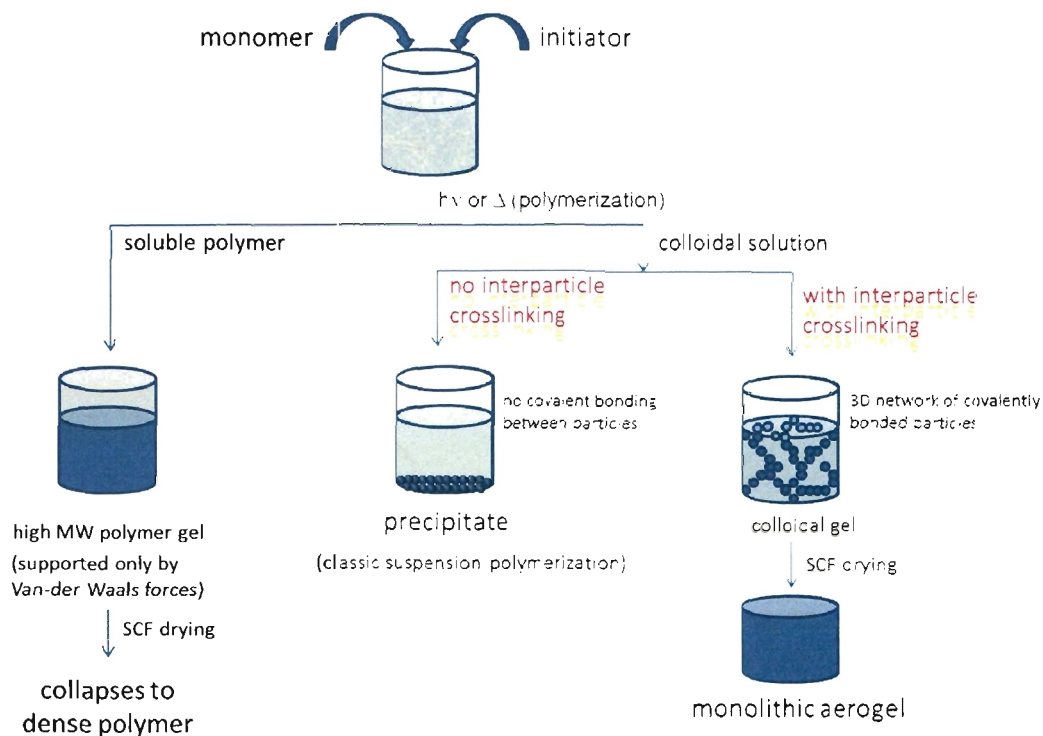
Scheme 1. Mechanism of gelation for different types of organic polymers

Biesmans has reported work on polyisocyanurate aerogels, which have high surface area, low thermal conductivity and they also yield carbon upon pyrolysis under inert atmosphere.[32,33] The drawbacks of these materials, however, are their fragility and the lack of chemical evidence for the formation of polyisocyanurate. After considering all those polymeric materials, and also from our previous findings with polyurea-crosslinked silica and vanadia aerogels, polyureas are reasonable candidate materials for the synthesis of purely organic aerogels.[30,31]

In general; polyurea aerogels described in the literature are prepared by reacting diisocyanates with amines (eq. 1).

$$R\text{-}NCO + R\text{-}NH_2 \longrightarrow R\text{-}NH\text{-}\overset{\overset{\displaystyle O}{\displaystyle \|}}{C}\text{-}NH\text{-}R \qquad (1)$$

amine   urea
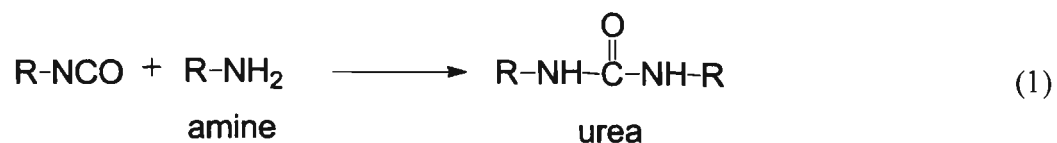
The present work demonstrates a novel and efficient method to synthesize polyurea (PUA) aerogels through the reaction of di or triisocyanate with water, resulting in the *in-situ* formation of amines (eq. 2), which react further with yet-unreacted isocyanate to form polyurea (eq. 1).

$$R-NCO + H_2O \longrightarrow R-NH-\overset{\overset{\textstyle O}{\|}}{C}-OH \overset{-CO_2}{\longrightarrow} R-NH_2 \qquad (2)$$

carbamic acid   *in-situ* amine
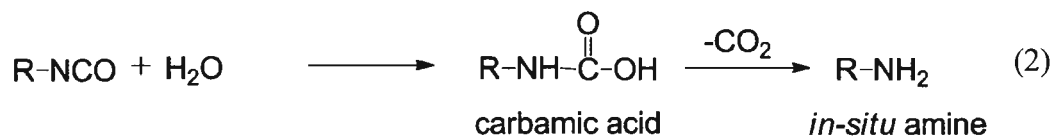
The sequence of reactions shown by eqs. 1 and 2 is well-known and is involved in the preparation of polyurethane foams by adding a small amount of water. Polyurea foams derived from this method have greater tensile strength and thermal stability than polyurethane and polyamide foams.[32]

Polyurea aerogels prepared using eqs. 1 and 2 have variable nanomorphology (ranging from fibrous to particulate as a function of the monomer concentration), demonstrate extremely high mechanical strength and flame retardancy. Upon pyrolysis under inert atmosphere (Ar), polyurea aerogels derived from oligomers of hexamethylene diisocyanate melt at low temperatures yielding only char or no residual carbon.[24] However, polyurea aerogels obtained from triphenylmethane-4,4',4"-triisocyante, yield ~50% w/w monolithic carbon, a yield similar to that of resorcinol-formaldehyde (RF) aerogels.[33-35] Carbon aerogels prepared by this method are macroporous and robust, making then useful in fuel cells and batteries.

1.5 METAL-DOPED CARBON AEROGELS

A few methods have been used to prepare of metal-doped carbon aerogels and they are summarized below.

1.5.1 Ion Exchange Method. In this method,[36,37] iron-doped carbon aerogels are prepared from a suspension of 2,4 dihydroxybenzoic acid in distilled water, treated with potassium carbonate, and vigorously stirred; to the reaction mixture, formaldehyde (37% w/v in water) is added, along with additional potassium carbonate serving as catalyst. The solution was stirred for 24 h, then transferred into vials and kept at 80 °C for 72 h. The resulting K^+-loaded gels were obtained as dark red monoliths. Gels were removed from the vials and soaked in an aqueous solution of 0.1 M $Fe(NO_3)_3$, $FeCl_3$, or $FeSO_4$ for a total of 72 h. Ion exchanged gels were washed in deionized water for 72 h to remove any unbound iron species, and then with acetone for 72 h to remove all water from the pores of the gel network. Those wet-gels are subsequently dried supercritically. The resulting iron-doped organic aerogels were carbonized at 600 °C, 800 °C, or 1050 °C in an inert atmosphere for 10.5 h. In 2003[36] and again 2007 [37], Baumann et al. reported the use of this method to incorporate metal nanoparticles dispersed homogeneously into ordered macroporous carbons (see below) for the growth of carbon nanotubes. The objective of Baumann's group for the preparation of carbon aerogels doped with Fe was to design a novel platform that could be a catalyst for the Chemical Vapor Deposition (CVD) growth of carbon nanotubes. In their previous work with Co- and Ni-doped carbon aerogels, the metal particles had become encased in graphitic carbon during the carbonization process, and as a result, the catalytic sites were inaccessible to CVD gases.

Cotet [37] also reported its use in the synthesis of carbon aerogels with high metal species content such as Fe, Co, Ni, Cu, and Pd.

1.5.2   Metal-Doped Macroporous Carbon. Baumann synthesized metal-doped ordered macroporous carbons.[38-41] They prepared a colloidal crystal-like template by filtrating a dilute solution of monodisperse polystyrene microparticles through a narrow-pore membrane, resulting in the accumulation of three dimensional ordered layers of the polystyrene spheres on the membrane surface. Subsequently, they used filtration to infuse an organic sol produced from the base-catalyzed polymerization of potassium 2,4–dihydroxybenzoate into the void spaces of the template. After formation of the K^+-doped hydrogel within the template, the resulting PS/sol-gel composite, isolated as thin monolithic disks, was soaked in a solution of $M(NO_3)_2$ for 48 h to exchange the potassium ions with the desired metal ion. The polystyrene template was then dissolved with toluene. After solvent exchange with acetone, the sol-gel replica of the polystyrene template was dried using SCF CO_2. The metal doped macroporous carbon was obtained through pyrolysis at 800 °C.

1.6   INTERPENETRATING NETWORKS OF RF/MOx AEROGELS

In this dissertation we have prepared mesoporous interpenetrating networks of resorcinol-formaldehyde (RF) and metal oxide aerogels (FeOx) by one-pot co-gelation of metal chloride hexahydrates with epichlorohydrine, resorcinol and formaldehyde. The strength of the monoliths was increased by crosslinking the skeletal nanoparticles with a triisocyanate-derived polymer according to well established procedures in our laboratory. That process casts a conformal polymer coating over the entire skeletal framework of the

composite material, leaving the mesopores open. In a smelting-like process, pyrolysis at 800-1000 °C under Ar of both the native (n-RF-FeOx) and the crosslinked (X-RF-FeOx) composites yields porous materials in monolithic form, with compositions closely resembling that of pig iron.[42] However, as it turns out crosslinking alters the thermolytic behavior of the two materials. The triisocyanate derived conformal coating melts at around 300 °C causing partial collapse of the skeletal framework creating macropores. Most importantly, however, the molten crosslinker plays the role of a "solvent" where RF and FeOx nanoparticles undergo more efficient mixing, depressing their reaction temperature by as much as 400 °C. Overall, although the chemical compositions of the resulting n-C-Fe and X-C-Fe aerogels are similar, the former are mesoporous and ferromagnetic, whereas the latter are macroporous and superparamagnetic. The method has been extended to RF-SnOx and RF-CuOx, RF-NiOx, RF-CrOx, RF-TiOx and RF-HfOx aerogels.[43]

1.7 THE ROLE OF COMPACTNESS ON THE CARBOTHERMAL CONVERSION OF RF/MOx TO POROUS METALS AND CARBIDES

Crushing and grinding in bulk metallurgical processes increases their efficiency by increasing the surface-to-volume ratio of the solid reactants. However, the compactness of the reactants plays also a very important role in the carbothermal conversion of metal oxides to metals or carbides, Specifically, it is found and reported that the compactness of nanoparticles obtained by the sol-gel method can be controlled by the drying process: SCF CO_2 gives aerogels with more open skeletal frameworks, while drying under ambient pressure yields much more compact xerogels. Owing to their compactness (case of xerogels) or induced compactness (case of X-aerogels), those

materials react carbothermally to yield metals or carbides at as much as 400 °C lower temperatures than the corresponding native aerogels (Figure 1.4).
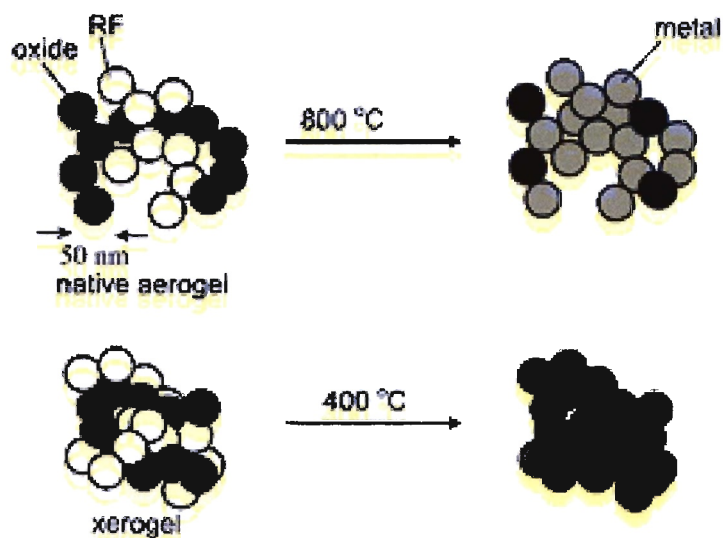
Figure 1.4   The effect of compactness of RF/MOx nanoparticles on their carbothermal reaction.

Carbothermal conversion of iron oxide (e.g., hematite) to iron in bulk metallurgical process is carried out at 2000 °C. Our study reports conversion of metal from interpenetrating networks of sol-gel derived metal oxide and resorcinol-formaldehyde (a carbon precursor) at temperatures as low as 400 °C.

REFERENCES

1. http://eetd.lbl.gov/ecs/aerogels/aerogels.htm

2. http://stardust.jpl.nasa.gov/tech/aerogel.html

3. Kistler, S. S. *J. Phys. Chem.* **1932,** *36*, 52-64.

4. Hrubesh, L.W.; Poco, J. F. J. *J.Non-Cryst.Solids.* **1995,** *188*, 46-53.

5. Reetalbach, T.; Sauberlich, S.; Korder, S.; Fricke, J. *J.Non-Cryst.Solids.* **1995,** *186*, 278-284.

6. Hrubesh, L.W.; Pekala, R. W. J. *J.Mater.Sci.* **1989,** *24*, 3221-3227.

7. Pekala, R.W.; US 5,081,163, **1992**.

8. http://www.aerogel.org/?p=71

9. Yamamoto, T.; Sugimoto, T.; Suzuki, T.; Mukai, S.R.; Tamon, H. *Carbon.* **2002,** *40*, 1345-1351.

10. Pekala, R. W.; Farmer, J.C.; Alviso, C. T.; tran, T.D.; Mayer, S.T.; Miller, J. M. Dunn, B. *J.Non-Cryst.Solids.***1998,** *225*, 74-80.

11. Kabbour, H.; Baumann, T.F.; Scatcher, J.H., jr.; Saulnier, A.; Ahn, C. C. *Chem. Mater.* 2006, *18*, 6085-6087.

12. Chan, K.; Ding, J.; Cheng, S.; Tsang, K. *J. Mater. Chem.* **2004,** 14, 505-516.

13. Jones, S. M. *J. Sol-Gel Sci. Technol.* **2006,** *40*, 351-357.

14. Brinker, C. Scherer, G. *Sol-Gel Science: The Physiscs and Chemistry of Sol-Gel Processing*, Academic press, Inc, **1990**, 518-546.

15. Wright, D. J.; Sommerdijk, A. J. M. *Sol-Gel Materials Chemistry and Applications*, CRC press, **2001**, 15-23.

16. Ilhan, F.; Fabrizio, E. F.; McCorkle, L.; Scheiman, D. A.; Dass, A.; Palczer, A.; Meador, M. A. B.; Johnston, J. C.; Leventis N. *J. Mater. Chem.* **2006,** *16*, 3046-3054.

17. Leventis, N.; Sotiriou-Leventis, C.; Zhang, G.; Rawashdeh, A.M. *NanoLett.* **2002,** *2*, 957-960.

18. Leventis, N. Acc. Chem. Res. **2007**, *40(9)*, 874-884.

19. Katti, A.; Shimpi, N.; Roy, S.; Lu, H.; Fabrizio, E.F.; Dass, A.; Capadona, L.A.; Leventis, N.
Chem. Mater. **2006**, *18*, 285-296.

20. Zhang, G.; Dass, A.; Rawashdeh, A.-M. M.; Thomas, J.; Counsil, J. A.; Sotiriou-Leventis, C.; Fabrizio, E. F.; Ilhan, F.; Vassilaras, P.; Scheiman, D. A.; McCorkle, L.; Palczer, A.; Johnston, J. C.; Meador, M. A. B.; Leventis, N. *J. Non-Cryst. Solids.* **2004**, *350*, 152-164.

21. Leventis, N.; Sotiriou-Leventis, C.; Mulik, S.; Dass, A.; Schnobrich, J.; Hobbs, A.; Fabrizio, E. F.; Lu, H.; Churu. G.; Zhang, Y.; LuO, H.; *J Mater Chem.* **2008**, *18*, 2475-2482.

22. Luo, H.; Lu, H.; Leventis, N. Mech. *Time-Depend. Mater.* **2006**, *10*, 83-111.

23. Capadona, L.A.; Meador, M. A. B.; Alunni, A; Fabrizio, E.F.; Vassilaras, P., Leventis, N. Polymer. **2006**, *47*, 5574-5761.

24. Meador, M. A. B.; Capadona, L. A.; McCorkle, L.; Papdopolos, D.S.; Leventis, N. *Chem. Mater.* **2007**, 19, 2247-2260.

25. Mulik, S.; Sotiriou-Levenis, C.; Churu, G.; Lu, H.; Leventis, N. *Chem. Mater.* **2008**, *20*, 5035-5046.

26. Leventis, N.; Vassilaras, P.; Fabrizio, E. F.; Dass, A. J. Mater. Chem. **2007**, *17*, 1502-1508.

27. Grubbs, R. H. *Angew. Chem. Int. Ed.* **2006**, *45*, 3760-3765.

28. Biesmans, G.; Randall D.; Francais E.; Perrut M.; *J.Non-Cryst.solids.* **1998**, *225*, 36-40.

29. Biesmans, G.; Mertens, A.; Duffours, L.; Woignier, T.; Phalippou, J.; *J.Non-Cryst.Solids.* **1998**, *225*, 64-68.

30. Lee, J. K.; Gould, G. L.; Rhine, W. *J. Sol-Gel Sci. Technol.* **2009**, *49*, 209-220.

31. Wen-Cui, L.; An-Hui, L.; Schueth, F.; *Chem. Mater.* **2005**, *17*, 3620–3626.

32. Wirspza, Z. "Polyurethanes: chemistry, technology and applications", Ellis Horwood Series in Polymer Science and Technology: **1994**.

33. Mulik, S.; Sotiriou-Leventis, C.; Leventis, N. *Chem.Mater.* **2008**, *20*, 6985-6997.

34. Jenkins, G. M.; Kawamura, K. Polymeric carbons- carbon fibre, glass and char, **1976.**

35. Xie, W.; Pan, P.; Chuang. K. C.; *J. Therm. Anal. Calorim.* **2001,** *64*, 477-485.

36. T. F. Baumann, J. H. Satcher, J. *Chem. Mater.* **2003,** *15,* 3745-3747.

37. Steiner, S.A.; Baumann, T. F.; Kong, J.; Satcher, J. H. *Langmuir* **2007,** *23,* 5161-5166.

38. Cotet, M.; Gich, A.; Roig, I.C.; Popescu, V.; Cosoveanu, E.; Molins, V. *J. Non-Cryst. Solids.* **2006,** *352,* 2772–2777.

39. Al-Muhtaseb, S. A.; J. A. Ritter, *Adv. Mater.*, **2003,** *15*, 101-114.

40. Moreno-Castilla, C.; Maldonado-Hódar.; F. J. *Carbon*, **2005,** *43*,455-465.

41. Moreno-Castilla, C.; Maldonado-Hódar.; F. J.; Perez-Cadenas.; A. F. *Langmuir*, **2003,** *19*, 5650-5655.

42. Leventis, N.; Chandrasekaran, N.; Sotiriou-Leventis, C.; Mumtaz, A. *J. Mater. Chem.* **2009,** *19*, 63–65.

43. Leventis, N.; Chandrasekaran, N.; Sadekar, G. A.; Sotiriou-Leventis, C.; Mumtaz, A. *J. Mater. Chem.* **2010,** *20*, 7456–7471.

PAPER

I. Multifunctional Polyurea Aerogels From Isocyanates and Water. A Structure-Property Case study

Nicholas Leventis[*,†], Chariklia Sotiriou-Leventis[*,†], Naveen Chandrasekaran[†], Sudhir Mulik[†], Zachary J. Larimore[‡], Hongbing Lu[*,§], Gitogo Churu[§] and Joseph T. Mang[*]

[†]*Department of Chemistry, Missouri University of Science and Technology, Rolla, Missouri 65409, United States , [‡]Department of Mechanical Engineering, Missouri University of Science and Technology, Rolla, Missouri 65409, United States , [§]Department of Mechanical Engineering, University of Texas at Dallas, Richardson, Texas 75080, United States, and Los Alamos National Laboratory, Los Alamos, New Mexico 87545, United States*

It is well known that isocyanates and water yield polyureas; however, that reaction is not generally the synthesis of the latter, being used instead for environmental curing of films bearing NCO groups or for foaming polyurethanes. Here we report that controlling the relative isocyanate/water/catalyst (Et$_3$N) ratio in acetone, acetonitrile or DMSO yields in polyurea (PUA) gels convertible to highly porous (up to 98.6% v/v) aerogels over a very wide density range (0.016-0.55 g cm^{-3}). The method has been implemented successfully to a variety of aliphatic and aromatic di- and triisocyanates, and it is simple enough to allow synthesis of density-gradient monolithic samples with ease. PUA aerogels have been studied at the molecular level (^{13}C-NMR, IR, XRD), the elementary nanoparticle level (SANS/USANS) and the microscopic level (SEM). Their porous structure has been probed with N$_2$-sorption porosimetry. Despite that the nanomorphology varies with density from fibrous at the low density end to particulate at the high density end, but irrespective of the morphology all samples consist of similarly-sized primary particles, which assemble differently, probably via a reaction-limited cluster aggregation mechanism at the low density end, changing into diffusion-limited

aggregation as the density increases. Higher density PUA aerogels (> 0.3 g cm^{-3}) are mechanically strong enough to tolerate the capillary forces of evaporating low surface tension solvents (e.g., pentane) and they can be dried under ambient pressure; under compression, they can absorb energy (up to 90 J g^{-1} at 0.55 g cm^{-3}) at levels observed only with polyurea-crosslinked silica and vanadia aerogels (120-190 J g^{-1} at similar densities). Once ignited, lower density PUA aerogels (<0.13 g cm^{-3}) burn completely, but surprisingly higher density samples (>0.2 g cm^{-3}) get self-extinguished. Upon pyrolysis >500 $^\circ$C under Ar, PUA aerogels from aromatic isocyanates yield carbon aerogels in high yields (up to ~60% w/w). Those properties, considered together with the simple synthetic protocol, renders PUA aerogels attractive multifunctional materials.

1. Introduction

Quasi-stable, low-density, three-dimensional assemblies of nanoparticles are referred to as aerogels, and typically are derived from drying wet-gels by turning the pore-filling solvent into a supercritical fluid (SCF).[1] Their large internal void space is responsible for low dielectric constants, low thermal conductivities and high acoustic attenuation. There are two types of aerogels, organic and inorganic. They were first reported together by S. Kistler in 1931, noting that certain organic aerogels (e.g., those of nitrocellulose) were more robust materials than their inorganic counterparts.[2] However, emphasis of early research on the latter created a momentum that left purely organic aerogels dormant for almost 60 years, till the late 1980s when R. Pekala started reporting his systematic studies on aerogels based on resorcinol-formaldehyde (RF) phenolic-type resins.[3] Phenolic (phenol-formaldehyde) resins were already in use since the late 1950s for the preparation of glassy (vitreous) carbon.[4] Thus, the impetus of Pekala's work and

almost all subsequent efforts on phenolic aerogels was their conversion to high surface area electrically conducting carbon aerogels.[5] Nevertheless, the record-low thermal conductivity of RF aerogels (0.012 W m^{-1} K^{-1} at 0.16 g cm^{-3}) was noticed early,[6] creating interest for a closer look and further development in the broader area of organic aerogels.

Part of that interest was due to the fact that applications of inorganic aerogels, and in particular those based on silica, were stumbling across fragility problems. Those issues have been addressed successfully by post-gelation casting of a thin conformal polymer coating over the entire internal porous surface of the pre-formed wet-gel nanostructure.[7] The coating connects chemically the skeletal nanoparticles and provides the interparticle necks with the extra chemical energy of the interparticle polymeric tethers. Thus, the internal void space is not compromised significantly, while the flexural strength of a typical monolith is increased by a factor of over 300× for a nominal increase in density by a factor of three. This process is referred to as crosslinking and the resulting aerogels as polymer-crosslinked aerogels (X-aerogels). New applications for aerogels, as in ballistic protection, are within reach.[8]

The crosslinking process was recently extended to RF aerogels in order to render them more robust. Thus, dangling hydroxyl groups on the surface of the RF skeletal nanoparticles (RF-OH) were connected via reaction with Desmodur N3300A, a trifunctional isocyanate supplied by Bayer (see below).[9] The polyurea aerogels described herewith were the result of a curious observation along that process: when the crosslinking reaction of the triisocyanate with the RF-OH groups was assisted (catalyzed) with a base (triethylamine, Et$_3$N), the triisocyanate bathing solution gelled, yielding a gel (RF) inside another, which clearly came from gelation of the isocyanate.

Direct gelation of isocyanates has been reported and studied since the 1950's as a side reaction during formation of polyurethanes. Specifically, it was noted that certain catalysts cause gelation of isocyanate-terminated polyurethane prepolymers by crosslinking polymeric chains through allophanate bridges, while others cause gelation through trimerization of the isocyanates into isocyanurates.[10] Without hard chemical evidence, the first purposeful conversion of a multifunctional isocyanate into polyisocyanurate aerogels was reported in the mid 1990s by De Vos and Biesmans;[11] the process used Suprasec DNR,[12] (a condensation oligomer of 4,4′-diphenylmethane diisocyanate, abbreviated as MDI) and several trimerization catalysts, most notably 1,4-diazobicyclo[2.2.2]octane (DABCO).[11] Those aerogels demonstrated exceptionally low thermal conductivities (8.5 and 15 W m^{-1} K^{-1} for evacuated (<10 mbar) and air-filled 0.21 g cm^{-3} samples, respectively), high surface areas (about 300 m^2 g^{-1} at 0.24 g cm^{-3}), and upon pyrolysis under inert atmosphere they yielded carbon aerogels with yields (~40% w/w) comparable to those obtained from RF aerogels (~50% w/w). However, the outer gel obtained during crosslinking of RF wet-gels was not the product of base-catalyzed trimerization of the isocyanate groups; that gel was found to consist of polyurea (abbreviated herewith as PUA) formed via the Et$_3$N-catalyzed reaction of the triisocyanate with residual water in the crosslinking bath.

In general, polyureas and polyurethanes are prepared from isocyanates and multifunctional amines or alcohols, respectively. High surface area polyurethanes as the stationary phase for chromatographic separations were reported in the early 1970s via reaction in CH$_2$Cl$_2$ of polymeric MDI (e.g., Mondur MR) and a pentafunctional oligomer made by oxypropylation of diethylenetriamine.[13] Those materials were first obtained as

precipitates rather than gels, however, later modification of the process with sugar derivatives as polyols and more polar solvents as the reaction medium yielded gels and eventually aerogels. For example, Tan *et al.* used toluene diisocyanate to crosslink and induce pyridine-catalyzed gelation of acetone solutions of cellulose acetate and cellulose acetate butyrate. The resulting wet-gels were dried to aerogels with SCF CO_2. The motivation of that work was synthesis of high impact strength aerogels, although the mechanical properties were not quantified.[14] A similar approach was followed later first by Rigacci who, with an eye to thermal suprinsulation, used DABCO-catalyzed reaction in DMSO/ethyl acetate mixtures of an MDI derivative with saccharose and pentaerythritol.[15] The MDI derivative was Lupranat M20S, a BASF product similar to Suprasec DNR by ICI, and the product was nanoparticulate polyurethane aerogels, whose macro- versus mesoporosity was controlled by adjusting the Hildebrand solubility parameter via the DMSO/ethylacetate ratio. Reported thermal conductivities were lower than those of standard polyurethane foams (0.022 vs. 0.030 W m^{-1} K^{-1}, respectively, at room temperature and atmospheric pressure and bulk densities, r_b, at ~0.2 g cm^{-3}).[15] Later, Fischer and Rigacci revisited the Tan *et al.* approach of crosslinking cellulose acetate in acetone using again Lupranat M20S and dibutyltin laurate as catalyst; those aerogels were considered "green," because they involved a natural product (cellulose), and demonstrated very high elastic moduli (in the 200-300 MPa range at $0.75 \leq \rho_b \leq 0.85$ g cm^{-3}) and low thermal conductivities ranging from 0.029 W m^{-1} K^{-1} (at atmospheric pressure) to 0.006 W m^{-1} K^{-1} (at 2×10^{-5} mbar) for samples with ρ_b=0.25 g cm^{-3}.[16]

Polyurea (PUA) aerogels were first mentioned in the De Vos – Biesmans 1994 U.S. Patent,[11a] while a detailed comparative study with polyurethane and silica aerogels,

mainly from a thermal insulation perspective, was published recently by Lee, Gould and Rhine.[17] Those PUA aerogels were synthesized in acetone via Et_3N-catalyzed reaction of MDI, or polymeric MDI-type isocyanates with triamines, while polyurethane aerogels were prepared from the same isocyanates and an ethylene oxide-modified polyether polyol (Multranol 9185). PUA aerogels were nanoparticulate like silica while polyurethane aerogels were nanofibrous, similar to the materials reported by Fischer and Rigacci (see above).[16] At similar densities (0.12-0.13 g cm^{-3}) PUA aerogels demonstrated lower thermal conductivities than polyurethane aerogels (0.018-0.019 W m^{-1} K^{-1}, vs. 0.027 W m^{-1} K^{-1}, respectively). Both aerogel types, however, had higher thermal conductivity values than silica (0.012 W m^{-1} K^{-1}) at 0.09 g cm^{-3}.

Polyureas are also prodced via reaction of isocyanates with water by a sequence that initially yields an amine through decomposition of an unstable carbamic acid (eq 1).

$$OCN^{\diagup R \diagdown}NCO \; + \; H_2O \; \rightleftharpoons \; \left[OCN^{\diagup R \diagdown}\underset{H}{N}\overset{O}{\diagup}\diagdown OH \right] \; \rightleftharpoons \; OCN^{\diagup R \diagdown}NH_2 \; + \; CO_2 \qquad (1)$$

carbamic acid
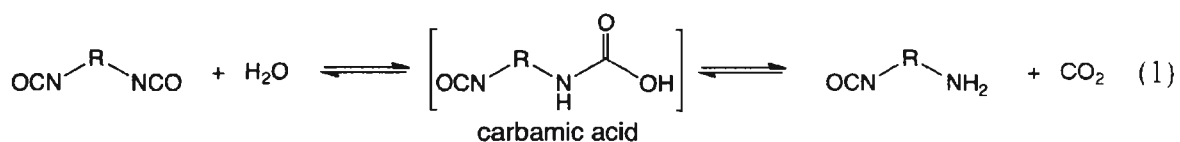
Subsequently, the amine reacts with yet-unreacted isocyanate yielding urea (eq 2).

$$OCN^{\diagup R \diagdown}NH_2 \; + \; OCN^{\diagup R \diagdown}NCO \; \rightleftharpoons \; OCN^{\diagdown R \diagup}\underset{}{\overset{H}{N}}\overset{}{\underset{O}{\diagup}}\overset{H}{N}^{\diagdown R \diagup}NCO \qquad (2)$$
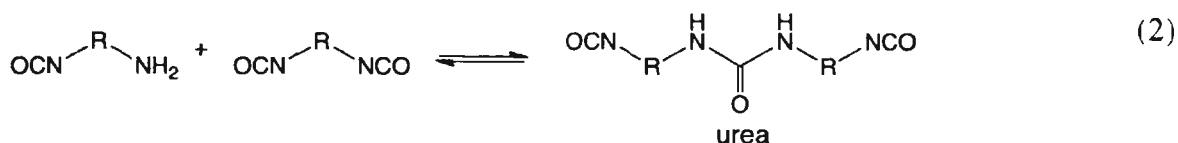
urea

Reaction 2 takes place much faster than reaction 1, because amines are much better nucleophiles than water.[18]

However, the sequence of the reactions 1 and 2 is not associated with the typical synthetic methods of bulk polyureas. Instead, it is involved in the environmental curing of films baring free isocyanates, while, owing to the CO_2 side product, it is also used for the formation of polyurethane foams whereas a small amount of water added in the reaction mixture acts as a foaming agent.[19] We find that process very attractive though, because it replaces use of expensive amines with "green" water. As it will become evident below, the method works best with triisocyanates such as Desmodur N3300A or Desmodur RE yielding aerogel monoliths over a quite wide density range (0.016-0.55 g cm^{-3}). Diisocyanates such as Desmodur N3200, toluene diisocyanate (TDI) or monomeric MDI also gel, but at higher concentrations, and the resulting aerogels are not as robust. The ensuing discussion is based on aerogels derived from: (a) Desmodur N3300A for their variable nanomorphology as a function of density, and their mechanical properties, which are comparable, and in some aspects superior to those of X-aerogels; (b) Desmodur RE for its high-yield conversion to carbon aerogels; and, (c) Desmodur N3200 as a typical example for the gelation of diisocyanates. The versatility and multifunctionality of those materials is best demonstrated with density-gradient monoliths whereas the high-density end combines high mechanical strength with flame retardancy, and relevant applications are discussed.
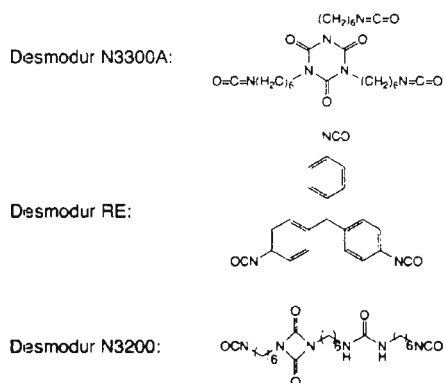
2. Experimental Section

Materials. Monomers Desmodur N3300A triisocyanate, Desmodur RE triisocyanate, Desmodur N3200 diisocyanate, toluene diisocyanate (Mondur TD) and MDI (Mondur CD) were donated generously from Bayer Corporation. All monomers except Desmodur RE are supplied in neat form and were used as received. Desmodur RE is supplied as a solution in ethyl acetate, which was removed with a rotary evaporator before use. Anhydrous acetone was produced from lower grade solvent by distilling over P_2O_5. Triethylamine (99% pure) was purchased from ACROS and was distilled before use.

Polyurea aerogels of different densities were prepared by varying the concentration of the monomer by first dissolving either 1.375 g, 2.75 g, 5.5 g, 11.0 g, 16.5 g or 33 g of Desmodur N3300A in a constant volume (94 mL) of dry acetone. (The seemingly arbitrary choice of monomer and solvent amounts bares no particular significance and stems from the fact that the method described here evolved from previous work with isocyanate crosslinked aerogels;[7-9] what matters is the molar concentrations of the individual components.) Subsequently, for each monomer concentration 1.5, 3.0 or 4.5 mol equivalents of water was added, and sols were obtained by adding triethylamine at either 0.3%, 0.6% or 0.9% w/w relative to the total weight of the isocyanate monomer plus solvent. The final N3300A monomer concentrations were approximately 0.029 M, 0.056 M, 0.11 M, 0.21 M, 0.30 M or 0.52 M. Thus, in a typical procedure, 1.375 g (0.0028 mol) of N3300A was dissolved in 94 mL of dry acetone, 1.5 mol equivalents of water (0.073 mL, 0.0042 mol) was added and finally the sol was obtained by adding 0.26 mL of triethylamine (0.3% w/w as defined above). The sol was shaken vigorously and it was poured into polypropylene syringes used as molds (AirTite

Norm-Ject syringes without needles purchased from Fisher, Part No. 14-817-31, 1.40 mm

I.D.). The top part of the syringes was cut off with a razor blade and, after the syringes

were filled with the sol, it was covered with multiple layers of Parafilm^{TM} and solutions

were left to gel. The particular sol of our example gelled in approximately 24 h. The

gelation time (defined as the point when a sol does not move by mild shaking) depends

on the concentration of the monomer, water and the catalyst and varies from 24 h to

approximately 5 min (at the highest concentrations of all three). For direct comparison,

gels with other isocyanates (Desmodur RE, Desmodur N3200 and Mondur TD) were

formulated by varying the amount of the monomer in such a way that the final molar

concentrations of the monomers in the sols would be about equal to those used for

N3300A. With Desmodur RE triisocyanate it was possible to obtain gels over the entire

concentration range used with Desmodur N3300A. Gels from Desmodur N3200 and

Mondur TD were obtained only for monomer concentrations above ~0.20 M. All

formulations and gelation times are summarized in Tables 1S-9S of the Supporting

Information (S.I.). All gels were aged for a day. Subsequently, gels were removed from

their molds and were placed individually into fresh acetone, approximately 4× the

volume of each gel. The solvent was changed two more times every 24 h. Finally, wet-

gels were dried into PUA aerogels with liquid CO_2 in an autoclave, taken out at the end

as a SCF. Alternatively, xerogels were obtained by ambient drying of acetone-filled wet-

gels, while aerogel-like materials were prepared from the two highest density samples

(those made with [N3300A] at 0.3 or 0.5 M) by exchanging acetone with pentane (4

washes), followed by drying at 40 °C under ambient pressure. Relevant properties of

xerogels and pentane-dried gels are provided in Table 10S of the S.I.

Variable-density PUA aerogels were synthesized by filling syringe molds, similar to those described above, with a high concentration sol (e.g., [N3300A]=0.52 M), which was simultaneously and constantly diluted using a second pump with a low concentration sol (e.g., [N3300A]=0.109 M).[20] For this we used two MINI-PUMP Variable Flow pumps, Model Number 13-876-2 (capable of delivering 0.4 - 85 mL min^{-1}) purchased from Fischer Scientific and run at 11 mL min^{-1}. The high-concentration sol container was stirred continuously with a magnetic stirrer. The resulting sols became hazy and gelled progressively from the bottom up. The resulting gels were removed from the molds and were processed in a similar fashion to the uniform density samples. The variable density was confirmed with NMR imaging (MRI) and direct measurement by cutting disks along the axis of the aerogel. Variable-density samples were tested for flammability by igniting them from the low-density end as described below.

Methods and Equipment. Drying with SCF CO_2 was conducted in an autoclave (SPI-DRY Jumbo Critical Point Dryer, SPI Supplies, Inc., West Chester, PA). Samples submerged in the last wash solvent were loaded in the autoclave and were extracted at 14 $^\circ$C with liquid CO_2 until no more solvent (acetone) was washed off. Then the temperature of the autoclave was raised above the critical point of CO_2 (32 $^\circ$C, 73.8 bar), and the pressure was released isothermally at 40 $^\circ$C. All dry gels were in cylindrical form so that bulk (envelop) densities (ρ_b) were determined from their mass and volume, which in turn was determined from the geometric dimensions of each sample. Skeletal densities (ρ_s) were determined using helium pycnometry with a Micromeritics AcuuPyc II 1340 instrument. Porosities, Π, were determined from the ρ_b and ρ_s values according to: $\Pi=100\times[(1/\rho_b)-(1/\rho_s)]/(1/\rho_b)$. Surface areas ($\sigma$) by the Brunauer-Emmett-Teller (BET)

method were determined by nitrogen sorption porosimetry using a Micromeritics ASAP 2020 Surface Area and Pore Distribution Analyzer. Samples for surface area and skeletal density determinations were outgassed for 24 h at 80 °C under vacuum before analysis. PUA aerogels were characterized chemically by infrared spectroscopy (IR) in KBr compressed pellets using a Nicolet-FTIR Model 750 Spectrometer, and by solids ^{13}C NMR spectroscopy with samples ground into fine powders and packed into 7 mm rotors, using a Bruker Avance 300 Spectrometer with 75.475 MHz carbon frequency, magic angle spinning (7 kHz), broad-band proton suppression, and the CPMAS TOSS pulse sequence for spin sideband suppression. ^{13}C NMR spectra were externally referenced to the carbonyl of glycine (176.03 ppm relative to tetramethylsilane). For magnetic resonance imaging (MRI) we used solvent-exchanged wet-gels filled with water on a 7 Tesla (300 MHz for proton) Varian MRI system equipped with a horizontal bore system and a QUAD-60 coil fitting samples with diameter <60 mm. 3D images were reconstructed by stacking 2D slices obtained using a multi-slice acquisition scheme and a spin-echo pulse sequence, whereas the imaging parameters were optimized to maximize the intensity gradients to reflect density variations. One scan covered 4 cm length divided up to 25 slices with 0.5-3.0 mm slice thickness and 30 μm resolution in 2D. The individual pores of the aerogels were not resolvable on the images from the MRI, but the imaging intensity on each slice varies as a function of the water content in the pores. Therefore, high gel density corresponds to low MRI signal intensity and low gel density to high MRI signal. Scanning Electron Microscopy (SEM) was conducted with samples coated with Au-Pd using a Hitachi S-4700 field emission microscope. X-ray photoelectron spectroscopy (XPS) was conducted with a Kratos Axis 165 Photoelectron

Spectrometer. Samples were pre-sputtered with Ar ions for 1 min prior to analysis. X-ray diffraction (XRD) was conducted using a Scintag 2000 diffractometer with Cu Kα radiation and a proportional counter detector equipped with a flat graphite monochromator. Degrees of crystallinity for the various PUA aerogels were calculated by drawing the baseline (amorphous halo) across the entire diffractogram passing just underneath the diffraction peaks, and dividing the area under the peaks left out of the amorphous hallo over the total area under the diffractogram. The fundamental building blocks of the aerogel microstructures were probed with ultra small- and small-angle neutron scattering (USANS and SANS). USANS measurements were performed at the National Institute of Standards and Technology Center for Neutron Research (NCNR) using the BT-5 Perfect Crystal SANS instrument,[21] while SANS measurements were performed at the NCNR, employing the NG7, 30-m SANS instrument,[22] and at the Manuel Lujan Jr. Scattering Center of the Los Alamos National Laboratory, using the time of flight, low-Q Diffractometer (LQD).[23] The combination of instruments allowed probing of structural features in the range of 0.001 – 20 μm. The scattering data are reported in the absolute units of differential cross section per unit volume (cm^{-1}) as a function of Q, the momentum transferred during a scattering event. In all cases, data were reduced by conventional methods and corrected for empty cell and background scattering. In the case of the USANS data, an additional correction was made for slit smearing.[24] Quasistatic mechanical characterization (compression testing) was conducted according to the ASTM D695-02a standard on cylindrical specimens, using a MTS machine (Model 810) equipped with a 55000 lb load cell, as described previously.[25] According to that ASTM standard, the height-to-diameter ratio of the specimen should be

2:1; typical samples were ~1.3 cm in diameter, ~2.6 cm long. Mechanical testing at cryogenic temperatures was conducted by wrapping samples in aluminum foil and dipping in liquid N_2 for 8 h. Samples never came in contact with liquid N_2. Subsequently, samples were unwrapped, quickly placed in the test platen and tested within 5 s. Thermogravimetric analysis TGA was conducted in air or under N_2, with a TA Instruments Model 2920 apparatus at a heating rate of 10 °C/min. For flammability testing, samples were held horizontal by one end and a Bunsen burner was brought to the unsupported end of the sample and left until the sample had ignited. Once ignited the Bunsen burner was removed and the samples were allowed to burn undisturbed. Movies were recorded with a digital camera either till the samples were consumed completely (case of low-density PUA aerogels) or till the flame was self-extinguished (case of high-density samples). Carbon aerogels were produced by pyrolysis of PUA samples at 800 °C in a tube furnace under flowing dry Ar (60-65 mL min^{-1}) for 3 h. Elemental analysis for CHN was conducted in house with a Perkin Elmer CHN analayzer, model 2400 calibrate with acetanilide.

3. Results and Discussion

This section describes the synthesis of PUA aerogels (Section 3.1), their characterization (Sections 3.2 and 3.3), and application specific properties (Section 3.4).

3.1. Synthesis of PUA aerogels. As summarized in Scheme 1, gelation is induced by adding water and Et_3N in solutions of polyfunctional isocyanates in acetone. Sols become progressively hazy and eventually turn into white gels. Without Et_3N gel in much longer time periods (~3 days), while use of NH_4OH as catalyst accelerates the process causing

fast precipitation rather than gelation. Wet-gels were aged to ensure complete reaction of the monomer and solvent-exchanged (washed) with anhydrous acetone. All washes were collected and no residue was detected, confirming that all isocyanate was incorporated in the gels. All sols able to gel can also be dried into robust aerogel monoliths (see photograph embedded in Scheme 1) by extracting the pore-filling solvent (acetone) with liquid CO_2 taken out at the end as a SCF. Gelation of triisocyanates (aliphatic Desmodur N3300A and aromatic Desmodur RE) takes place with monomer concentrations as low as 0.029 M, while gelation of diisocyanates [aliphatic Desmodur N3200, aromatic Mondur TD (toluene diisocyanate; TDI) and aromatic Mondur CD (4,4′-diphenylmethane diisocyanate; MDI)] takes place only at higher monomer concentrations (>0.2 M, see Tables S.1-S.9 in S.I.) Using Desmodur N3300A triisocyanate as our model system, the gelation time (Figure 1, and Tables 1S-6S in S.I.) decreases with increasing concentrations of the isocyanate, while the concentration effect of water and the catalyst (Et_3N) is more pronounced at the lower monomer concentrations.

Scheme 1. Synthesis of Uniform-density Polyurea (PUA) Aerogels and Photograph of Samples Made of Desmodur N3300A (densities below each sample in mg cm^{-3})
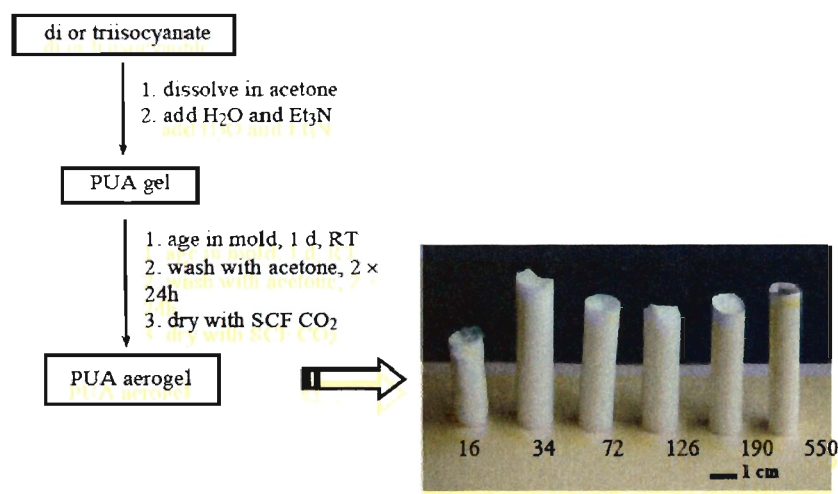
Taking gelation time as a rate indicator, it is found that within the large margin of error associated with the innate system parameters (mainly the concentration of the catalyst),[26] the overall process is first order in both H_2O and Et_3N (see Insets in Figure 1), suggesting rate=k[N3300A][H_2O][Et_3N] as the rate law, and eq. 5 (Scheme 2) as the rate determining step. It is noted further that liquids ^{13}C NMR in acetone-d_6 under the gelation conditions for N3300A (Figure 1S in S.I.) shows a gradual decrease of all monomer resonances, with no new peaks assignable to urea. By the gelation point all resonances have been lost.

This observation is also in accord with the rate-determining step occurring before formation of the carbamic acid. Afterwards, reactions should proceed fast to the final product that gets phase-separated (hence the loss of NMR signal) and no accumulation of intermediates is observed.[27] According to that model, PUA elementary (primary) particles should start coming together almost right after the polymer is formed, while further polymerization could still occur at dangling reactive sites (-NH_2 and –NCO) on the surface of newly formed nanoparticles, thus justifying a post-gelation aging step, although the actual need or the effect of the latter have not been investigated systematically.

Gelation proceeds qualitatively similarly in acetonitrile, while in DMSO it takes place very fast causing large bubbles of CO_2 to be trapped in translucent gels. Although not pursued further, those DMSO-derived aerogels are interesting materials in their own right as they combine large foam-like macroporosity with nanoporous walls similar to those obtained in acetone or acetonitrile as described in Section 3.2 below. If acetone wet-gels are left to dry under ambient conditions, they undergo extensive shrinkage and

yield xerogel-like materials. Alternatively, by applying a method developed previously with polyurea-crosslinked silica aerogels,[27] wet-gels made with the two highest isocyanate concentrations (~0.3 and 0.5 M) and solvent-exchanged with a low vapor pressure/surface-tension solvent like pentane, can be dried under ambient pressure at slightly elevated temperature (e.g., 40 °C), yielding materials similar in appearance and properties to those obtained by the SCF CO_2 route. (Selected data for PUA xerogels and pentane-dried samples are listed in Table 10S of the S.I.) The ambient pressure drying method is currently used for making larger monolithic aerogel pieces for evaluation in certain aeronautical and anti-ballistic applications. For consistency, however, the presentation below focuses on samples obtained through SCF CO_2 drying.

Scheme 2. Gelation Mechanism through Reaction of Isocyanates with Water
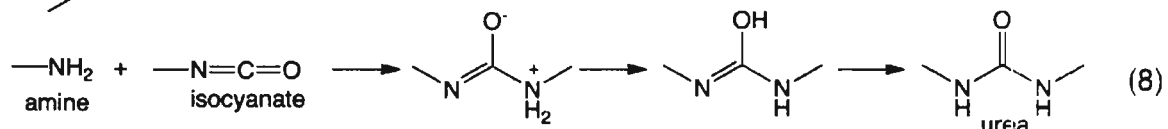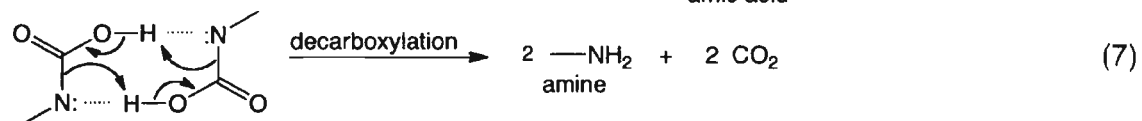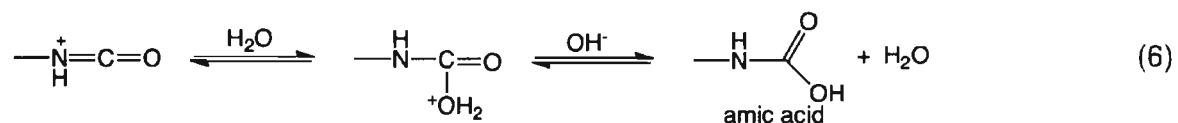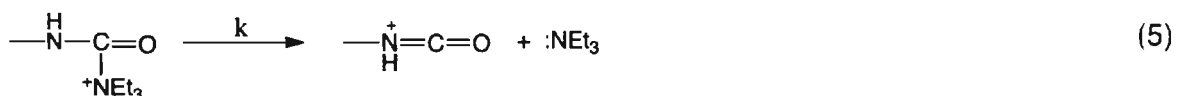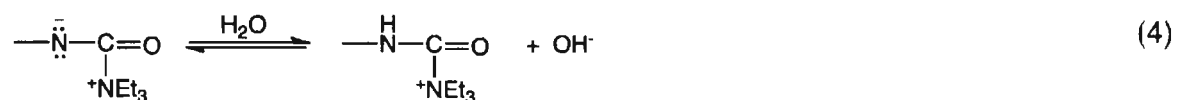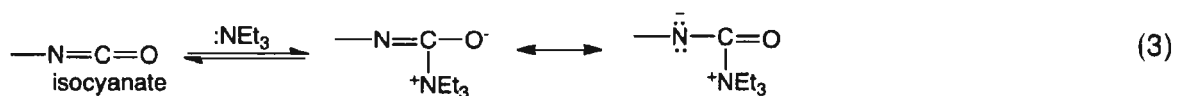
3.2. Characterization of PUA Aerogels. 3.2a. *Chemical Characterization.* The chemical identity of PUA aerogels was probed with IR and solids ^{13}C NMR. The degree of molecular order within the solid framework was investigated with x-ray diffraction (XRD).

Using solids ^{13}C NMR and Desmodur N3300A-derived aerogels as the model system, the NCO carbon resonance at 121 ppm has disappeared completely, the resonance of the isocyanurate carbonyl carbon at 149 ppm is still present and the new resonance of the urea C=O carbon has shown up at 159.6 ppm (Figure 2). The relative intensities of the urea, isocyanurate and aliphatic carbon resonances remain the same irrespective of the relative amounts of water, catalyst, or the concentration of the isocyanate (compare for example Figures 2A and 2B). Similar data are shown in Figures 2S and 3S of the S.I. for Desmodur RE triisocyanate- and Desmodur N3200 diisocyanate-derived aerogels.

IR spectroscopic data (Figure 3) agree well with the ^{13}C NMR data. Again, disappearance of the NCO absorption (2264 cm^{-1}) confirms complete reaction of the NCO groups. The relative intensities of the CH$_2$ and isocyanurate carbonyl stretches (~2990 cm^{-1} and 1690 cm^{-1}) remain the same between the monomer and the aerogel signifying that trimerization of the NCO groups is not a viable gelation mechanism in our case. Instead, we observe prominent new absorptions at 3373 cm^{-1} and 1563 cm^{-1} assigned to the polyurea NH stretching and bending vibrations, respectively.

XRD of PUA aerogels derived from Desmodur N3300A and Desmodur RE triisocyanates show broad but well-defined diffractions indicating the presence of

nanocrystallinity. On the other hand, PUA aerogels derived from N3200 diisocyanate are completely amorphous (Figure 4). The angle of diffraction from N3300A-derived PUA aerogels (21°) is similar to that reported for chemically similar poly(hexamethyleneurea) derived from hexamethylene-1,6-diisocyanate and hexamethylene-1,6-diamine.[29] Neither the degree of crystallinity nor the angle of diffraction (see Table 1) vary with the density of the samples, implying that the average distance between adjacent molecules within the solid PUA framework remains the same, or conversely that the polymer chains are packed the same way irrespective the gelation time, again consistently with reaction 5 (Scheme 2) being the rate determining step. Overall, the ^{13}C NMR, IR and XRD data together point to that the concentrations of isocyanate, water and catalyst have no effect on the chemical make-up of the PUA aerogels. Therefore, the variation of the nanomorphology as a function of the bulk density that we shall see below, cannot be attributed to differences in the chemical composition, or the way molecules are packed together. It will have to be attributed to the way elementary particles come together to form the framework.

3.2b. General Material Properties. Those are summarized in Table 1 for samples prepared using the middle formulations of water and triethylamine (i.e., 3.0 molar excess of H_2O and 0.6% w/w Et_3N, as detailed in the Experimental Section), for each concentration of the isocyanates (Desmodur N3300A, Desmodur RE and Desmodur N3200). The complete data for all N3300A samples prepared with all water and catalyst formulations are given in Tables 11S-16S of the S.I.

First, all samples shrink relative to their molds. The linear shrinkage of N3300A-derived aerogels is about constant for samples prepared with isocyanate concentrations

between 0.029 M and 0.30 M, and varies between 9 and 15% (Table 1 and Figure 5A). The shrinkage for samples prepared with [N3300A] = 0.52 M is much higher, ~25%. By the same token, however, it is noted that the 9-15% shrinkage for the first five samples does not take place during gelation, aging or washing. Those samples come out of the molds after aging still in tight contact with the mold walls. Shrinkage in the middle- to low-density PUA samples seems to takes place exclusively during the SCF CO_2 drying step. Increasing the number of post-aging acetone washes from two to four seems to decrease linear shrinkage to between 8 and 10%, but does not eliminate it. On the other hand, the larger shrinkage of the samples prepared with [N3300A]=0.52 M occurs during gelation. Shrinkage is a subject discussed by all previous authors in the area of polyurethane and polyurea aerogels; for isocyanate/amine-derived polyurea aerogels, shrinkage was observed explicitly during aging and drying, it was minimized by increasing the amount of the isocyanate, and therefore it has been attributed to crosslinking of polymeric chains.[17] Clearly, this is not the case in isocyanate/water derived PUAs. Based on our observations above, shrinkage for samples prepared with [N3300A]<0.30 M could be partly attributed to surface tension forces traced to residual gelation water (which is reduced with more post-aging acetone washes), but mostly to the natural tendency of the dry polymer to "settle" in order to maximize Van der Waals interactions between non-covalently bonded polymeric segments in close proximity. The disproportionally higher shrinkage (24-27%) of the most concentrated samples ([N3300A] = 0.52 M) is practically invariant of the water and catalyst concentration (see Table S.10), hence of the gelation time. The higher shrinkage of those samples has to be attributed to their vastly different nanomorphology, i.e., the way elementary building

blocks assemble to form the nanostructure – see Section 4.2.3 below. The discontinuity in the shrinkage above [N3300A]=0.30 M is certainly reflected upon the bulk densities (ρ_b, Table 1): while up to that point ρ_b varies linearly with the concentration of the isocyanate in the sol (Figure 5A), it appears disproportionally higher beyond that point. On the other hand, skeletal densities, ρ_s, are all within the range of 1.20-1.30 g cm^{-3}, indicating absence of closed porosity and in agreement with the same chemical composition and packing of the polymer chains within the elementary building blocks (particles, fibers). Consequently, porosities, Π, as % v/v of empty space, formally calculated from the ρ_b and ρ_s values, show the same discontinuity as ρ_b at [N3300A]>0.30 M (Table 1), so that at the end Π and ρ_b correlate linearly over all formulations (Figure 5B). Finally, BET surface areas (Table 1) are also relatively high (220-250 m^2 g^{-1}) for samples prepared with [N3300A]<0.11 M, dropping suddenly to 169 m^2 g^{-1} for [N3300A] = 0.21 M and below 70 m^2 g^{-1} for [N3300A]>0.3 M, suggesting again a change in microstructure.

Table 1 also includes similar data for aerogels derived from aromatic Desmodur RE triisocyanate and aliphatic Desmodur N3200 diisocyanate. Those samples show no identifiable trends in shrinkage, and consequently we observe no sudden jumps in their bulk density or their porosity. Nevertheless, the BET surface areas of the Desmodur RE-derived PUA samples show a sudden drop from ~320 m^2 g^{-1} to the 70-20 m^2 g^{-1} range when [Desmodur RE]>0.056 M, that is much earlier (density-wise) than what is observed in the N3300A-derived samples. (As we saw above, a similar drop in surface area was observed at [N3300A]> 0.3 M.) Further, it is noteworthy that despite high porosities (e.g., 85% v/v), the BET surface area of the Desmodur N3200-derived samples is uniformly very low, <20 m^2 g^{-1}, over all possible densities.

Table 1. Selected material properties of PUA aerogels prepared with the isocyanates indicated using the middle H_2O and Et_3N formulations. that is 3.0 mol equivalents of water and 0.6% w/w Et_3N (refer to Tables 1S-8S)

[isocyanate] in sol (M)	diameter (cm) [a]	linear shrinkage (%) [a,b]	bulk density. ρ_b (g cm^{-3}) [a]	skeletal density. ρ_s (g cm^{-3}) [c]	crystallinity (%) [2θ]	porosity. Π (% void space)	BET surface area. σ (m^2 g^{-1})	average pore diameter (nm) [d]
Desmodur N3300A								
0.0285	1.28±0.01	13.3±0.56	0.016±0.000₄	1.24=0.23	28 [21.1]	98.6	222.4	53.7 [50.0]
0.0561	1.35±0.01	9.12±0.85	0.034±0.000₄	1.31±0.06	34 [20.5]	97.5	243.5	38.9 [39.0]
0.1092	1.27±0.01	14.8±0.18	0.072±0.005	1.21=0.03	33 [20.3]	93.9	234.7	32.3 [32.0]
0.2073	1.32±0.01	10.6±0.18	0.126±0.001	1.30=0.07	35 [20.3, 44]	90.3	169.4	41.6 [41.0]
0.2960	1.27±0.03	14.1±1.78	0.19±0.01	1.21=0.02	35 [20.5, 45]	84.2	67.5	40.7 [41.0]
0.5171	1.11±0.02	25.0±1.3	0.55=0.03	1.20=0.00₁	35 [20.5, 45]	54.1	53.8	38.7 [39.0]
Desmodur RE								
0.0284	1.29±0.01	13±0.64	0.023±0.002	1.24=0.14	8.2 [23.4, 43.5]	98.1	222.4	12 [11.8]
0.0563	1.21±0.04	18.5±2.7	0.037±0.003	1.30=0.01	9.1 [25.3, 43.5]	97.1	320.7	7.6 [8.4]
0.1099	1.29±0.01	12.8±0.7	0.062±0.005	1.23=0.03	9.0 [24.7, 43.7]	95	6.55	7.5 [8.7]
0.2101	1.28±0.03	13.3±2.1	0.15±0.02	1.24±0.23	12.0 [24.3, 43.9]	87.8	6.49	7.75 [7.6]
0.3019	1.3=0.6	12.4±0.4	0.18=0.01	1.24=0.25	14.9 [20.8, 43.2]	85.7	19.9	10.6 [11.2]
0.5360	1.31±0.01	12.1±0.2	0.25=0.02	1.24=0.28	10.8 [21.2, 43.8]	79.8	3.24	6.6 [7.8]
Desmodur N3200								
0.2066	1.26±0.01	14.6±1.0	0.175±0.007	1.15=0.01	0.0	84.6	4.3	7.4 [8.2]
0.2955	1.13±0.01	24.7±0.8	0.37=0.01	1.15±0.01	0.0	68.5	12.8	8.5 [9.1]
0.5166	1.05±0.05	14.3±0.9	0.54=0.07	1.15=0.03	0.0	52.7	23.6	12.0[12.3]

a. Average of 5 samples. (Mold diameter: 1.40 cm.) b. Shrinkage = 100 × (sample diameter – mold diameter)/(mold diameter). c. Single sample. average of 50 measurements. d. By the BJH-desorption method: in brackets: width at half maximum.

3.2c. Microscopic Characterization. The structure of PUA aerogels as a function of their preparation conditions was probed semi-quantitatively with N_2 sorption porosimetry and SEM, and quantitatively with SANS/USANS.

By SEM (Figure 6) all N3300A derived samples appear macroporous with voids larger than 50 nm. This macroporosity is clearly evident in the N_2 sorption data included in Figure 6: the adsorption branch rises sharply above relative pressure (P/P_o) of 0.9, and it does not reach saturation at the condensation point of N_2 at (P/Po)~1. The presence of hysteresis loops, however, implies the presence of some mesoporosity as well. BJH-desorption plots (insets in Figure 6) are quite broad and they look like overlapping pore-size distributions (only the absolute maximum is reported in Table 1).

As far as the skeletal framework is concerned, according to Figure 6 at low densities (e.g., <0.072 g cm^{-3}) N3300A-derived PUA aerogels are fibrous, but they clearly turn particulate at higher densities (e.g., at 0.55 g cm^{-3}). The nanomorphology at each density depends only on the concentration of the isocyanate in the sol and it is independent of the concentration of water or the catalyst (see Figure S.4). The morphology switch seems to take place in the 0.13-0.19 g cm^{-3} range. At higher magnification (Figure 6, insets) fibers at first (0.016 g cm^{-3}) appear relatively smooth but "knotty", and later (e.g., at 0.034 g cm^{-3}, or at 0.072 g cm^{-3}) they are clearly rough, as if they consist of agglomerations of particles. This situation becomes very pronounced at 0.13 g cm^{-3}, particulated strings seem to dominate at 0.19 g cm^{-3} and by 0.55 g cm^{-3} there is practically no remnance of any fibrous structure. Upon a more careful look at the 0.072-0.19 g cm^{-3} samples, strings appear consisting of disk-like structures (indicated by

circles and arrows). The idenity of those disk-like structures as independent building blocks of the fibers is confirmed by SANS/USANS below.

By changing the triisocyanate from flexible aliphatic N3300A to rigid aromatic Desmodur RE, Figure 7 shows an analogous behavior: at low densities the structure starts fibrous progressively turning particulate. That change takes place at much lower densities than in N3300A-derived aerogels; by 0.062 g cm^{-3} the RE-derived structure is particulate. The morphology of the Desmodur RE-derived fibers is different from those observed with N3300A aerogels; they consist of well-defined beads connected with narrow necks (see the 0.023 g cm^{-3} sample in Figure 7). As the density increases to 0.037 g cm^{-3}, the particle size remains about the same, but the interparticle necks have become wider; upon further increase in density the material appears nanoparticulate with a very faint remnance of strings, if any. With N3200-aerogels (Figure 8) the situation resembles the higher density Desmodur RE samples (refer to Figure 7), namely we observe a particulate structure, but overall particles now are larger than those of the RE aerogels by a factor of 2×.

The makeup of the features observed by SEM would give information about the gelation process post-phase separation. Since Desmodur N3300A-derived PUA aerogels show a broader range of nanomorphologies than those from Desmodur N3200 and Desmodur RE, they were chosen for further quantitative investigation with SANS/USANS at length scales extending from 1 nm to 20 μm (Figure 9).

By SANS/USANS, N3300A-derived PUA aerogels display density-dependent multi-length scales with at least two power-law regions (linear sections in the log-log

plots of Figure 9). The solid lines in Figure 9 are fits to the Unified Model of G. Beaucage (equation 9),[30] which distinguishes Guinier regimes overlapping significantly with Porod (power law) regimes and is used for analyzing data from multi-scale structures such as foams.

$$I(Q) = \sum_i G_i \exp\left(\frac{-Q^2(R_g)_i^2}{3}\right) + B_i \exp\left(\frac{-Q^2(R_g)_{i+1}^2}{3}\right) \times \left\{\left[\frac{erf(Qk(R_g)_i)}{\sqrt{6}}\right]^3 / Q\right\}^{\beta_i} \quad (9)$$

where $I(Q)$ is the scattering intensity, "i" refers to the structural level, $G_i = N_i(\Delta\rho)_i^2 V_i^2$, $B_i = 2\pi(\Delta\rho)_i^2 N_i S_i$, N_i is the number density of primary particles (i.e., the number of scatterers per unit volume), $(\Delta\rho)_i$ is the difference in scattering-length density between scatterers and the medium, S_i is the surface area of a scatterer, V_i is an average particle volume, k is an empirical constant (for polymeric mass fractals k=1.06) and β_i is the scattering exponent.[30] Data derived from Figure 9 are summarized in Table 2. To facilitate matching of data with scattering features (see footnotes in Table 2), scattering profiles in Figure 9 have been divided in several regions, starting with Porod scattering as Region I at high Q values. In that power-law region lower density aerogels ($\leq$0.072 g cm^{-3}) display exponents slightly more negative than -4.0, indicating that the smallest elementary building blocks of the aerogels (primary particles) have fuzzy interfaces, namely they display variations in density acress their interfaces. The origin of the fuzziness is unclear at this moment. It usually comes from core-shell structures, but in this case that is improbable.

Table 2. Results from Small Angle Neutron Scattering (SANS/USANS) of Polyurea Aerogels Derived from Desmodur N3300A

bulk density (ρ_b, g cm^{-3})	Primary particles				Secondary structures		
	t (nm)	R_g (nm)	$<R>$ (nm)	PSD ($m;\sigma$)	R_g (nm)	D_m	D_s
0.016[a]	0.8 ± 0.1	7.4 ± 0.9 [d]	3.5 [d]	3.2; 0.39	[n]	2.51 ± 0.06[e]	[n]
0.034[b]	1.1 ± 0.1	12.5 ± 0.2 [d]	5.1 [d]	4.7; 0.42	91 ± 3[f]	2.2 ± 0.1[g]	2.85 ± 0.02[h]
0.072[b]	0.90 ± 0.02	7.0 ± 0.5 [d]	3.0 [d]	2.7; 0.41	166 ±20 [j]	2.0 ± 0.3,[i] 2.74 ± 0.02[k]	--
0.13[b]	[c]	21.7 ± 0.1 [d]	10.4 [d]	9.7; 0.39	805 ± 145[l]	1.98 ± 0.02,[l] 2.35 ± 0.07[m]	--
0.55[a]	[c]	20.9 ± 0.5 [d]	12.5 [d]	12; 0.34	[n]	[n]	[n]

a. By SANS; b. By SANS/USANS; c. abrupt interface. For footnotes d.-m. refer to Figure 9: d. From the Guinier Region II in all samples; e. Sample 0.016, Region III; f. Sample 0.034, Region IV; g. Sample 0.034, Region III; h. Sample 0.034, Region V; i. Sample 0.072, Region III; j. Sample 0.072, Region IV; k. Sample 0.072, Region V; l. Sample 0.13, by deconvolution of Region III; m. Sample 0.13, Region IV; n. Q was not extended to low enough values to obtain data for these quantities.

The interfacial thicknesses, t, are calculated via eq. 10, by assuming Gaussian distribution of matter at the nanoparticle interface with

$$t = (2\pi)^{0.5}\sigma \tag{10}$$

standard deviation σ, and fitting the scattering intensity to the modified Porod's law (eq. 11).[31]

$$I(Q)=2\pi N(\Delta\rho)^2 S Q^{-4} \exp[-\sigma^2 Q^2] \tag{11}$$

All t fall at around 1 nm (Table 2). Higher density samples (>0.13 g cm^{-3}) give exponents equal to -4.0 indicating sharp (abrupt) interfaces. In Region II, all samples display a Guinier "knee," which is indicative of a fundamental length-scale and is attributed to the primary particles forming the materials. Analysis according to the Unified Model provides the radius of gyration (R_g), where for monodispersed spherical particles $R_g \approx 0.77R$ (R is the radius of the particles).[32] However, the monotonic fall-off in Region I implies polydispersity (monodisperse particles give rise to "ripples" in that region). Therefore, R_g values were analyzed further assuming particle polydispersity and log-normal distributions for the particle size. According to that analysis the radius of gyration is related to the mean radius of the scatterers by eq 12,[33]

$$(R_g)^2 = (3/5) (<R^8>/<R^6>) \tag{12}$$

where $<R^n>=m^n \exp(n^2\sigma^2/2)$, m is related to the mean, by $<R>=m \exp(\sigma^2/2)$ and σ is the standard deviation of the log-normal distribution. Table 2 provides both the R_g values and the mean primary particle radii, $<R>$, as well as the particle size distribution (PSD) in terms of m and σ. Overall, the elementary building blocks of all samples, fibrous or

particulate, are primary particles with radii increasing with ρ_b from ~3 nm to 12.5 nm. That increase in size may be attributed either to the length of the polymer (degree of polymerization) before phase separation, or to monomer reacting and accumulating on the surface of newly formed primary particles before they assemble to higher structures. Both explanations are quite probable; the second one finds support from the smoothing of the surface fuzziness of the primary particles, and from the neck broadening in the case of the Desmodur RE-derived samples (Figure 7: refer to the wider necks in the 0.037 g cm^{-3} samples relative to the 0.023 g cm^{-3} ones.)

In Region III, samples exhibit power law scattering again, with exponents between -2 and -3, indicating that primary particles form mass fractal secondary aggregates. The mass-fractal dimensions, D_m, are given by the slopes. The Guinier Region IV provides a second radius of gyration that is related (via $R_g \approx 0.77R$) to the radii of the secondary aggregates formed by the primary particles. Overall, with increasing ρ_b (and therefore primary particle size), the R_g values of the secondary aggregates increase (from 91 nm to 805 nm) while their fractal dimensions decrease (from 2.51 to 1.98) indicating that larger primary particles form larger, but less dense secondary aggregates. In that regard, the 0.072 g cm^{-3} and the 0.13 g cm^{-3} samples are particularly interesting. Here specifically, since both of $D_m \approx 2.0$, it is concluded that primary particles are aggregating to form disk-like secondary structures (with R_g equal to 166 nm and 805 nm, respectively). Disk-like structures are in fact visible in SEM (Figure 9, insets, disks are pointed at by arrows and circles) and they are stuck to form strings.

Indeed, similar analysis in the remaining regions of Figure 9 shows that secondary aggregates do assemble to form higher fractal agglomerates (fibers, Figure 6). Thus, in the sample with ρ_b=0.034 g cm^{-3} the exponent in power-law Region V is >3, indicating surface fractals with fractal dimension D_s=2.85±0.02. Based on the range of Q where that fractality appears, and by considering the SEM of that sample (Figure 6), surface fractality should be created by the fiber entanglement, whereas, apparently, an attempt to measure the surface area would depend on the surface area of the probe. In the case of the 0.072 g cm^{-3} sample, strings consisting of disk-like structures form mass fractals (D_m=2.74), which are more dense than those formed by the 0.13 g cm^{-3} samples (D_m=2.35).

The most dense samples (ρ_b=0.55 g cm^{-3}) appear as a classic aerogel: by SEM they appear as a collection of nanoparticles, while SANS indicates that they consist of smooth primary particles (<R>=12.5 nm) that assemble into larger secondary clusters (by SEM).

Putting all the chemical and microscopic evidence together, the structure of the PUA aerogels seems to be controlled by phase separation. Since Desmodur N3200 diisocyanate yields a flexible, more soluble linear polymer, phase separation takes place later leading to larger particles that tend to "collapse" in order to maximize Van der Waals interactions, hence the overall smoother microstructure observed in SEM (Figure 8) and the very small BET surface areas (Table 1). Triisocyanates develop a 3D molecular structure leading to earlier phase separation and smaller particles. The evolution of the microstructure with increasing density (SEM, Figures 6 and 7) could

have been explained by particles accumulating on newly formed strings. However, SANS/USANS data clearly show that this is not the case: primary particles assemble into secondary aggregates, which in turn are shown (whenever USANS data are available) to form higher fractal agglomerates (surface or mass). This hierarchical structure from primary particles to secondary globules or disks, to larger string-like aggregates precludes a particle-on-fiber growth model. Assembly of secondary particles into organized structures like fibers or strings should proceed via a reaction-limited cluster aggregation mechanism;[34] it is speculated that since particles are expected to be chemically connected through reaction of surface –NCO on one particle with -NH$_2$ or –NHCONH- groups on another, at low isocyanate concentrations formation of strings versus globules may be favored for steric reasons: in globules, the chemical energy stabilization by formation of interparticle urea bridges would be compromised by the energy to overcome crowding. At intermediate isocyanate concentrations, disks-like objects maximize chemical bond formation by stucking on top of one another in a string-like fashion. At higher isocyanate concentrations, or when the polymer solubility is low, the fast rise in the concentration of nanoparticles may lead to a diffusion-limited aggregation mechanism and the structure turns into nanoparticulate/globular (as in the 0.55 g cm^{-3} sample).[35] Both the smoothing of the primary particles and their size increase at higher N3300A concentrations (Table 2), as well as the SEM data for the Desmodur RE-derived PUAs, indicate that all mechanisms may be convoluted with monomer-cluster growth processes.[36] Nanoparticulate structures are more prone to shrink in order to maximize non-covalent interactions between polymer chains.

Table 3. Mechanical Characterization Data under Quasi-Static Compression at Room (23 °C) and cryogenic (-173 °C) temperatures of Desmodur N3300A-derived PUA Aerogels [a]

bulk density $(\rho_b,\ g\ cm^{-3})$	strain rate (s^{-1})	Young's Modulus $(E,\ MPa)$	speed of sound $(m\ s^{-1})$	yield stress at 0.2% offset strain (MPa)	ultimate strength $(UCS,\ MPa)$	ultimate strain (%)	Poisson ratio at strain: 5% [70% or 40%] [b]	specific energy abs. $(T,\ J\ g^{-1})$ [c]
23 °C								
polyurea aerogels								
0.016±0.000₄		[d]	[d]	[d]	[d]	[d]	[d]	[d]
0.034±0.000₄	0.05	3.868	337	0.12	3.9±0.5	90±1	0.20±0.03 [0.16±0.01]	9.7
0.072±0.005	0.05	7.027	312	0.20	45	92	0.21±0.02 [0.16±0.02]	22.75
0.126±0.001	0.05	20±3	398	1.1±0.1₄	54±3	91±0.₀	0.23±0.03 [0.17±0.04]	21±9
0.19±0.01	0.05	33±2	416	1.6±1.1	106±7	88±2	0.21±0.02 [0.18±0.03]	26.0
0.55±0.03	0.05	300±47	738	13±2	631±39	88±3	0.23±0.18 [0.22±0.04]	91±5
X-silica aerogels								
0.548±0.005	0.005	233±8	652	6.0±0.6	186±22	68±1	0.18	47.0±0.7
X-vanadia aerogels								
0.436±0.004	0.005	206±14	687	5.6±0.4	371±32	91±2	0.21±0.02 [0.23±0.03]	192±12
Cryogenic Temperature								
polyurea aerogels (-173 °C)								
0.016±0.000₄		[e]	[e]	[e]	[e]	[e]	[e]	[e]
0.034±0.000₄		[e]	[e]	[e]	[e]	[e]	[e]	[e]
0.072±0.005	0.05	2.77±0.04	196	0.10±0.03	10±1	72.0±0.2	0.30±0.03 [0.28±0.04]	33.25
0.126±0.001	0.05	25±7	445	3.0±0.2	8.0±0.1	45.0±0.1	0.31±0.04 [0.28±0.04]	28±2
0.19±0.01	0.05	75.5±0.5	632	9±1	19±4	50.0±0.0₃	0.32±0.04 [0.29±0.06]	26±2
0.55±0.03	0.05	490±8	943	50±3	100±6	42.0±0.2	0.33±0.05 [0.31±0.05]	54.6±0.0₁
X-silica aerogels (-196 °C)								
0.548±0.005	0.05	635±8	1076	19.9±1.8	107±12	16±1	0.20±0.03 [f]	9.9±0.6
X-vanadia aerogels (-196 °C)								
0.444±0.004	0.05	438±11	993	13.6±1.5	183±17	72±3	0.27±0.06 [f]	163±2

Table 4. Selected Material Properties of Desmodur N3300A- Derived Aerogels after Full Compresion

bulk denisty before compression. ρ (g cm^{-3}) [a]	diameter after full compression (cm) [b]	bulk density after compression ρ (g cm^{-3}) [c]	skeletal density ρ (g cm^{-3}) [d]	porosity. Π (% v/v void space)	BET surface area. σ (m^2 g^{-1})	average pore diameter (nm) [e]
0.072±0.005	1.4±0.25	0.35±0.32	1.22±0.12	71.6	67.8	8.5 [122]
0.126=0.001	1.42=0.18	0.55±0.14	1.22±0.01	54.8	8.22	31.3 [491]
0.19±0.01	1.42=0.13	0.66±0.51	1.24±0.05	46.7	0.9	25.3 [3171]
0.55±0.03	2.31=0.07	0.76±0.38	1.25±0.08	39.5	5.3	29.7 [393]

3.3. Macroscopic Properties Related to the Nanostructure. As evident from the Introduction, organic aerogels are mainly pursued for thermal insulation and for their conversion to carbon aerogels as electrodes for fuel cells and supercapacitors and as catalyst supports.[36] As it will be discussed below, conversion of PUA aerogels to carbons is particularly important because of its relevance to the synthesis of nanoporous metals and ceramics, while, from a fundamental perspective, one line of reasoning suggests that since the exceptional mechanical properties of polymer-cross-linked aerogels are traced to their conformal polymer coating, if aerogels consist only of polymer with similar nanostructure and interparticle connectivity as in polymer cross-linked aerogels, they should possess similar mechanical properties. According to Section 4.2.3 above, PUA aerogels appear to satisfy this condition, setting the stage for a detailed study of their mechanical behavior.

3.3a. Mechanical characterization. For direct comparison with polyurea-cross-linked inorganic aerogels (silica and vanadia, abbreviated as X-silica and X-vanadia), this study focuses on compression testing. Desmodur N3300A-derived aerogels were used again as the model system, and properties such as stiffness (quantified by Young's modulus, E), yield strength at 0.2% offset strain, ultimate compressive strength at maximum strain (UCS) and toughness (T, quantified by the specific energy absorption) were evaluated as a function of the density at both room and cryogenic temperatures under quasistatic conditions (i.e., low strain rates). Figure 10 shows typical stress-strain curves of cylindrical specimens under compression at both room and cryogenic temperatures. A room-temperature stress strain curve under repetitive loading-unloading conditions is also included (red line). The inset shows a magnification of the stress-strain curve at low

strains, from which we extract the Young's modulus and the compressive yield strength at 0.2% offset strain. Comprehensive data for the N3300A-derived PUA aerogels are summarized in Table 3 along with similar data from high-density X-silica and X-vanadia aerogels. Materials characterization data of fully compressed samples after testing are presented in Table 4. At room temperature, N3300A-drived aerogels are linearly elastic only under small compressive strains (<3%) and then exhibit plastic deformation until about 70% compressive strain, followed by densification and inelastic hardening, in pretty similar fashion to X-silica and X-vanadia aerogels. PUA samples do not buckle under compression, and they do not ultimately break into fragments, behaving in that regard similarly to X-vanadia, yielding transparent/translucent disks (above 80% strain, Figure11) where porosity has been decreased, although has not disappeared, and almost all surface area has been lost (see Table 4). Skeletal densities are basically equal before and after compression (compare Tables 1 and 4) signifying absence of closed pores, while the wide discrepancy between average pore diameters calculated by two methods (see footnote e in Table 4) indicates that the surviving porosity is mostly due to the macropores visible by SEM (Figure 11). The Poisson's ratios (Table 3) are small within the linear elastic range (up to 5% strain) and remain small as strain increases (even up to 70% strain, Table 3). This behavior is: (a) important because low Poisson's ratios at the nonlinear region prevent the rapid increase of radial and transverse strains that are often responsible for failure of materials in compression and (b) different from that of other solid materials such as dense polymers and metals where the Poisson's ratio is relatively low (0.25-0.35) in the elastic range, but it gets quite high (near 0.5) in the plastic regime (whenever one is observed).[37] Interestingly, as further noted in Table 3, all Poisson's

ratios are uniformly lower at the end of the plastic deformation regime (e.g., at 70% strain) than at the end of the elastic range (at 5% strain), indicating a mechanism change in the deformation process. Indeed, in the elastic range deformation (expansion) is due to the flexibility of the polymer, while in the plastic regime monoliths collapse and get absorbed within their own pores. In addition, the sample micromorphology after compression (Figure 11) shows signs of melting and fusion of the skeletal nanostructures. Further, negative slopes during unloading (meaning that the material continues to contract despite the load release) and the ensuing hysteresis loops during repetitive load-unload cycles along the stress-strain curve (see Figure 10) can be also attributed to local softening and prolonged flow of the polymer for a short while even after pressure has been released. N3300A-derived polyurea melts at around 130 °C.[9] Therefore, both the direct (SEM) as well as the indirect evidence for melting (load-unload curve behavior) have to be attributed to pressure-induced sintering effects. Overall, the combination of the material being absorbed within its own porosity with softening-flow-and-retreat of the polymer within the pores reverses the natural tendency of materials to expand under compression and leads to lower Poisson ratios at higher strains. Further insight into the mechanical behavior of the PUA aerogels can be obtained by looking more closely at the three regions of the stress-strain curve. By comparison with X-silica and X-vanadia aerogels of similar density (ρ_b = 0.45-0.55 g cm^{-3}), the elastic range of PUA aerogels is somewhat shorter, but their elastic modulus is comparable to that of the former aerogels. The shorter linear elastic range of PUA aerogels (up to 3% strain compared with 4% and 3.5% for X-silica and X-vanadia, respectively) is reflected on the lower yield strength at 0.2% offset yield strain (see Table 3). As discussed previously,[24] the elastic modulus of

X-silica aerogels (see Table 3) is determined by and is practically equal to that of the underlining oxide framework (e.g., 92 ± 7 MPa for native silica at 0.19 g cm^{-3} and 129 ± 8 MPa for X-silica at 0.48 g cm^{-3}). On the other hand, stiffness in PUA aerogels should be controlled by the intersecondary particle (or interfiber) bridges, which are polymeric.

Despite apparent changes in nanomorphology (Figure 6), the elastic modulus of N3300A-derived PUA aerogels scales exponentially with bulk density over the entire density range considered (Figure 12) obeying a power-law relationship, $E = (\rho_b)^a$, where $a = 1.63(0.17$.By comparison, native silica, X-silica, and X-vanadia are more sensitive to the bulk density [exponents equal to 2.59-3.53,[8b] 3.10,[24] and 1.87,[8b] respectively]. The lower density sensitivity of the Young's modulus of PUA aerogels reflects probably the more flexible nature of the exclusively polymeric framework. Finally, the Young's modulus, E, is further used for the calculation of the speed of sound, v, in PUA monoliths using $v = (E/\rho_b)^{1/2}$. Results are included in Table 3. The values for the lower density samples are as low as the speed of sound in open dry air at 20 °C (343 m s^{-1}), increasing to just over double that value in the most-dense PUA samples of this study (0.55 g cm^{-3}). Therefore, it is inferred that all PUA aerogels, and particularly those with medium to lower density, are expected to be excellent acoustic attenuators. The ultimate compressive strength, UCS, of PUA aerogels can be quite high and, as noted in Table 3, at comparable densities PUA aerogels can be as strong materials as X-silica and X-vanadia. The failure mechanism, however, is very different from that of X-silica and resembles that of X-vanadia, most probably due to the striking similarity of their fibrilar nanostructures. In X-silica, when compression reaches a compressive strain nearly equal to the porosity, all pores are nearly fully closed and necessarily the material has to expand

laterally. Thus, X-silica fails into fragments as a result of high radial and circumferential strains. In the case of X-vanadia aerogels, when compression reaches a strain level near to their porosity, pores again are nearly closed and further increase in compressive strain would induce high lateral strains. However, the entangled worm-like nanostructure seems to prevent fragmentation. Instead, nanoworms are sintered together by stress-induced melting of the polymer at the points of contact between the nanoworms,[8] and what is observed macroscopically is development of only a few radial cracks at the last stages of compression. Thus, X-vanadia samples remain as single pieces and continue to carry high compressive stresses. Overall, higher density polyurea aerogels (0.5 g cm^{-3}) fail in a manner similar to X-vanadia, while lower density samples (e.g., ≤ 0.2 g cm-3) do not even develop radial cracks (Figure 11). Compressed disks continue to carry loads until the platens of the testing machine come in contact. In that regard, the UCS values presented in Table 3 can be considered as lower bounds for UCS. The UCS of PUA aerogels obeys a power law relationship with the bulk density, UCS = $(\rho_b)^b$, where b = 1.74 ± 0.27. The low value of exponent "b" implies that at low densities PUA aerogels are relatively stronger materials than X-silica and X-vanadia (e.g., the corresponding exponent for X-silica is b = 4.14). In turn, this has an additional, even more important consequence for the energy absorption capability (toughness, T) of PUA aerogels. The latter is the figure of merit for antiballistic applications and is calculated from the integrated area underneath the stress-strain curve. At ρ_b = 0.55 g cm^{-3}, PUA aerogels absorb as much as 91 J g^{-1} falling between X-silica and X-vanadia of similar densities (Table 3), but they far surpass materials typically considered strong such as acrylic polymers (8 J g^{-1} at 1.04 g cm^{-3}), Kevlar-49 epoxy (11 J g^{-1} at 1.04 g cm^{-3}), 4130 steel (15

J g^{-1} at 7.84 g cm^{-3}), and SiC ceramics (20 J g^{-1} at 3.02 g cm^{-3}).38 More importantly though, the energy absorption of PUA aerogels also obeys a power law with bulk density T = (ρ$_b$)^c, where c = 0.75 (0.15,meaning that PUA aerogels remain exceptionally good energy absorbers at low densities. The effect of the fiber entanglement is particularly prevalent at cryogenic temperatures. At -173 °C, N3300Aderived aerogels become stiffer (e.g., E = 490MPa at ρ$_b$= 0.55 g cm^{-3}) and more brittle, failing by fragmentation at lower strains (42-72%) than at room temperature (88-92%, Table 3). The increased stiffness is reflected on the Poisson's ratios at 5% strain, which are higher (0.30-0.33) than those observed at room temperature (0.20-0.23); but again, Poisson's ratios decrease at higher strains (0.28-0.31). The overall cryogenic behavior of PUA aerogels is intermediate between that of X-silica aerogels, which become much more brittle at those temperatures failing at just 16% compressive strain (versus 68% at room temperature), and X-vanadia aerogels, which remain ductile (Table 3). As above, those phenomena are again attributed to pressure-induced local sintering, which is given time to take effect by the entangled nanofibers of PUA and X-vanadia aerogels but not by the nanoparticulate structure of X-silica. In summary, PUA aerogels have high strength, they are exceptional energy absorbers, and they possess high acoustic attenuation capabilities. Those properties, in combination with a facile synthesis and the expected low thermal conductivities, render those materials very attractive for several structural applications.

3.3b. Pyrolytic Conversion of PUA Aerogels to Porous Carbons. Generally, carbonizable polymers are capable of either cyclizing, or undergoing ring fusion and chain coalescence by heating.[39] For this, the chain should either contain aromatic moieties, or be aromatizable (usually by oxidation – e.g., polyacrylonitrile). In the former case, there

should be just one carbon atom between aromatic rings; otherwise, pyrolytic chain

scission will prevail leading to loss of fragments.[42] Certain PUA aerogels of this study

fulfill these criteria. Indeed, by TGA under N_2 (Figure 14B) PUA aerogels from aliphatic

isocyanates (Desmodur N3300A and N3200) decompose completely leaving only trace

residues. On the other hand, PUA aerogels from aromatic isocyanates Desmodur RE,

Mondur TD (toluene diisocyanate, TDI) and Mondur CD (4,4′-diphenylmethane

diisocyanate, MDI) leave substantial amounts of residue above 500 °C. Gravimetric

results after pyrolysis in a tube furnace at 800 °C under a flowing stream of argon, along

with CHN elemental analysis data are summarized in Table 5. The residue yield from

Desmodur RE-derived aerogels is as high as that obtained from RF and polyimide

aerogels.[5,43] Residues from all Desmodur RE formulations contain 78-82% w/w C, no H

and 5-9% w/w N. By XPS (Figure 16A), they also contain O in an atomic ratio to N of

about equal to one.

Table 5. Carbonization data for various PUA aerogels upon pyrolysis at 800 °C under Ar

PUA from:[a]	residue yield % w/w	% w/w [b]		
		C	H	N
Desmodur N3300A	1.8			
Desmodur N3200	3.2			
Desmodur RE	56	80.72±0.79	0.0	8.59±0.41
Mondur CD (MDI)	19	65.42±0.20	0.0	4.97±0.12
Mondur TD (TDI)	25	76.66±1.01	0.0	8.40±0.69

a. All samples synthesized using about 0.2 M isocyanate solutions (see Table 1) with 3.0 mol equivalents of water and 0.6% w/w Et₃N (as defined in the Experimental Section). b. All formulations run three times from samples from three different batches.

Thus, focusing on Desmodur RE-derived carbons, XRD shows very broad diffractions (Figure 16B), typical Raman spectra (Figure 16C) show both the G (graphitic) and D (disordered) peaks at 1597 cm^{-1} and 1352 cm^{-1}, respectively, with an integrated peak intensity ratio I_D/I_G=1.12, all indicative of nanocrystalline carbon. Indeed, all skeletal densities are in the range of 1.78 g cm^{-3} to 1.89 g cm^{-3} (within the range, 1.8-2.0 g cm^{-3}, for amorphous carbon),[44] reflecting also the similar chemical composition of all samples. (Other pertinent materials characterization data are given in Table S.17 in S.I.) Looking closer to the microstructure (by SEM, Figure 17) all Desmodur RE-derived carbon samples appear macroporous and similar in appearance. The two lowest density samples have lost their string-like structure completely, although they do retain a faint memory of the wider necks observed in the 0.037 g cm^{-3} samples versus those at 0.023 g cm^{-3} (compare Figures 7 and 17). The morphology of the nanoparticulate structures above 0.062 g cm^{-3} (Figure 7) is retained more closely. Based on those data, sintering phenomena during heating should not be ruled out, and a closer study of this type of PUA-derived carbons is certainly necessary.

The importance of converting Desmodur RE-derived PUA aerogels into carbon in satisfactory yields cannot be overemphasized. Their utility in the context of the search of efficient methods to porous carbons is self-evident. However, if that conversion is looked at from a polymer-crosslinked aerogels perspective, it has even farther-reaching implications. Recently, polyacrylonitrile (PAN)-coated silica was converted to highly porous (70% v/v) monolithic silicon carbide (SiC) aerogels.[45] That process required: (a) use of a bidentate surface-confined free radical initiator; and, (b) aromatization of the PAN coating before carbonization and carbothermal reaction with silica. The method

worked well with silica, but cannot be extended easily to other oxide aerogels. On the other hand, polyurea-crosslinking is a "genetic" approach that has been demonstrated with a variety of non-silica aerogels.[7d,8,46] Hence, Desmodur RE-crosslinked aerogels should be directly convertible to a variety of porous metals and ceramics (carbides) according to carbothermal methods demonstrated recently in interpenetrating metal oxide/RF aerogel networks.[47]

4. Conclusions – Outlook

With increasing concerns over the environmental impact of the chemical industry and the unavoidable switch from a growth to a more sustainable economy, the synthesis of PUA aerogels from isocyanates and water exemplifies a more environmentally friendly approach than the classic synthesis of polyurea, because it replaces expensive amines with water. The synthesis of PUA aerogels from isocyanates and water is environmentally friendlier than the classic synthesis of polyurea as it avoids use of expensive amines. The method is also quite versatile as materials properties can be tuned conveniently and effectively by varying the chemical identity of the isocyanate among several commercially available di- and triisocyanates, aromatic versus aliphatic. The implications of the variable nanomorphology from fibrous to particulate, by merely varying the concentration of a single reagent (the isocyanate), cannot be overemphasized. All those nanostructures consist of primary particles assembling together to form mass-fractal secondary aggregates, which in turn assemble to yet larger (mass or surface) fractal agglomerates that include fibers. Those results, considered together with our recent findings with polyimide aerogels, whereas chemically identical particles or fibers all consist of same-size primary particles,[40] seem to have fundamental significance and

raise the question regarding the driving force that under certain conditions directs assembly of particles into fibers rather than globular agglomerations. Formation of primary particles is rationalized by phase separation of an insoluble polymer. However, being able to control their assembly into fibers seems to have practical significance. Consistently with previous results obtained with inorganic fibers (e.g., vanadia) coated with polymer, the macroscopic result of entanglement is to keep the material together (via the bird nest effect) allowing for sintering phenomena to take place, thus increasing the ultimate strain under compression and depressing the ductile-to-brittle transition upon cooling. Both effects cause an increase of the specific energy absorption of PUA aerogels into regimes unattainable even by materials that are typically considered strong (e.g., Kevlar-49 epoxy, 4130 steel, and SiC ceramics). Finally, the importance of the high yield conversion of Desmodur RE-derived PUA aerogels into carbon is also multifaceted. Apart from the obvious implications in the context of the search for efficient methods to porous carbons, if that conversion is looked at from the perspective of the polymer-cross-linked aerogels, it can easily be seen how it may lead to new materials. For instance, recently, polyacrylonitrile (PAN)-coated silica was converted to highly porous (70% v/v) monolithic silicon carbide (SiC) aerogels.[42] That process required (a) use of a bidentate surface-confined free radical initiator and (b) aromatization of the PAN coating before carbonization and carbothermal reaction with silica. Thus far, that method has worked well with silica but cannot be extended easily to other oxide aerogels. On the other hand, polyurea cross-linking is a "genetic" approach that has been demonstrated with several nonsilica aerogels.[7d,8,43] Hence, Desmodur RE-cross-linked aerogels are directly convertible to a variety of porous metals and ceramics (carbides) according to

carbothermal methods demonstrated recently with interpenetrating metal oxide/RF aerogelnetworks.[44]

Supporting Information Available: Formulations and gelation times of all samples using Desmodur N3300A, Desmodur N3200, Desmodur RE, andMondur TD (Tables 1S-9S); comparison of PUA xerogels, aerogels, and samples dried under ambient pressure from pentane (Table 10S); detailed data for all formulations of water and catalyst for all PUA samples prepared with Desmodur N3300A triisocyanate (Tables 11S-16S); characterization data for carbon aerogels from Desmodur RE Aerogels (Table 17S); spectroscopic characterization data for Desmodur N3300A, Desmodur RE and Desmodur N3200 (Figures 1S-3S); additional ^{13}C NMR data (Figures 4S-6S); SEM of Desmodur

N3300A derived PUA aerogels as a function of H_2O and Et_3N concentration (Figure 7S) ;

SEM of Desmodur RE and PUA aerogels as a function of H_2O and Et_3N concentration.

This information is available free of charge via the Internet at http://pubs.acs.org.

5. References

1. Pierre, A. C.; Pajonk, G. M. *Chem. Rev.* **2002**, 102, 4243-4265.

2. (a) Kistler, S. S. *Nature* **1931**, *127*, 3211. (b) Kistler, S. S. *J. Phys. Chem.* **1932**, 36, 52-63.

3. (a) Pekala, R. K. "Low Density, Resorcinol-Formaldehyde Aerogels," U.S. Patent No. 4,873,218 (1989). (b) Pekala, R. W. *J. Mater. Sci.* **1989**, *24*, 3221–3227. (c) Pekala, R. W.; Alviso, C. T.; Kong, F. M.; Hulsey, S. S. *J. Non-Cryst. Solids* **1992**, *145*, 90–98. (d) Pekala, R. W.; Schaefer, D. W. *Macromolecules* **1993**, *26*, 5887–5893.

4. (a) Redfern, B. "Bodies and Shapes of Carbonaceous Materials and Processes for their Production," U.S. Patent No. 3,109,712 (1963). (b) Cowlard, F. C.; Lewis, J. C. *J. Mater. Sci.* **1967**, *2*, 507–512.

5. (a) Mayer, S. T.; Pekala, R. W.; Kaschmitter, J. L. *J. Electrochem. Soc.* **1993**, *140*, 446-451. (b) Ritter, J. A.; Al-Muhtaseb, S. A. *Adv. Mater.* **2003**, *15*, 101–114.

6. Lu, X.; Arduini-Schuster, M. C.; Kuhn, J.; Nilsson, O.; Fricke, J.; Pekala, R. W. *Science* **1992**, *255*, 971-972.

7. (a) Leventis, N.; Sotiriou-Leventis, C.; Zhang, G.; Rawashdeh, A.-M. M. *NanoLetters* **2002**, *2*, 957-960. (b) Zhang, G.; Dass, A.; Rawashdeh, A.-M. M.; Thomas, J.; Counsil, J. A.; Sotiriou-Leventis, C.; Fabrizio, E. F.; Ilhan, F.; Vassilaras, P.; Scheiman, D. A.; McCorkle, L.; Palczer, A.; Johnston, J. C.; Meador, M. A. B.; Leventis, N. *J. Non-Cryst. Solids* **2004**, *350*, 152-164. (c) Leventis, N.; Mulik, S.; Wang, X.; Dass, A.; Sotiriou-Leventis, C.; Lu, H. *J. Am. Chem. Soc.* **2007**, *129*, 10660-10661. (d) Leventis, N. *Acc. Chem. Res.* **2007**, *40*, 874-884. (e) Mulik, S.; Sotiriou-Leventis, C.; Churu, G.; Lu, H.; Leventis, N. *Chem. Mater.* **2008**, *20*, 5035-5046. (f) Leventis, N.; Sotiriou-Leventis, C. "Methods and Compositions for Preparing Silica Aerogels," U.S. Patent No. 7,771,609 (2010).

8. (a) Leventis, N.; Sotiriou-Leventis, C.; Mulik, S.; A. Dass, A.; Schnobrich, J.; Hobbs, A.; Fabrizio, E. F.; Luo, H.; Churu, G.; Zhang, Y.; Lu, H. *J. Mater. Chem.* **2008**, *18*, 2475-2482. (b) Luo, H.; Churu, G.; Schnobrich, J.; Hobbs, A.; Fabrizio, E. F.; Dass, A.; Mulik, S.; Sotiriou-Leventis, C.; Lu, H.; Leventis, N. *J. Sol-Gel Sci. Technol.* **2008**, *48*, 113-134.

9. Leventis, N.; Mulik, S.; Sotiriou-Leventis, C. *Chem. Mater.* **2008**, *20*, 6985-6997.

10. (a) Britain, J. W. *I&EC Product* **2003**, *44*, 46-47. *Res. Develop.* **1962**, *1*, 261-264.
(b) Richter, F. U.; Schmitz, J.; Laas, H.-J.; Halpaap, R. *Polym. Preprints*

11. (a) De Vos R.; Biesmans, G. L. J. G. "Organic Aerogels," U.S. Patent No. 5,484,818 (1994). (b) Biesmans, G.; Randall, D.; Francais, E.; Perrut, M. *J. Non-Cryst. Solids* **1998**, *225*, 36-40. (c) Biesmans, G.; Mertens, A.; Duffours, L.; Woignier, T.; Phalippou, J. *J. Non-Cryst. Solids* **1998**, **225**, 64-68. (d) Biesmans, G. L. J. G. "Polyisocyanate Based Aerogels," U.S. Patent No. 5,990,184 (1999). (e) Biesmans, G. L.; Mertens, A. "Organic Aerogels," U.S. Patent No. 5,942,553 (1999).

12. Resins for Coatings, Chemistry, Properties and Applications, Stoye, D.; Freitag, W. Eds. Hanser/Gardner Publications, Inc. 1996, p 186.

13. (a) Ross, W. D.; Jefferson, R. T. *J. Chromatogr. Sci.* **1970**, *8*, 386-389. (b) Hileman, F. D.; Sievers, R. E.; Hess, G. G.; Ross, W. D. *Anal. Chem.* **1973**, *45*, 1126-1130.

14. Tan, C.; Fung, B. M.; Newman, J. K.; Vu, C. *Adv. Mater.* **2001**, *13*, 644-646.

15. Rigacci, A.; Marechal, J. C.; Repoux, M.; Moreno, M.; Achard, P. *J. Non-Cryst. Solids* **2004**, *350*, 372-378.

16. Fischer, F., Rigacci, A.; Pirard, R.; Berthon-Fabry, S.; Achard, P. *Polymer* **2006**, *47*, 7636-7645.

17. Lee, J. K.; Gould, G. L.; Rhine, W. *J. Sol-Gel Sci. Technol.* **2009**, *49*, 209-220.

18. Wicks, Z. W. Jr.; Jones, F. N.; Pappas, S. P. "Organic Coatings, Science and Technology, Second Edition," Wiley-Interscience, New York, N.Y.: 1999, Chapter 10, p 180.

19. Odian, G. "Principles of Polymerization, Fourth Edition," Wiley-Interscience, New York, N.Y.: 2004, p. 130-132.

20. Jones, M. S. *J. Sol-Gel Sci. Technol.* **2007**, *44*, 255-258.

21. Barker, J. G.; Glinka, C. J.; Moyer, J. J.; Kim, M. H.; Drews, A. R.; Agamalian, M. *J. Appl. Cryst.* **2005**, *38*, 1004-1011.

22. Glinka, C. J.; Barker, J. G.; Hammouda, B.; Krueger S.; Moyer, J. J.; Orts, W. J. *J. Appl. Cryst.* **1998**, *31*, 430-445.

23. Seeger, P. A.; Hjelm, R. P. Jr. *J. Appl. Cryst.* **1991**, *24*, 467-478.

24. Kline, S. R. *J. Appl. Cryst.* **2006**, *39*, 895-900.

25. Katti, A.; Shimpi, N.; Roy, S.; Lu, H.; Fabrizio, E. F.; Dass, A.; Capadona, L. A.; Leventis, N. *Chem. Mater.* **2006**, *18*, 285-296.

26. The amine product of the reaction between an isocyanate and water is expected to act as a co-catalyst; therefore, similar log-log plotting for the isocyanate fails to give straight lines, and the rate law is considered first order in [N3300A] based on Scheme 2.

27. Consideration of Hildebrand solubility parameters for the solvent ($\delta_{acetone}$=9.77 $cal^{0.5} cm^{-1.5}$) and polyurea (δ_{PUA}~10 $cal^{0.5} cm^{-1.5}$,[15] taken as approximately equal to that of polyurethanes) would predict high solubility of polyureas, however, the highly crosslinked 3D structure of N3300A-derived polyurea seems to promote early phase separation.

28. Leventis, N.; Palczer, A.; McCorkle, L.; Zhang, G.; Sotiriou-Leventis, C. *J. Sol-Gel Sci. Tech.* **2005**, *35*, 99-105.

29. Yadav, S. K.; Khilar, K. C.; Suresh, A. K. *J. Membrane Sci.* **1997**, *125*, 213-218.

30. (a) Beaucage, G. *J. Appl. Cryst.* **1995**, *28*, 717-728. (b) Beaucage, G. *J. Appl. Cryst.* **1996**, *29*, 134-146.

31. Koberstein, J. T.; Morra, B.; Stein, R. S. *J. Appl. Cryst.* **1980**, *13*, 34-45.

32. Guinier, A; Fournet, G. "Small-Angle Scattering of X-rays," John Wiley and Sons, New York, N.Y., 1955.

33. Beaucage, G.; Kammler, H. K.; Pratsinis, S. E. *J. Appl. Cryst.* **2004**, *37*, 523-535.

34. Keefer, K. D.; Schaefer, D. W. *Phys. Rev. Lett.* **1984**, *53*, 1383-1386.

35. Witten, T. A. Jr.; Sander, L. M. *Phys. Rev. Lett.* **1981**, *47*, 1400-1403.

36. (a) Keefer, K. D.; Schaefer, D. W. *Phys. Rev. Lett.* **1986**, *56*, 2376-2379. (b) Keefer, K. D.; Schaefer, D. W. *Phys. Rev. Lett.* **1986**, *56*, 2199-2202.

37. Callister, W. D. "Materials Science and Engineering, An Introduction 7th Edition," John Wiley & Sons, New York: 2008, Appendix B.

38. (a) American Society for Metals, ASM Engineering Materials Handbook, Composites, Volume 1: ASM International: Materials Park, OH, p 178, Table 2, 1998. (b) Luo, H.; Chen, W. *Intern. J. Appl. Ceram. Techn.* **2004**, *1*, 254-260. (c) Luo, H.; Chen, W.; Rajendran, A. M. *J. Am. Ceram. Soc.* **2006**, *89*, 266-273.

39. The Polyurethanes Book, Randall, D.; Lee, Eds.; S Wiley: 2002, p 57.

40. Leventis, N.; Mulik, S.; Wang, X.; Dass, A.; Patil, V. U.; Sotiriou-Leventis, C.; Lu, H.; Churu, G.; Capecelatro, A. *J. Non-Cryst. Solids* **2008**, *354*, 632-644.

41. (a) Smirnova, A.; Ding, X.; Hara, H.; Vasiliev, A.; Sammes, N. *International Journal of Hydrogen Energy* **2005**, *30*, 149-158. (b) Kwon, O. J.; Jung, Y. S.; Kim, J. H.; Oh, S. M. *J. Power Sources* **2004**, *125*, 221-227. (c) Fialkov, A. S. *Russ. J. Electrochem.* **2000**, *36*, 345-366.

42. Jenkins, G. M.; Kawamura, K. "Polymeric Carbons, Carbon Fibre, Glass and Char," Cambridge University Press: New York, N.Y., 1976.

43. Chidambareswarapattar, C.; Larimore, Z.; Sotiriou-Leventis, C.; Mang, J. T.; Leventis, N. *J. Mater. Chem.* **2010**, *20*, (in press).

44. McKenzie, D. R.; Muller, D.; Pailthorpe, B. A. *Phys. Rev. Lett.* **1991**, *67*, 773–776.

45. Leventis, N.; Sadekar, A.; Chandrasekaran, N.; Sotiriou-Leventis, C. *Chem. Mater.* **2010**, *22*, 2790-2803.

46. Leventis, N.; Vassilaras, P.; Fabrizio, E. F.; Dass, A. *J. Mater. Chem.* **2007**, *17*, 1502-1508.

47. (a) Leventis, N.; Chandrasekaran, N.; Sadekar, A. G.; Mulik, S.; Sotiriou-Leventis, C. *J. Mater. Chem.* **2010**, *20*, 7456–7471. (b) Leventis, N.; Chandrasekaran, N.; Sadekar, A. G.; Sotiriou-Leventis, C.; Lu, H. *J. Am. Chem. Soc.* **2009**, *131*, 4576-4577. (c) Leventis, N.; Chandrasekaran, N.; Sotiriou-Leventis, C.; Mumtaz, A. *J. Mater. Chem.* **2009**, *19*, 63-65.

6. Figures
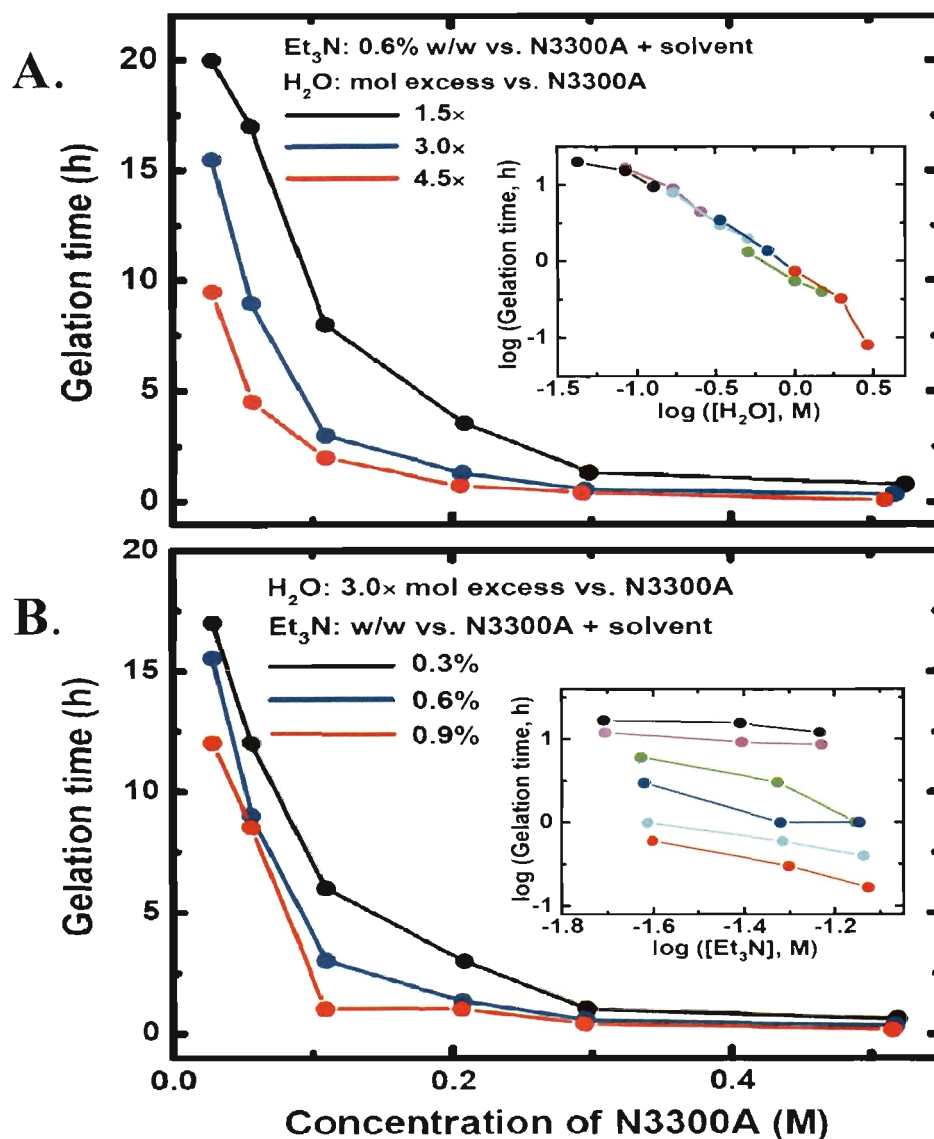
Figure 1. Gelation time as a function of the concentration of Desmodur N3300A triisocyanate. (A) For three different water ratios, keeping the catalyst ratio constant; (B) For three different catalyst ratios, keeping the water ratio constant. Insets: log-log plots as shown. (A) slope = 1.2±0.1. (B) slope = 0.9±0.5.
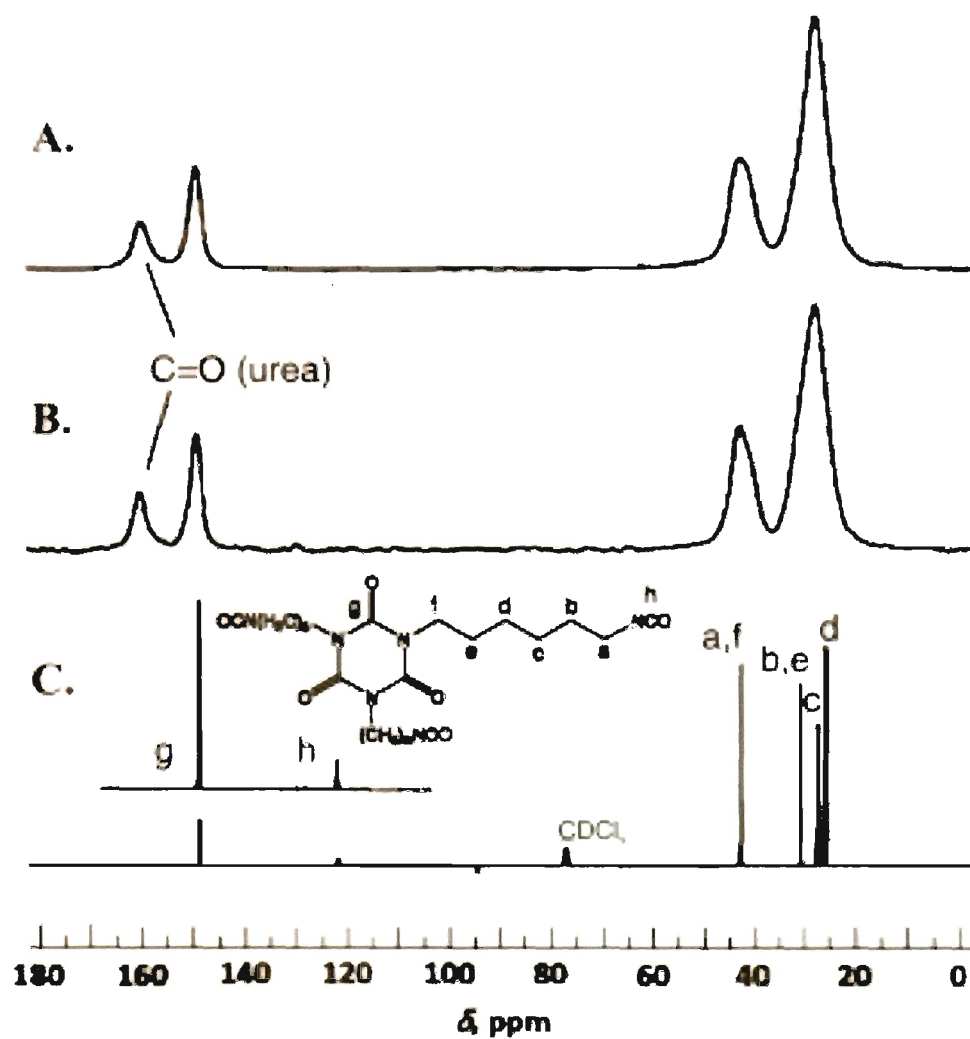
Figure 2. A, B. Solids ^{13}C NMR of two PUA aerogels made with Desmodur N3300A triisocyanate at 0.0285 M (A) and 0.5172 M (B) using in both cases 3.0 mol equivalents of H_2O and 0.6% (w/w) Et_3N as defined in the Experimental Section. (C) Liquids ^{13}C NMR of the monomer in $CDCl_3$.
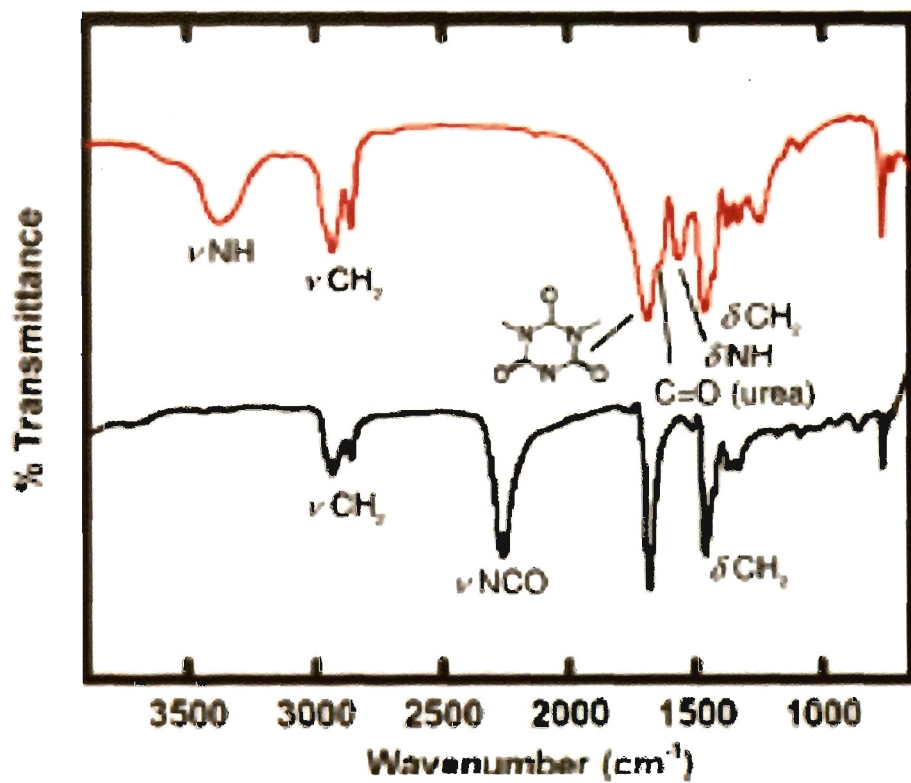
Figure 3. Red (top): Typical infrared (IR) spectrum of a PUA aerogel derived from Desmodur N3300A. Back (bottom): IR of the monomer.
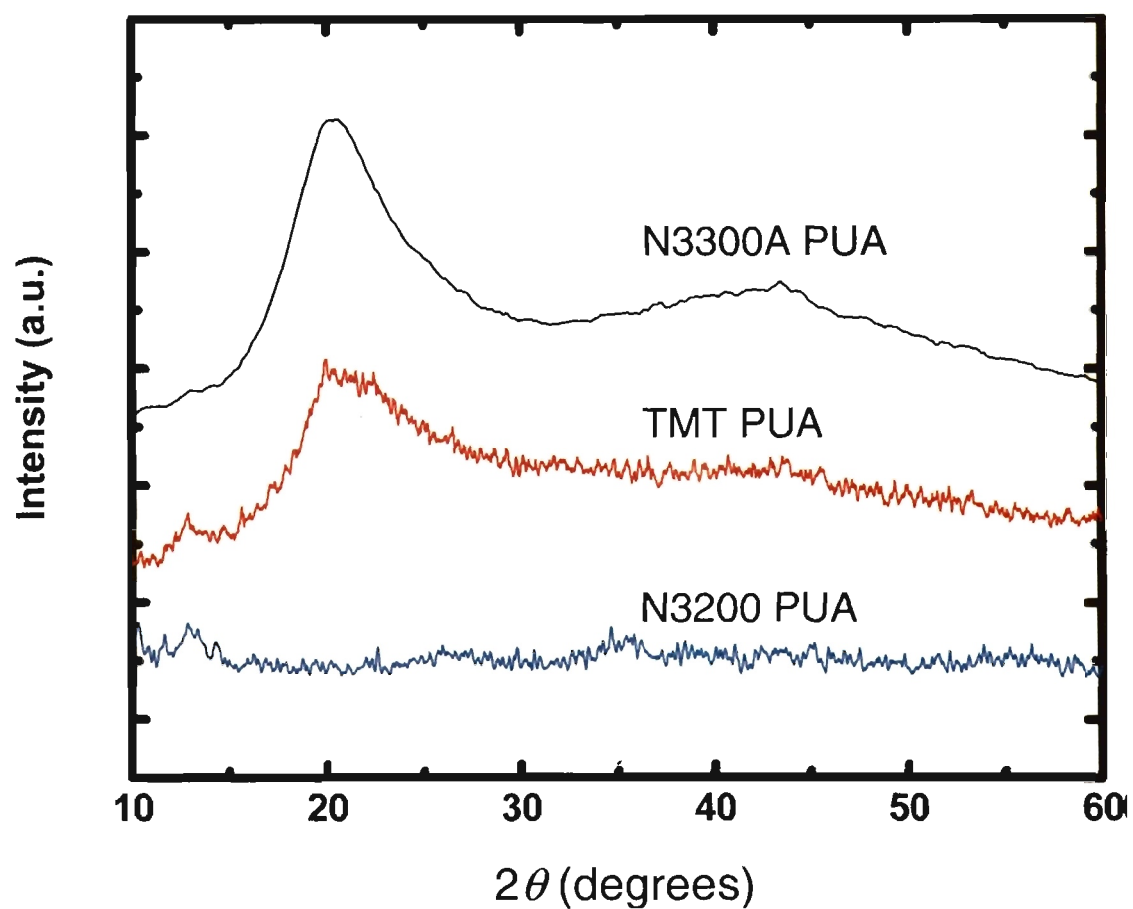
Figure 4. Typical X-ray diffraction patterns of PUA aerogels derived from three different isocyanates as indicated. Data for all formulations are shown in Table 1.
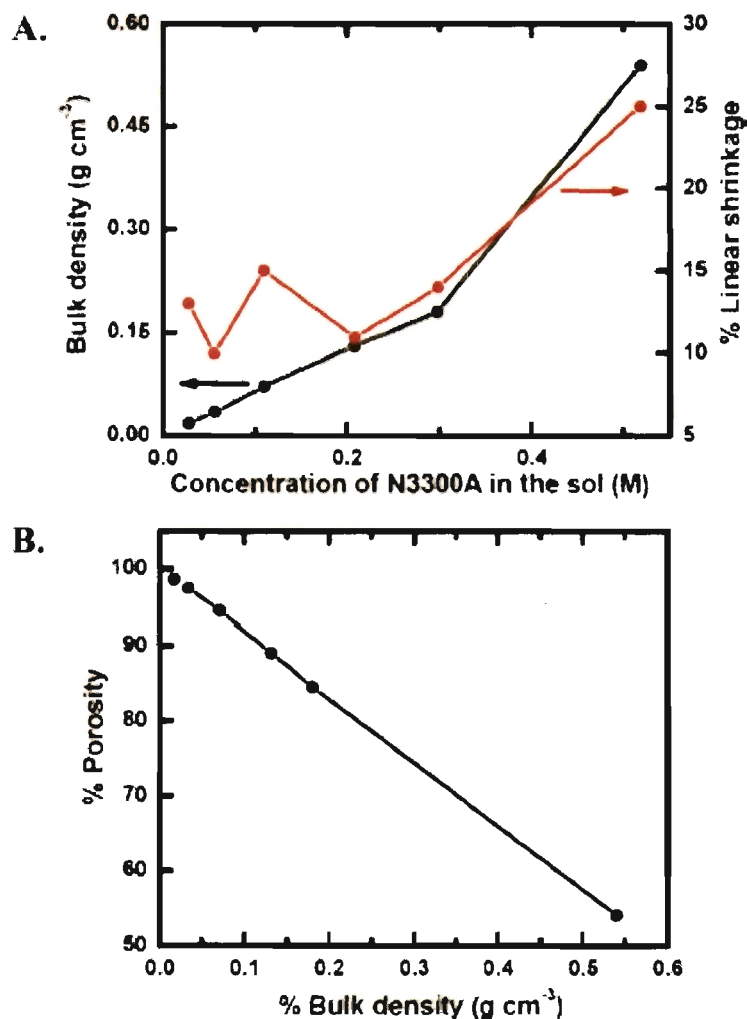
Figure 5. A. Bulk density of PUA aerogels as a function of the monomer concentration in the sol using 3.0 mol equivalents of H_2O and 0.6% (w/w) Et_3N as defined in the Experimental Section. B. Correlation of porosity (% v/v of void space) and bulk density.
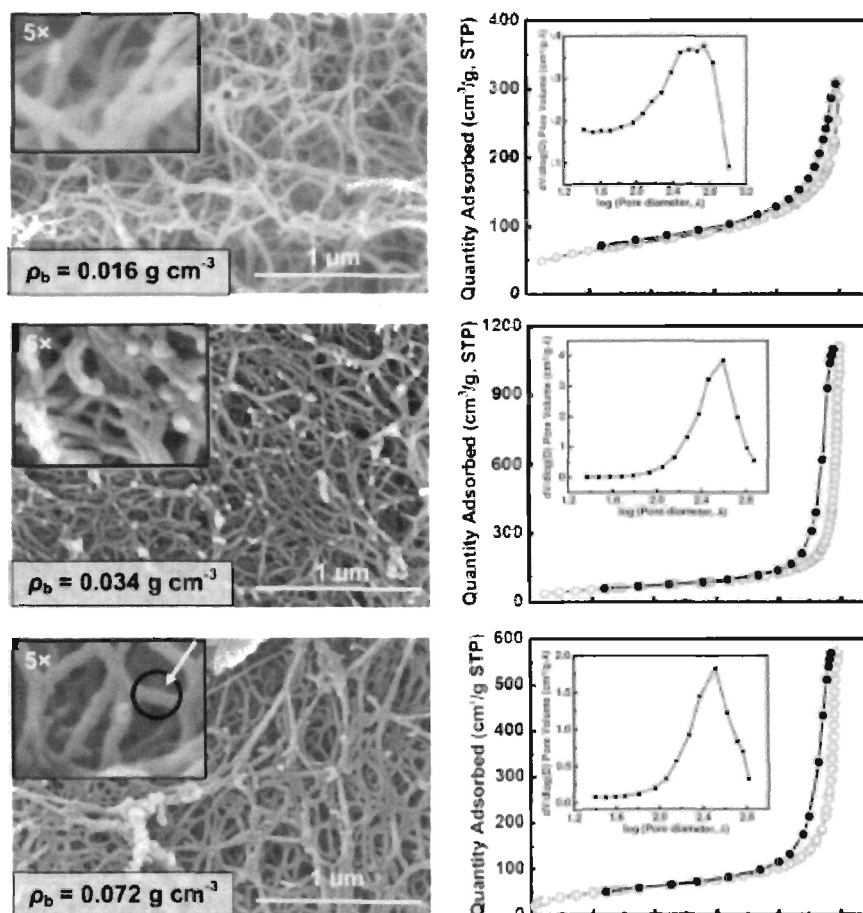
Figure 6. Scanning electron microscopy (SEM) and N_2 sorption porosimetry as a function of density of PUA aerogels derived from Desmodur N3300A triisocyanate using 3.0 mol equivalents of H_2O and 0.6% w/w Et_3N as defined in the Experimental Section. (For the effect of water and catalyst concentration in the microstructure at constant isocyanate concentration refer to Figure 7S in S.I.)
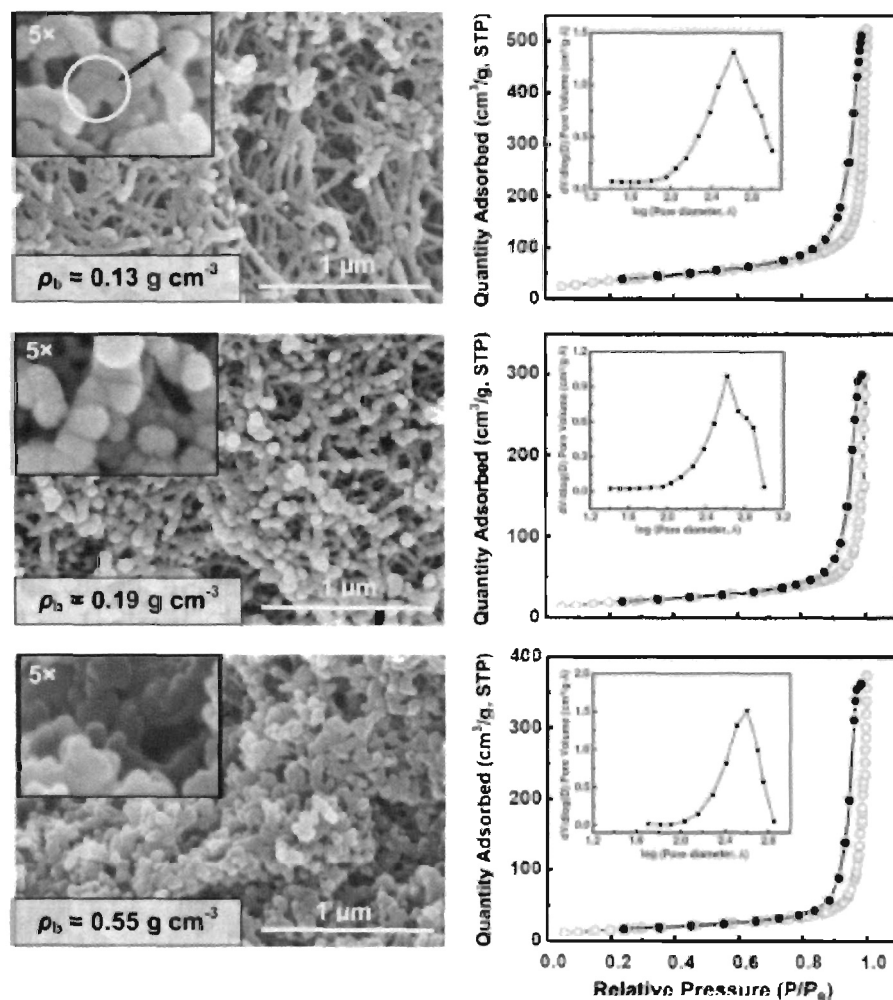
Figure 6. Scanning electron microscopy (SEM) and N_2 sorption porosimetry as a function of density of PUA aerogels derived from Desmodur N3300A triisocyanate using 3.0 mol equivalents of H_2O and 0.6% w/w Et_3N as defined in the Experimental Section. (For the effect of water and catalyst concentration in the microstructure at constant isocyanate concentration refer to Figure 7S in S.I.) (Continued)
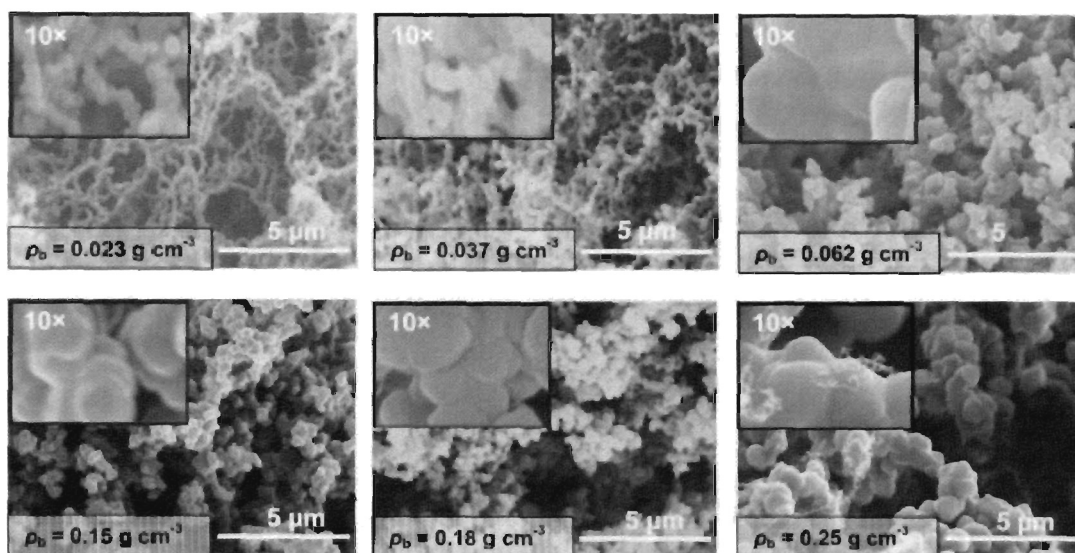
Figure 7. SEM as a function of density of PUA aerogels derived from Desmodur RE triisocyanate using 3.0 mol equivalents of H_2O and 0.6% (w/w) Et_3N as defined in the Experimental Section.
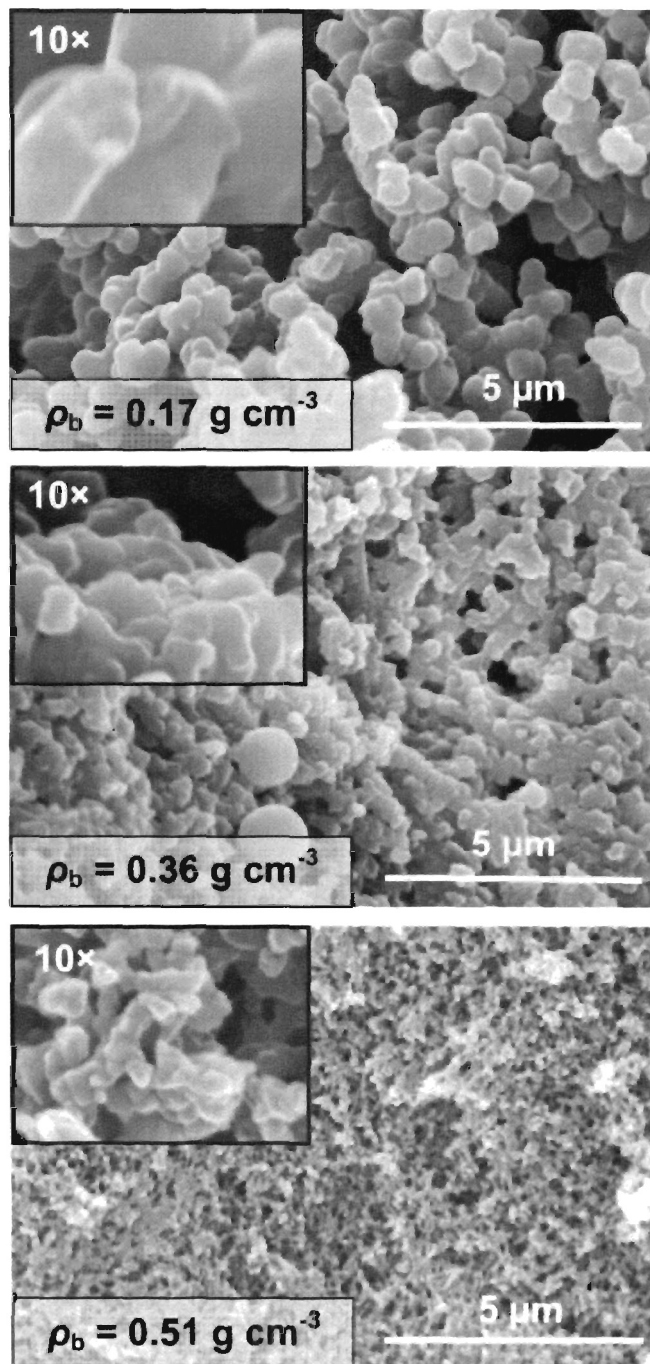
Figure 8. SEM as a function of density of PUA aerogels derived from Desmodur N3200 diisocyanate using 3.0 mol equivalents of H_2O and 0.6% (w/w) Et_3N as defined in the Experimental Section.
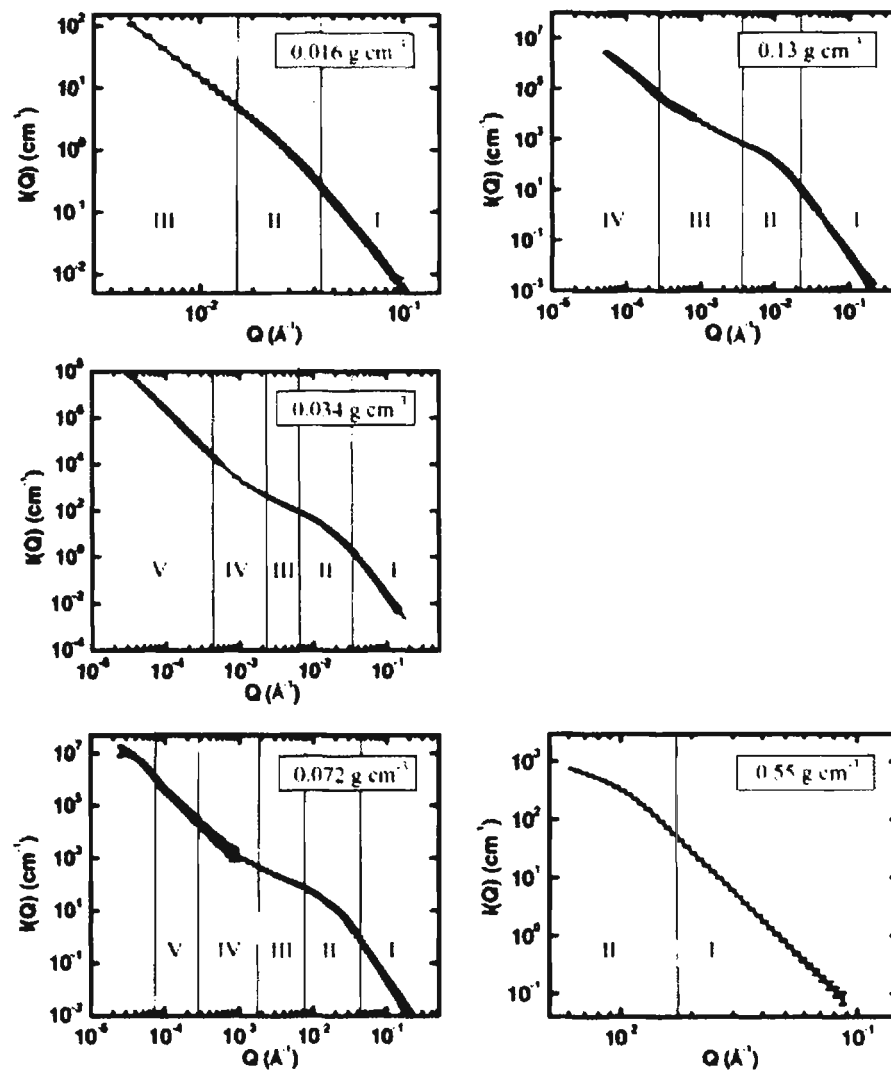
Figure 9. SANS/USANS data as a function of PUA aerogels derived from Desmodur N3300A triisocyante using 3.0 mol equivalents of H_2O and 0.6% w/w Et_3N as defined in the Experimental section. Vertical lines separate scattering profiles in regions that provide the data presented in Table 2.
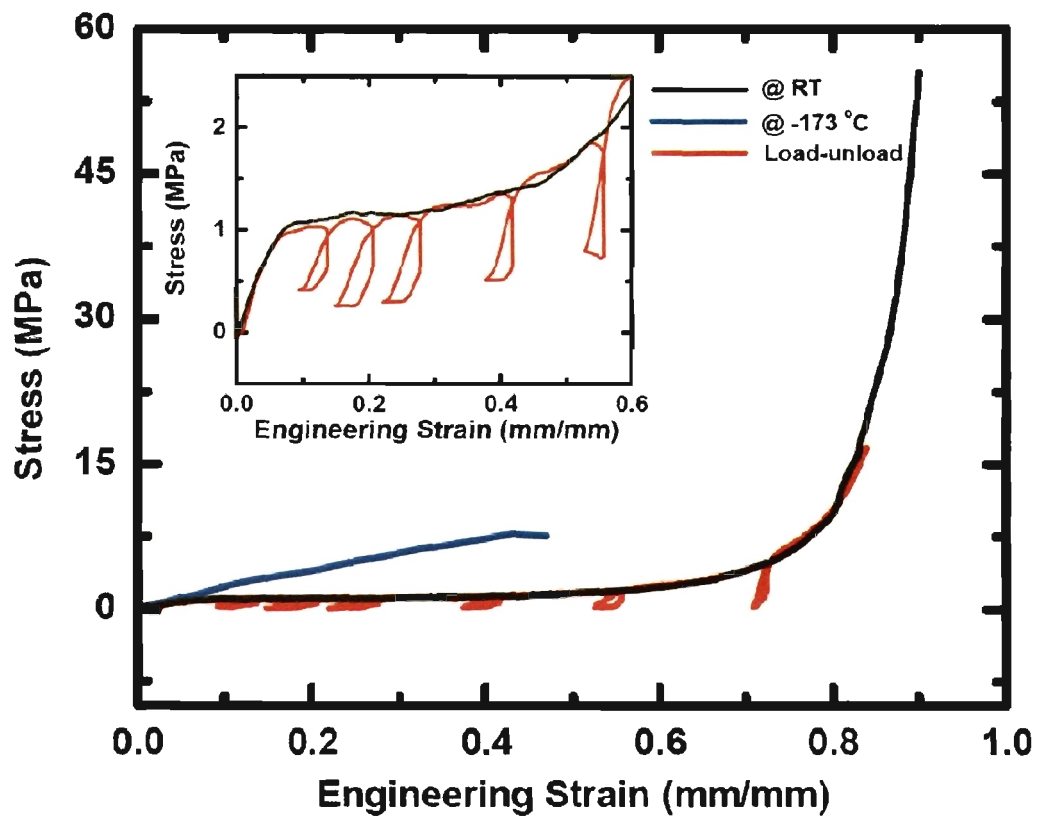
Figure 10. Quasi-static (strain rate = 0.05 s^{-1}) compression testing of PUA aerogel monoliths (ρ_b=0.13 g cm^{-3}) derived from Desmodur N3300A triisocyanate, under the conditions shown within the frame.
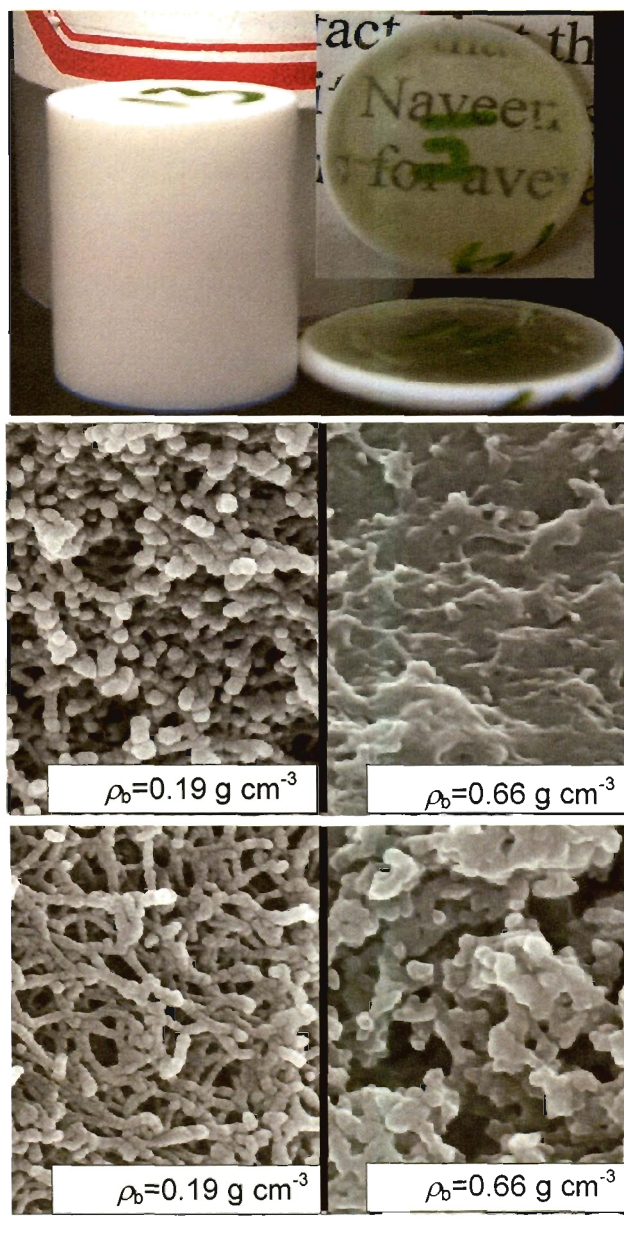
Figure 11. Optical and SEM images of a PUA aerogels before and after compression testing. Scale bar at 1 μm.
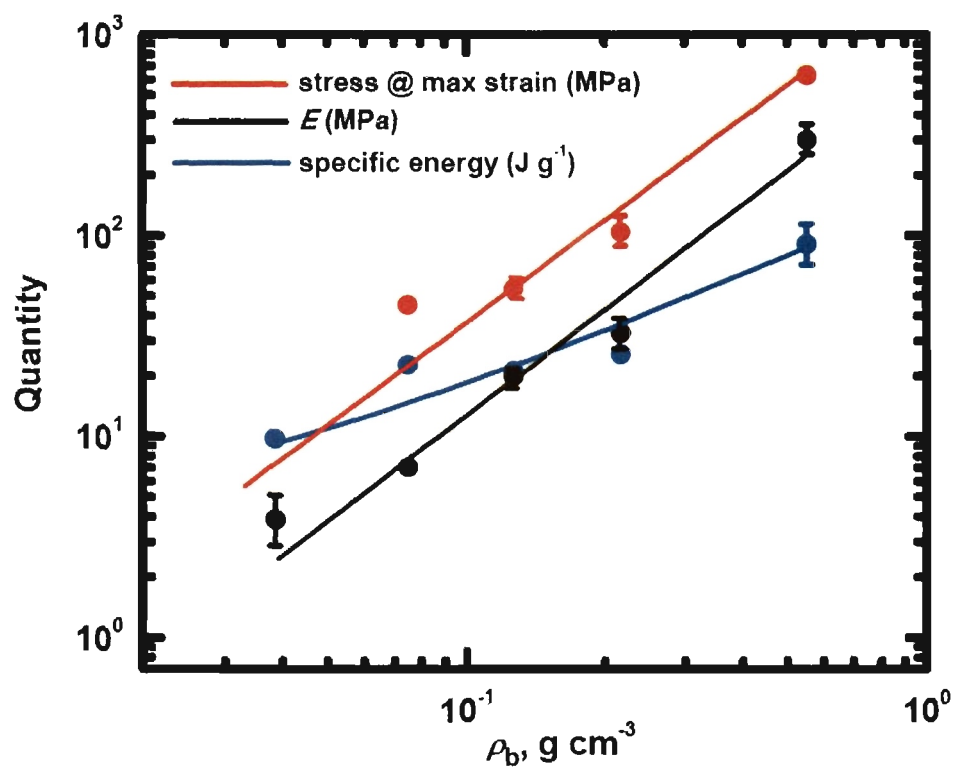
Figure 12. Log-log plot correlation of the stress at maximum strain, Young's modulus and specific energy absorption as a function of the density of PUA aerogels derived from Desmodur N3300A triisocyanate. (Data from Table 3).
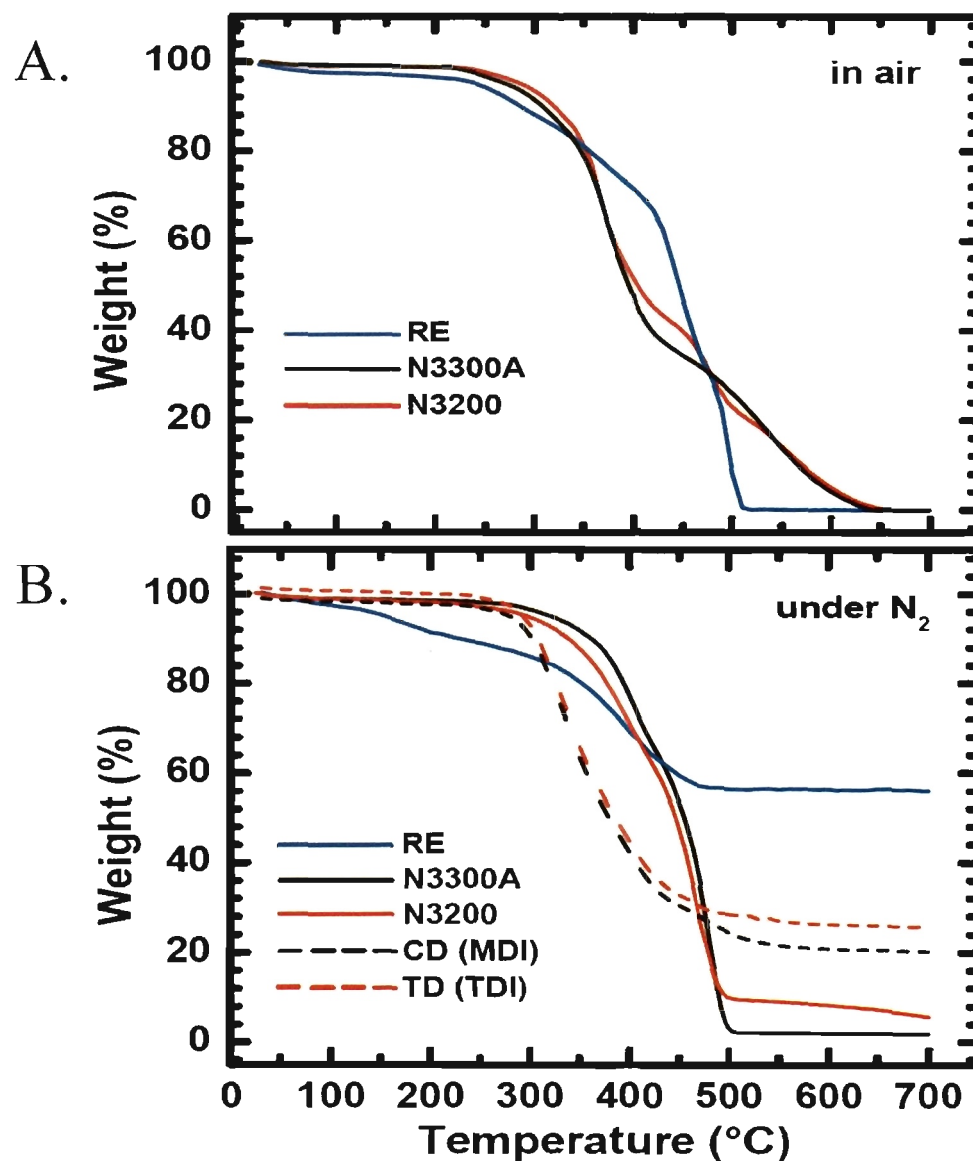
Figure 13. Thermogravimetric analysis (TGA) of PUA aerogels derived from the isocyanates shown within the frames. (A) TGA in air. (B) TGA under N_2.
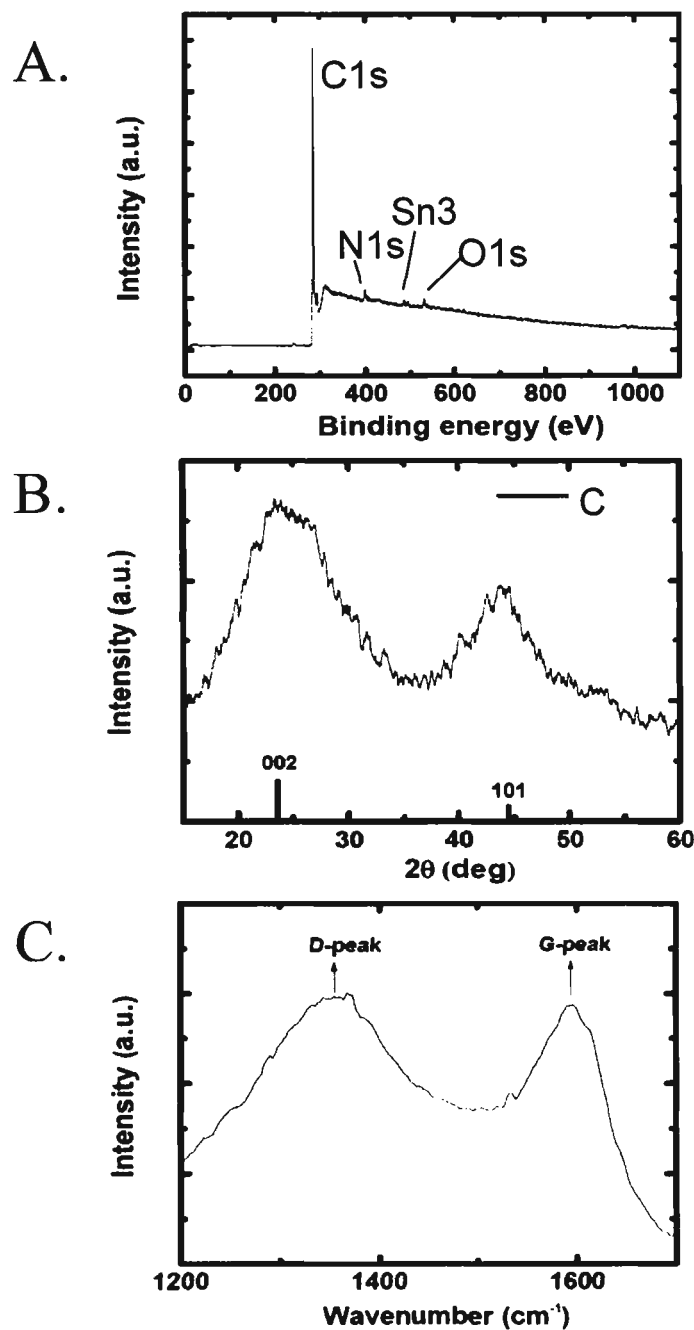
Figure 14. Representative data for carbon aerogels derived from pyrolysis of PUA aerogels (ρ_b=0.15 g cm^{-3}) made from Desmodur RE aromatic triisocyanate. (A) XPS. (Sn comes from the sample holder). (B) XRD. (C) Raman spectrum.
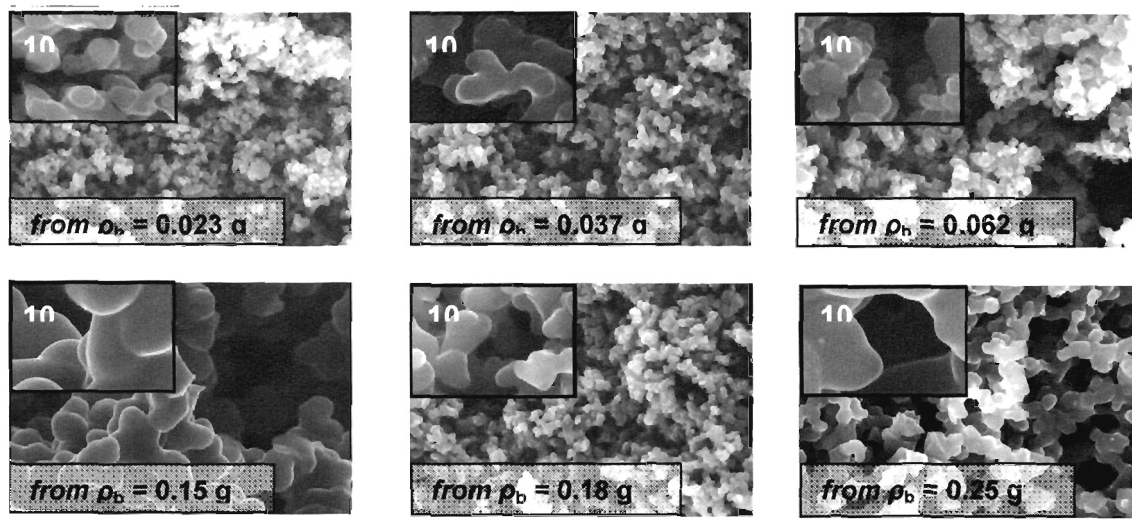
Figure 15. SEM of carbon aerogels derived from PUA aerogels made of Desmodur RE triisocyanate. Densities reported are those of the parent PUA aerogels. Scale bar: 5 μm. Morphologies should be compared with those of the PUA aerogels before pyrolysis (Figure 7). Densities of the actual C samples (from left to right); Top row: not measured (sample broke to pieces); 0.29±0.06 g cm^{-3}; 0.40±0.02 g cm^{-3}; Lower row: 0.62±0.08 g cm^{-3}; 0.72±0.03 g cm^{-3}; 0.78±0.01 g cm^{-3}.

7. Supporting Information

Table 1S. Gelation times of Desmodur N3300A sols, at the 1.375 g in 94 mL acetone formulation, as a function of the amount of water and triethylamine (Et$_3$N)

Density of Desmodur N3300A: 1.17 g cm^{-3}

amount of N3300A in sol (g)	mol equivalents of H$_2$O (mL)	% w/w Et$_3$N (mL)	concentration of N3300 A (M)	gelation time
1.375	1.5 (0.073)	0.3 (0.26)	0.0286	~ 24 h
1.375	1.5 (0.073)	0.6 (0.52)	0.0285	~ 20 h
1.375	1.5 (0.073)	0.9 (0.78)	0.0284	~ 19 h
1.375	3.0 (0.147)	0.3 (0.26)	0.0285	~ 17 h
1.375	3.0 (0.147)	0.6 (0.52)	0.0285	~ 15 h 30 min
1.375	3.0 (0.147)	0.9 (0.78)	0.0284	~ 12 h
1.375	4.5 (0.219)	0.3 (0.26)	0.0285	~ 10 h
1.375	4.5 (0.219)	0.6 (0.52)	0.0284	~ 9 h 30 min
1.375	4.5 (0.219)	0.9 (0.78)	0.0284	~ 9 h

Table 2S. Gelation times of Desmodur N3300A sols, at the 2.75 g in 94 mL acetone formulation, as a function of the amount of water and triethylamine (Et$_3$N)

Density of Desmodur N3300A: 1.17 g cm^{-3}

amount of N3300A in sol (g)	mol equivalents of H$_2$O (mL)	% w/w Et$_3$N (mL)	concentration of N3300A (M)	gelation time
2.75	1.5 (0.147)	0.3 (0.266)	0.0564	~ 18 h
2.75	1.5 (0.147)	0.6 (0.532)	0.0562	~ 17 h
2.75	1.5 (0.147)	0.9 (0.798)	0.0561	~ 14 h
2.75	3.0 (0.295)	0.3 (0.266)	0.0563	~ 12 h
2.75	3.0 (0.295)	0.6 (0.532)	0.0561	~ 9 h
2.75	3.0 (0.295)	0.9 (0.798)	0.0560	~ 8 h 30 min
2.75	4.5 (0.441)	0.3 (0.266)	0.0562	~ 6 h
2.75	4.5 (0.441)	0.6 (0.532)	0.0561	~ 4 h 30 min
2.75	4.5 (0.441)	0.9 (0.798)	0.0559	~ 3 h

Table 3S. Gelation times of Desmodur N3300A sols, at the 5.5 g in 94 mL acetone formulation, as a function of the amount of water and triethylamine (Et$_3$N)

Density of Desmodur N3300A: 1.17 g cm^{-3}

amount of N3300A in sol (g)	mol equivalents of H$_2$O (mL)	% w/w Et$_3$N (mL)	concentration of N3300A (M)	gelation time
5.5	1.5 (0.295)	0.3 (0.327)	0.1099	8 h 35 min
5.5	1.5 (0.295)	0.6 (0.654)	0.1095	~ 8 h
5.5	1.5 (0.295)	0.9 (0.981)	0.1092	7h 40 min
5.5	3.0 (0.589)	0.3 (0.327)	0.1095	6 h
5.5	3.0 (0.589)	0.6 (0.654)	0.1092	3 h
5.5	3.0 (0.589)	0.9 (0.981)	0.1088	1 h
5.5	4.5 (0.884)	0.3 (0.327)	0.1092	5 h 30 min
5.5	4.5 (0.884)	0.6 (0.654)	0.1088	~ 2 h
5.5	4.5 (0.884)	0.9 (0.981)	0.1085	1 h 33 min

Table 4S. Gelation times of Desmodur N3300A sols, at the 11 g in 94 mL acetone

Density of Desmodur N3300A: 1.17 g cm^{-3}

amount of N3300A in sol (g)	mol equivalents of H$_2$O (mL)	% w/w Et$_3$N (mL)	concentration of N3300A (M)	gelation time
11.0	1.5 (0.589)	0.3 (0.35)	0.2092	4 h
11.0	1.5 (0.589)	0.6 (0.70)	0.2085	3h 33 min
11.0	1.5 (0.589)	0.9 (1.05)	0.2078	~ 3h
11.0	3.0 (1.178)	0.3 (0.35)	0.2080	~3 h
11.0	3.0 (1.178)	0.6 (0.70)	0.2073	1h 20 min
11.0	3.0 (1.178)	0.9 (1.05)	0.2066	1 h
11.0	4.5 (1.767)	0.3 (0.35)	0.2068	1 h 30 min
11.0	4.5 (1.767)	0.6 (0.70)	0.2062	~ 45 min
11.0	4.5 (1.767)	0.9 (1.05)	0.2055	30 min

Table 5S. Gelation times of Desmodur N3300A sols, at the 16.5 g in 94 mL
acetone formulation, as a function of the amount of water and triethylamine (Et₃N)

Density of Desmodur N3300A: 1.17 g cm⁻³

amount of N3300A in sol (g)	mol equivalents of H₂O (mL)	% w/w Et₃N (mL)	concentration of N3300A (M)	gelation time
16.5	1.5 (0.884)	0.3 (0.375)	0.2994	2 h
16.5	1.5 (0.884)	0.6 (0.75)	0.2983	1 h 20 min
16.5	1.5 (0.884)	0.9 (1.125)	0.2973	1 h 10 min
16.5	3.0 (1.767)	0.3 (0.375)	0.2970	1 h
16.5	3.0 (1.767)	0.6 (0.75)	0.2960	34 min
16.5	3.0 (1.767)	0.9 (1.125)	0.2950	24 min
16.5	4.5 (2.650)	0.3 (0.375)	0.2946	38 min
16.5	4.5 (2.650)	0.6 (0.75)	0.2936	25 min
16.5	4.5 (2.650)	0.9 (1.125)	0.2926	15 min

Table 6S. Gelation times of Desmodur N3300A sols, at the 33 g in 94 mL
acetone formulation, as a function of the amount of water and triethylamine (Et₃N)

Density of Desmodur N3300A: 1.17 g cm⁻³

amount of N3300A in sol (g)	mol equivalents of H₂O (mL)	% w/w Et₃N (mL)	concentration of N3300A(M)	gelation time
33.0	1.5 (1.767)	0.3 (0.439)	0.5263	~1 h
33.0	1.5 (1.767)	0.6 (0.878)	0.5244	~ 45 min
33.0	1.5 (1.767)	0.9 (1.32)	0.5226	~ 35 min
33.0	3.0 (3.53)	0.3 (0.439)	0.5189	~ 35 min
33.0	3.0 (3.53)	0.6 (0.878)	0.5171	~ 20 min
33.0	3.0 (3.53)	0.9 (1.32)	0.5153	10 min
33.0	4.5 (5.30)	0.3 (0.439)	0.5118	10 min
33.0	4.5 (5.30)	0.6 (0.878)	0.5100	5 min
33.0	4.5 (5.30)	0.9 (1.32)	0.5082	5 min

Table 7S. Gelation times of Desmodur N3200 sols, at the middle water and triethylamine (Et₃N) formulations (refer to Desmodur N3300A, Tables S.1-S.6); Solvent: acetone, 94 mL

Density of Desmodur N3200: 1.13 g cm^{-3}

amount of N3200 in sol (g)	mol equivalents of H₂O (mL)	% w/w Et₃N (mL)	concentration of N3200 (M)	gelation time
1.3	3.0 (0.147)	0.6 (0.618)	0.0283	no gelation
2.6	3.0 (0.294)	0.6 (0.628)	0.0560	no gelation
5.2	3.0 (0.588)	0.6 (0.650)	0.1091	no gelation
10.4	3.0 (1.177)	0.6 (0.696)	0.2066	30 min
15.6	3.0 (1.765)	0.6 (0.735)	0.2955	15 min
31.2	3.0 (3.53)	0.6 (0.864)	0.5166	5 min

Table 8S. Gelation times of 4,4′,4″-triphenylmethane triisocyanate sols (TMT, from Desmodur RE), at the middle water and triethylamine (Et₃N) formulations (refer to Desmodur N3300A, Tables S.1-S.6); Solvent: acetone, 94 mL

Density of TMT: 1.015 g cm^{-3}

amount of TMT in sol (g)	mol equivalents of H₂O (mL)	% w/w Et₃N (mL)	concentration of TMT (M)	gelation time
1	3.0 (0.147)	0.6 (0.61)	0.0284	~ 36 h
2	3.0 (0.294)	0.6 (0.62)	0.0563	24 h
4	3.0 (0.588)	0.6 (0.64)	0.1099	~ 9 h
8	3.0 (1.177)	0.6 (0.674)	0.2101	2 h
12	3.0 (1.765)	0.6 (0.706)	0.3019	45 min
24	3.0 (3.53)	0.6 (0.80)	0.5360	10 min

Table 9S. Gelation times of Mondur TD (toluene isocyanate, TDI) sols, at the middle water and triethylamine (Et_3N) formulations (refer to Desmodur N3300A, Tables S.1-S.6); Solvent: acetone, 94 mL

Density of Mondur TDS: 1.214 g cm^{-3}

amount of Mondur TDS in sol (g)	mol equivalents of H_2O (mL)	% w/w Et_3N (mL)	concentration of TDI (M)	gelation time
0.474	3.0 (0.147)	0.6 (0.61)	0.0286	no gelation
0.947	3.0 (0.294)	0.6 (0.614)	0.0568	no gelation
1.89	3.0 (0.588)	0.6 (0.622)	0.1121	no gelation
3.79	3.0 (1.177)	0.6 (0.64)	0.2201	5 min
5.68	3.0 (1.765)	0.6 (0.67)	0.3213	2 min
11.36	3.0 (3.53)	0.6 (0.72)	0.5886	<1 min

Table 10S. The effect of the drying conditions on selected properties of polyurea (PUA) aerogels prepared with Desmodur N3300A triisocyanate using the middle water and triethylamine (Et₃N) formulations, that is 3.0 mol equivalents of water and 0.6% w/w triethylamine (refer to Tables S.1-S.6)

concentration of N3300A (M)	diameter (cm)	shrinkage (%) [e]	bulk density, ρ_b (g cm⁻³)	skeletal density, ρ_s (g cm⁻³) [f]	porosity, Π (% v/v void space)
0.0285					
xerogel [a,b]	0.38	73.0	0.932	1.21±0.15	22.3
aerogel [c]	1.28±0.01	13.3±0.6	0.016±0.000₄	1.24±0.23	98.6
pentane-dried [d,b]	0.42	70.0	0.734	1.23±0.31	40.3
0.0561					
xerogel [a,b]	0.44	68.5	0.951	1.25±0.18	23.9
aerogel [c]	1.35±0.01	9.1±0.9	0.034±0.000₄	1.31±0.06	97.5
pentane-dried [d,b]	0.48	65.7	0.667	1.27±0.28	47.5
0.1092					
xerogel [a,b]	0.56	60.0	0.988	1.21±0.22	18.3
aerogel [c]	1.27±0.01	14.8±0.2	0.072±0.005	1.21±0.03	93.9
pentane-dried [d,b]	0.57	59.2	0.719	1.26±0.24	43.0
0.2073					
xerogel [a,b]	0.66	52.8	1.01	1.22±0.26	17.2
aerogel [c]	1.32±0.01	10.6±0.2	0.126±0.001	1.30±0.07	90.3
pentane-dried [d,b]	0.74	47.1	0.640	1.21±0.25	47.1
0.2960					
xerogel [a,b]	0.76	45.7	1.03	1.28±0.14	19.5
aerogel [c]	1.27±0.03	14.1±1.8	0.192±0.012	1.21±0.02	84.2
pentane-dried [d,b]	1.20	14.2	0.243	1.23±0.15	80.2
0.5171					
xerogel [a,b]	0.92	34.2	1.04	1.29±0.28	19.3
aerogel [c]	1.11±0.02	25.0±1.4	0.55±0.03	1.20±0.00₁	54.1
pentane-dried [d,b]	1.14	18.5	0.490	1.19±0.13	58.8

a. Acetone-soaked wet-gels dried under ambient temperature and pressure. b. Single sample. c. Average of 5 samples dried with SCF CO_2. d. Pentane-soaked wet-gels dried under ambient pressure at 40 °C.
e. Shrinkage = 100 × (sample diameter – mold diameter)/(mold diameter). Mold diameter: 1.40 cm.
f. Single sample, average of 50 measurements.

Table 11S. Selected properties of PUA aerogels prepared using about 0.0285 M of Desmodur N3300A triisocyanate (refer to Table S.1) and all water and triethylamine (Et₃N) formulations, that is 1.5, 3.0, and 4.5 mol equivalents of water and 0.3, 0.6, and 0.9% w/w triethylamine

H_2O-Et₃N (x mol-% w/w)	diameter (cm) [a]	shrinkage (%) [a,b]	bulk density, ρ_b (g cm⁻³) [a]	skeletal density, ρ_s (g cm⁻³) [c]	porosity, Π (% void space)	BET surface area, σ (m² g⁻¹)	average pore diameter (nm) [d]	particle radius, r (nm) [e]
1.5-0.3	1.30±0.01₆	12.50±1.30	0.016±0.001	1.28±0.12	98.7	159.8	8.5 [1545]	14.6
1.5-0.6	1.27±0.00₅	14.0±0.3	0.015±0.002	1.32±0.01	98.8	230.1	13.5 [1145]	9.9
1.5-0.9	1.27±0.01₂	14.3±0.9	0.017±0.001	1.29±0.03	98.6	162.2	8.9 [1433]	14.3
3.0-0.3	1.28±0.01	13.30±0.56	0.017±0.001	1.25±0.18	98.6	288.9	11.7 [803]	8.3
3.0-0.6	1.28±0.01	13.30±0.56	0.016±0.000₄	1.24±0.23	98.6	222.4	12.0 [1109]	10.8
3.0-0.9	1.29±0.01	13.00±0.61	0.017±0.001	1.25±0.22	98.7	131.2	10.5 [1769]	18.2
4.5-0.3	1.29±0.01	12.80±0.47	0.016±0.000₆	1.24±0.28	98.6	157.5	11.0 [1566]	15.3
4.5-0.6	1.30±0.01	12.50±0.75	0.016±0.000₉	1.24±0.25	98.8	150.9	11.5 [1635]	16.0
4.5-0.9	1.29±0.01	13.10±0.33	0.016±0.001	1.28±0.31	98.7	199.5	10.5 [1237]	11.7

a. Average of 5 samples. (Mold diameter: 1.40 cm.) b. Shrinkage = 100 × (sample diameter – mold diameter)/(mold diameter). c. Single sample, average of 50 measurements. d. By the 4 × V_{Total}/σ method. For the first number, V_{Total} was calculated by the single-point adsorption method; for the number in brackets V_{Total} was calculated via $V_{Total} = (1/\rho_b)-(1/\rho_s)$. e. Calculated via $r = 3/\rho_s\sigma$.

Table 12S. Selected properties of PUA aerogels prepared using about 0.0561 M of Desmodur N3300A triisocyanate (refer to Table S.2) and all water and triethylamine (Et₃N) formulations, that is 1.5, 3.0, and 4.5 mol equivalents of water and 0.3, 0.6, and 0.9% w/w triethylamine

H₂O-Et₃N (× mol-% w/w)	diameter (cm) [a]	shrinkage (%) [a,b]	bulk density, ρ_b (g cm⁻³) [a]	skeletal density, ρ_s (g cm⁻³) [c]	porosity, Π (% void space)	BET surface area, σ (m² g⁻¹)	average pore diameter (nm) [d]	particle radius, r (nm) [e]
1.5-0.3	1.32±0.01	11.10±0.54	0.031±0.002	1.25±0.04	97.5	216.2	16.8 [581]	11.1
1.5-0.6	1.31±0.01	11.50±0.60	0.032±0.003	1.25±0.03	97.6	231.6	13.5 [526]	10.4
1.5-0.9	1.30±0.02	12.20±0.74	0.033±0.002	1.25±0.04	97.6	271.7	18.1 [434]	8.8
3.0-0.3	1.32±0.01	10.70±0.50	0.034±0.002	1.27±0.04	97.6	230.3	19.1 [497]	10.3
3.0-0.6	1.35±0.01₂	9.12±0.85	0.034±0.000₄	1.31±0.06	97.5	243.5	20.4 [471]	9.4
3.0-0.9	1.32±0.00₅	11.10±0.33	0.033±0.001	1.27±0.05	97.4	281.3	10.5 [420]	8.4
4.5-0.3	1.33±0.01	10.40±0.69	0.032±0.011	1.27±0.06	97.5	304.2	11.0 [401]	7.8
4.5-0.6	1.32±0.01	10.70±0.66	0.033±0.001	1.28±0.06	97.3	255.5	16.3 [462]	9.2
4.5-0.9	1.32±0.00₅	10.50±0.33	0.032±0.001	1.28±0.05	97.3	236.7	14.0 [514]	9.9

a. Average of 5 samples. (Mold diameter: 1.40 cm.) b. Shrinkage = 100 × (sample diameter − mold diameter)/(mold diameter). c. Single sample, average of 50 measurements. d. By the 4 × V_{Total}/σ method. For the first number, V_{Total} was calculated by the single-point adsorption method; for the number in brackets V_{Total} was calculated via $V_{Total} = (1/\rho_b)-(1/\rho_s)$. e. Calculated via $r = 3/\rho_s\sigma$.

Table 13S. Selected properties of PUA aerogels prepared using about 0.1092 M of Desmodur N3300A triisocyanate (refer to Table S.3) and all water and triethylamine (Et₃N) formulations, that is 1.5, 3.0, and 4.5 mol equivalents of water and 0.3, 0.6, and 0.9% w/w triethylamine

H$_2$O-Et$_3$N (x mol-% w/w)	diameter (cm) [a]	shrinkage (%) [a,b]	bulk density, ρ_b (g cm^{-3}) [a]	skeletal density, ρ_s (g cm^{-3}) [c]	porosity, Π (% void space)	BET surface area, σ (m^2 g^{-1})	average pore diameter (nm) [d]	particle radius, r (nm) [e]
1.5-0.3	1.28±0.01	13.50±0.41	0.072±0.008	1.24±0.16	94.1	177.6	23.3 [292.6]	13.6
1.5-0.6	1.32±0.00₄	10.60±0.32	0.069±0.001	1.24±0.01	94.4	198.8	27.7 [275.3]	12.1
1.5-0.9	1.28±0.02	13.60±1.42	0.077±0.003	1.26±0.02	93.6	200.2	25.9 [239.7]	11.8
3.0-0.3	1.31±0.06	11.40±0.32	0.070±0.003	1.24±0.12	94.4	182.8	25.7 [293]	13.2
3.0-0.6	1.27±0.01	14.80±0.18	0.072±0.005	1.21±0.03	93.9	234.7	23.6 [222.5]	10.5
3.0-0.9	1.25±0.03	16.60±0.42	0.073±0.005	1.20±0.01	93.8	185.0	28.8 [276]	13.5
4.5-0.3	1.30±0.02	12.30±0.50	0.069±0.001	1.22±0.01	94.5	176.4	32.5 [310]	13.9
4.5-0.6	1.31±0.01	11.40±0.78	0.064±0.002	1.26±0.02	95.1	174.7	32.5 [339]	13.6
4.5-0.9.1	1.27±0.02	14.10±1.21	0.070±0.002	1.22±0.03	94.1	167.9	19.7 [318]	14.6

Average of 5 samples. (Mold diameter: 1.40 cm.) b. Shrinkage = 100 × (sample diameter − mold diameter)/(mold diameter). c. Single sample, average of 50 measurements. d. By the 4 × V_{Total}/σ method. For the first number, V_{Total} was calculated by the single-point adsorption method; for the number in brackets V_{Total} was calculated via V_{Total} = $(1/\rho_b)-(1/\rho_s)$. e. Calculated via r = $3/\rho_s\sigma$.

Table 14S. Selected properties of PUA aerogels prepared using about 0.2073 M of Desmodur N3300A triisocyanate (refer to Table S.4) and all water and triethylamine (Et$_3$N) formulations, that is 1.5, 3.0, and 4.5 mol equivalents of water and 0.3, 0.6, and 0.9% w/w triethylamine

H$_2$O-Et$_3$N (x mol-% w/w)	diameter (cm) [a]	shrinkage (%) [a,b]	bulk density, ρ_b (g cm^{-3}) [a]	skeletal density, ρ_s (g cm^{-3}) [c]	porosity, Π (% void space)	BET surface area, σ (m^2 g^{-1})	average pore diameter (nm) [d]	particle radius, r (nm) [e]
1.5-0.3	1.30±0.01	12.10±0.79	0.131±0.005	1.26±0.03	89.6	177.4	19.5 [154]	13.4
1.5-0.6	1.33±0.02	10.30±1.40	0.128±0.004	1.23±0.02	89.6	171.9	34.1 [163]	14.1
1.5-0.9	1.30±0.01	12.10±0.42	0.128±0.001	1.24±0.03	89.7	154.6	36.1 [181]	15.6
3.0-0.3	1.32±0.01	10.60±1.01	0.126±0.004	1.22±0.01	89.7	200.1	32.1 [142.1]	12.2
3.0-0.6	1.32±0.01	10.60±0.18	0.126±0.001	1.30±0.07	90.3	169.4	33.4 [169.3]	13.6
3.0-0.9	1.33±0.01	10.30±0.55	0.127±0.003	1.20±0.01	89.3	153.4	26.3 [183.5]	16.2
4.5-0.3	1.32±0.01	10.60±0.67	0.125±0.005	1.24±0.02	89.9	123.7	20.4 [233]	19.5
4.5-0.6	1.33±0.01	10.40±0.37	0.122±0.001	1.25±0.02	90.2	133.6	23.5 [241]	17.9
4.5-0.9	1.32±0.02	10.60±0.28	0.130±0.006	1.25±0.03	90.7	126.0	18.1 [218]	19.0

a. Average of 5 samples. (Mold diameter: 1.40 cm.) b. Shrinkage = 100 × (sample diameter – mold diameter)/(mold diameter). c. Single sample, average of 50 measurements. d. By the 4 × V_{Total}/σ method. For the first number, V_{Total} was calculated by the single-point adsorption method; for the number in brackets V_{Total} was calculated via $V_{Total} = (1/\rho_b)-(1/\rho_s)$. e. Calculated via $r = 3/\rho_s\sigma$.

Table 15S. Selected properties of PUA aerogels prepared using about 0.2960 M of Desmodur N3300A triisocyanate (refer to Table S.5) and all water and triethylamine (Et₃N) formulations, that is 1.5, 3.0, and 4.5 mol equivalents of water and 0.3, 0.6, and 0.9% w/w triethylamine

H₂O-Et₃N (× mol-% w/w)	diameter (cm) [a]	shrinkage (%) [a,b]	bulk density, ρ_b (g cm⁻³) [a]	skeletal density, ρ_s (g cm⁻³) [c]	porosity, Π (% void space)	BET surface area, σ (m² g⁻¹)	average pore diameter (nm) [d]	particle radius, r (nm) [e]
1.5-0.3	1.28±0.03	13.30±2.09	0.194±0.012	1.19±0.01	83.8	51.67	21.5 [333]	48.7
1.5-0.6	1.28±0.01	13.40±0.88	0.212±0.004	1.25±0.01	83.1	153.5	23.6 [102]	15.6
1.5-0.9	1.29±0.02	12.70±1.11	0.194±0.001	1.23±0.01	84.2	153.1	29.1 [113]	15.9
3.0-0.3	1.31±0.01	11.10±0.85	0.181±0.003	1.18±0.01	84.7	149.1	19.7 [125.4]	17.1
3.0-0.6	1.27±0.03	14.10±1.78	0.192±0.012	1.21±0.02	84.2	67.5	27.8 [259]	36.7
3.0-0.9	1.27±0.02	13.90±1.48	0.197±0.009	1.22±0.01	83.8	49.2	13.4 [345]	49.9
4.5-0.3	1.28±0.04	13.50±2.40	0.189±0.008	1.21±0.01	84.4	68.9	23.6 [259]	35.9
4.5-0.6	1.26±0.01	15.10±0.77	0.22±0.01	1.23±0.01	82.2	51.0	23.3 [292]	47.8
4.5-0.9	1.27±0.02	14.40±1.45	0.191±0.010	1.23±0.02	84.5	24.8	23.1 [712]	98.3

a. Average of 5 samples. (Mold diameter: 1.40 cm.) b. Shrinkage = 100 × (sample diameter – mold diameter)/(mold diameter). c. Single sample, average of 50 measurements. d. By the 4 × V_{Total}/σ method. For the first number, V_{Total} was calculated by the single-point adsorption method; for the number in brackets V_{Total} was calculated via $V_{Total} = (1/\rho_b)-(1/\rho_s)$. e. Calculated via $r = 3/\rho_s\sigma$.

Table 16S. Selected properties of PUA aerogels prepared using about 0.5171 M of Desmodur N3300A triisocyanate (refer to Table S.6) and all water and triethylamine (Et₃N) formulations, that is 1.5, 3.0, and 4.5 mol equivalents of water and 0.3, 0.6, and 0.9% w/w triethylamine

H₂O-Et₃N (× mol-% w/w)	diameter (cm) [a]	shrinkage (%) [a,b]	bulk density, ρ_b (g cm⁻³) [a]	skeletal density, ρ_s (g cm⁻³) [c]	porosity, Π (% void space)	BET surface area, σ (m² g⁻¹)	average pore diameter (nm) [d]	particle radius, r (nm) [e]
1.5-0.3	1.13±0.03	23.50±1.37	0.56±0.02	1.19±0.00₁	53.2	53.3	31.1 [70.5]	47.2
1.5-0.6	1.12±0.01	24.20±0.88	0.56±0.02	1.19±0.00₁	53.2	52.7	22.7 [71.3]	47.8
1.5-0.9	1.12±0.02	24.50±1.11	0.54±0.04	1.20±0.00₁	84.2	46.9	33.3 [86.7]	53.3
3.0-0.3	1.12±0.01	24.60±0.85	0.54±0.02	1.19±0.00₂	54.5	56.9	26.7 [70.9]	44.3
3.0-0.6	1.11±0.02	25.01±1.35	0.55±0.03	1.20±0.00₁	54.1	53.8	31.9 [73.3]	46.4
3.0-0.9	1.10±0.02	25.50±1.30	0.55±0.03	1.20±0.00₂	54	52.7	14.8 [74.8]	47.4
4.5-0.3	1.10±0.02	25.50±1.30	0.54±0.04	1.20±0.01	54.9	57	26.7 [71.3]	45.5
4.5-0.6	1.08±0.04	26.50±0.30	0.56±0.02	1.20±0.02	52.5	71.7	25.1 [52.8]	34.8
4.5-0.9	1.10±0.02	25.80±0.70	0.54±0.02	1.20±0.01	55.2	56.1	29.6 [72.8]	45.2

a. Average of 5 samples. (Mold diameter: 1.40 cm.) b. Shrinkage = 100 × (sample diameter – mold diameter)/(mold diameter). c. Single sample, average of 50 measurements. d. By the 4 × V_{Total}/σ method. For the first number, V_{Total} was calculated by the single-point adsorption method; for the number in brackets V_{Total} was calculated via $V_{Total} = (1/\rho_b)-(1/\rho_s)$. e. Calculated via $r = 3/\rho_s\sigma$.

Table 17S. Selected properties of carbon aerogels prepared from Desmodur RE triisocyanate PUA aerogels

[RE] in sol (M)	diameter (cm) [a]	shrinkage (%) [a,b]	bulk density, ρ_b (g cm^{-3}) [a]	density, ρ_s (g cm^{-3})	skeletal Π (% void space)	porosity, % carbon
0.0284	c	c	c	1.78±0.12	c	48
0.0563	0.43±0.08	42.0±1.8	0.287±0.063	1.82±0.31	84.2	52
0.1099	0.48±0.01	36.0±2.3	0.395±0.017	1.86±0.53	78	49
0.2101	0.54±0.03	30.0±1.7	0.62±0.08	1.88±0.37	67	56
0.3019	0.51±0.12	33.0±0.9	0.721±0.028	1.81±0.25	61	53
0.5360	0.48±0.13	36.6±1.5	0.776±0.013	1.89±0.52	59	59

a. Average of 3 samples. (Mold diameter: 1 cm)

b. Shrinkage = 100 × (sample diameter – mold diameter) / (mold diameter).

c. Irregular sample, bulk density was not determined.
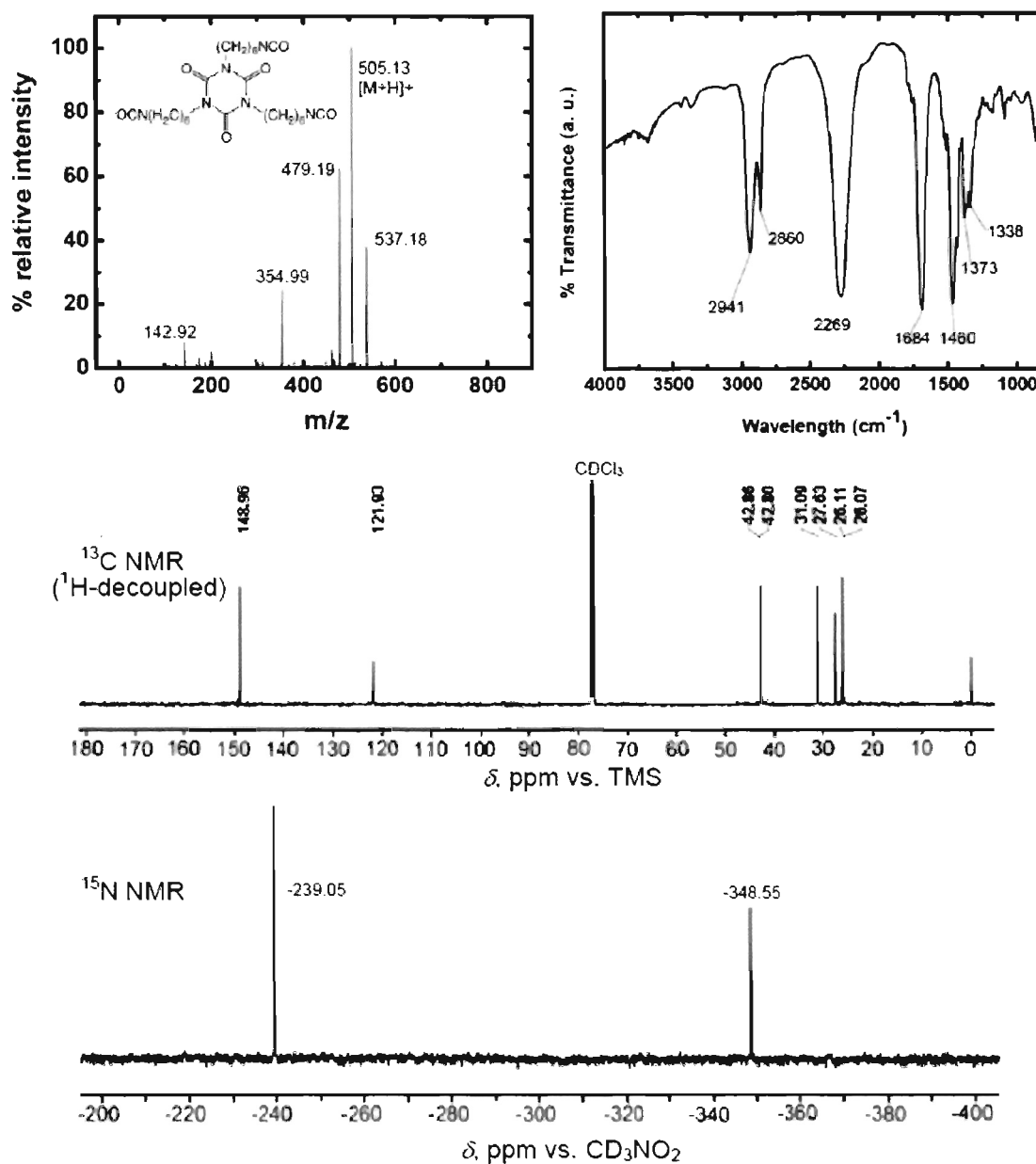
Figure 1S. Spectroscopic characterization of Desmodur N3300A. The MS analysis used atmospheric pressure chemical ionization by proton transfer (*Anal. Chem.* **2005**, *77*, 7826). CH_3OH was flowing into the source at 10 μL min^{-1}. The sample was dissolved in CH_2Cl_2. The peak at m/z=479.19 corresponds to the reaction product of one NCO of Desmodur N3300A with moisture (H_2O).
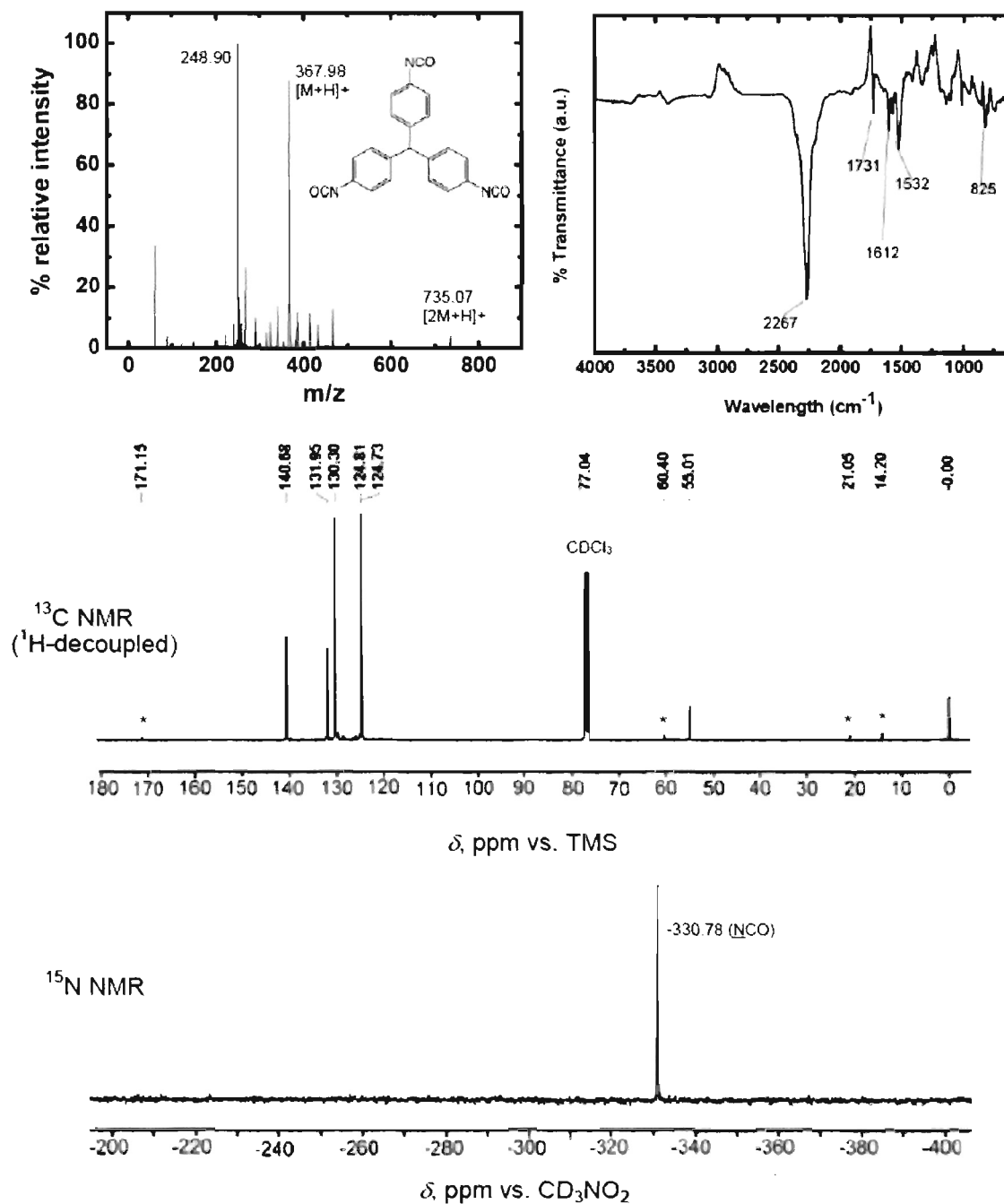
Figure 2S. Spectroscopic characterization of Desmodur RE. For MS analysis the sample was used as supplied by Bayer (a 27% w/w solution in EtOAc). No flowing CH$_3$OH. The peak at m/z=248.90 is of the fragment: OCN-Ph-(CH)+-Ph-NCO. Asterisks in the ^{13}C NMR spectrum are due to ethylacetate.
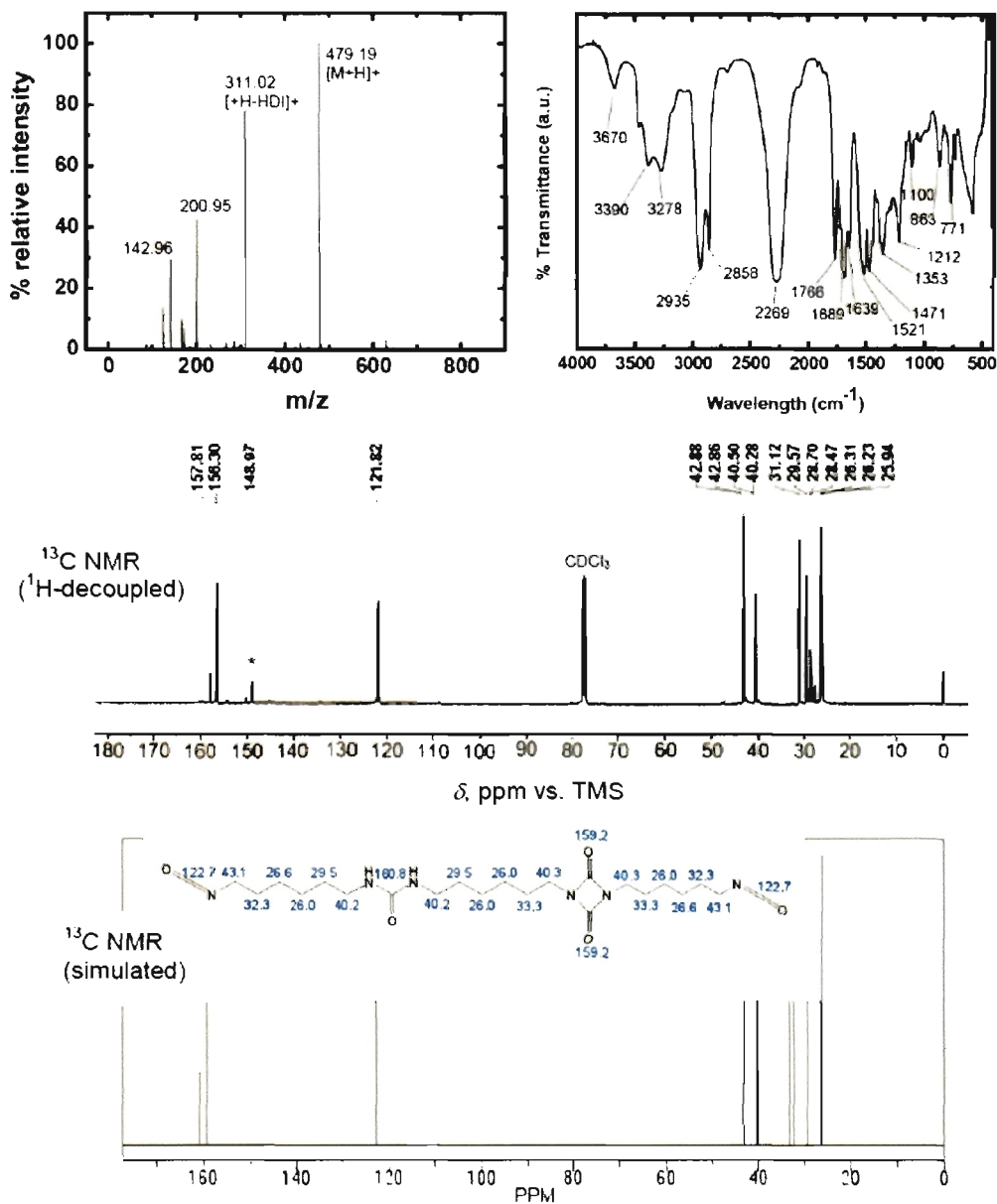
Figure 3S. Spectroscopic characterization of Desmodur N3200. HDI in the mass spectrum refers to monomeric hexamethylene diisocyanate. The ^{13}C NMR peak marked with an asterisk is an unidentified impurity that contains the isocyanurate ring (refer to the spectrum of Desmodur N3300A above).
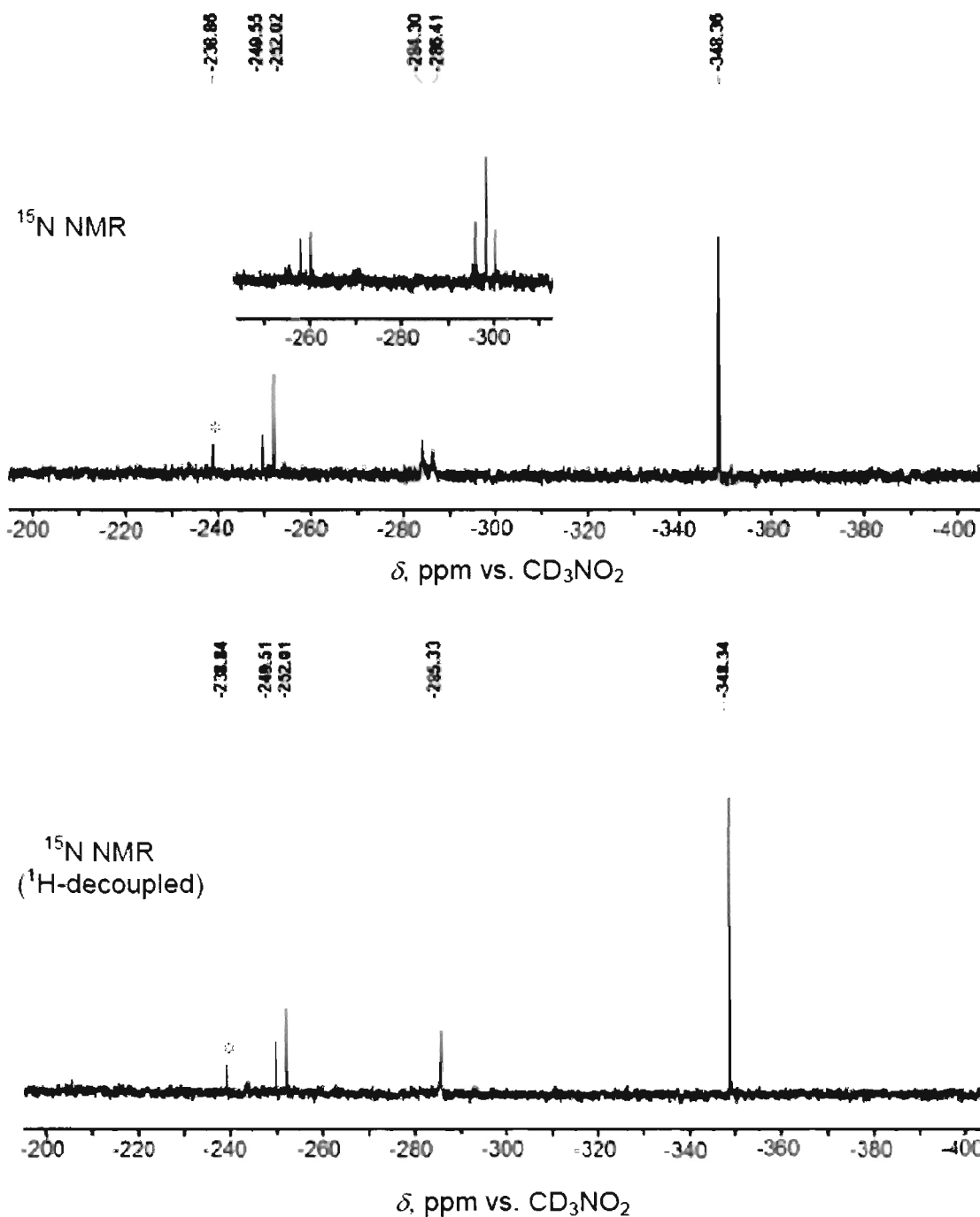
Figure 3S. Spectroscopic characterization of Desmodur N3200. HDI in the mass spectrum refers to monomeric hexamethylene diisocyanate. The ^{13}C NMR peak marked with an asterisk is an unidentified impurity that contains the isocyanurate ring (refer to the spectrum of Desmodur N3300A above).(Continued)
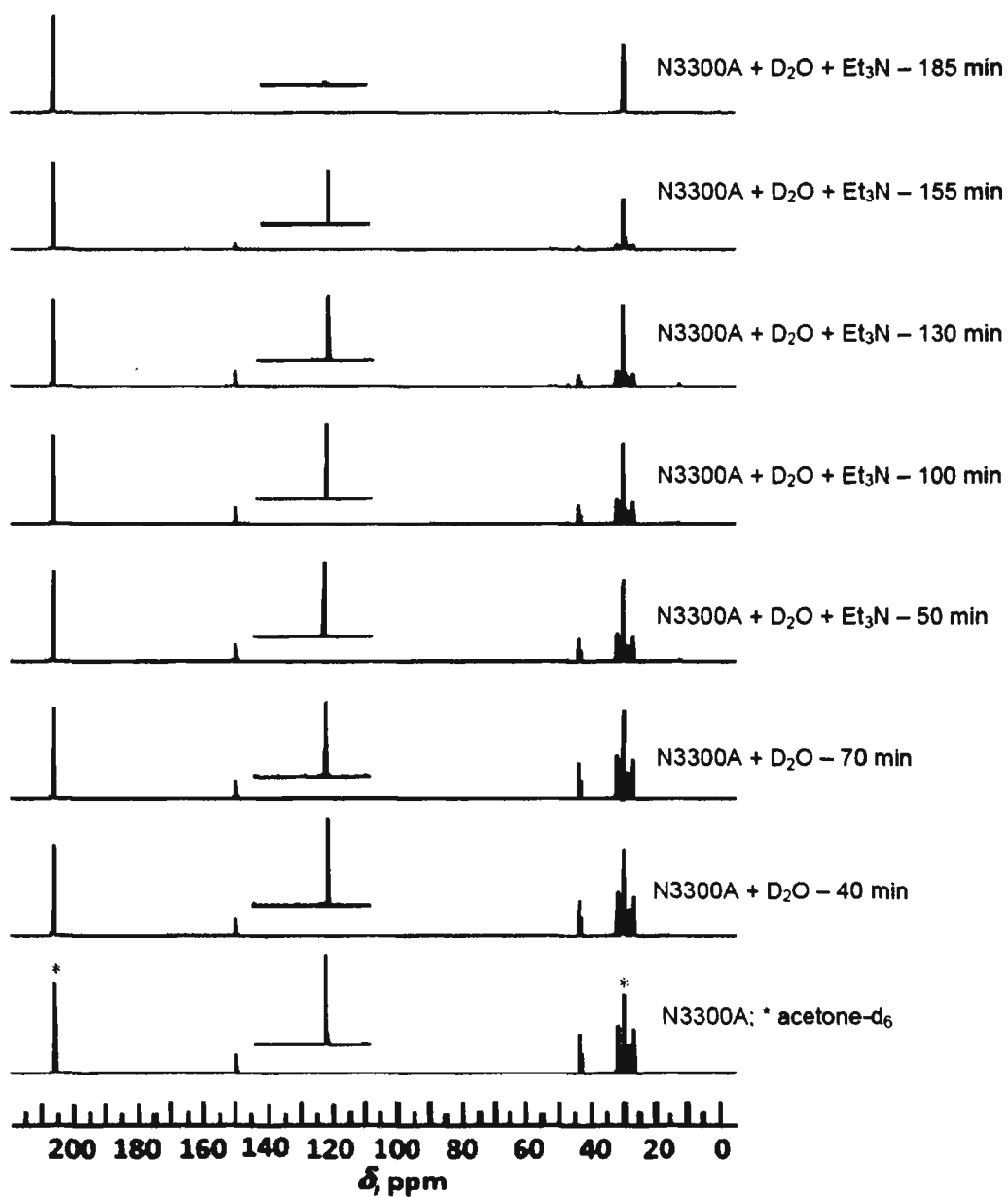
Figure 4S. Liquid ^{13}C NMR during gelation of Desmodur N3300A (0.109 M) in acetone $-d_6$ using 3 mol excess of H_2O and 0.6% w/w Et_3N, as defined in this work (Table 3S)
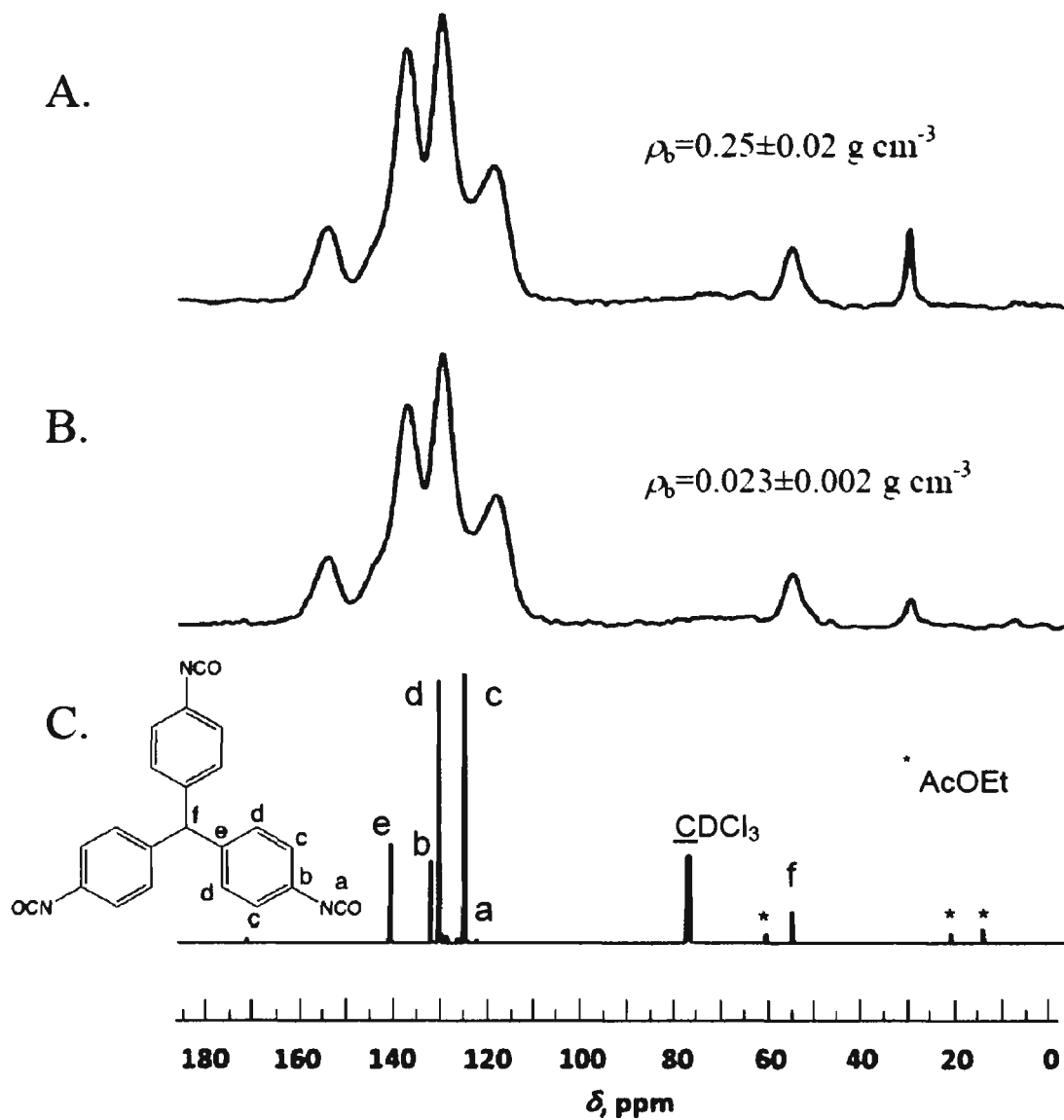
Figure 5S. Solids CPMAS ^{13}C NMR of a high-density PUA aerogel made of Desmodur RE triisocyanate (A), in comparison with a low-density sample (B), and the liquids ^{13}C NMR of the monomer in $CDCl_3$ (C). (PUA samples prepared as in Table 8S)
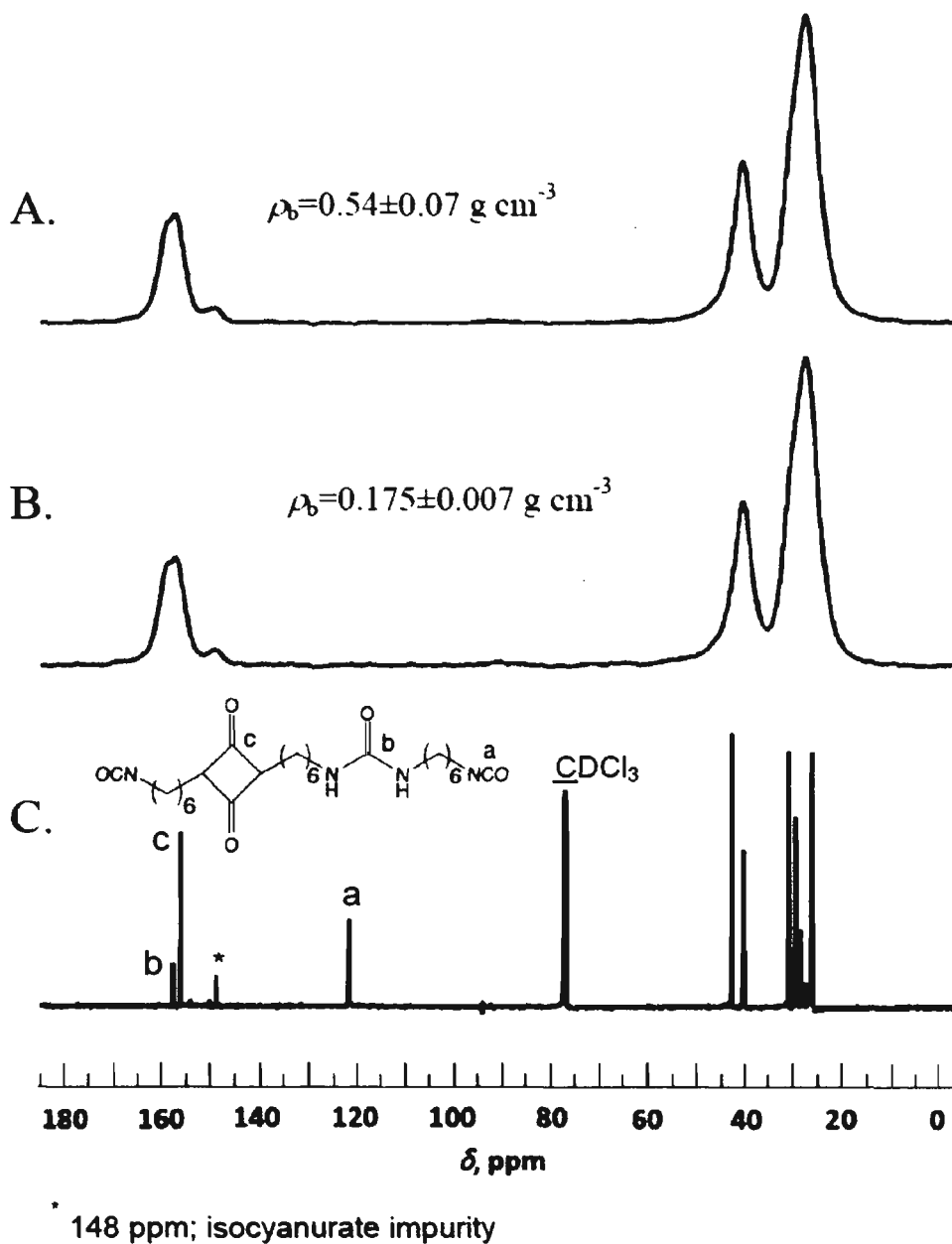
Figure 6S. Solids CPMAS ^{13}C NMR of a high-density PUA aerogel made of Desmodur N3200 diisocyanate (A), in comparison with a low-density sample (B), and the liquids ^{13}C NMR of the monomer in CDCl$_3$ (C). (PUA samples prepared as in Table 7S.)
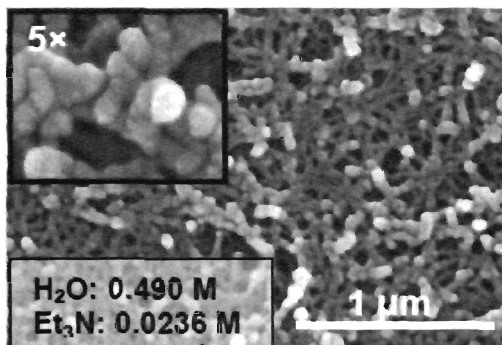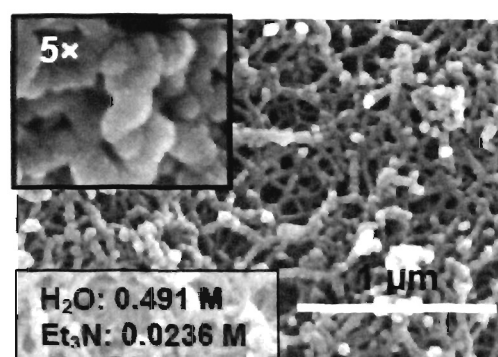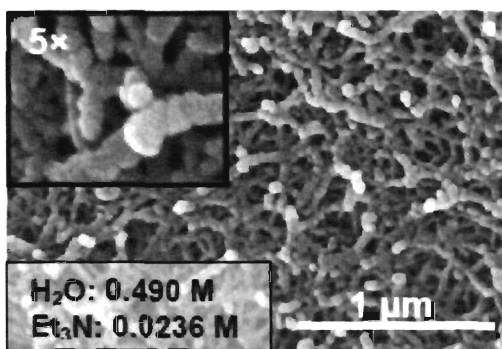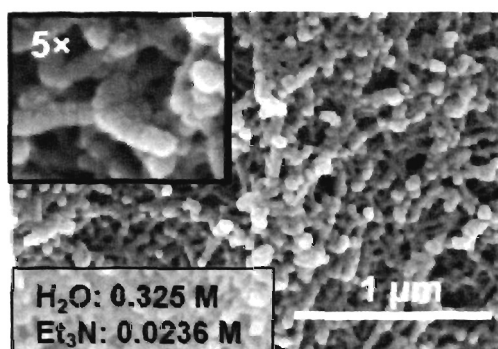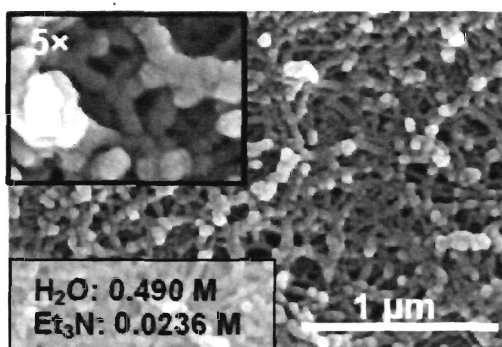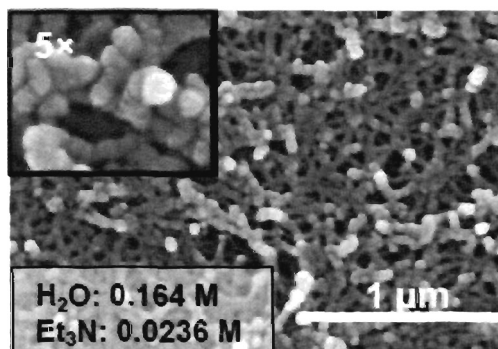
Figure 7S. Morphology of Desmodur N3300A-derived polyurea aerogels at constant N3300A concentration (0.109 M) as a function of H_2O and Et_3N concentrations.

II . Smelting in the age of nano: iron aerogels

Nicholas Leventis,[*a] Naveen Chandrasekaran[a], Chariklia Sotiriou-Leventis,[*a] Arif Mumtaz[b]

[a]*Department of Chemistry, Missouri University of Science & Technology, Rolla, MO, 65409, USA.*
[b]*Department of Physics, Quaid-i-Azam University, Islamabad, Pakistan.*

Smelting of interpenetrating networks of resorcinol-formaldehyde (RF) and iron oxide (FeOx) aerogels yields porous ferromagnetic and superparamagnetic materials in monolithic form with compositions closely resembling that of pig iron.

About 3000 years ago humankind entered the iron age by inventing the smelting process, where an iron ore (*e.g.*, hematite) is reduced by carbon to metallic iron according to:

$$Fe_2O_3 + C \rightarrow Fe + CO_2$$
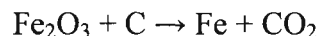
In the beginning, the source of carbon was charcoal and later coke. Charcoal is produced by burning wood under limited oxygen supply. Interestingly, highly porous carbon (C) aerogels are made by an analogous method, namely by pyrolysis under N_2 or Ar of organic resorcinol-formaldehyde (RF) aerogels.[1] C aerogels with low loading of iron (typically <5% w/w) have been explored in catalysis and they are made by either dissolving an iron salt in the RF sol,[2,3] or by substituting R with potassium 2,4-dihydroxybenzoate, which is ion-exchanged later in the gel state forming a salt with the dopant (Fe^{3+}).[4,5] Importantly, pyrolysis of Fe^{3+}-doped RF networks of nanoparticles yields Fe-doped C aerogels in one step.[2,5,6] Thus, in order to produce porous iron by a smelting-like process, the quest becomes one of producing porous intimate mixtures of RF and iron oxide aerogels. The condensation of resorcinol (R) and formaldehyde (F) is catalyzed effectively by HCl.[7] Thus, by moving from the typical $Na_2CO_3/H_2O/80$ °C

system,[8] to a HCl/CH₃CN/room temperature gelation protocol it has been possible to accelerate the RF gelation process from 7 days at 80 °C to a couple of hours at room temperature.[7] Meanwhile, hydrated metal oxides such as $[Fe(H_2O)_6]^{3+}$, are fairly strong Brønsted acids (pK_a ~3.5).[9] That property is used successfully in conjunction with the irreversible proton-consuming ring opening of epoxides (*e.g.*, epichlorohydrin) for the formation of metal–oxygen–metal networks leading to gelation and ultimately to metal oxide aerogels.[9,10] Reasoning that the acidity of a $[Fe(H_2O)_6]^{3+}$ sol gelling towards iron oxide could be utilized for the co-gelation of a RF network, we prepared sols by mixing solution A containing 0.337 g (3.06 mmol) R and 0.455 mL of a commercial 37% w/w solution of F (6.11 mmol) in 5.75 mL CH₃CN, and solution B containing 0.89 g (3.3 mol) FeCl₃·6H₂O, and 2.75 mL (33 mmol) of epichlorohydrin in 5 mL EtOH. That sol was poured into glass molds and it was allowed to react at 80 °C for 1 h followed by room temperature aging for 24 h. Gelation occurs in 10 min, but there is no way of knowing which network is formed first, because the red color of the iron salt obscures the red color of *o*-quinone methide that develops upon gelation of the RF system.[7] Thus, the duration of the post-gelation aging was decided by monitoring of the pH during gelation, and on control experiments with RF-hafnia.

The HCl/CH₃CN:EtOH (1:1 v/v)/RF system gels at 80 °C in 10 min and its pH remains around zero throughout the process. The $[Fe(H_2O)_6]^{3+}$/CH₃CN : EtOH (1:1 v/v)/RF system gels at 80 °C in ~50 min (confirming the role of the hydrated iron salt as a catalyst for the RF gelation), and its pH remains very acidic rising from 0.2 to 0.6 during the process. The $[Fe(H_2O)_6]^{3+}$/CH₃CN : EtOH (1:1 v/v)/epichlorohydrin system (no RF) gels in ~10 min and consumes protons.[9] Indeed the pH starts at 0.6, gelation

takes place at pH ~4.2 and it reaches pH ~7.0 in ~50 min where it remains constant thereafter. The complete $[Fe(H_2O)_6]^{3+}$/CH$_3$CN:EtOH (1:1 v/v)/RF/epichlorohydrin system gels also in ~10 min; the pH starts at 0.6, gelation occurs at pH ~3.8 and it keeps rising reaching a value of ~5.5 after 70 min. The analogous RF-hafnia control system gels also in ~10 min, but the initial gels are almost colorless, allowing observation of the red color of the RF network developing in ~40 min. The pH data and the RF-hafnia system together indicate that the iron oxide network is formed first. Since at about neutral pHs the RF system is expected to gel in a day,[11] RF/FeOx wet gels were aged for another 24 h in their molds. RF-FeOx wet gels were washed with CH$_3$CN : EtOH (1 : 1 v/v, 3×) and solvent-exchanged with acetone (4×). They were either dried supercritically to native n-RF-FeOx aerogels, or in order to increase their mechanical integrity they were crosslinked with a hexamethylene diisocyanate oligomer (Desmodur N3300A, supplied by Bayer) that yields a conformal polyurea coating over the entire skeletal framework according to procedures well established in our laboratory.[12] The crosslinked samples are designated X-RF-FeOx. All wash solvents were collected, dried and the solid residue was pyrolyzed at 800 °C in air yielding a small amount of pure Fe_2O_3, corresponding to 98.9% mol/mol of the initial iron in the sol retained in the gel. Both n- and X-RF-FeOx were characterized thermogravimetrically (TGA), microscopically (SEM), physically (N$_2$ sorption porosimetry), chemically (energy dispersive spectroscopy: EDS or EDAX, and XRD) and magnetically (*MH* curves).

By TGA in air n-RF-FeOx loses 65% of its mass by 375 °C, showing that it consists of about 65% w/w RF. Under the same conditions X-RF-FeOx loses 90% of its mass by 500 °C, consistent with a massive polymer uptake during crosslinking. SEM

(Fig. 1) confirms that both n- and X-RF-FeOx aerogels consist of networks of nanoparticles. In X-RF-FeOx, polymer coats clusters of nanoparticles leaving a vast interstitial space open in agreement with our previous studies.[12] Porosities (as % v/v empty space) were calculated from bulk and skeletal densities (ρ_b = 0.046 g cm^{-3} and ρ_s = 2.86 ± 0.12 g cm^{-3} for n-RF-FeOx; ρ_b = 0.418 ± 0.015 g cm^{-3} and ρ_s = 1.42 ± 0.031 g cm^{-3} for X-RF-FeOx) and they are equal to 98.2 ± 0.2% and 70.6 ± 1.0% for n- and X-RF-FeOx, respectively. The corresponding BET surface area of n- and X-RF-FeOx are 410 m^{2}g^{-1} and 80 m^{2}g^{-1}, respectively.

Pyrolysis under a flowing stream of Ar in the 200–1000 °C range yields different chemical and structural evolution for the two materials. By SEM, X-RF-FeOx display macroporosity as early as 400 °C, consistently with previous findings with crosslinked RF aerogels:[13] based on extensive correlation of SEM, ^{13}C-NMR, TGA and DSC data, the chemical bonding between the crosslinking polymer (polyurea) and the RF network breaks at ~250 °C; the polymer, finding itself above its melting point (123 °C), melts and exerts surface tension forces to the surrounding network that cause partial collapse creating macropores.[13] That morphology survives after pyrolysis at 1000 °C and the material resulting from X-RF-FeOx (called X-C-Fe) is clearly macroporous with a BET surface area σ = 97 m^2 g^{-1}. By comparison n-C-Fe is mesoporous with σ = 163 m^2 g^{-1}.

By EDS (see Fig. 2) the O content as a function of the pyrolysis temperature in both n- and X-RF-FeOx samples decreases monotonically to zero. The C content in both cases reaches a maximum at ~35% after pyrolysis at 600 °C and then decreases to <5% w/w after pyrolysis at 1000 °C. The Fe content, however, behaves differently in the two materials: it increases monotonically in n-RF-FeOx, but it shows a local minimum at 400

°C in X-RF-FeOx. Clearly, n- and X-RF-FeOx have different chemical evolutions as confirmed by XRD (Fig. 3 and Table 1).

Table 1 Percent compositions (w/w) by XRD after pyrolysis at different temperatures (in parentheses, crystallite size in nm, by the Scherrer equation)

n-RF-FeOx	200 °C	400 °C	600 °C	800 °C	1000 °C
γ-Fe$_2$O$_3$	100 (4.1)	100 (16)	100 (28)	4.3 (19)	
Fe$_3$C				48.8 (33)	
Fe				10.9 (36)	100 (35)
Fe$_{15.1}$C				18.2	
C				17.8 (7.8)	
X-RF-FeOx					
γ-Fe$_2$O$_3$	100 (4.6)	49.5 (27)	11.3 (23)	4.8 (19)	
Fe$_3$C		44.3 (30)	74.5 (36)	43.7 (33)	75.0 (30)
Fe			14.2	13.3 (9.6)	25.0 (25)
Fe$_{15.1}$C				9.9	
C				28.3 (3.2)	
FeO		6.1 (35)			

As-made n- and X-RF-FeOx are both amorphous. At 200 °C, we observe broad reflections corresponding to microcrystalline maghemite (γ-Fe$_2$O$_3$) with crystallite size of only 4.1 nm. At 400 and 600 °C, n-RF-FeOx continues to show γ-Fe$_2$O$_3$ as the only crystalline phase present while the reflections become sharper and the crystallite size increases. At 800 °C, a small amount of γ-Fe$_2$O$_3$ is still present in both samples, but their main crystalline make up includes Fe$_3$C, iron, austenite (Fe$_{15.1}$C) and graphite. After pyrolysis at 1000 °C, the only crystalline phase of n-C-Fe is iron, even though EDS shows a small amount of (presumably amorphous) carbon (4.9%). The behavior of X-RF-FeOx is quite different. As early as 400 °C, we note the formation of Fe$_3$C and a small

amount of wustite (FeO). At 600 °C, wustite is no longer present and we note the formation of Fe. At 800 °C, the two main crystalline components of X-C-Fe are Fe_3C and Fe, while at 1000 °C those are the only ones. Based on the Fe_3C : Fe w/w ratio of 3 : 1 (see Table 1) the amount of carbon in the crystalline components of X-C-Fe is calculated at 5.0%. By EDS, the total amount of carbon after pyrolysis at 1000 °C was 6.08%. Therefore, X-C-Fe produced at 1000 °C consists almost exclusively of crystalline Fe_3C and Fe with about the same crystallite sizes ($\sim$25–30 nm, Table 1), and presumably a small amount (about 1.1%) of amorphous carbon. Basically, the chemical composition of both n- and X-C-Fe is very similar to that of pig iron. Obviously, however, the thermolytic behavior of the two materials has been different and this is attributed to the molten crosslinker that first causes partial collapse of the RF and FeOx networks and subsequently it plays the role of a "solvent" where nanoparticles undergo more efficient mixing and reaction.

After pyrolysis at 800 or 1000 °C n-C-Fe and X-C-Fe are both electrically conducting and magnetic (attracted by small laboratory magnets). Analysis of *MH* loops, however, reveals that their magnetic properties are also quite different. After pyrolysis at 800 °C, n-C-Fe shows ferromagnetic behavior with a hysteresis loop and nonvanishing magnetization at zero field (Fig. 4A). The demagnetization curve follows a concave shape (rather than the more conventional convex shape), a behavior that is enhanced as the temperature is raised to 325 K, where a pinched-shaped hysteresis loop is evident. Finally, the magnetization at 20 kOe does not reach saturation, which is a typical behavior of small particles with modified surfaces.[14] On the other hand, after pyrolysis at 800 °C X-C-Fe is superparamagnetic at 300 K (it shows zero coercivity and remanence at

zero field, Fig. 4B) consistent with smaller particles (refer to the corresponding SEM) and a lower blocking temperature (at around 140 K). It is noted, however, even though the loop of X-C-Fe has collapsed at the origin, there is yet significant hysteresis at higher fields. The anomalous behavior of both n- and X-C-Fe samples, in one case the pinched hysteresis loop and in the other case a nonvanishing hysteresis at high fields, most probably stems from the presence of two ferromagnetic phases namely, the soft Fe phase and a relatively hard Fe_3C phase.

In conclusion, porous pig iron is produced by smelting interpenetrating RF and FeOx aerogels. Crosslinking alters the thermolytic behavior leading to macropores, but most importantly by melting it mixes intimately the skeletal RF and FeOx nanoparticles depressing their reaction temperature by as much as 400 °C. This is explored further with other interpenetrating networks of nanoparticles.

Acknowledgements

Notes and References

1. Al-Muhtaseb, S. A.; Ritter, J. A. *Adv. Mater.*, **2003**, *15*, 101-114.

2. Moreno-Castilla, C.; Maldonado-Hódar, F. J. *Carbon*, **2005**, *43*, 455-465.

3. Moreno-Castilla, C.; Maldonado-Hódar, F. J.; Perez- Cadenas, A.F. *Langmuir*, **2003**, *19*, 5650-5655.

4. Baumann, T. F.; Fox, G.A.; Scatcher, N.; Yoshizawa, R.; Dresselhaus, M.S. *Langmuir*, **2002**, *18*, 7073-7076.

5. Steiner, S.A.; Baumann, T. F.; Kong, J.; Satcher, J. H. *Langmuir*, **2007**, *23*, 5161-5166.

6. Cotet, L.C.; Gich, M.; Roig, A.; Popescu, I.C.; Mollins, E.; Danciu, M. J. Non-Cryst Solids, **2006**, *352*, 2772-2777.

7. Pekala, R.W. J. Mater. Sci, **1989**, *24*, 3221-3277.

8. S. Mulik, C. Sotiriou-Leventis and N. Leventis, *Chem. Mater.*, 2007, **19**, 6138-6144.

9. Gash, A. E.; Tillotson, T. M.; Satcher, J. H.; Poco, J. F.; Hrubesh, L. W.; Simpson, R. L. *Chem. Mater.*, **2001**, *13*, 999-1007.

10. Leventis, N.; Vassilaras, P.; Fabrizio, E. F.; Dass, A. *J. Mater. Chem.*, **2007**, *17*, 1502-1508.

11. Bekyarova, E.; Kaneko, K. *Adv. Mater.*, **2000**, *12*, 1625-1628.

12. Leventis, N.; *Acc. Chem. Res.*, **2007**, *40*, 874-884.

13. Mulik, S.; Sotiriou-Leventis, C. ; and Leventis, N.; *Chem. Mater.*, **2008**, *20*, 6985-6997.

14. Kodama, R. H.; Berkowitz, A. E.; McNiff, E. J.; and S. Foner, *Phys. Rev. Lett.*, **1996**, *77*, 394-397.

Figures

native (n-samples)   crosslinked (X-samples)

1000 °C 163 m^{2}g^{-1} 1000 °C 97 m^{2}g^{-1}

800 °C 303 m^{2}g^{-1} 800 °C 160 m^{2}g^{-1}

600 °C 416 m^{2}g^{-1} 600 °C 207 m^{2}g^{-1}

400 °C 81 m^{2}g^{-1} 400 °C 308 m^{2}g^{-1}

200 °C 246 m^{2}g^{-1} 200 °C 76 m^{2}g^{-1}
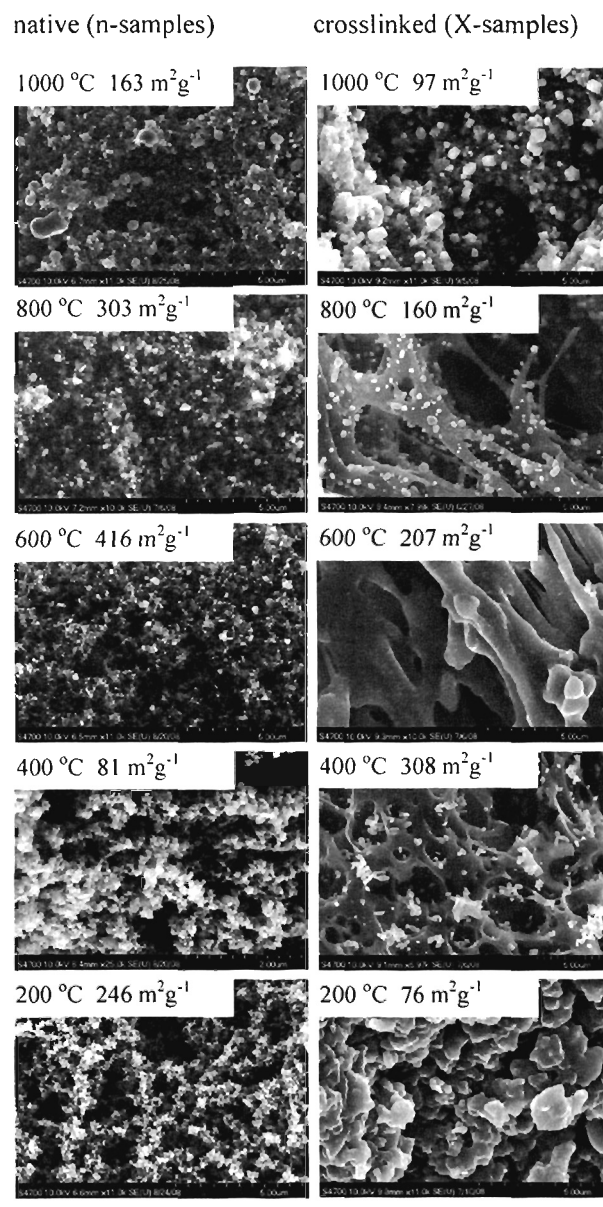
Fig .1 SEMs of native (n-RF-FeOx) and crosslinked (X-RF-FeOx) monoliths after pyrolysis under Ar at different temperatures. The length bar is 5 µm. BET surface areas for each sample are also provided.
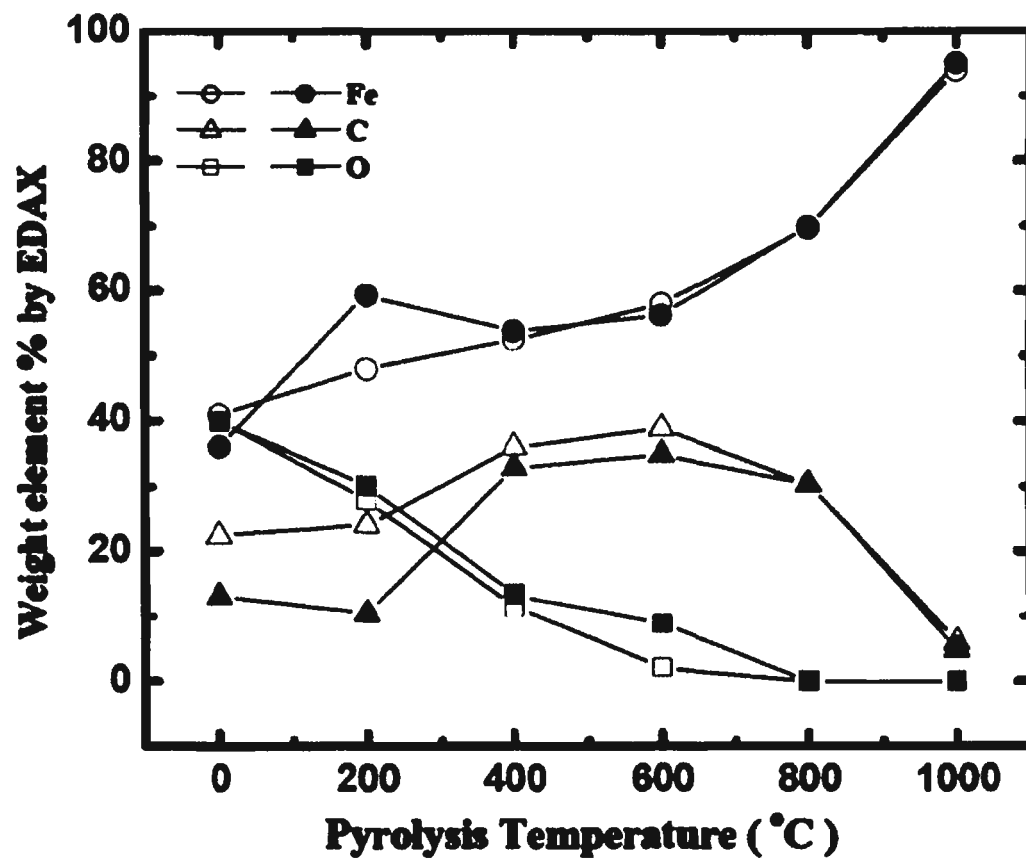
Fig 2. EDS analysis of n-RF-FeOx (open symbols) and X-RF-FeOx (dark symbols) after pyrolysis at different temperatures.
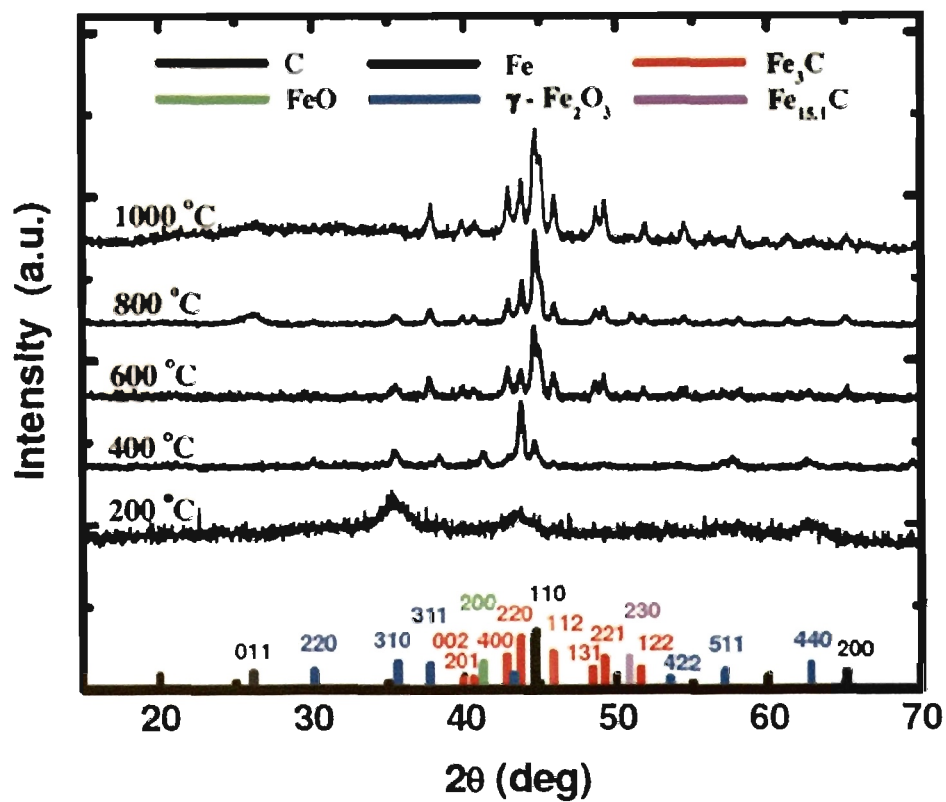
Fig 3. XRD data of X-RF-FeOx aerogels after pyrolysis under Ar at different temperatures (for the XRD data of n-RF-FeOx, see ESI†).
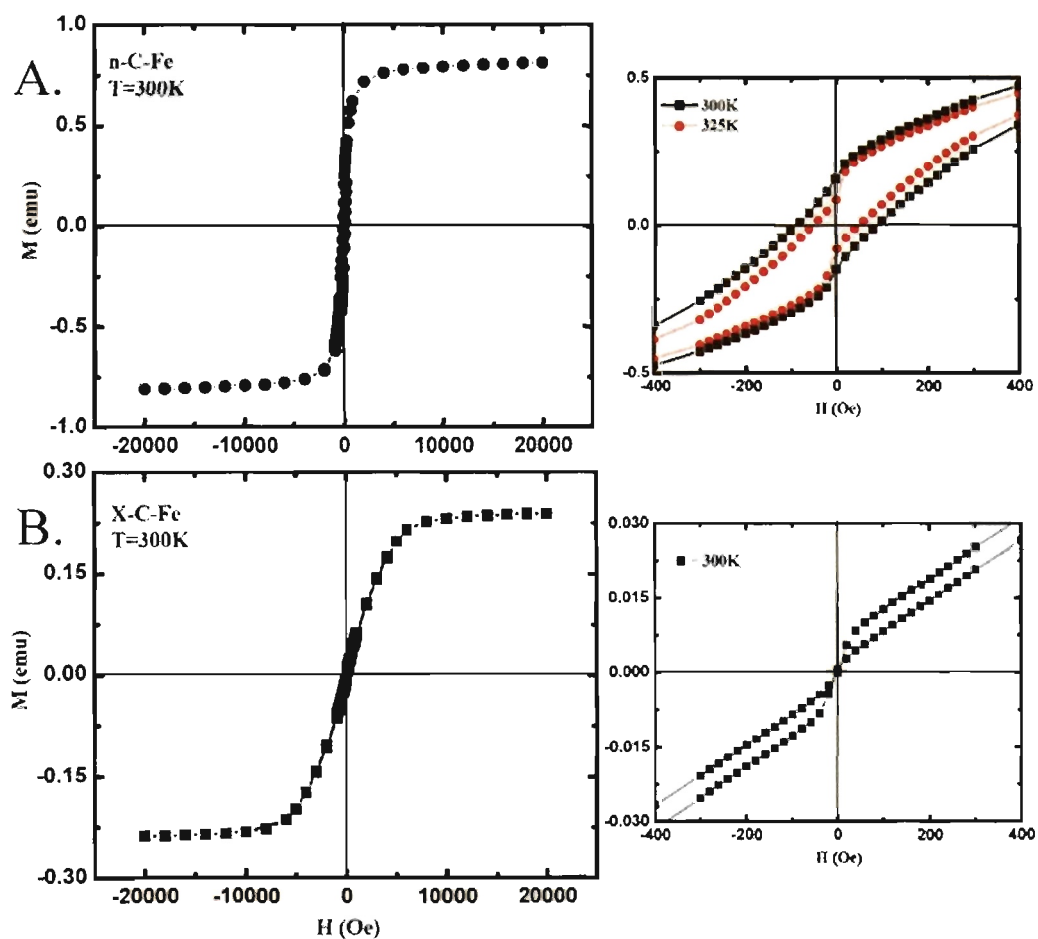
Fig 4. Magnetization loops of the materials obtained by pyrolysis at 800 °C of n-RF-FeOx (A), and of X-RF-FeOx (B). Figures on the right magnify the region around the origin. n-C-Fe shows ferromagnetic and X-C-Fe superparamagnetic behavior.

Supporting Information

Fig. 1S Photographs of native (n-) and crosslinked (X-) resorcinol-formaldehyde/iron oxide aerogels before (n-RF-FeOx, X-RF-FeOx), and after pyrolysis at 1000 °C under Ar (n-C-Fe and X-C-Fe)
   a. n-RF-FeOx aerogel as prepared
   b. X-RF-FeOx aerogel as prepared
   c. n-C-Fe by pyrolysis of a n-RF-FeOx aerogel at 1000 °C under Ar
   d. X-C-Fe by pyrolysis of a X-RF-FeOx aerogel at 1000 °C under Ar
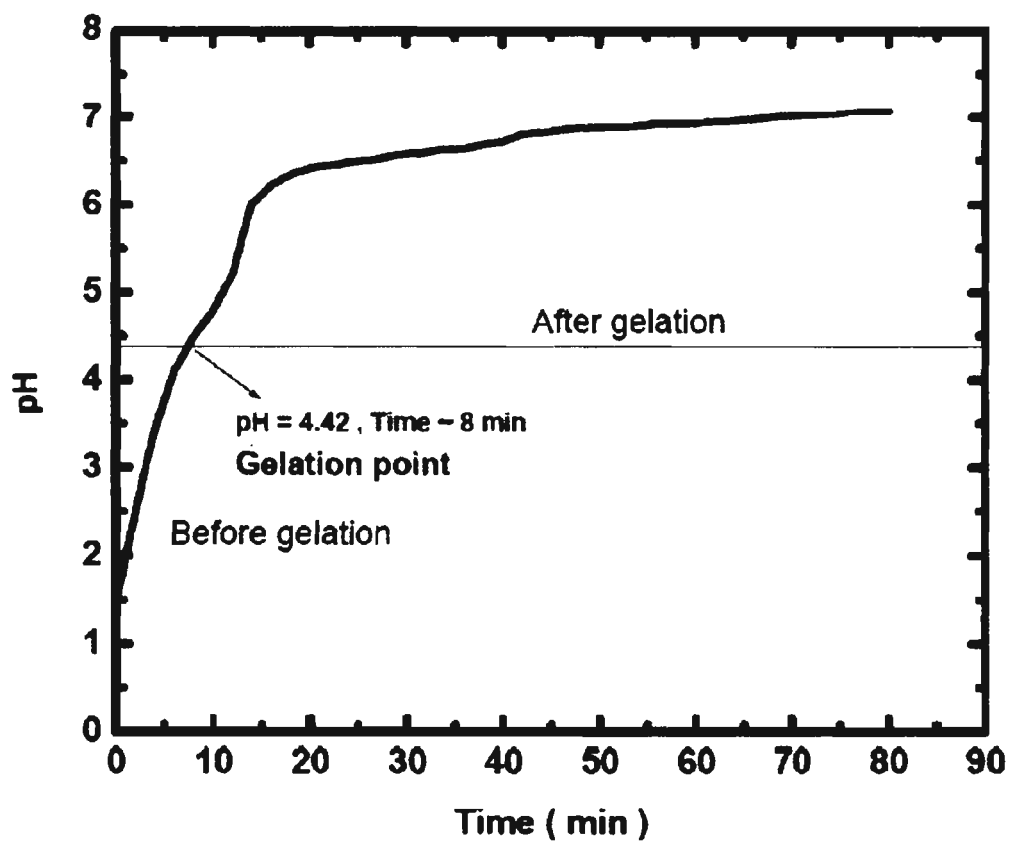
Fig. 2S pH changes during gelation at 80 °C of: $[Fe(H_2O)_6]^{3+}/CH_3CN:EtOH$ (1:1 v/v) epichlorohdrine
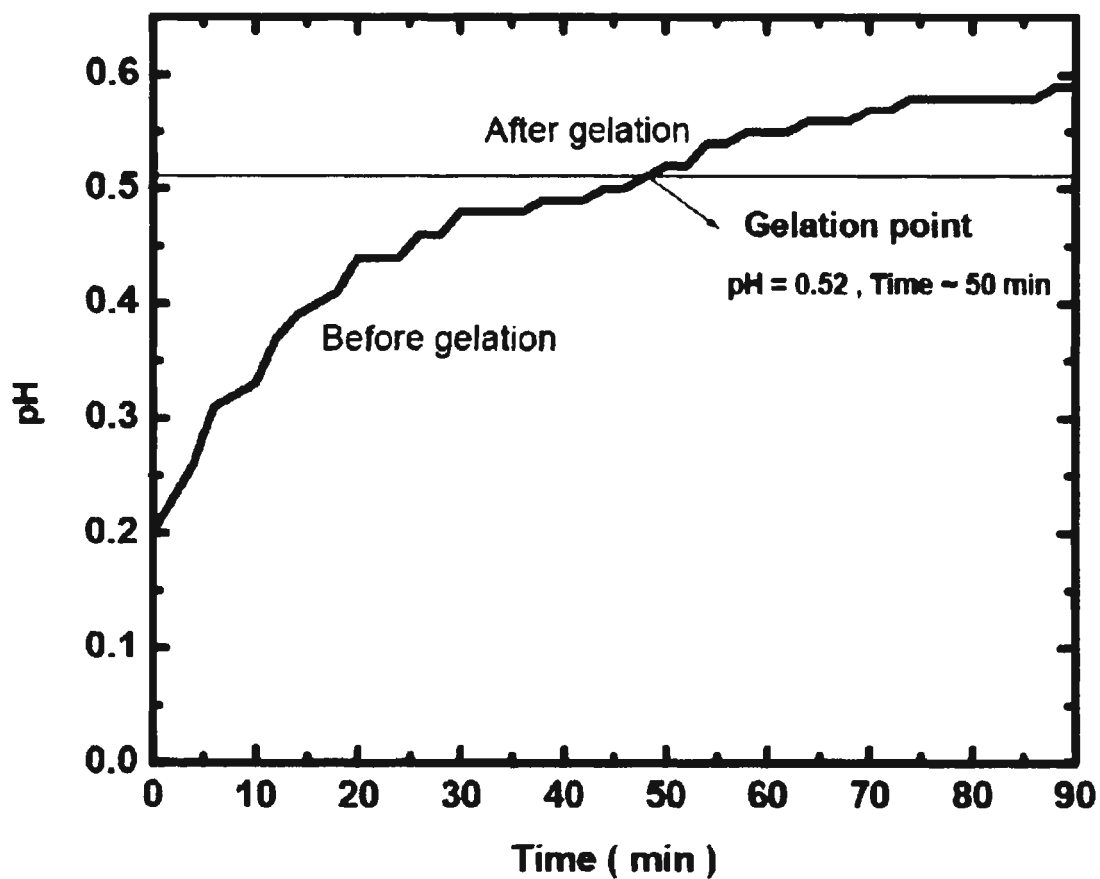
Fig. 3S pH changes during gelation at 80 °C of: $[Fe(H_2O)_6]^{3+}/CH_3CN:EtOH$ (1:1 v/v)
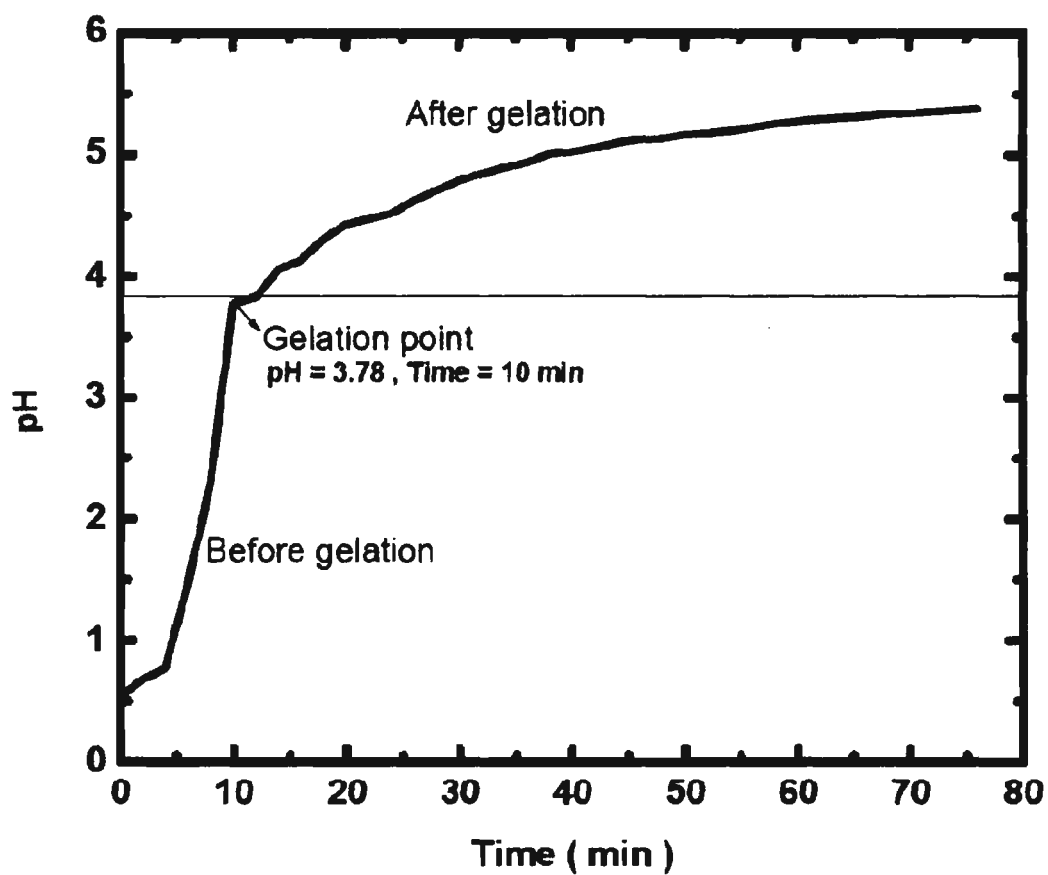
Fig. 4S pH changes during gelation at 80 °C of: $[Fe(H_2O)_6]^{3+}/CH_3CN:EtOH$ (1:1 v/v)/RF/epichlorohydrine
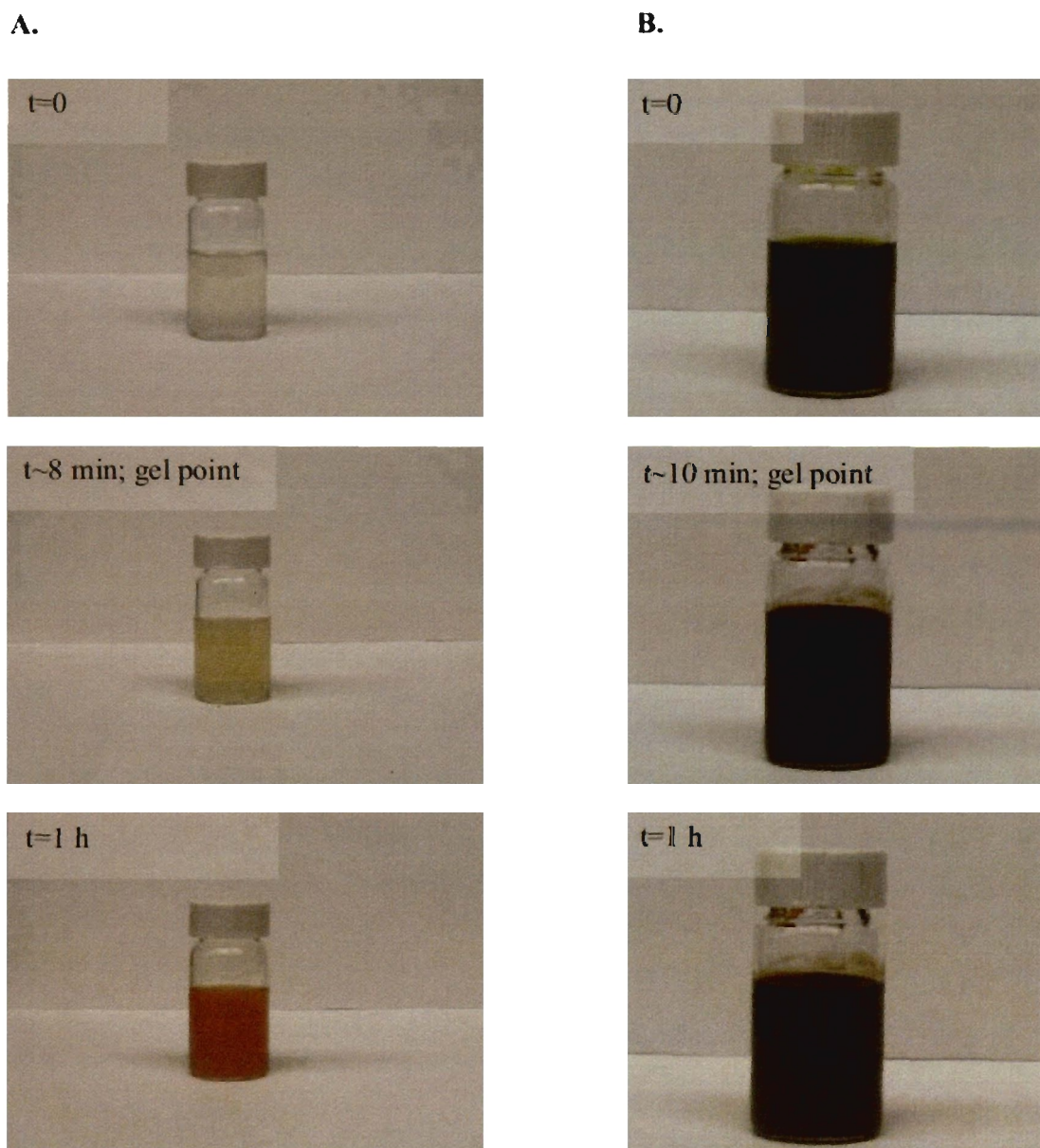
Fig. 5S Photographs of the: $[Hf(H_2O)_6]^{3+}$/CH$_3$CN:EtOH (1:1 v/v)/RF/epichlorohydrine (A) and the $[Fe(H_2O)_6]^{3+}$/CH$_3$CN:EtOH (1:1 v/v)/RF/epichlorohydrine (B) system during gelation.
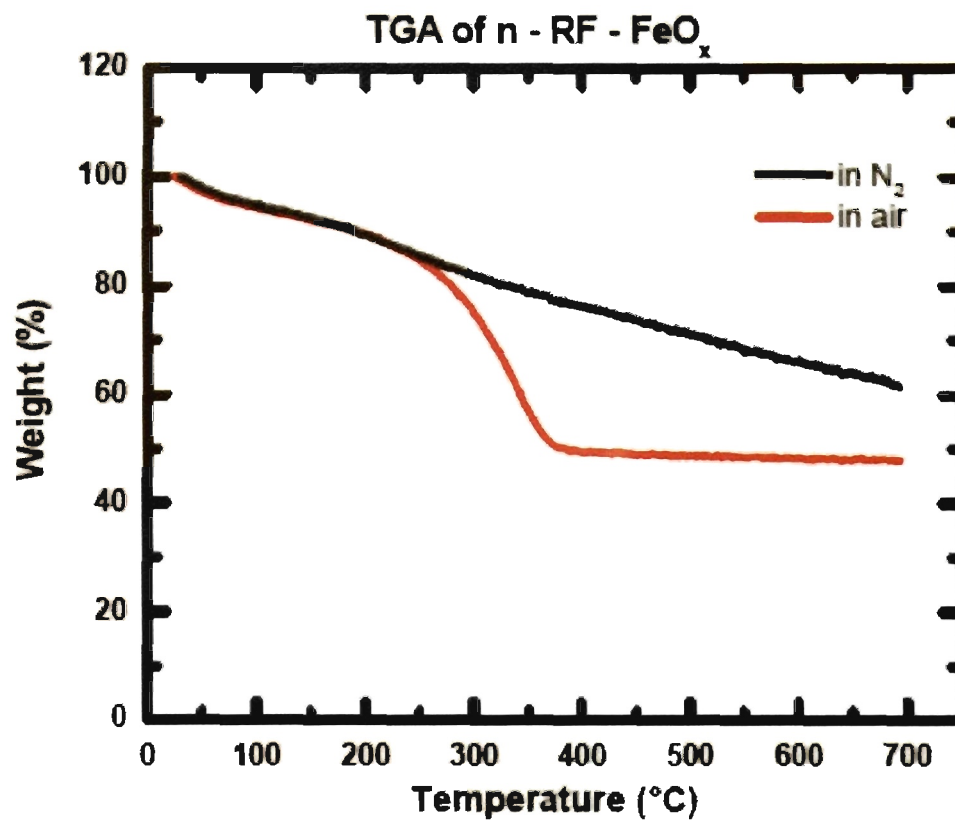
Fig. 6S TGA of n-RF-FeOx aerogel
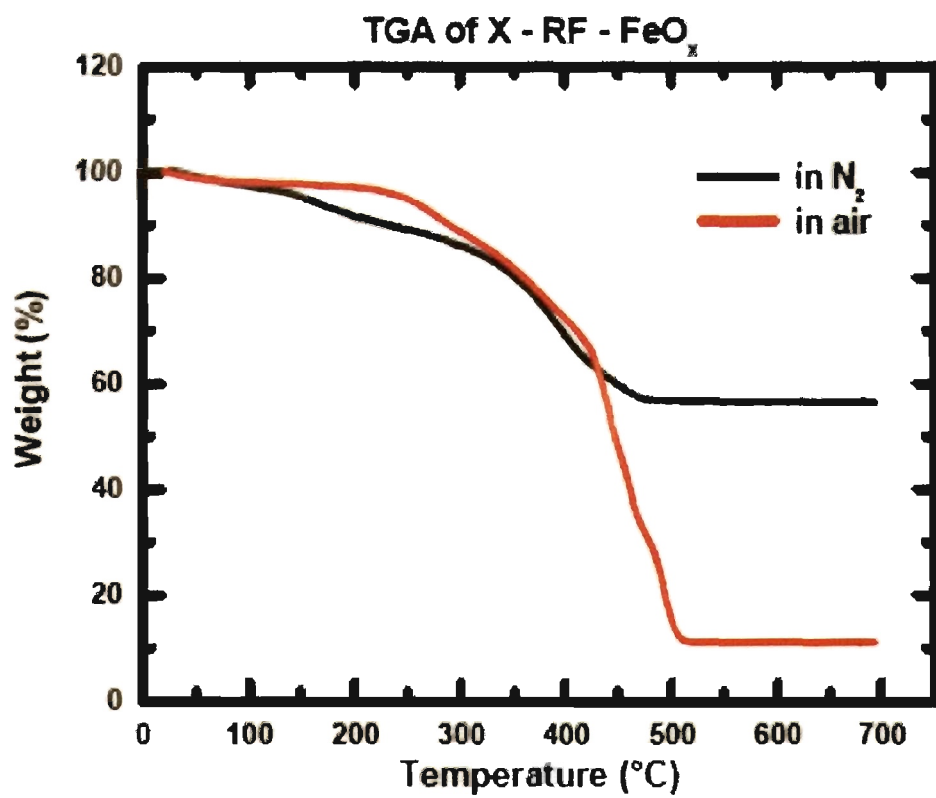
Fig. 7S TGA of X-RF-FeOx aerogel

Scanning electron microscopy (SEM) and energy-dispersive x-ray spectroscopy (EDS) were conducted with a Hitachi S-4700 field emission microscope. RF-FeOx aerogel samples for SEM were sputter-coated with Au/Pd for 2 min to avoid charging; thattreatment was not necessary for iron aerogels, because they were electrically conducting.

Element	Weight %	Atomic %
Fe	59.41	27.87
C	10.41	22.71
O	30.18	49.43

Fig. 8S Typical EDS data for n-RF-FeOx aerogels pyrolysed at 200 °C

Element	Weight %	Atomic %
Fe	95.10	80.66
C	4.90	19.34
O	0.00	0.00

Fig. 9S Typical EDS data for n-RF-FeOx aerogels pyrolysed at 1000 °C

Element	Weight %	Atomic %
Fe	48.00	21.0
C	24.10	46.00
O	27.9	33.00

Fig. 10S Typical EDS data for X-RF-FeOx aerogels pyrolysed at 200 $^{\circ}$C

Element	Weight %	Atomic %
Fe	93.92	76.85
C	6.08	23.15
O	0.00	0.00

Fig. 11S Typical EDS data for X-RF-FeOx aerogels pyrolysed at 1000 °C

Experimental details for XRD:

X ray diffraction experiments were performed with powders of the corresponding materials with a Scintag 2000 diffractometer using Cu K_ radiation. The detector used was a proportional counter detector equipped with a flat graphite monochromator.

Quantitative analysis and Particle size analysis:

Phase composition was estimated via Rietveld refinement of the x-ray diffraction patterns utilizing RIQAS software (Materials Data, Inc., version 4.0.0.26). Structural information for each phase was obtained from the ICSD database version 2.01. Particle size was estimated using Jade software (version 5.0, Materials Data, Inc.). A Gaussian correction for instrumental broadening was applied utilizing NIST SRM 660a LaB6 to determine the instrumental broadening.

Fig. 12S XRD experimental and data for n-RF-FeOx aerogels as a function of the pyrolysis temperature.
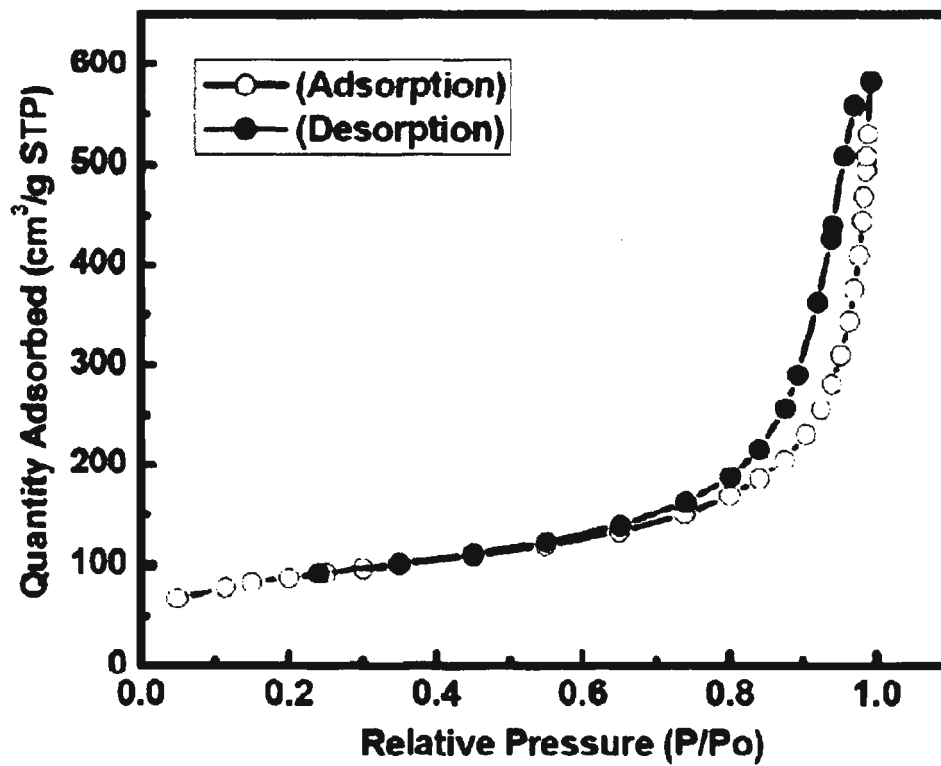
Fig. 13S N_2 sorption isotherm of n-RF-FeOx aerogel before pyrolysis.
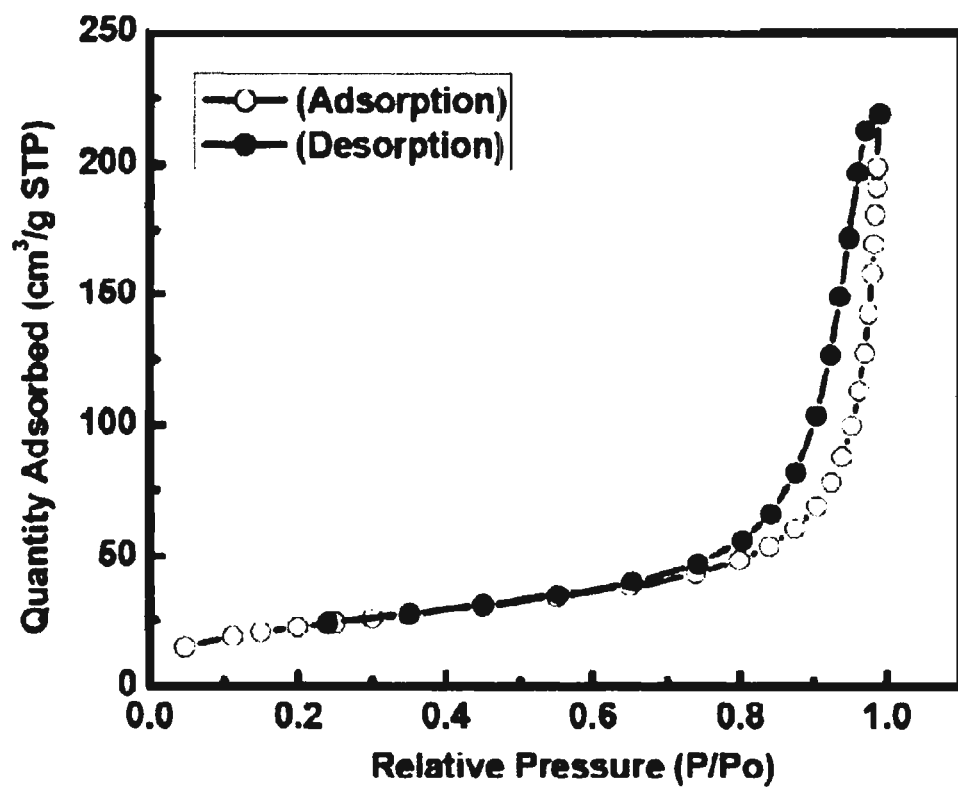
Fig. 14S N_2 sorption isotherm of X-RF-FeOx aerogel before pyrolysis.
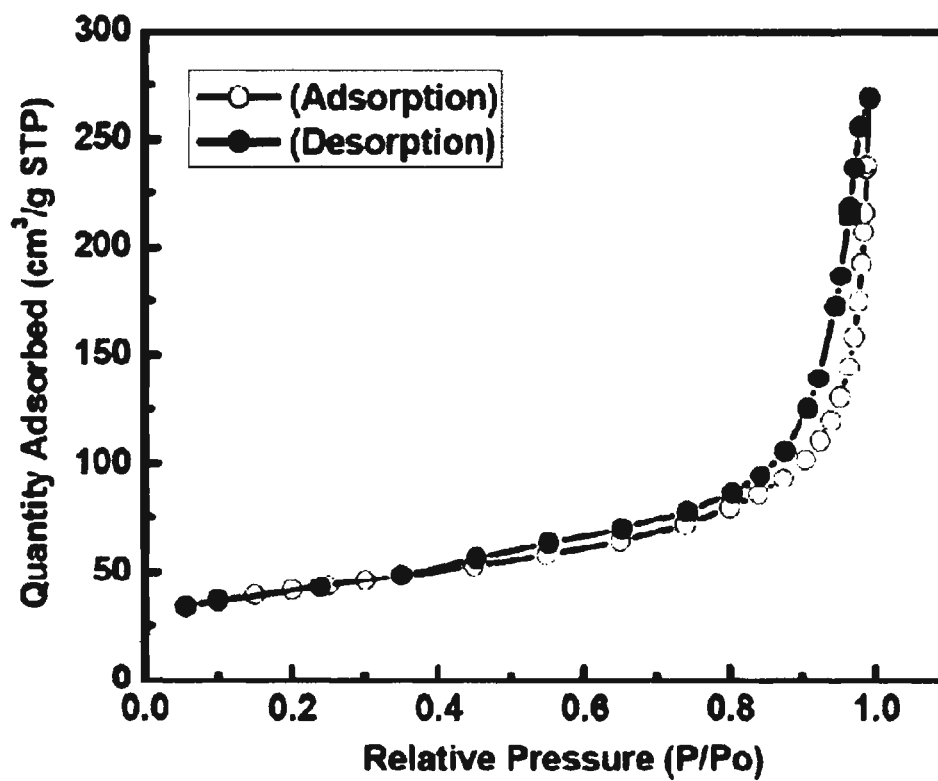
Fig. 15S N_2 sorption isotherm of n-RF-FeOx aerogel after pyrolysis at 800 °C
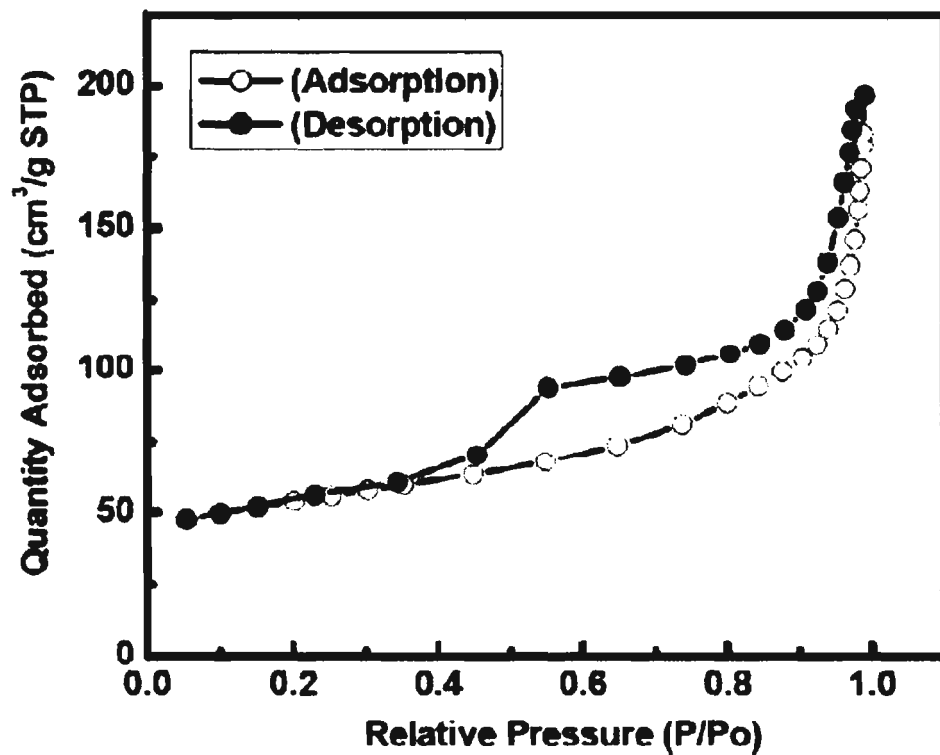
Fig. 16S N_2 sorption isotherm of X-RF-FeOx aerogel after pyrolysis at 800 $^{\circ}$C
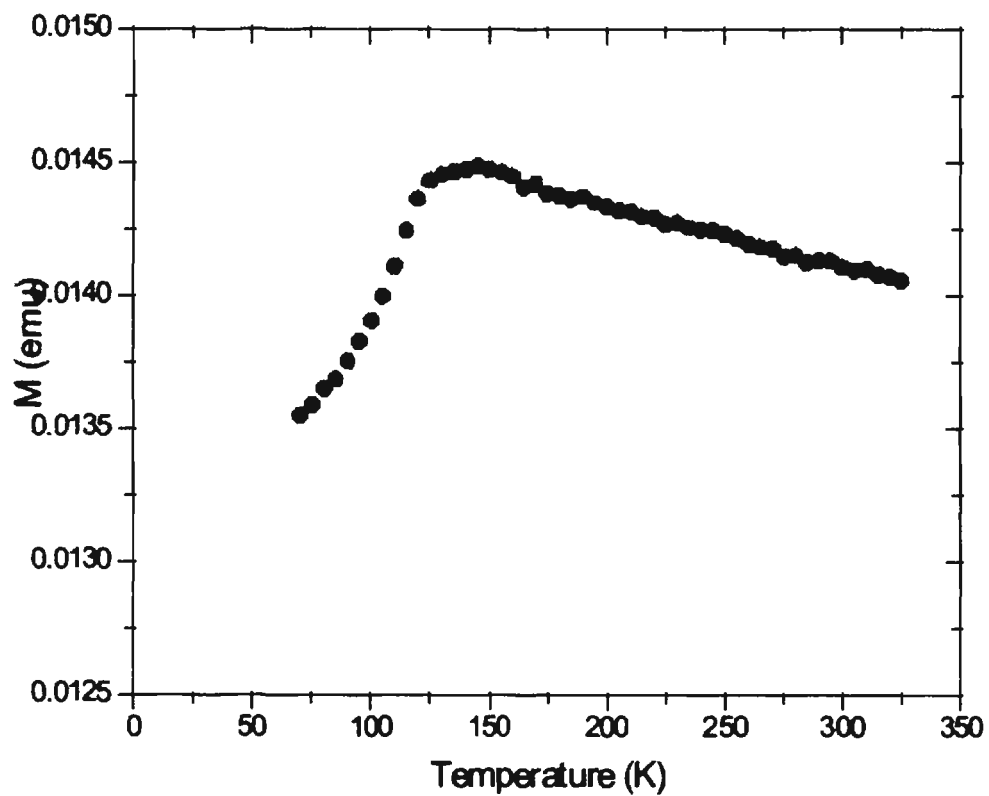
Fig. 17S Temperature dependence of the zero-field-cooled magnetization for the X-C-Fe sample produced by pyrolysis of X-RF-FeOx at 800 °C under Ar.

III. One-Pot Synthesis of Interpenetrating Inorganic/Organic Networks of Cuo/Resorcinol-Formaldehyde Aerogels: Nanostructured Energetic Materials

Nicholas Leventis,[*†], Naveen Chandrasekaran,[†] Anand G. Sadekar, [†] Chariklia Sotiriou-Leventis[*,†]and Hongbing Lu[‡]

[†]*Department of Chemistry, Missouri University of Science and Technology, Rolla, Missouri 65409, and*
[‡]*Departmentof Mechanical and Aerospace Engineering, Oklahoma State University, Stillwater, Oklahoma 74078*

Mesoporous3D assemblies of nanoparticles are classified as aerogels.[1] Mixed aerogels, therefore, can be perceived as designer interpenetrating networks of nanoparticles with synergistic chemical and physical properties. Such chemical synergism is typically encountered in energetic materials (e.g., explosives, propellants, and pyrotechnics). Those consist of an oxidizer and a fuel and decompose into heat and gases.[2] Low-order explosives, LEs, are simple mixtures of the two components (e.g., black powder). High explosives, HEs, are compounds with both the oxidizing agent and the fuel within their molecule (e.g., TNT, RDX). The tradeoff is high energy content with slow rates of energy release (LEs) versus lower energy content with high reaction rates (HEs). To improve the reaction rates of LEs, the oxidizer and the fuel need to be mixed as intimately as possible, ideally at the nanoscopic level. A recent approach, along the lines of the general procedures of doping aerogels,[3] utilizes sol-gel chemistry to produce 3D assemblies of Fe_2O_3, NiO, or WO_3 nanoparticles (the oxidant), whereas Al (the fuel) is added to the sol and is trapped in the porous network of the gel.[4] These energetic materials are classified as thermites, and their reaction (e.g., $Fe_2O_3 + 2Al \rightarrow 2Fe + Al_2O_3$) generates heat, but not gases. Here, we report interpenetrating nanoparticle networks of a typical inorganic oxidant $(CuO)^5$ and an organic fuel (resorcinol-formaldehyde polymer: RF) made in one-pot by two sol-gel processes running concurrently, whereas the

precursor of the one catalyzes the other. Upon pyrolysis in Ar, composite CuO/RF aerogels undergo smelting to metallic Cu. Pure RF aerogels do not burn easily in air, but CuO/RF composites sustain combustion, burning completely leaving only CuO (generated continuously by air oxidation of Cu) as a solid residue. Under acid catalysis (HCl) gelation of resorcinol (R) with formaldehyde (F) in CH_3CN takes place in ~2 h at 23 °C as opposed to 7 days at 80 °C under base catalysis.6 Meanwhile, CuO gels have been reported in isopropanol by dehydration of $CuCl2 \cdot xH2O$ with an epoxide.[7] Our process design uses the acidity of a gelling $CuCl_2 \cdot xH_2O$/epichlorohydrine sol (see Supporting Information) to catalyze cogelation of the RF system. However, the issue initially was that the R/F system does not gel in alcohols, and $CuCl_2 \cdot 2H_2O$ does not dissolve in CH_3CN. A common solvent is DMF, in which the R/F system does gel, but the $CuCl_2 \cdot xH_2O$/ epichlorohydrine sol does not gel under *any* conditions. It was noted though that DMF sols of the $CuCl_2 \cdot xH_2O$/epichlorohydrine system become viscous upon heating. Thus, a solution (A) made of 0.565 g (0.0033 mol) of $CuCl_2 \cdot 2H_2O$ (Aldrich), 0.240 mL (0.013 mol) of H_2O, 2.75 mL (0.03 mol) of epichlorohydrine, and 5 mL of DMF was heated at 80 °C for 30 min. Spin coating of the resulting viscous solution on a 5 cm × 5 cm glass slide and drying either under ambient conditions or by using supercritical fluid (SCF) CO_2 in an autoclave gave films that by FE-SEM/EDS (Energy Dispersive Spectroscopy) consist of CuO nanoparticles (Figure 1A). Subsequently, solution A was mixed with a solution B made of 0.337 (0.00306 mol) of R, 0.455 mL of a 37% w/w commercial solution of F (0.0061 mol), and 5 mL of DMF, and it was left at 80 °C to gel (4 h). Gels were aged in their molds (48 h, 23 °C), washed with DMF and acetone (3 × with each solvent, 8 h each time, using 4 × the volume of the gel for each

wash), and dried with SCF CO_2 yielding aerogel monoliths with bulk density $\rho_b = 0.083$ ± 0.009 g cm^{-3}, skeletal density $\rho_s = 2.65 \pm 0.14$ g cm^{-3}, and a calculated porosity (= $[(1/\rho_b) - (1/\rho_s)]/(1/\rho_b)$) of 98.2 ± 0.3% v/v of empty space. All DMF and acetone wash solutions were combined and analyzed for Cu,[8] showing that only 2.3 mol % of the original metal in the sol was lost during processing. Clearly, the oxide remains trapped in the mesoporous voids of the RF network. Figure 1B shows that the composite aerogels consist of a network of nanoparticles as designed. N_2 adsorption isotherms indicate the presence of mesoporosity (BET surface area $A = 108$ m^2 g^{-1}, average pore size = 11.8 nm by the $4V_T/A$ method; V_T: total pore volume); EDS analysis shows no chlorine and an isotropic distribution of C, O, and Cu (Supporting Information); XRD shows no diffraction pattern and therefore absence of crystallinity. The absence of chlorine and crystallinity from our composites signifies that our inorganic component is distinctly different from the material reported from isopropanol sols ($Cu_2(OH)_3Cl$).[7] (The difference is attributed to the low solubility of $CuCl_2 \cdot 2H_2O$ in that solvent.)

By thermogravimetric analysis (TGA) in air, CuO/RF aerogels (Figure 2) give a sharp mass loss at ~200 °C and a residual mass of 78%, equal to the weight percent of CuO in the composite. Also, considering the early (<100 °C) ~2% w/w mass loss of adsorbed solvents (H_2O) leads to ~20% w/w RF. Thus, the mol ratio of the CuO/RF repeat unit in the composite is ~6.3. Based on the composition of the sol, our CuO/RF composites should contain ~60% w/w RF. Therefore, ~67% of resorcinol was lost during processing, presumably due to incomplete gelation. By TGA under N_2, CuO/RF aerogels give three distinct steps, one below 100 °C, one at ~200 °C, and one above

500 °C (Figure 2). The mass remaining at 700 °C is 85% of the original. In contrast, TGA of pure RF aerogels under the same conditions gives the initial mass loss of adsorbed solvents at <100 °C and only one additional step above 400 °C, yielding at 700 °C a carbon aerogel with a mass of ~50% of the original. However, the mass remaining at 700 °C from the CuO/RF composite is not a superposition of the thermal evolution of the two components. To begin with, the mass loss from CuO/RF at ~200 °C is accompanied by a sharp exotherm in the DSC (Figure 2), indicating a chemical reaction between the two components. Subsequently, different CuO/RF samples were pyrolyzed in a tube furnace under flowing Ar at different temperatures from 200 to 1000 °C. EDS analysis shows that the amount of Cu increases and the amounts of C and O decrease. XRD analysis of the resulting materials (Figure 3) shows that the dominant crystalline phase is cubic metallic Cu even for pyrolysis at as low as 400 °C. A similar smelting reaction has been observed recently in analogous Fe_2O_3/RF composite aerogels at ≥800 °C.[9] At those temperatures, however, the RF framework is first converted to a porous carbon network.[10] The much lower reaction temperature observed in the CuO/RF composites suggests direct oxidation of RF by CuO. The RF framework contains 7–8 carbon atoms per repeat unit (depending on the degree of cross-linking) and thus requires at least 15 mol equiv of CuO for complete oxidation to CO_2 and H_2O. Hence, the substoichiometric mole ratio of CuO to RF (~6.3:1, identified by TGA in air above) precludes complete conversion of RF to gaseous products. Nevertheless, upon ignition with a flame in the air, CuO/RF aerogels sustain combustion burning rapidly, leaving behind a solid residue of microparticulate CuO (Figure 4D). By comparison, RF aerogel monoliths neither sustain the flame nor burn once inside the flame (Figure 4B). By considering all data together, it is concluded

that CuO mediates the oxidation of CuO/RF aerogels ignited in air via the smelting process:

$$RF + CuO \longrightarrow CO_2 + H_2O + Cu$$

$$2Cu + O_2 \text{ (air)} \longrightarrow 2CuO$$
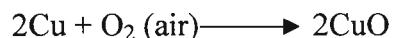
Reportedly, sol–gel RF networks actually *desensitize* energetic materials entrapped in their porous network.[11] In our case, the energetic material is the CuO/RF nanocomposite itself, and even as it stands now it is adequate for pyrotechnics. The catalytic role identified for CuO in the combustion of RF is investigated further in three component mixtures along with an independent oxidizer and RF as fuel. The cogelation of RF and metal oxide networks is a quite general process, and it has been demonstrated in our laboratory with both smeltable (Co_2O_3, NiO, SnO) and nonsmeltable oxides (e.g., Cr_2O_3, HfO_2).

References

1. Pierre, A. C., and Pajonk, G. M. Chem. Rev. 2002, 102, 4243– 4265.

2. Overviews of Recent Research on Energetic Materials; Shaw, R. W., Brill, T. B., and Thompson, D. L., Eds.; Advanced Series in Physical Chemistry, Vol. 16; World Scientific Publishing, Co.: London, U.K., 2005.

3. (a) Morris, C. A., Anderson, M. L., Stroud, R. M., Merzbacher, C. I., and Rolison, D. R. Science 1999, 284, 622– 624. (b) Leventis, N.; Elder, I. A.; Long, G. J.; Rolison, D. R. *Nano Lett.* **2002**, *2*, 63–67. (c) Bertino, M. F.; Hund, J. F.; Zhang, G.; Sotiriou-Leventis, C.; Tokuhiro, A. T.; Leventis, N. *J. Sol-Gel Sci. Technol.* **2004**, *30*, 43–48. (d) Leventis, N. *Acc. Chem. Res.* **2007**, *40*, 874–884.

4. (a) Gash, A. E.; Pantoya, M.; Satcher, J. H.; Simpson, R. L. *Polym. Prep.* **2008**, *49*, 558–559. (b) Prentice, D.; Pantoya, M.; Gash, A. *Energy Fuels* **2006**, *20*, 2370–2376. (c) Plantier, K. B.; Pantoya, M. L.; Gash, A. E. *Combust. Flame* **2005**, *140*, 299–309.

5. For example, CuO is used to complete oxidation of organic compounds in the quantitative analysis of C and H: Skoog, D. A.; Holler, F. J.; Nieman, T. A. *Principles of Instrumental Analysis*, 5th ed.; Brooks Cole: Florence, KY, 1998.

6. (a) Mulik, S.; Sotiriou-Leventis, C.; Leventis, N. *Chem. Mater.* **2007**, *19*, 6138–6144. (b) Mulik, S.; Sotiriou-Leventis, C.; Leventis, N. *Chem. Mater.* **2008**, *20*, 6985–6997.

7. Sisk, C. N.; Hope-Weeks, L. J. *J. Mater. Chem.* **2008**, *18*, 2607–2610.

8. Analysis for Cu in the wash solvents by evaporation to dryness, pyrolyzing the residue at 800 °C in air and weighing the resulting CuO.

9. Leventis, N.; Chandrasekaran, N.; Sotiriou-Leventis, C. *J. Mater. Chem.* **2009**, *19*, 63–65.

10. Al-Mutaseb, S. A.; Ritter, J. A. *AdV. Mater.* **2003**, *15*, 101–114.

11. (a) Tappan, B. C.; Brill, T. B. *Propellants, Explosives, Pyrotechnics* **2003**, *28*, 72–76. (b) Tappan, B. C.; Brill, T. B. *33rd Int. Ann. Conf. of ICT(Energetic Materials)* **2002**, 38/1-38/10.

Figures
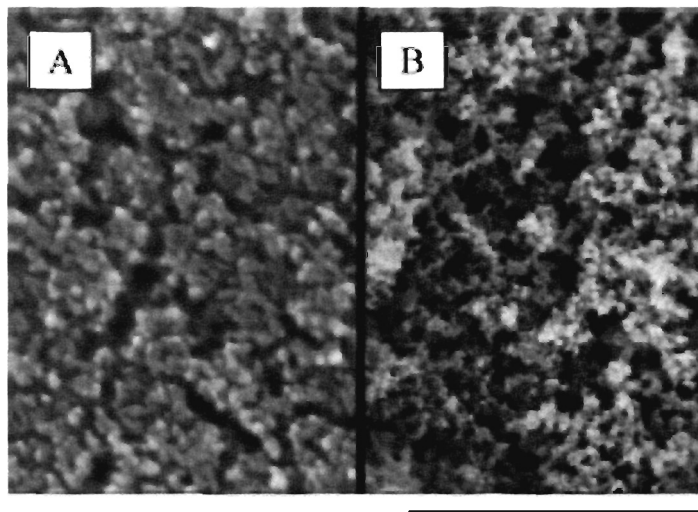
Figure 1. (A) SEM of a CuO xerogel film spin-coated on glass. Scale bar, 500 nm.
(B) SEM of a CuO/RF aerogel composite. Scale bar, 5 μm.
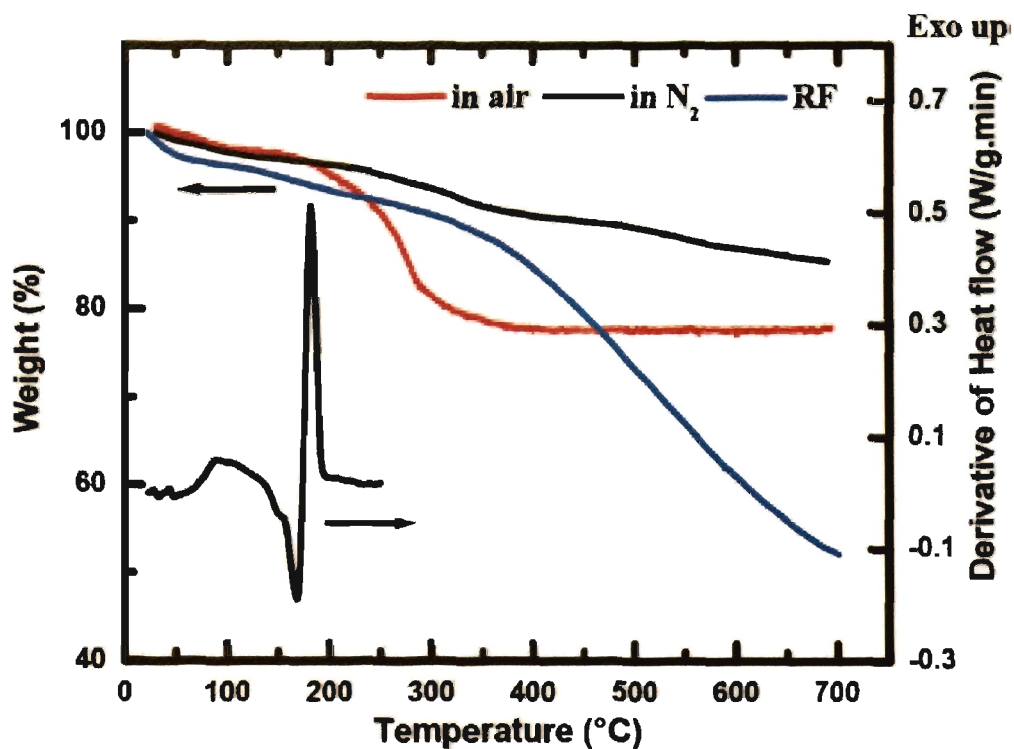
Figure 2. TGA (10 °C min⁻¹) and DSC (5 °C min⁻¹) of CuO/RF composite aerogels under the conditions shown. The TGA trace of a pure RF aerogel prepared by HCl-induced gelation of solution B has also been included for comparison (blue line).
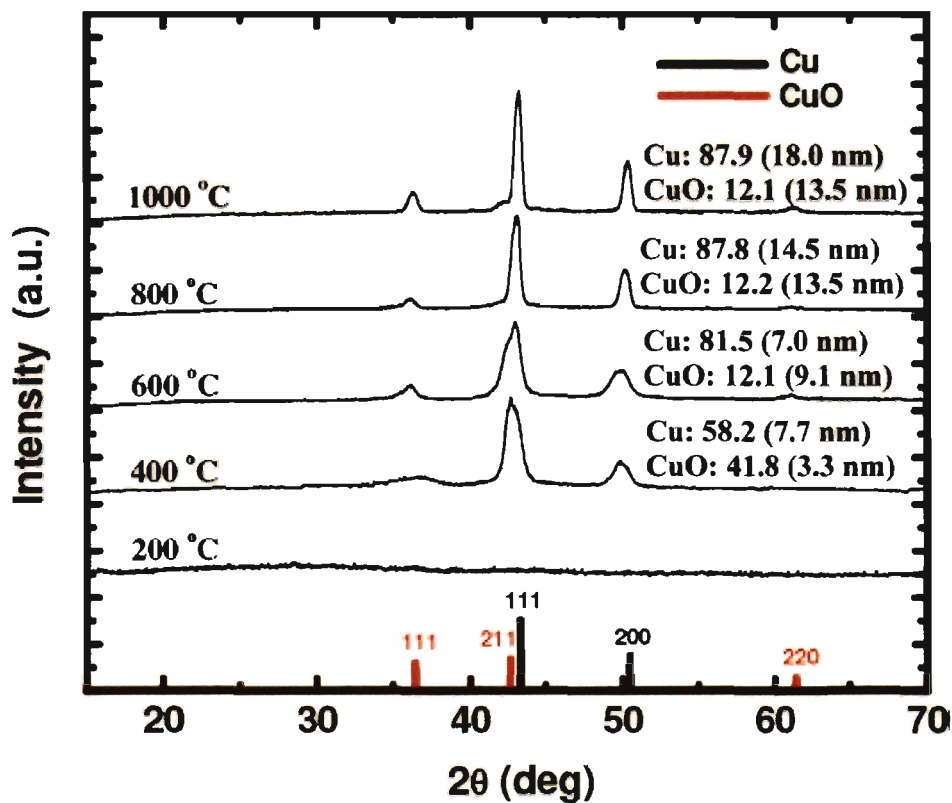
Figure 3. Powder XRD of CuO/RF composite aerogels pyrolyzed in Ar at the temperatures indicated. Insets: Percent weight of the two components; crystallite sizes by peak-width analysis via the Scherrer equation.
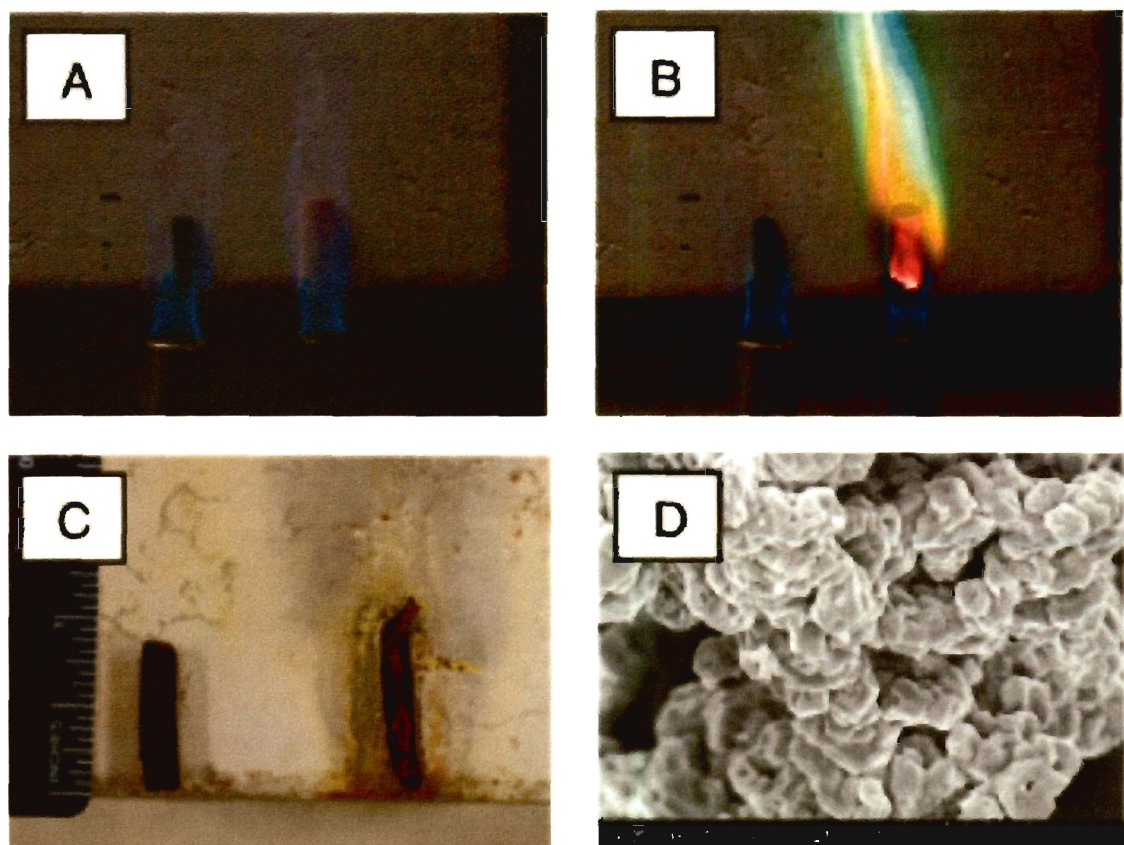
Figure 4. Aerogel monoliths (pure RF, left; CuO/RF, right) glued in vertical position on a ceramic tile. (A) Before ignition (gels behind the flames); (B) 15 s after placing in the flames; (C) after complete combustion (~2 min; Flames were removed 60 s after ignition; Note that only a shadow of the original CuO/RF monolith remains); (D) SEM of the traces of solid residue from the CuO/RF monolith (CuO).

Supporting Information
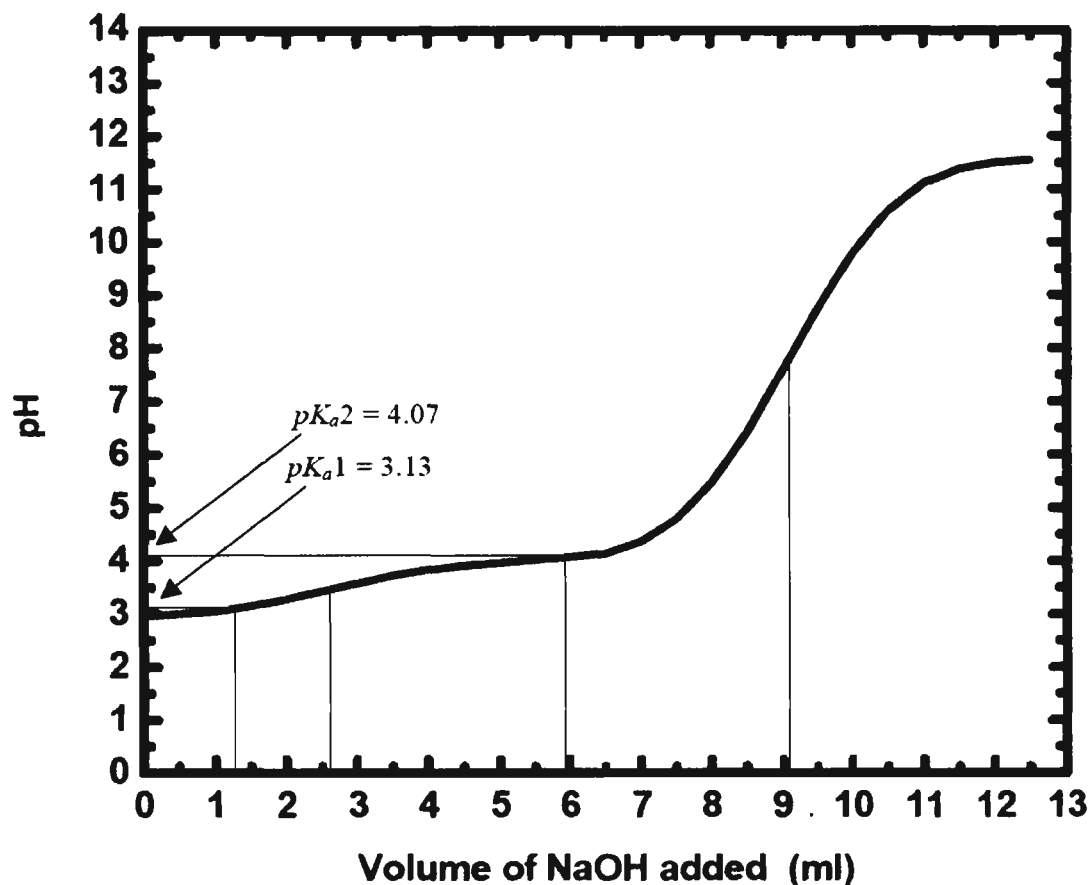
Figure 1S. Titration of $CuCl_2.xH_2O$ with aq. NaOH in DMF $CuCl_2.2H_2O$ (0.5 g, 0.0029 mol) was dissolved in 24.4 mL of dry DMF (Aldrich) and 4 mol equivalents of water (0.6 mL) was added. $[CuCl_2.6H_2O]$=0.118 M. This solution was titrated with an aqueous NaOH solution (0.5 M) and the pH was monitored with a Denver Instrument Model UB-5 pH meter. The two successive dissociations with $pKa1$=3.13 and $pKa2$=4.07, confirm the capability of hydrated cupric chloride to generate a strongly acidic environment, which as it turns out is capable of catalyzing the gelation of the R/F system.
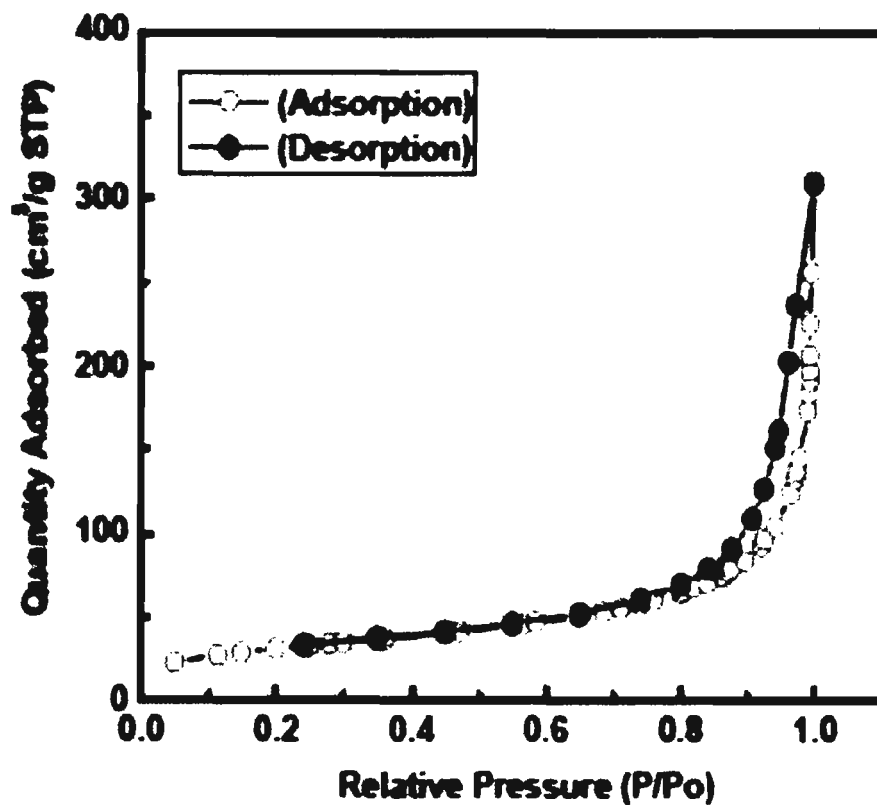
Figure 2S. N_2 adsorption isotherms of CuO/RF composite aerogels. Data obtained with a Quantachrome Autosorb-1 Surface Area/Pore Distribution analyzer. Samples were degassed at 80 °C for 24 h before analysis.

SEM and energy-dispersive x-ray spectroscopy (EDS) were conducted with a Hitachi S-4700 field emission microscope. Samples were sputter-coated with Au for 2 min to avoid charging.

Element	Weight %	Atomic %
Cu	46.84	16.85
C	15.24	28.99
O	37.92	54.16

Element maps:
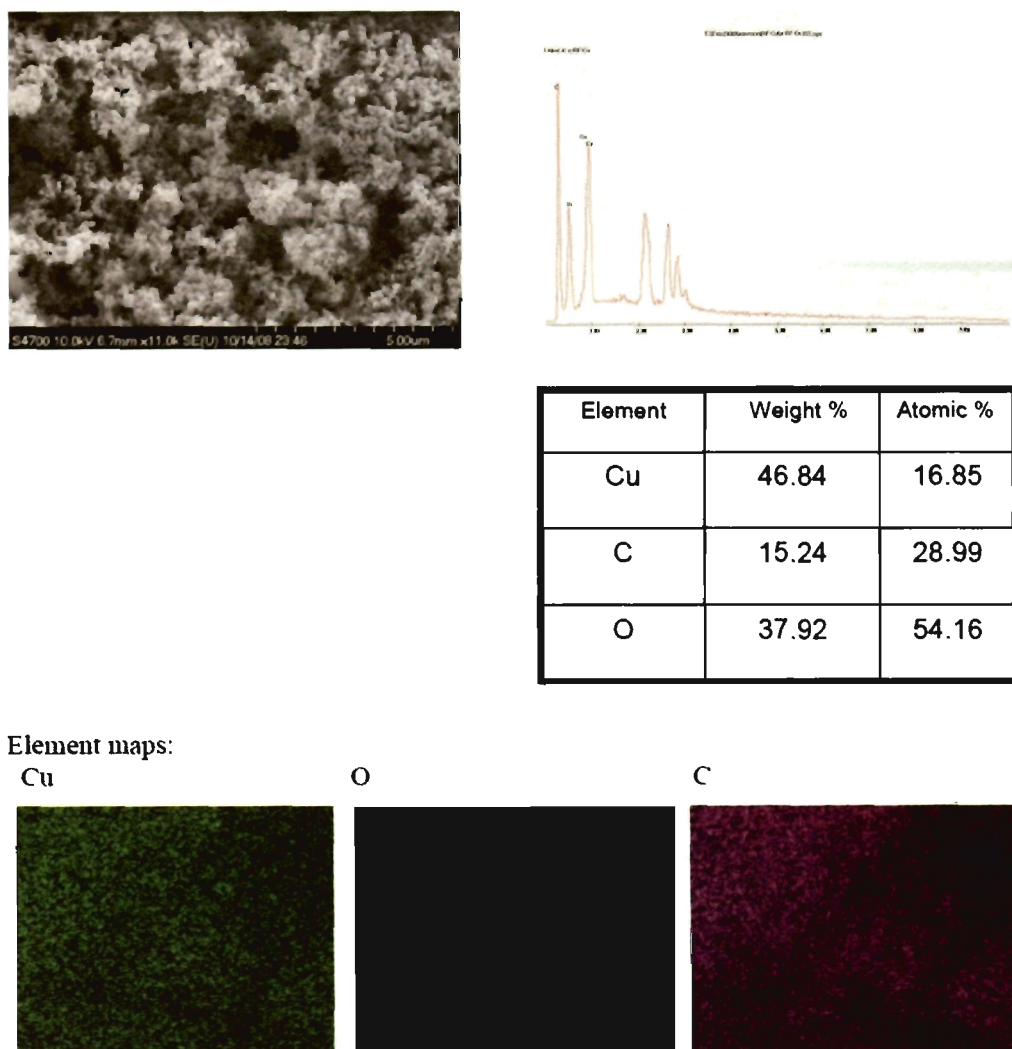
Figure 3S. EDS analysis of as-made CuO/RF composite aerogels
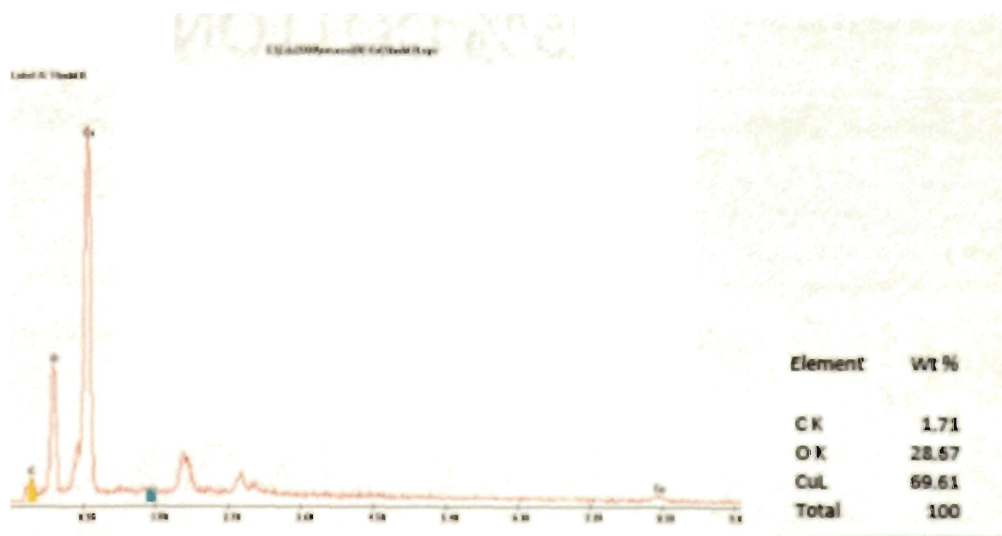
Maps:

SEM image:
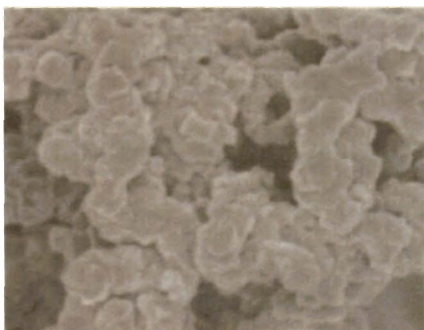
C map:

O map:

Cu map:
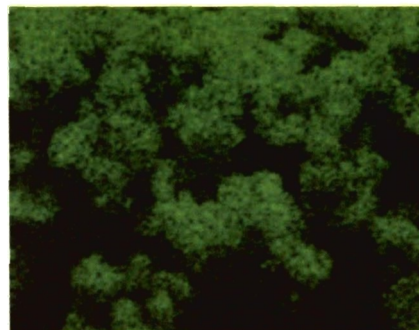
Figure 4S. EDS analysis of the residue after ignition in the open air

Experimental details for XRD:

X ray diffraction experiments were performed with powders of the corresponding materials with a Scintag 2000 diffractometer using Cu Kα radiation. The detector used was a proportional counter detector equipped with a flat graphite monochromator.

Quantitative analysis and Particle size analysis:

Phase composition was estimated via Rietveld refinement of the x-ray diffraction patterns utilizing RIQAS software (Materials Data, Inc., version 4.0.0.26). Structural information for each phase was obtained from the ICSD database version 2.01. Particle size was estimated using Jade software (version 5.0, Materials Data, Inc.). A Gaussian correction for instrumental broadening was applied utilizing NIST SRM 660a LaB6 to determine the instrumental broadening.

IV. The effect of compactness on the carbothermal conversion of interpenetrating metal oxide/resorcinol-formaldehyde nanoparticle networks to porous metals and carbides

Nicholas Leventis,[*] Naveen Chandrasekaran, Anand G. Sadekar, Sudhir Mulik, and Charklia Sotiriou-Leventis[*]

Department of Chemistry, Missouri University of Science and Technology, Rolla, MO 65409, U.S.A.

This study establishes that the necessary and sufficient condition for efficient reaction between nanoparticles includes both high surface-to-volume ratios and high compactness. For this, a wide range of interpenetrating networks of resorcinol-formaldehyde (RF) and metal oxide (MOx, M: Fe, Co, Ni, Sn, Cu, Cr, Ti, Hf, Y, Dy) nanoparticles were synthesized *via* a simple one-pot process using the acidity of gelling solutions of hydrated metal ions to catalyze gelation of RF. The compactness of the nanoparticles in the dry composites is controlled by the drying method: supercritical fluid (SCF) CO_2 drying affords aerogels with open skeletal frameworks, while drying under ambient pressure yields much more compact xerogels. A second independent method to impart compactness is by crosslinking the framework nanoparticles with a conformal polyurea (PUA) coating followed by drying with SCF CO_2: although those materials (X-aerogels) have an open aerogel-like structure, upon heating in the 200 °C range, the conformal PUA coating melts and causes local structural collapse of the underlying framework creating macropores defined by xerogel-like walls. Depending on the chemical identity of the metal ion, pyrolysis at higher temperatures sets off carbothermal processes yielding pure metal monolithic nanostructures (up to 800 °C; cases of M;Fe, Co, Ni, Sn, Cu) or carbides (up to 1400 °C; cases of M: Cr, Ti, Hf). Irrespective of the specific chemical

processes responsible for those transformations, the rate determining factor is the innate compactness of the xerogels, or the induced skeletal compactness in X-aerogels: both kind of materials react at as much as 400 °C lower temperatures than their corresponding native aerogels. By comparison, bulk (micron size) mixtures of the corresponding oxides and carbon black remained practically unreacted in the entire temperature range used for the nanoparticle networks. In addition to the significance of the RF-MOx interpenetrating networks in the design of new materials (mesoporous and macroporous monolithic metals and carbides), the effect of compactness on the activation of the carbothermal processes has important implications for process-design engineering.

1 Introduction

With little hope for prices of crude oil falling to the 2000 levels, coal liquefaction *via* for example the Fischer–Tropsch process are becoming viable. In that regard, the initial objective of this work was the facile sol–gel synthesis of high-surface area meso- and macroporous supported metal catalysts from interpenetrating nanoparticle networks of reducible metal oxides (*e.g.*, Fe, Co, Ni) and a carbonizable resin (resorcinol-formaldehyde). Along the way, however, we stumbled across interesting reactivity patterns between the two networks that depend on their compactness, and the scope of the work was broadened. Thus, although the original goal has been achieved and selected materials described herewith are already evaluated as catalysts, this report extends beyond material synthesis and addresses a more fundamental issue, namely the reactivity of nanoparticles in intimate contact.

It is often cited that nanoparticles demonstrate increased reactivity relative to bulk materials.[1] In extreme cases of exothermic processes, fast reactions lead to large amounts of energy released in very short time periods with clear implications for energetic materials (explosives, propellants, pyrotechnics).[2] Those phenomena are attributed to the high surface-to-volume ratio of nanoparticulate matter, thereby to the increased contact area between the reactants. That contact area is maximized in core-shell nanoparticles,[3] but fabrication of such structures may not be easy or feasible. At the other end, simple mechanical pulverization and mixing of solid reactants leads to more facile reactions as the mixing energy dose increases, and therefore, as the particle size decreases. For example, mechanochemical studies with Al and C show a decrease of up to 800 °C in the synthesis temperature of Al_4C_3, suggesting a mechanism change from liquid-solid (case of high temperature reaction of bulk Al and C) to solid-solid.[4] Further along the same lines, mechanochemical studies have also shown a clear direct correlation between the synthesis temperature and the coherent scattering domain size of the particles (they both decrease similarly), suggesting compactness as the most significant factor for reactions between nanoparticles.[5] Alternatively, it is also well-known that melting points depend strongly on particle size, and that has lead to the advancement of a so called melt-dispersion mechanism.[6] Thus, for example, while bulk Al melts at 934 K, Al_{100}^+ clusters melt at 640 K, above which the activation barrier of N_2 chemisorption on the nanoclusters drops by 1 eV and the reaction proceeds 108 times faster. Interestingly, although surface melting should have led to decreased surface energies, and consequently to higher activation barriers, the increased mobility of the atoms in the liquid must have over-

compensated entropically for the enthalpic loss, overall decreasing the free enthalpy of activation.[7]

Based on the above, irrespective of the operating mechanism (melting point depression or higher contact area between solids) carbothermal processes is a class of reactions that would clearly and directly benefit from reactions between nanoparticulate reactants.[8] Those reactions take place at high temperatures (typically >800 °C) between metal or semimetal oxides and carbon yielding either pure metals (*e.g.*, case of smeltable oxides of Fe, Co, Ni, Sn, Cu) or carbides. In that regard, this report first describes a convenient one-pot bottom-up sol–gel synthesis of interpenetrating nanoparticle networks of various metal oxides (MOx) and a carbon precursor (resorcinol/formaldehyde, RF). Thus, along the lines of Shea's work on iron oxide/organo- silsesquioxane interpenetrating networks, whereas the acidity of a gelling hydrated ferric ion/epoxide system apparently catalyzed co-gelation of silicon alkoxides,[9] our method utilizes the acidity of a wide variety of hydrated metal ions gelling towards the respective inorganic nanoparticle networks to catalyze co-gelation in one pot of an independent RF network.[10] In addition to the validity of this approach for the synthesis of an exceptionally wide range of nanostructured materials, another important aspect is the ability to tune the compactness, and therefore, the contact area between the two components. That is realized by drying interpenetrating RF-MOx wet-gels either under ambient conditions to xerogels, or by using supercritical fluid CO_2 (SCF CO_2) to aerogels. Aerogels retain the volume of their wet-gel precursors, and therefore, on average chains of nanoparticles stay further apart compared with the respective xerogels that undergo extensive shrinkage to

small volume fractions of the original wet-gels, thereby nanoparticles assume a more compact morphology.[11]

A different method to impart compactness of the skeletal nanoparticles is through crosslinking with a polymer. Polymer-crosslinked aerogels (X-aerogels) are 3D core-shell structures consisting of the typical nanoparticulate aerogel skeletal framework conformally coated with a polymer.[12,13] Those materials are pursued for their exceptional mechanical properties (stiffness, strength, toughness), which under compression may surpass per unit weight those of other strong materials (steel, Kevlar, SiC ceramics).[14] Recently, it was found also that pyrolysis under inert atmosphere of polyurea (PUA)-crosslinked RF aerogels yields *macroporous* carbons,[15] whereas it is well-known that pyrolysis of native RF networks leads to typical mesoporous carbon aerogels. Using SEM in combination with solids ^{13}C NMR, it was established that at the early stages of pyrolysis (200–250 °C) polyurea is detached chemically from the RF skeletal framework, finds itself above its melting point (123 °C), and by melting causes local framework collapse with creation of macropores surrounded by xerogel-like walls.

Pyrolysis of interpenetrating MOx-RF networks in all three forms (native aerogels, xerogels and X-aerogels) triggers carbothermal processes yielding the corresponding metals or carbides. Mesoporous materials are obtained from native MOx-RF aerogels, while their crosslinked (X-) counterparts yield macropores. However, the significant finding is that xerogels and polyurea-crosslinked networks react at as much as 400 °C lower temperatures relative to the corresponding aerogels. In the case of MOx-RF xerogels, the acceleration of the carbothermal processes is attributed directly to their compactness relative to the respective native aerogels. In the case of the X-MOx-RF

aerogels, the possible role of the crosslinking polymer (polyurea) as a co-reactant was considered and in most cases it was ruled out. In general, the acceleration of the carbothermal processes in X-RF-MOx aerogels is again due to melting of polyurea that either creates xerogel-like compactness within the macroporous walls or provides a liquid (*i.e.*, solution-like) medium in which skeletal nanoparticles can move and collide with one another efficiently. By comparison, bulk (micron size) mixtures of the oxides and carbon black remain unreactive in the temperature range considered. Overall, our results suggest that an aerogel-like high surface to- volume ratio is a necessary, but not a sufficient condition for efficient reaction between nanoparticles. A high surface-to-volume ratio must be combined with high compactness.

2 Results

Scheme 1 summarizes the processes that will be discussed below: synthesis and characterization of RF-MOx networks (Section 2.1), and their pyrolysis (Section 2.2).

2.1 Synthesis of native RF-MOx aerogels, xerogels and polyurea (PUA)-crosslinked aerogels

2.1.a Co-gelation of RF and hydrated metal salts. RF-MOx networks are formed by adding solutions of a hydrated metal chlorides and an epoxide (epichlorohydrin) in a solution of resorcinol and formaldehyde in a suitable solvent as summarized in Table 1. Metals for the RF-MOx systems were chosen among those, which are expected either to be reduced to the elements via reaction with carbon (e.g., Fe, Co, Ni, Sn, Cu), or to be converted to the corresponding carbides (e.g., refractories Cr, Ti, Hf, and rare earths Y, Dy).[16] It is noted further that the term "metal oxide" (MOx) is used loosely: although

detailed analysis was not conducted here, our previous studies with rare earth aerogels, xerogels and X-aerogels (including the YOx and DyOx systems of this study) have shown that even though oxides are the dominant components the materials also contain hydroxides (from incomplete condensation), carbonates (by reaction with CO_2), chlorides (from the original salts) and acetates (from oxidation of the solvent, ethanol).[17]

As it is well documented since the 1930's, gelation of hydrated metal ions (usually in the +3 or +4 oxidation states, with few exceptions like Ni^{2+} and Cu^{2+}) can be carried out through irreversible proton transfer to an epoxide, followed by ring opening (Scheme 2).[18] Interestingly, it seems that that process has been explored commercially more by the ceramics community for preparing fine nanosized powders as ceramic precursors (by peptization of the gels in water followed by precipitation) rather than by the sol-gel community.[19]

Titrations of the hydrated ions of this study, $[M(H_2O)_6]^{n+}$, with NaOH (e.g., see Figure 1) according to eq. 1 in the solvents used for Solutions B (no epichlorohydrin added) confirmed the acidity of the media.

$$[M(H_2O)_6]^{(n-1)+} + HO^- \rightleftharpoons [M(H_2O)_5(OH)]^{(n-1)+} + H_2O \qquad (1)$$

In all cases, two acid dissociation constants were identified (Figure 1) and the pK_a values are included in Table 1. Epichlorohydrin (10× mol) induced gelation except in $[Co(H_2O)_6]^{2+}$ and $[Cu(H_2O)_6]^{2+}$ that just became viscous. Drying of films cast from those viscous solutions either under ambient conditions or with SCF CO_2 has shown the presence of nanoparticles.[10b] Consistently with consumption of protons (Scheme 2), during gelation the solution pH increases (e.g., see Figure 2A).

Scheme 1 Synthesis and pyrolysis of RF-MOx systems

```
┌─────────────────────────┐      ┌──────────────────────────────┐
│ Solution A              │      │ Solution B                   │
│ resorcinol (3.06 mmol ) │      │ MCl₃ or ₄.6H₂O (3.3 mmol)    │
│ formaldehyde (6.11 mmol)│      │ EtOH (5 mL)                  │
│ CH₃CN (5.75 mL)         │      │ epichlorohydrin (33 mmol)    │
└─────────────────────────┘      └──────────────────────────────┘
```

sol

   pour in molds
   80 °C

gel

   age in molds. 2 days. room temp.
   wash with 1:1 v/v EtOH/CH₃CN
   wash with acetone (3x8h)

| SCF CO₂ drying | drying under ambient pressure | N3300A bath (acetone) wash with acetone (3x8h) SCF CO₂ drying |

| native RF-MOx aerogels | RF-MOx xerogels | X-RF-MOx aerogels |

heating (200-1400 °C)
Ar (60 mL min⁻¹)

```
┌──────────────────────────────────────────────────┐
│ • smelting to metals (M: Fe. Co. Ni. Sn. Cu)     │
│ • conversion to carbides (M: Cr. Ti. Hf)         │
│ • no reaction (M: Y. Dy)                          │
└──────────────────────────────────────────────────┘
```

The terminal asymptotic pH value corresponds to the acidity of the skeletal MOx nanoparticle framework. Uncatalyzed resorcinol-formaldehyde solutions do not gel. Typically, RF gel formation is induced in aqueous solutions with Na_2CO_3 (base) and takes several days.[20] Base-catalyzed gelation in non-aqueous environments (alcohols) has been also described and still takes a few days.[21] Most notably, HCl-catalyzed gelation of R/F in acetonitrile ([HCl]=0.363 mM, pH≈0) occurs in about 2h at room temperature and in about 10 min at 80 °C, developing the characteristic red color of o-quinone methides;

mesoporous RF aerogels obtained by either the base- or the acid-catalyzed processes are chemically identical.[22] If hydrated metal ions are used as catalysts instead of HCl (i.e., mixing the R/F and metal ion solutions with no epichlorohydrin added), the R/F system gels at 80 °C in about 30 min to one hour (with the exception of the copper salt, Table 1), and the pH does not change drastically, consistent with the catalytic role of the acid (Figure 2A). (We attribute the longer gelation time relative to the HCl-catalyzed process to the weaker acidity of the hydrated metal ions relative to HCl, as well as the use of ethanol as solvent that is expected to reduce the concentration of formaldehyde by forming acetals.[21]) Mixtures of R/F solutions with hydrated metal ions and epichlorohydrin gel in about the same time as the corresponding solutions of the hydrated metal ions with epichlorohydrin (Table 1). Figure 3 shows representative examples of the visual changes taking place during the gelation process in cases where the metal ion is colorless (e.g., cases of Hf and Sn) or it is quite distinct from the red color associated with the RF network formation.

Scheme 2 Gelation mechanism of hydrated metal ions with epoxides[18]
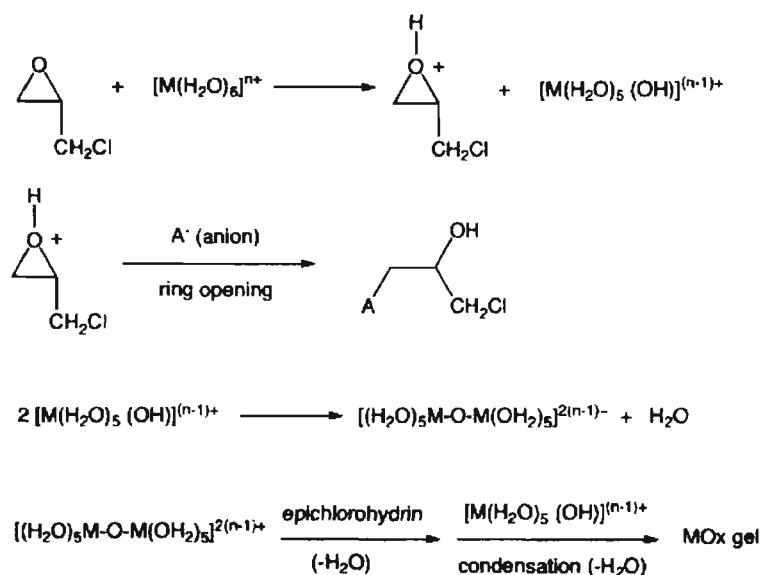
Owing again to the irreversible reaction of protons with epichlorohydrin, the pH rises significantly during the co-gelation of the organic and inorganic networks (Figure 2C), and therefore–relatively long aging times (48 h) were allowed for the RF network formation.[23] RF-MOx wet-gels were dried either in an autoclave with supercritical CO_2 to yield native RF-MOx aerogels, or under ambient pressure to RF-MOx xerogels. Alternatively, the RF-MOx skeletal framework was coated conformally (crosslinked) with a triisocyanete-derived polyurea in an analogous fashion to what has been accomplished before for the RF and the MOx networks independently; the resulting wet-gels were dried with supercritical CO_2 towards polyurea-crosslined X-RF-MOx aerogels.

2.1.b Characterization of native RF-MOx aerogels, xerogels and X-RF-MOx aerogels. All three forms of the RF-MOx systems remain monolithic through processing. Materials characterization data are summarized in Table 2. As expected, xerogels shrink significantly (50-60 %) relative to the molds. Native aerogels shrink less (10-30 %) and X-networks shrink the least (only ~6%) in agreement with previous observations.[12-15] Shrinkage is immediately reflected on relative the bulk densities (ρ_b) of xerogels and native aerogels. Skeletal densities (ρ_s) are used for evaluating the morphology of the skeletal frameworks. Specifically, the ρ_s values of the xerogels should be equal to those of the corresponding aerogels; nevertheless, they are lower (typically~25%), a fact attributed to closed pores created during drying. Support for this is found in the N_2 sorption data as discussed below. On the other hand, the skeletal densities of the native interpenetrating networks and of the X-samples are within 5% weighted averages of the organic (RF,[22a] ρ_s=1.45 g cm^{-3}; polyurea,[15] ρ_s=1.201 g cm^{-3}) and inorganic (MOx) components,[24] signifying absence of closed pores. (Calculated skeletal densities for the

native and X-aerogels are cited in brackets next to the experimental values in Table 2, and the calculation method is described in footnote c.) Bulk and skeletal densities are used together for calculating the porosities, Π, of the samples according to eq. 2,

$$\Pi = \frac{1/\rho_b}{(1/\rho_b)-1/\rho_s)} \qquad (2)$$

Such porosities (Table 2) for native RF-MOx aerogels are up to 98% v/v of empty space, followed by X-aerogels (~70% v/v) and finally by xerogels (34-54% v/v). By TGA in air (e.g., see Figure 4), native interpenetrating networks loose ~25% w/w of their mass (RF) and yield polycrystalline oxides. Under nitrogen the mass of interpenetrating networks with smeltable metals (Fe, Co, Ni, Sn, Cu) does not level off at 700 °C. In polyurea crosslinked systems (X-RF-MOx) the major component is the crosslinking polymer (Table 1). Those samples reach constant weight (e.g., at ~500 °C in the case of X-RF-FeOx, Figure 4) either under air or nitrogen. Considered together, TGA data in air and under N_2 suggest that a reaction takes place between RF and MOx that proceeds slower in the native samples and is facilitated by crosslinking with polyurea.

Microscopically (SEM) all native RF-MOx networks appear as 3D agglomerations of nanoparticles. Figure 5 shows two representative cases: RF-CoOx and RF-HfOx. At this level, the chemical identity of the individual particles is uncertain. In our experience, TEM is generally difficult with polymeric aerogels, because of melting/decomposition of the organic component. Here however, owing to the large Z-attenuation difference expected between the organic and inorganic components of the RF-MOx systems.

Table 1. Selected Properties of RF-MOx Systems

sample	diameter (cm) [a]	shrinkage (%) [a,b]	bulk density, ρ_b (g cm^{-3}) [a]	skeletal density, ρ_s (g cm^{-3}) [c]	porosity, Π (% v/v)	MOx:RF:PUA [d] (w/w/w)	BET surf. area, σ (m^2 g^{-1})	average pore diam. (nm) [half width (nm)] [e]	particle radius, r (nm) [f]
RF-FeOx									
aerogel	0.946±0.01	13.2±1.31	0.047±0.001	2.86±0.12 [2.45]	98	78:22:00	298	33.8 [26.2]	3.5
xerogel	0.38±0.02	63.4±0.49	1.00±0.04	1.81±0.01	45		184	4.8 [3.2]	9.0
X-aerogel	1.00±0.03	6.16±0.58	0.42±0.01	1.42±0.01 [1.37]	71	49:14:37	80	28.8 [33.1]	26.4
RF-CoOx									
aerogel	0.783±0.024	21.6±2.51	0.082±0.001	2.34±0.19 [g]	97	77:23:00	143	36.3 [45.3]	9.0
xerogel	0.43±0.04	58.6±0.53	0.81±0.12	1.93±0.04	35		123	4.8 [3.5]	12.6
X-aerogel	0.91±0.02	6.16±0.58	0.37±0.03	1.42±0.05 [g]	71	23:7:70	52	22.3 [26.2]	40.9
RF-NiOx									
aerogel	0.69±0.015	29.7±1.25	0.059±0.003	2.59±0.13 [2.62]	98	74:26:00	309	22.9 [24.3]	3.7
xerogel	0.55±0.02	47.1±0.32	1.24±0.07	1.87±0.004	34		h	h	
X-aerogel	0.93±0.04	8.6±1.1	0.397±0.015	1.38±0.01 [1.41]	69	20:7:73	150	17.7 [15.0]	14.5
RF-SnOx									
aerogel	0.756±0.005	24.3±0.57	0.135±0.031	2.58±0.13 [2.34]	95	74:26:00	147	37.1 [41.4]	7.9
xerogel	0.37±0.03	64.4±0.58	1.15±0.08	1.85±0.02	39		h	h	
X-aerogel	0.86±0.01	13.8±0.42	0.31±0.01	1.27±0.004 [1.29]	77	11:4:85	60	31.6 [34.7]	39.3
RF-CuOx									
aerogel	0.903±0.021	16.3±1.92	0.083±0.009	2.65±0.14 [g]	98	78:22:00	189	43.6 [49.6]	6.0
xerogel	0.496±0.055	52.3±1.2	1.33±0.009	2.01±0.29	34		159	4.7 [3.2]	9.4
X-aerogel	0.97±0.02	10.5±1.96	0.42±0.05	1.37±0.003 [g]	71	83.5:88.5	21	38.9 [45.2]	30.8
RF-CrOx									
aerogel	0.89±0.02	11.3±1.52	0.108±0.005	2.42±0.01	96	74:26:00	472	23.9 [17.1]	2.6
xerogel	0.51±0.01	50.9±1.05	1.16±0.072	1.78±0.04	35		117	4.8 [1.89]	14.4

Table 2. Selected Properties of RF-MOx Systems (Continued)

xerogel	0.43±0.017	58.8±0.48	0.934±0.035	2.04±0.21	54		145	7.2 [4.83]	10.1
X-aerogel	0.91±0.01	9.0±1.2	0.414=0.009	1.34±0.82 [1.25]	69	5.0:1.6:93.4	69	30.1 [15.1]	48.6
RF-HfOx									
aerogel	0.853±0.015	14.7±1.52	0.128=0.004	2.59±0.01 [2.71]	95	75:25:00	282	22.9 [37.9]	4.1
xerogel	0.45±0.026	57.3±0.25	1.08±0.057	1.92±0.18	44		159	3.1 [1.03]	9.8
X-aerogel	0.926±0.025	7.3±1.5	0.442±0.006	1.42±0.08 [1.35]	69	15:5:80	57	34.6 [32.7]	37.1
RF-YOx									
aerogel	0.88±0.01	12.6±0.47	0.124=0.005	2.07±0.05 [2.12]	94	80.1:19.9:00	302	36.3 [32.1]	4.8
xerogel	0.38±0.019	63.2±0.78	1.12±0.11	1.98±0.11	43		122	6.0 [1.83]	12.4
X-aerogel	0.94±0.05	6.0±0.18	0.330=0.003	1.25±0.01 [1.27]	74	10.1:2.4:87.5	99	22.3 [24.1]	24.2
RF-DyOx									
aerogel	0.86±0.05	17.0±1.73	0.089=0.008	2.55±0.01 [2.41]	97	76.5:23.5:00	290	52.4 [32.8]	4.1
xerogel	0.51±0.025	50.6=0.82	1.17±0.031	2.18±0.24	46		98	7.6 [5.3]	14.0
X-aerogel	0.93±0.01	6.80±1.7	0.34±0.03	1.40±0.04 [1.29]	68	11:3.4:85.6	132	45.7 [37.2]	15.2

[a]. Average of 3 samples. (Mold diameter: 1.04 cm.) [b]. Shrinkage = 100 × (mold diameter - sample diameter)/(mold diameter). [c]. Single sample, average of 50 measurements; in brackets: calculated skeletal densities based on the thermogravimetric analysis data of the next column and the skeletal densities of native MOx, RF and PUA aerogels prepared independently (see text). [d]. By thermogravimetric analysis (TGA) in air up to 700 °C; PUA: Desmodur N3300A triisocyanate-derived polyurea crosslinking polymer. [e]. By the BJH-desorption method; in brackets: width at half maximum. [f]. Calculated via $r = 3/\rho_s \sigma$ using experimental skeletal density data and surface areas. [g]. Could not be calculated because native CoOx and CuOx did not gel, and therefore their skeletal densities could not be determined. [h]. Unable to obtain identifiable isotherms.

By TGA in air (e.g., see Figure 4), native interpenetrating networks loose ~25% w/w of their mass (RF) and yield polycrystalline oxides. Under nitrogen the mass of interpenetrating networks with smeltable metals (Fe, Co, Ni, Sn, Cu) does not level off at 700 $^{\circ}$C. In polyurea crosslinked systems (X-RF-MOx) the major component is the crosslinking polymer (Table 1). Those samples reach constant weight (e.g., at ~500 $^{\circ}$C in the case of X-RF-FeOx, Figure 4) either under air or nitrogen. Considered together, TGA data in air and under N_2 suggest that a reaction takes place between RF and MOx that proceeds slower in the native samples and is facilitated by crosslinking with polyurea.

Microscopically (SEM) all native RF-MOx networks appear as 3D agglomerations of nanoparticles. Figure 5 shows two representative cases: RF-CoOx and RF-HfOx. At this level, the chemical identity of the individual particles is uncertain. In our experience, TEM is generally difficult with polymeric aerogels, because of melting/decomposition of the organic component. Here however, owing to the large Z-attenuation difference expected between the organic and inorganic components of the RF-MOx systems, even in the extreme case of native-RF-CoOx aerogels where the inorganic network by itself does not gel, bright field TEM does show an interconnected dark (inorganic) particle network surrounded by and embedded in a matrix of more "transparent" (RF) particles (Figure 6). SEM and TEM data considered together support the proposed structure for the RF-MOx skeletal frameworks as random distributions of interpenetrating strings of RF and MOx nanoparticles. Further support of this model is found in the reactivities of those systems (see Discussion Section below).

Microscopically, xerogels consist also of nanoparticles, however, the network appears collapsed and the nanoparticles are in closer contact with one another (Figure 5). In some

cases (e.g., X-RF-HfOx) the X-aerogel framework looks very similar to that of the corresponding native aerogel as expected from a coating of polyurea applied conformally around the entire skeletal framework of the native material. In some other cases (e.g., X-RF-CoOx) the framework is more fibrous, presumably owing to free polyurea formation in the pores catalyzed by the metal ions on the surface of the MOx nanoparticles. (Sol-gel polyurea produced by reaction of isocyanates with water is fibrous.[15]) In some X-samples (polyurea) fibers are less pronounced (as in X-RF-CoOx, Figure 5), however, in some other ones (e.g., X-RF-CuOx, see Figure 10 below) they comprise a dominant feature.

The pore structure, and by extrapolation the compactness (degree of contact between nanoparticles) was evaluated further by N_2 sorption studies. Representative isotherms are included in Figure 5 and relevant data are summarized in Table 2. All three types of materials, native aerogels, xerogels and X-aerogels give typical Type IV isotherms reaching saturation.[25] Native and X-aerogels show H1 hysteresis loops frequently associated with cylindrical pores. Xerogels adsorb significantly less N_2 than native and X-aerogels, and they show H2 desorpion loops characterizing ink-bottle pores, presumably formed by structural collapse during drying. (It is further suggested here that some of the ink-bottle necks become quite narrow or get closed altogether, thus explaining the lower skeletal densities of the xerogels relative to the corresponding aerogels.) Average pore diameters were determined by the BJH method applied on the desorption branch of the N_2 sorption isotherms and the data are provided in Table 2. Although the BJH method tends to understimate average pore diameters by 10-20%,[26] nevertheless data appear internally consistent showing that native and X-aerogels have significantly larger pore diameters (~18-46 nm) than the corresponding xerogels (3-8 nm)

as expected. On the other hand, native samples seem to have larger pores than the corresponding X-samples, but this is a weak generalization as the pore size distributions (estimate by the width at the half maximum of the BJH curves – data included in Table 2) is quite broad.

Despite the small pore diameters of the xerogels, their BET surface areas are still quite high, at ~50% of those of the corresponding native samples. On the other hand, despite their minimal shrinkage relative to the molds, X-aerogels show greatly reduced surface areas, which is consistent with a conformal polyurea coating filling the smaller crevices of the native framework and thus blocking access to the probe (N_2) in those spaces. Within this line of reasoning, the apparent particle size of the X-aerogels should be significantly larger than the particle size of the native materials, a fact supported by particle radius calculations (see Table 2). Nevertheless, it should be also pointed out that if polyurea was just filling crevices in the native framework, then the average pore diameters of the X-aerogels should have been shifted to larger diameters; the fact, however, that the trend for the BJH pore diameters of the X-samples is to remain similar to those of the corresponding native samples, or even decrease, is attributed to that the polymer does not just fill crevices on the native skeletal framework, but it keeps accumulating on the surface of the new skeletal RF-MOx-polymer agglomerates.

Overall, SEM, TEM and N_2 sorption porosimetry create a model whereas interpenetrating RF-MOx networks consist of random distributions of two independent networks of nanoparticles, which in the native and the X-aerogel forms are looser with less points of contact, while xerogels are more compact, as expected.

2.2 The reaction between RF and MOx nanoparticles.

Chemical transformations (Section 2.2.a) taking place upon pyrolysis under Ar of native-, xero- and X-RF-MOx systems have been monitored as a function of temperature by XRD in EDAX. Morphological changes have been followed by SEM and N_2 sorption porosimetry (section 2.2.b).

Table 2. Quantitative phase analysis (% w/w by XRD) of RF-MOx networks with smeltable metal oxides as a function of temperature (in parentheses: crystallite size, nm)

	200 °C	400 °C	600 °C	800 °C	1000 °C
n-RF-FeOx					
γ-Fe$_2$O$_3$	100 (4.1)	100 (16)	100 (28)	4.3 (19)	
Fe$_3$C				48.8 (33)	
Fe				10.9 (36)	100 (35)
Fe$_{15.1}$C				18.2	
C				17.8 (7.8)	
xero-RF-FeOx					
Fe$_3$C		11.4 (30)	8.8 (34)	4.2 (37)	1.6 (44)
Fe		88.6 (13)	91.2 (13)	95.8 (14)	98.4 (15)
X-RF-FeOx					
γ-Fe$_2$O$_3$	100 (4.6)	49.5 (16)	11.3 (23)	4.8 (19)	
FeO		6.1 (35)			
Fe$_3$C		44.5 (30)	74.5 (36)	43.7 (33)	75.0 (30)
Fe			14.2	13.3 (9.6)	25.0 (25)
Fe$_{15.1}$C				9.9	
C				28.3 (3.2)	
n-RF-CoOx					
α-Co		59 (9.5)	72.6 (11)	84.6 (11)	100 (16)
β-Co		27.2 (8.8)	20.2 (12)	8.5 (13)	
CoO		14.3 (13)	7.2 (14)	6.9 (15)	
xero-RF-CoOx					
α-Co		85.9 (13)	92.5 (13)	100 (15)	100 (15)
β-Co		14.1 (8.9)	7.5 (9.7)		
X-RF-CoOx					
α-Co		82.5 (12)	87.8 (12)	100 (14)	100 (15)
β-Co		17.5 (10)	12.2 (11)		

2.2.a Chemical Transformations. Smeltable systems: Section 2.2.a.1; Systems yielding carbides: Section 2.2.a.2.

2.2.a.1 Smeltable RF-MOx systems (M: Fe, Co, Ni, Sn, Cu). Typical EDAX and XRD results are exemplified by the RF-CuOx system (Figure 7). Data for the other four systems are given in Supporting Information (S.I.). EDAX (Figure 7 and S.I.) shows that as the pyrolysis temperature increases the composition changes: the percent weight of the metal steadily increases and the amount of carbon, and most importantly of oxygen, decrease. In most cases, oxygen is ultimately undetectable. Quantitative analysis for the crystalline phases developing upon pyrolysis as well as the associated crystallite sizes are summarized in Table 3. What is immediately obvious from the XRD spectra is that all systems in all three forms (native aerogels, X-aerogels and xerogels) yield metals in their element forms. Exception is the RF-FeOx system that also yields iron carbide. Clearly, metal ions are reduced by the organic matter to the respective elements. What is also obvious is that the reaction is more efficient (proceeds faster) in xerogels and X–aerogels, which in fact behave quite similarly: while in several native RF-MOx systems the metallic phase is still mixed with the oxide even after treatment at 800 °C or 1000 °C (e.g., Fe, Co Sn, Cu), in several xerogels and X-aerogels (e.g., those with M: Co, Sn, Cu), the only detectable crystalline phase above 400 °C is the metallic one. In the case of xero- and X-RF-FeOx we observe formation of Fe_3C at as low as 400 °C, while the case of RF-NiOx comprises an exception whereas all three forms of the material yield Ni^0 as the only crystalline phase at all temperatures above 400 °C. It is noted in passing that the crystallite size increases with the processing temperature, presumably owing to sintering of the metal nanoparticles.

In native aerogels and xerogels the only possible reaction is between solid MOx and either RF, or gases produced during carbonization of RF, or carbon produced terminally from RF. Reaction between MOx and gasses from the decomposition of RF should be ruled out, because there should be no substantial difference in the behavior of native aerogels and xerogels. Therefore, all reductions should be solid-solid reactions and the significantly lower reaction temperatures of the interpenetrating xerogel networks should be attributed to their more dense structure. In most native RF-MOx systems (with the exception of RF-NiOx) quantitative reduction starts taking place at or about the onset of carbonization of RF (600 $^{\circ}$C), therefore, it is reasonable to assume that it occurs mainly because of reaction between MOx and carbon. By the same token, in some native samples (RF-NiOx, RF-SnOx and RF-CuOx) and in all xerogels formation of the metallic face is observed below the carbonization temperature range of RF, hence reaction should take place directly between the MOx and RF nanoparticles, or between MOx and early solid decomposition products of RF.

Polyurea cross-linked aerogels include a second organic component that conceivably could react directly with MOx yielding the metallic face. In fact, polyurea, being a conformal coating on the MOx particles, could be more prone to react with the latter than RF, explaining the facile reaction (lower temperatures) of the X-systems. That possibility was investigated by pyrolysis of X-FeOx, X-NiOx and X-SnOx aerogels at 400 and 600 $^{\circ}$C. (Since the CoOx and CuOx systems do not gel by themselves, it was not possible to synthesize the corresponding crosslinked samples.) XRD analysis (Figure 8) shows no metallic or carbide phases for X-FeOx even at 600 $^{\circ}$C. On the other hand there is formation of about equal amounts of Ni^0 both at 400 $^{\circ}$C and 600 $^{\circ}$C (56 to 58% w/w),

while major reduction of SnOx to Sn^0 is observed already at 400 °C and complete

reduction is obtained at 600 °C. Those results indicate that polyurea may indeed react

directly with some of the inorganic networks. However, since RF-FeOx xerogels show

formation of Fe^0 at as low as 400 °C, while RF-NiOx and RF-SnOx xerogels (no

polyurea present) are completely converted to Ni^0 and Sn^0 at that temperature, we are

forced to conclude that the dominant reaction in the X-RF-MOx systems must be

between the RF and the MOx nanoparticles, as opposed to between MOx and their

conformal polyurea coating. Therefore, although counterintuitive, the similar thermal

behavior of X-RF-MOx and the corresponding xerogels must be attributed to

morphological similarities.

2.2.a.2 RF-MOx systems yielding carbides. Interpenetrating RF-MOx networks with M:

Cr, Ti, Hf, Y, Dy did not yield any reaction up to the 800-1000 °C range. Upon further

pyrolysis up to 1400 °C interpenetrating networks with refractories Cr, Ti, Hf yielded

carbides, while those with rare earths Y and Dy remained as mixtures of carbon and the

oxides. Figure 9 shows representative XRD results as a function of the temperature for

the RF-CrOx system in the three forms of this study while data for the remaining systems

(M: Ti, Hf, Y, Dy) are given as S.I.

Table 4 summarizes results from the quantitative phase analysis from pyrolyses of

RF-CrOx, RF-TiOx and RF-HfOx. In a similar fashion to the smeltable metals, xerogels

and X-aerogels behave similarly, yielding carbides at up to 200 °C lower processing

temperatures than the corresponding native aerogels. Again, more facile reaction in

xerogels relative to aerogels has to be attributed to compactness. And since the possibility

of reaction of the crosslinking polymer with MOx is clearly excluded (by 800 °C all

metals remain as oxides, and all organic matter has either decomposed or transformed to carbon) the only reasonable explanation for the similar behavior of xerogels and X-aerogels has to be looked for in the nanomorphology of the samples.

Overall, for both types of RF-MOx systems, the smeltable and those that are transformed to carbides, the analogous behavior of xerogels and X-aerogels has been attributed to morphological similarities. But since cross-linking "freezes" the dimensions of the X-samples closer to the dimensions of the wet-gels (refer to shrinkage data in Table 2), the topological relationship of the RF and MOx nanoparticles in the X-RF-MOx systems must be similar to, or even more "loose" than that in the native samples. Thus, more facile reaction between RF and MOx in the X-RF-MOx systems must be attributed to certain morphological changes innate to the X-samples, taking place during pyrolysis.

2.2.b Morphological changes during pyrolysis of the RF-MOx systems. As it has been discussed before based on ^{13}C NMR and SEM data,[15] upon pyrolysis X-RF aerogels undergo morphrological changes, which are attributed to physicochemical transformations of the crosslinker. Specifically, at around 200-250 $^{\circ}C$ the carbamate links of the polyurea tethers to the RF nanoparticle surfaces break and the free polymer finds itself above its melting point (~123 $^{\circ}C$) causing partial collapse of the nanoparticulate RF network. That process creates macropores. Importantly, inside the macroporous walls RF nanoparticles assume a xerogel-like (collapsed) morphology as it might have been expected.

Table 3. Quantitative phase analysis (% w/w by XRD) of RF-MOx systems yielding carbides as a function of temperature (in parenthesis: crystallite size, nm)

	800 °C 800 °C	1000 °C 1000 °C	1100 °C 1100 °C	1200 °C 1200 °C	1400 °C 1400 °C
n-RF-CrOx					
Cr_2O_3	100 (11)	100 (11)	100 (13)	100 (17)	29.1 (21)
Cr_7C_3					51.2 (19)
Cr_3C_2					19.7 (11)
xero-RF-CrOx					
Cr_2O_3		100 (13)	38.9 (15)	22.9 (14)	
Cr_7C_3			19.3 (10)		
Cr_3C_2			41.8 (15)	77.1 (18)	
X-RF-CrOx					
Cr_2O_3	100 (14)	66.8 (15)	48.2 (15)	6.9 (23)	
Cr_7C_3		9.1 (6.6)	16.9 (8.7)	70.1 (11)	86.5 (12)
Cr_3C_2		24.1 (11)	34.9 (12)	23.0 (15)	13.5 (17)
n-RF-TiOx					
TiO_2	100 (9.1)	100 (9.6)	100 (10)	100 (14)	
TiC					100 (20)
xero-RF-TiOx					
TiO_2		100 (10)	100 (14)		
TiC				100 (29)	
X-RF-TiOx					
TiO_2	100 (11)	100 (12)	100 (14)		
TiC				100 (19)	100 (23)
n-RF-HfOx					
HfO_2	100 (14)	100 (14)	100 (15)	100 (15)	
HfC					100 (29)
xero-RF-HfOx					
HfO_2		100 (13)	100 (15)		
HfC				100 (29)	
X-RF-HfOx					
HfO_2	100 (10)	100 (11)	100 (11)		
HfC				100 (19)	100 (27)

Similar behavior is observed in X-RF-MOx systems. Figure 10 follows the structural evolution of a representative smeltable system (native and X-RF-CuOx aerogels), while Figure 11 follows the structural evolution of RF-HfOx. All X-materials develop macropores at the same temperature range as typical X-RF aerogels (below 400 °C). Occasional fractures during sample preparation (see inset in Figure 10, frame showing SEM of the native RF-CuOx sample after treatment at 400 °C) allows a view inside the macroporous walls revealing a typical xerogel-like morphology, just as in the case of X-RF aerogels.

3 Discussion

The work just described has a dual significance on materials synthesis and the reactivity of nanoparticles. In the field of material science, interpenetrating networks originally were developed for polymers, and are pursued for the same basic reasons as simple polymer blends, or more complex derivatives such as block, graft and AB-graft copolymers, namely for the synergism of the components for improved thermal, mechanical and chemical properties.[28]

Interpenetrating inorganic sol-gel composites with polymers have been pursued primarily for preventing shrinkage and cracking upon drying of wet inorganic gels (e.g., silica) into xerogels, but also with proper particle size and refractive index matching for improving the optical properties of sol-gel glasses.[29] As reviewed early by Wilkes,[30] the methodology for the synthesis of such networks is conceptually similar to what has been used for the synthesis of interpenetrating polymer networks, namely, the two networks can be formed simultaneously by including polymerizable monomers in the inorganic sol,

or by starting with preformed polymers. Thus in a variation of the last method inorganic sol precursors (e.g., alkoxides) may be included in the swelling solution of crosslinked, ionomeric or crystalline polymers followed by triggering the sol-gel reaction. If any of the synthetic procedures is carried out in relatively dilute solutions under conditions that promote gelation rather than precipitation, and if the solvent is subsequently removed without significant shrinkage (e.g., by SCF drying), the resulting low-density materials are classified as aerogels. That approach was explored early for imparting ductility, or even rubbery behavior, into brittle silica aerogels.[31] More recently, an Aspen Aerogels patent reports a multistep process to interpenetrating networks of polyimide and a variety of metal oxide aerogels by adding an epoxide and the appropriate metal salt in a polyamic acid solution, followed by addition of acetic anhydride/pyridine for imidization.[32] According to that patent, pyrolysis under Ar of the resulting composites yielded, depending apparently on the relative stoichiometry and the chemical identity of the metallic element precursor, metal carbide aerogels, metal carbide-carbon aerogels or carbon aerogels with dispersed metal particles.

On the other hand, the synthesis of interpenetrating RF-MOx networks as decribed above is a versatile one-pot process based on two facts considered together: (a) gelation of R with F can be also carried out effectively in organic media by acid catalysis; and, (b) hydrated metal salts undergoing gelation in organic media through an epoxide route (Scheme 2) are fairly strong Brønsted acids able to catalyze gelation of RF. Meanwhile, RF aerogels are the primary precursors of carbon aerogels to which they are converted pyrolytically in inert atmosphere. The latter are pursued as high surface area electrodes for supercapacitors and fuel cells,[33] as well as supports for catalysts.[34] Catalyst precursors

are usually included as metal salts in the RF sol. Since the RF network is produced typically by Pekala's aqueous base-catalyzed process, a common problem is leaching of the metal ions during the solvent exchange steps required before SCF drying. Another issue, again related to the high solubility of the metal ions in the aqueous sol, is segregation of large crystallites of the dopant (>15 nm in diameter) at the surface of the RF nodules. A successful method that halts leaching and yields uniform distribution of the dopant involves use of chelating potassium 2,4-dihydrobenzoate instead of resorcinol.[35] Better dispersion of the dopant has been reported by anchoring metal ions to the RF network by employing complexing agents able to react and incorporate themselves within RF in a process referred to as "cogelation."[36] Clearly, in our case leaching of the metal ion or segregation on the surface of the RF nanoparticles are no issues. The MOx network gels first, and inferring from the gelation time of that network by itself and in the presence of the RF precursors, the two gelation processes do not interfere with one another. However, the segregation issue might be still present and in fact opposite to the one faced by metal ion doping of RF in the literature namely, RF, gelling second, might accumulate on the surface of the MOx particles in a core-shell like fashion. As mentioned in the Results Section, the RF and MOx networks should look identical, and although we clearly see the MOx nanoparticles in TEM, the location of the RF network is less clear. Nevertheless, the possibility of a core-shell structure is excluded on relative reactivity grounds between native aerogels and xerogels: if RF and MOx had formed core-shell structures, the contact area between them would have been as high as possible and therefore subsequent carbothermal reactions would always take place at similar temperature ranges. Now, since most literature studies on metal-oxide doping of

RF aerogels have been conducted from a catalysis perspective, the level of metal doping has been low, never reported above 10% w/w.[37] Furthermore, one persistent observation reported rather in passing has been that in selected cases (Fe, Co, Ni, Cu) the dopant of the resulting carbon aerogel is not the original salt or the corresponding oxide but the metal itself.[37,38] It is inferred, therefore, that in those cases the metal ions have been reduced by carbon, in analogy to the smelting process that has been used in extractive metallurgy for millennia. Here, our ability to form two networks and to induce quantitative reduction to the metal (see EDAX data in Figures 7 and S.1) has lead to monolithic Fe, Co, Ni, Sn and Cu aerogels (for detailed characterization of those materials refer to Tables S.1-S.5 in S.I.) rather than simple doping of carbon with metals. It should be mentioned then that typically porous metals can be synthesized reductively using polymer or surfactant templating (e.g., cases of Ag and Pt, respectively[39]), by chemical vapor deposition (on carbon templates, cases of Ir and Re[40]), or by alloying and selective removal (de-alloying) of one component (case of nanoporous Au by alloying with Ag, and removal of the latter electrochemically[41]). More recently, low density ($\sim$0.01 g cm^{-3}), high surface area (>250 m^{2}g^{-1}) monolithic metal nanofoams (Fe, Co, Ni, Cu, Ag, Au, Pd, Pt, Ti) have been described through self-propagating combustion synthesis of selected transition metal complexes with high-nitrogen containing ligands.[42] The carbothermal method via interpenetrating RF-MOx networks described herewith competes quite favorably with those methods in terms of simplicity. Other systems (cases of RF-CrOx, RF-TiOx and RF-HfOx) yielded monolithic carbides, while still other failed to give reaction up to 1400 °C even though carbides of those metals are known (cases of RF-YOx and RF-DyOx).[43] Those results are interesting on their own right, as well-

characterized carbide aerogels are not many. For example monolithic NbC aerogels (surface area up to 74 m^2g^{-1}) have been obtained through a pseudomorphic solid-state reaction by passing a mixture of CH_4-H_2 over a Nb_2O_5 aerogel (surface area 344 m^2g^{-1}) at high temperatures (1173-1373 K).[44] Mo_2C and WC nanoparticles have been observed in carbon aerogels after pyrolysis at 1000 °C under flowing H_2/Ar or pure N_2, respectively, of molybdenum(VI) or tungsten(VI)-doped RF aerogels.[45] In the case of Mo_2C, it has been proposed that Mo(VI) is reduced to Mo(IV) (i.e., MoO_2) by the carbon matrix, and Mo(IV) is further reduced by CH_4 or CH_x species that are formed from the gasification of the carbon matrix at high temperature in the presence of H_2. In the case of WC, it appears that WC is formed by direct reduction of W(VI) by the carbon matrix. In the same realm, SiC wiskers and TiC nanoparticles have been produced by pyrolysis under Ar (above 1300 °C) of silica or titania aerogels made by mixing ethanolic silica or titania sols with carbonaceous ethanolic sols prepared from petroleum green coke.[46] We have been also successful in producing monolithic SiC aerogels by pyrolysis of X-silica aerogels crosslinked with polyacrylonitrile via a surface initiated polymerization process.[47] However, although highly efficient, that method is not general and cannot be extended easily to other carbides beyond silica as the method described here. Finally, the same melt-and-flow mechanism that in the case of X-RF aerogels has produced macroporous carbons, seems to be in operation here as well allowing an extra degree of freedom in the design of porous metals and carbides.

Now, the reactivity difference among aerogels, xerogels and X-aerogels is extremely interesting with far-reaching implications on the activation of carbothermal processes yielding metals or carbides. Among the four possible mechanisms for carbothermal

processes,[48] that is: (a) reaction of the oxide with carbon producing gaseous intermediates CO and CO_2 that sustain the reduction; (b) oxide reduction through gaseous carbides formed from metal vapors and carbon; (c) reduction by H_2 produced from C and H_2O; and (d) thermal dissociation of the oxide into metal and O_2 that subsequently reacts with C, process (b) is excluded based on the low pressure of the metals at the reaction temperatures, process (c) is excluded based on the stoichiometry of the reactions (it requires an unrealistically high amount of water), while process (d) has received some attention based on relatively high partial pressures of O_2 detected in some carbothermal systems. That mechanism should not be in operation in the RF-MOx systems, because if the reaction is initiated by decomposition of MOx , or for this matter by gaseous products from decomposition of RF, then in principle there should be no difference in the reactivity between native aerogels and xerogels. It might be counter-argued, however, that the presence of closed pores in the skeletal framework of xerogels might lead to gas retention allowing faster reaction. This hypothesis though is not supported by the high reactivity of X-aerogels, which do not have closed pores in their skeletal framework. Therefore, within the model that calls for direct reaction between carbon and MOx nanoparticles (or even between RF and MOx nanoparticles), it seems that the only viable reason for the facile carbothermal processes in xerogels and X-aerogels is the innate high nanoparticle compactness in the former, and the induced compactness by melting of the crosslinker in the latter.

4 Experimental

Materials

All metal chlorides, solvents, resorcinol, formaldehyde solution and epichlorohydrin were purchased from Aldrich-Sigma and were used without further purification. Demodur N3300A was provided courtesy of Bayer Corporation.

Preparation of RF-MOx xerogels and native aerogels. RF-MOx xerogels and native aerogels were prepared by mixing two solutions: Solution A containing 0.337 g (0.00306 mol) of resorcinol, 0.455 mL (0.00611 mol) of a formaldehyde solution (37% w/w, methanol stabilized) and 5.75 mL of CH_3CN (AN) or DMF (cases of RF-CoOx, RF-NiOx, RF-CuOx; refer to Table 1), and a just-made Solution B containing 0.003311 mol of the corresponding metal chloride, epichlorohydrin (2.75 mL, 0.0316 mol) and 5 mL of ethanol (EtOH) or DMF (cases of RF-CoOx, RF-NiOx, RF-CuOx; refer to Table 1). It is noted that in the cases of cobalt- and copper-systems, which do not gel by themselves, Solution B was incubated at 80 °C for 20 min before it was mixed with Solution A. It is noted further that if the stoichiometry of the coordination water in the metal chloride was less than "6" the correct amount of water was added to solution B, prior to the addition of epichlorohydrin, to bring the metal:H_2O mol ratio to 6. The sol resulting from the mixing of the two solutions was poured immediately into polypropylene molds (Wheaton polypropylene Omni-Vials, PartNo.225402, 1 cm in diameter), which were covered with Teflon tape and were placed in an oven at 80 °C until the expected gelation point of the RF/hydrated metal chloride system by itself (i.e., the gelation point of Solutions A plus B without epichlorohydrin added – see below). (Solvents systems, gelation times and other

pertinent information relevant to the particular systems of this study are summarized in Table 1.) After gelation, wet gels were aged for 48 h at room temperature and then washed three times with the gelation solvent system (EtOH:AN 1:1 v/v, or DMF, see Table 1) followed by three acetone washes. Acetone-filled wet-gels were processed in three different ways: (a) they were dried under ambient conditions in a fume hood for 48 h to xerogels (xero-RF-MOx); (b) they were dried in a autoclave with SCF CO_2 to native aerogels (n-RF-MOx); or, (c) they were crosslinked with polyurea by placing them in a bath (4× the volume of each gel) containing 11 g of a triisocyanate (Desmodur N3300A)

Desmodur N3300A:
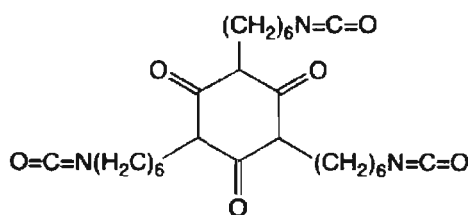
in 94 mL acetone, letting them for equilibration for 24 h at room temperature, heating them in the isocyanate bath at 50 °C for 48 h, followed by three washes with fresh acetone at room temperature and drying in an autoclave with SCF CO_2 to X-aerogels (X-RF-MOx). All washes lasted 8 h each and they were conducted using 4× the volume of each gel as solvent each time.

For control purposes gelation of the hydrated metal ions via reaction with epichlorohydrin was carried out independently in a suitable solvent that dissolves the salt (Table 1). The concentration of the metal ion was adjusted at the same level as in the final mixture of Solutions A and B by diluting Solution B with a volume of solvent equal to the volume of Solution A; the gelation conditions were the same as in the complete mixture (80 °C) The solution pH was monitored during gelation, and the gelation point

was recorded (Table 1). The capability of hydrated metal ions to induce gelation of the R/F system was evaluated by mixing Solution A with Solution B in which no epichlorohydrin was added; the gelation conditions were the same as in the complete mixture (80 °C). The pH was monitored, photographs were taken at various stages of the reaction, and the gelation time was recorded (Table 1). Hydrated metal ions do not gel in the absence of epichlorohydrin.

Preparation of metal and metal carbide aerogels. Native aerogels, xerogels and X-aerogels of smeltable networks (RF-FeOx, RF-SnOx, RF-CuOx, RF-CoOx and RF-NiOx) were pyrolyzed under flowing Ar (60 mL min^{-1}) in a tube furnace for 3 h at 200 °C, 400 °C, 600 °C 800 °C and 1000 °C. Corresponding networks of systems capable of yielding carbides (RF-HfOx, RF-CrOx, RF-TiOx, RF-YOx and RF-DyOx) were pyrolyzed under flowing Ar (60 mL min^{-1}) for 3 h at 1000 °C, 1100 °C, 1200 °C and 1400 °C. Prior to pyrolysis the tube furnace was purged with Ar for 10 min and heating was conducted at 5 °C min^{-1}. Since two systems, RF-YOx and RF-DyOx, remained as oxide/carbon mixtures even after prolonged pyrolysis at 1400 °C, no temperature dependence studies were conducted.

Methods

Acid dissociation constants (pKa values) were determined by titrations with an aqueous NaOH solution (0.1 M) of Solutions B for each hydrated metal ion (0.003311 M) with no epichlorohydrin added. The pH was monitored with a UB-5 pH-meter from Denver Instruments. The pH during gelation of: (a) hydrated metal ions with epichlorohydrine; (b) of RF with the same metal ions as catalysts (no epichlorohydrin added), and (c) of the

complete RF/hydrated metal chloride/epichlorohydrin systems were monitored with a Accumet Research AR20 pH meter from Fisher Scientific. Photographs were taken at various stages of the gelation process under ambient laboratory illumination (no lighting compensation was used) with a digital camera at the macro-mode. Supercritical fluid (SCF) CO_2 drying of native and polyurea-crosslinked wet-gel networks to the corresponding native and X-aerogels was conducted in an autoclave (SPI-DRY Jumbo Supercritical Point Drier, SPI Supplies, Inc., West Chester, PA) as described before. Bulk densities (ρ_b) were calculated from the weight and the physical dimensions of the samples. Skeletal densities (ρ_s) were determined using helium pycnometry with a Micromeritics AcuuPyc II 1340 instrument. Porosities, ρ, were determined from the ρ_b and ρ_s values. Surface areas (σ) were measured via the Brunauer-Emmet-Teller (BET) method by nitrogen sorption porosimetry using a Micromeritics ASAP 2020 Surface Area and Pore Distribution analyzer. Pore size distributions were determined using the Barrett–Joyner–Halenda (BJH) method applied on the desorption isotherm. Prior to analysis, samples for skeletal density and surface area characterization were outgassed at 80 °C for 12 h.

5 Conclusions

Synthesis of RF-MOx interpenetrating networks is straightforward and highly versatile. Reasoning by analogy, the range of possible materials can be expanded to MOx not considered in this work, and most importantly those materials can be used as precursors for the synthesis of other aerogels whose synthesis either has not been reported before, or it is quite elaborate. Study of the kinetics of those processes in the classical phenomenological sense (rate as a function of time, temperature, and relative amounts of

MOx and RF) should afford information related to the interparticle contacts in the two types of networks (native aerogels and xerogels), and that should be useful for improving the efficiency of reactions between nanoparticles.

Acknowledgements

Notes and References

1. Henz, B. J.; Hawa, T.; Zachariah, M. *J. Appl. Phys.* **2009**, *105*, 124-310.

2. (a) Pivkina, A.; Ulyanova, P.; Frolov, Y.; Zavyalov, S.; Schoonman, J. *Propellants, Explosives, Pyrotechnics* **2004**, *29*, 39-48. (b) Ferguson, J. D.; Buechler, K. J.; Weimer, A. W.; George, S. M. *Powder Technology* **2005**, *156*, 154-163. (c) Prentice, D.; Pantoya, M. L.; Gash, A. E. *Energy & Fuels* **2006**, *20*, 2370-2376. (d) Sarawadekar, R. G.; Agrawal, J. P. *Defence Science Journal* **2008**, *58*, 486-495.

3. (a) Schneider, J. J. *Adv. Mater.* **2001**, *13*, 529-533. (b) Esmaeili, B.; Chaouki, J.; Dubois, C. *AIChE Journal* **2009**, *55*, 2271-2278.

4. Streletskii, A. N.; Povstugar, I. V.; Borunova, A. B.; Lomaeva, S. F.; Butyagin, P. Yu. *Colloid Journal* **2006**, *68*, 470-480.

5. Streletskii, A. N.; Kolbanev, I. V.; Permenov, D. G.; Povstugar, I. V.; Borunova, A. B.; Dolgoborodov, A. Yu.; Makhov, M. N.; Butyagin, P. Yu. *Rev. Adv. Mater. Sci.* **2008**, *18*, 353-359.

6. Levitas, V. I. *Combustion and Flame* **2008**, *156*, 543-546.

7. Cao, B.; Starace, A. K.; Judd, O. H.; Jarrold, M. F. *J. Am. Chem. Soc.* **2009**, *131*, 2446-2447.

8. Vodop'yanov, A. G.; Kozhevnikov, G. N.; Baranov, S. V. *Russian Chemical Reviews* **1988**, *57*, 810-823.

9. Zhao, L.; Clapsaddle, B. J.; Satcher, J. H.; Schaefer, D. W.; Shea, K. J. *Chem. Mater.* **2005**, *17*, 1358-1366.

10. (a) Leventis, N.; Chandrasekaran, N.; Sotiriou-Leventis, C.; Mumtaz, A. *J. Mater. Chem.* **2009**, *19*, 63-65. (b) Leventis, N.; Chandrasekaran, N.; Sadekar, A. G.; Sotiriou-Leventis, C.; Lu, H. *J. Am. Chem. Soc.* **2009**, *131*, 4576-4577.

11. Brinker, C. J.; Scherer, G. W. *Sol-gel science. The physics and chemistry of sol-gel processing*; Academic Press: New York, 1990.

12. (a) Leventis, N.; Sotiriou-Leventis, C.; Zhang, G.; Rawashdeh, A.-M. M. *NanoLetters* **2002**, *2*, 957-960. (b) Meador, M. A. B.; Capadona, L. A.; MacCorkle, L.; Papadopoulos, D. S.; Leventis, N. *Chem. Mater.* **2007**, *19*, 2247-2260. (c) Leventis, N.; Mulik, S.; Wang, X.; Dass, A.; Sotiriou-Leventis, C.; Lu, H. *J. Am. Chem. Soc.* **2007**, *129*, 10660-10661.

13. Leventis, N. *Acc. Chem. Res.* **2007**, *40*, 874-884.

14. (a) Leventis, N.; Sotiriou-Leventis, C.; Mulik, S.; Dass, A.; Schnobrich, J.; Hobbs, A.; Fabrizio, E. F.; Luo, H.; Churu, G.; Zhang, Y.; Lu, H. *J. Mater. Chem.* **2008**, *18*, 2475-2482. (b) Luo, H.; Churu, G.; Schnobrich, J.; Hobbs, A.; Fabrizio, E. F.; Dass, A.; Mulik, S.; Sotiriou-Leventis, C.; Lu, H.; Leventis, N. *J. Sol-Gel Sci. Techn.* **2008**, *48*, 113-134.

15. Leventis, N.; Mulik, S.; Sotiriou-Leventis, C. *Chem. Mater.* **2008**, *20*, 6985-6997.

16. Cotton, F. A.; Wilkinson, G.; Murillo, C. A.; Bochmann, M. "Advanced Inorganic Chemistry Sixth Edition," Wiley: New York, N.Y. (1999).

17. Leventis, N.; Vassilaras, P.; Fabrizio, E. F.; Dass, A. *J. Mater. Chem.* **2007**, *17*, 1502-1508.

18. (a) Ziese, W. *Ber* **1933**, *66*, 1965-1972. (b) Kearby, K.; Kistler, S. S.; Swann, S. Jr. *Ind. Eng. Chem.* **1938**, *30*, 1082-1086. (c) Sydney, L. E. Preparation of sols and gels. British Patent No.: 2,111,966 (**1983**). (d) Gash, A. E.; Tillotson, T. M.; Satcher, J. H.; Hrubesh, L. W.; Simpson, R. L. *J. Non-Cryst. Solids* **2001**, *285*, 22-28. (e) Gash, A. E.; Tillotson, T. M.; Satcher, J. H.; Poco, J. F.; Hrubesh, L. W.; Simpson, R. L. *Chem.Mater.* **2001**, *13*, 999-1007. (f) Sisk, C. N.; Hope-Weeks, J. *J. Mater. Chem.* **2008**, *18*, 2607-2610.

19. Jones, R. W. Fundamental principles of sol-gel technology. The Institute of Metals, **1989**, London: UK.

20. (a) Pekala, R. W. *J. Mater. Sci.* **1989**, *24*, 3221–3227. (b) Pekala, R. W.; Alviso, C. T.; Kong, F. M.; Hulsey, S. S. *J. Non-Cryst. Solids* **1992**, *145*, 90-98.

21. Qin, G.; Guo, S. *Carbon* **2001**, *39*, 1929-1941.

22. (a) Mulik, S.; Sotiriou-Leventis, C.; Leventis, N. *Chem. Mater.* **2007**, *19*, 6138-6144. (b) Reuß, M.; Ratke, L. *Sol-Gel Sci. Technol.* **2008**, *47*, 74-80.

23. Bekyarova, E.; Kaneko, K. *Adv. Mater.* **2000**, *12*, 1625-1628.

24. Skeletal densities of native MOx aerogels (by He pycnometry): $\rho_{s,FeOx}$=3.03 g cm^{-3}; $\rho_{s,NiOx}$=3.65 g cm^{-3}; $\rho_{s,SnOx}$=2.98 g cm^{-3}; $\rho_{s,CrOx}$= 3.69 g cm^{-3}; $\rho_{s,TiOx}$=3.77 g cm^{-3}; $\rho_{s,HfOx}$=3.81 g cm^{-3}; $\rho_{s,YOx}$=2.39 g cm^{-3}; $\rho_{s,DyOx}$=3.02 g cm^{-3}.

25. Sing, K. S. W.; Everett, D. H.; Haul, R. A. W.; Moscou, L.; Pierotti, R. A.; Rouquerol, J.; Siemieniewska T. *Pure and Appl. Chem.* **1985**, *57*, 603-619.

26. Lukens, W. W. Jr.; Schmidt-Winkel, P.; Zhao, D.; Feng, J.; Stucky, G. D. *Langmuir* **1999**, *15*, 5403-5409.

27. Suda, Y.; Kawasaki, H.; Terajima, R.; Emura, M. *Jpn. J. Appl. Phys.* **1999**, *38*, 3619-3621.

28. Interpenetrating Polymer Networks. Klempner, D.; Sperling, L. H.; Utracki, L. A. Eds, American Chemical Society, Washington DC (1994).

29. (a) Pope, E. J. A.; Asami, M.; Mackenzie, J. D. *J. Mater. Res.* **1989**, *4*, 1018-1026. (b) Philipp, G.; Schmidt, H. *J. Non-Cryst. Solids* **1984**, *63*, 283-292. (c) Huang, H. H.; Orler, B.; Wilkes, G. L. *Macromolecules* **1987**, *20*, 1322-1330. (d) Sanchez, C.; Robot, F. *New J. Chem.* **1994**, *18*, 1007-1047.

30. Wen, J.; Wilkes, G. L. *Chem. Mater.* **1996**, *8*, 1667-1681.

31. (a) Hu, Y.; Mackenzie, J. D. *J. Mater. Sci.* **1992**, *27*, 4415-4420. (b) Novak, B. M.; Auerbach, D.; Verrier, C. *Chem. Mater.* **1994**, *6*, 282-286. (c) Kramer, S. J.; Rubio-Alonso, F.; Mackenzie, J. D. *Mat. Res. Soc. Symp. Proc.* **1998**, *435*, 295-300.

32. Rhine, W.; Wang, J.; Begag, R. Polyimide aerogels, carbon aerogels, and metal carbide aerogels and methods of making same. US Pat No: 7,074,880 (2006).

33. Al-Muhtaseb, S. A.; Ritter, J. A. *Adv. Mater.* **2003**, *15*, 101–114.

34. (a) Moreno-Castilla C.; Maldonado-Hódar, F. J. *Carbon* **2005**, *43*, 455-465. (b) Sánchez- Polo, M.; Rivera-Utrilla, J.; von Gunten, U. *Water Res.* **2006**, *40*, 3375-3384.

35. (a) Baumann, T. F.; Fox, G. A.; Satcher, J. H.; Yoshizawa, N.; Fu, R.; Dresselhaus, M. S. *Langmuir* **2002**, *18*, 7073-7076. (b) Baumann, T. F.; Satcher, J. H. *Chem. Mater.* **2003**, *15*, 3745-3747.

36. Job, N.; Picard, R.; Vertruyen, B.; Colomer, J.-F.; Marien, J.; Picard, J.-P. *J. Non-Cryst. Solids* **2007**, *353*, 2333-2345.

37. Fu, R.; Baumann, T. F.; Cronin, S.; Dressekhaus, G.; Dresselhaus, M. S.; Satcher, J. H. *Langmuir* **2005**, *21*, 2647-2651.

38. (a) Maldonado-Hódar, F. J.; Moreno-Castilla, C.; Rivera-Utrilla, J.; Hanzawa, Y.; Yamada,Y. *Langmuir* **2000**, *16*, 4367-4373. (b) Yoshizawa, N.; Hatori, H.; Soneda, Y.; Hanzawa, Y.; Kaneko, K.; Dresselhaus, M. S. *J. Non-Cryst. Solids* **2003**, *330*, 99-105. (c) Maldonado-Hódar, F. J.; Moreno-Castilla, C.; Pérez-Cadenas, A. F. *Micropor. Mesopor. Mater.* **2004**, *69*,119-125. (d) Steiner, S. A.; Baumann, T. F.; Kong, J.; Satcher, J. H.; Dresselhaus, M. S. *Langmuir* **2007**, *23*, 5161-5166.

39. (a) Walsh, D.; Arcelli, L.; Toshiyuki, I.; Tanaka, J.; Mann, S. *Nat. Mater.* **2003**, *2*, 386-390. (b) Song, Y.; Yang, Y.; Medforth, C. J.; Pereira, E.; Singh, A. K.; Xu, H.; Jiang, Y.; Brinker, C. J.; van Swol, F.; Shelnutt, J. *J. Am. Chem. Soc.* **2004**, *126*, 635-645.

40. Sherman, A. J.; Williams, B. E.; Delarosa, M. J.; Laferla, R. Characterization of porous cellular materials fabricated by CVD. In Mechanical Properties of Porous and Cellular Materials; Sieradzki, K.; Green, D.; Gibson, L. J. Eds, *Materials Research Society Symposium Proceedings* **1991**, *207*, Materials Research Society: Pittsburgh, PA, pp 141-149.

41. (a) Biener, J.; Hodge, A. M.; Hamza, A. V.; Hsiung, L. L.; Satcher, J. H. *J. Appl. Phys,* **2005**, *97*, 1-4.

42. Tappan, B. C.; Huynh, M. H.; Hiskey, M. A.; Chavez, D. E.; Luther, E. P.; Mang, J. T.; Son, S. F. *J. Am. Chem. Soc.* **2006**, *128*, 6589-6594.

43. Speddding, F. H.; Gschneidner, K. Jr.; Daane, A. H. *J. Am. Chem. Soc.* **1958**, *80*, 44 4499-4503.

44. (a) Teixeira da Silva, V. L. S.; Ko, E. I.; Schmal, M.; Oyama, S. T. *Chem. Mater.* **1995**, *7*, 179-184. (b) Kim, H. S.; Bugli, G.; Djéga-Mariadassou, G. *J. Solid-State Chem.* **1999**, *142*, 100-107.

45. (a) Pérez-Cadenas, A. F.; Maldonado-Hódar, F. J.; Moreno-Castilla, C. *Langmuir* **2005**, *21*, 10850-10855. (b) Maldonado-Hódar, F. J.; Pérez-Cadenas, A. F.; Moreno-Castilla, C. *Carbon* **2003**, *41*, 1291-1299.

46. (a) Li, X. K.; Liu, L.; Zhang, Y. X.; Shen, Sh. D.; Ge, Sh.; Ling, L. Ch. *Carbon* **2001**, *39*, 159-165. (b) Li, X. K.; Liu, L.; Ge, Sh.; Shen, Sh. D.; Song, J. R.; Zhang, Y. X.; Li, P. H. *Carbon* **2001**, *39*, 827-833.

47. (a) Leventis, N.; Sadekar, A. G.; Chandrasekaran, N.; Sotiriou-Leventis, C. *Chem. Mater.* in press. (b) Mulik, S.; Sotiriou-Leventis, C.; Churu, G.; Lu, H.; Leventis, N. *Chem. Mater.* **2008**, *20*, 5035-5046.

48. L'vov, B. V. *Thermochim. Acta* **2000**, *360*, 109-120.

49. J. H. Harreld, W. Dong and B. Dunn, Mater. Res. Bull., 1998, 33, 561–567; J. W. Long, K. E. Swider-Lyons, R. M. Stroud and D. R. Rolison, Electrochem. Solid-State Lett., 2000, 3, 453–456;

50. M. S. Doescher, J. J. Pietron, B. M. Dening, J. W. Long, C. P. Rhodes, C. A. Edmondson and D. R. Rolison, Anal. Chem., 2005, 77, 7924–7932.

6 Figures
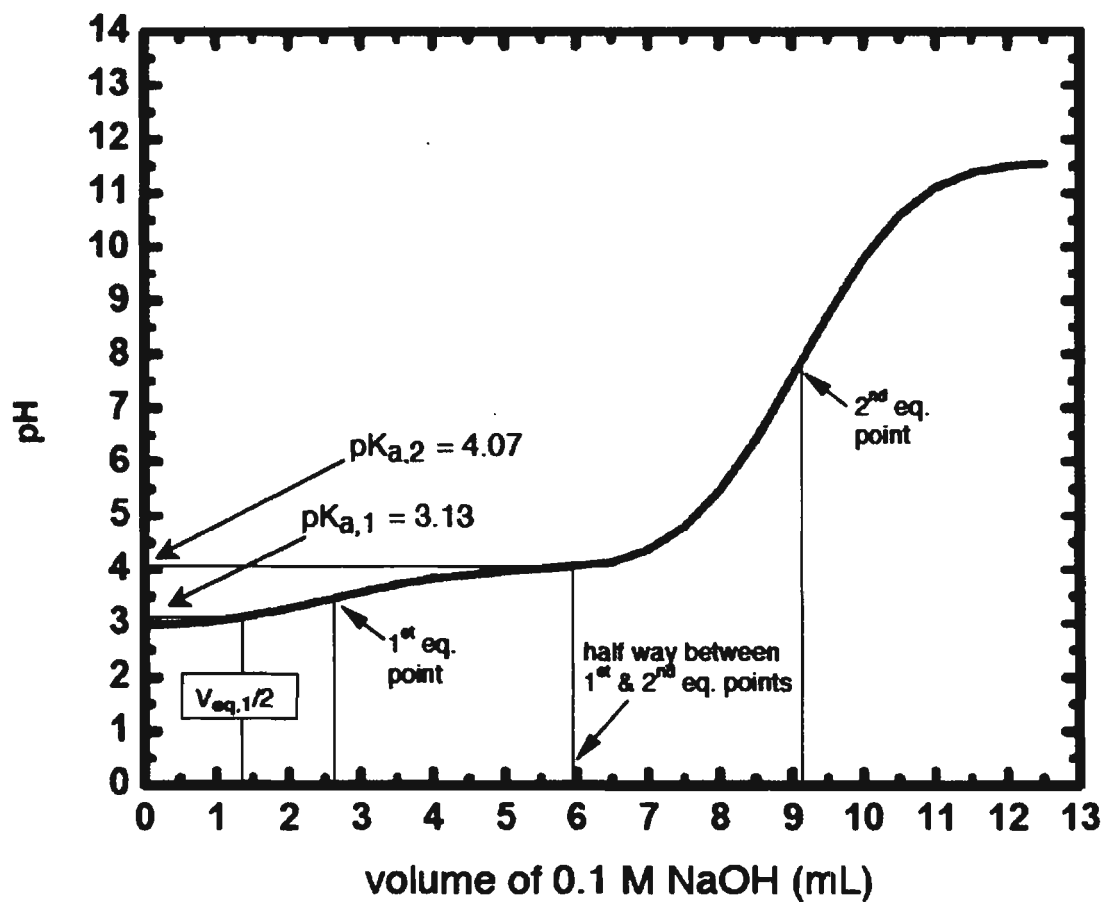
Fig. 1 A representative titration curve for hydrated metal chlorides in the organic media used for gelation (case shown: $CuCl_2.6H_2O$; 0.66 M in DMF).
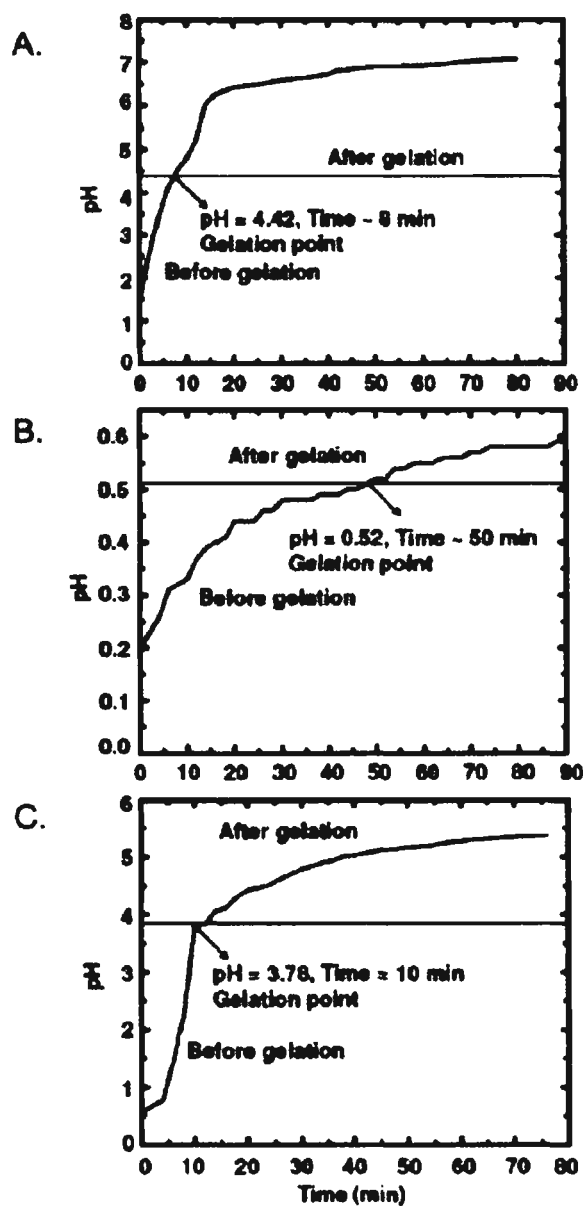
Fig. 2 Typical pH changes during gelation of: (A) a hydrated metal ion with epichlorohydrin (case of $[Fe(H_2O)_6]^{3+}$, 0.66 M in ethanol). (B) RF in ethanol:acetonitrile using $Fe(H_2O)_6]^{3+}$ as catalyst (0.29 M; no epichlorohydrin added). (C) the complete $RF/[Fe(H_2O)_6]^{3+}$/epichlorohydrin system in ethanol/acetonitrile (see Experimental).
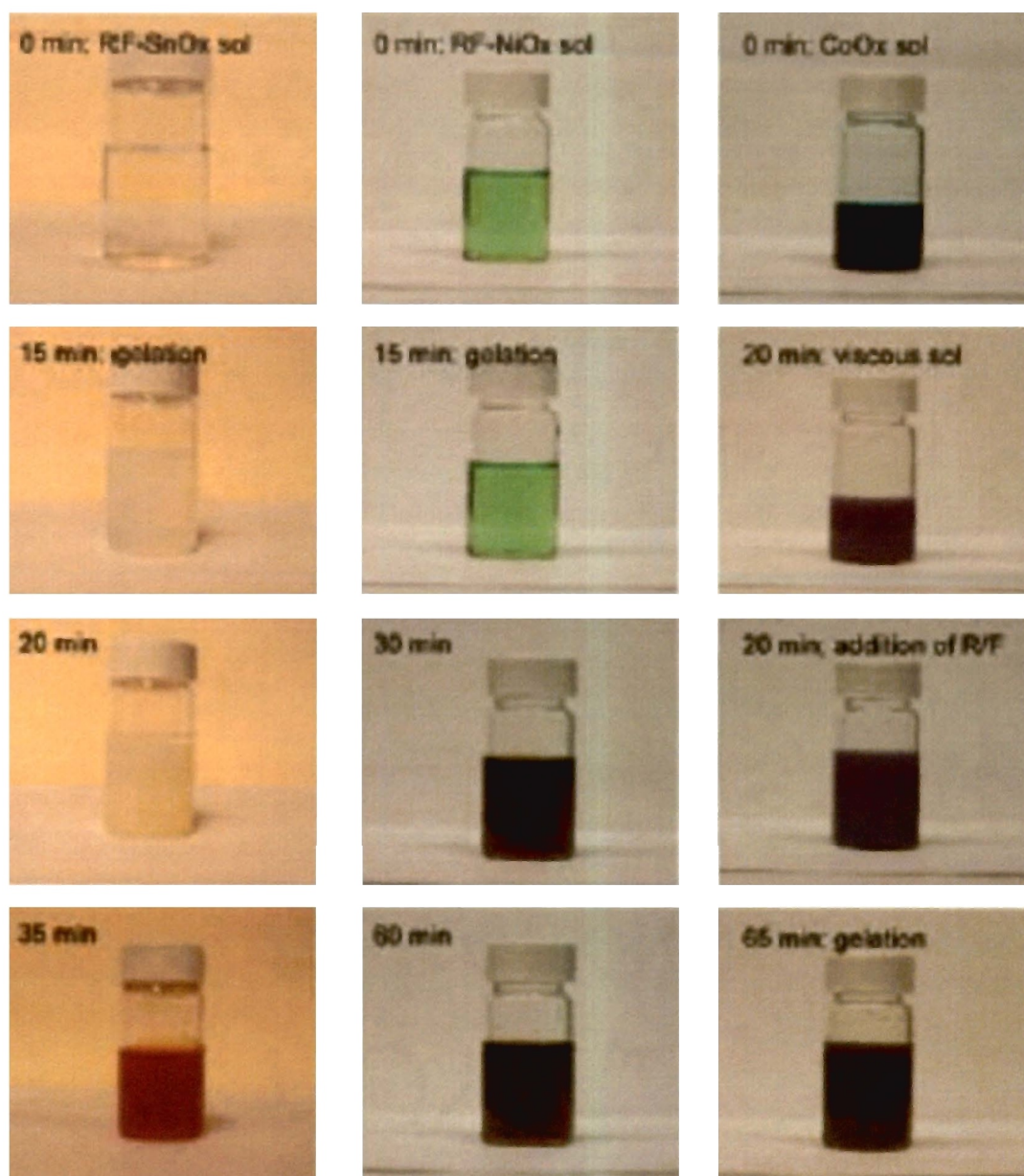
Fig. 3 Chromatic changes during gelation of three $[RF/M(H_2O)_6]^{n+}$/epichlorohydrin sols in the solvents of Table 1.
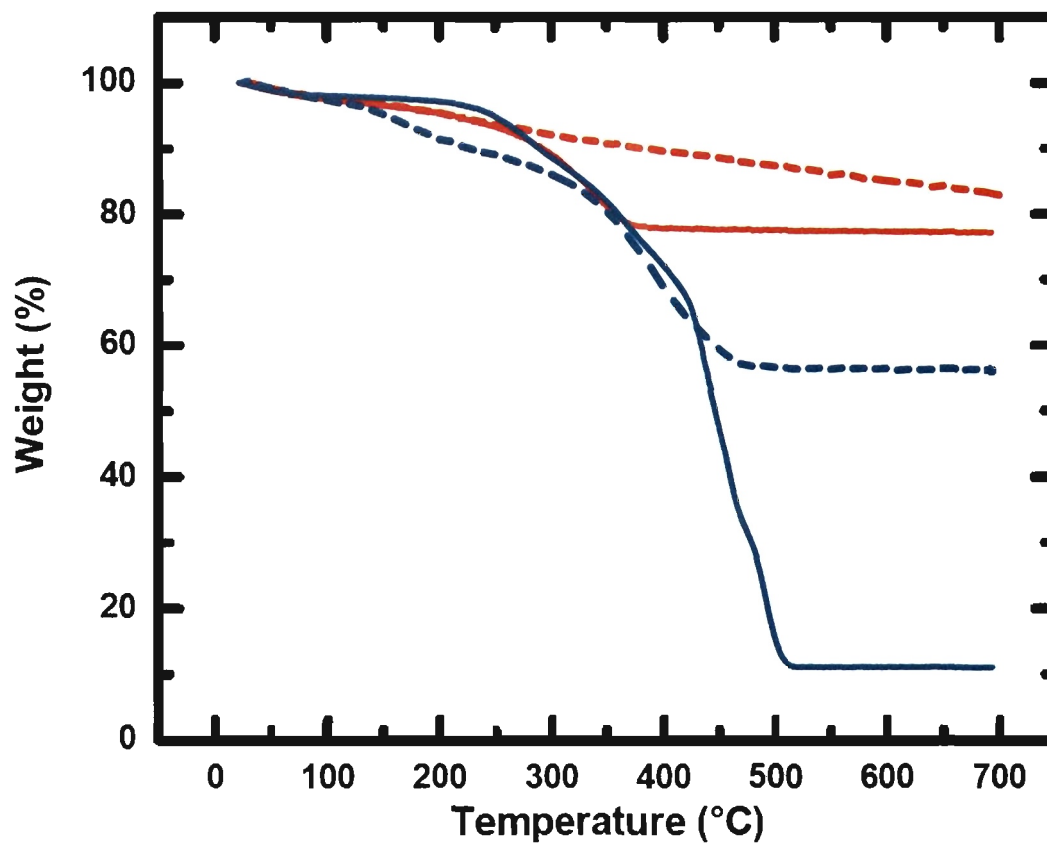
Fig. 4 Typical thermogravimetric analysis data (TGA, 10 ^{o}C min^{-1}) for smelatable RF-MOx systems (M: Fe, Co, Ni, Sn, Cu). Red: n-RF-FeOx (ρ_b= 0.047±0.001 g cm^{-3}); Blue: X-RF-FeOx (ρ_b=0.42±0.01 g cm^{-3}). Solid lines: in air; dashed lines: under N$_2$.

A. RF-CoOx
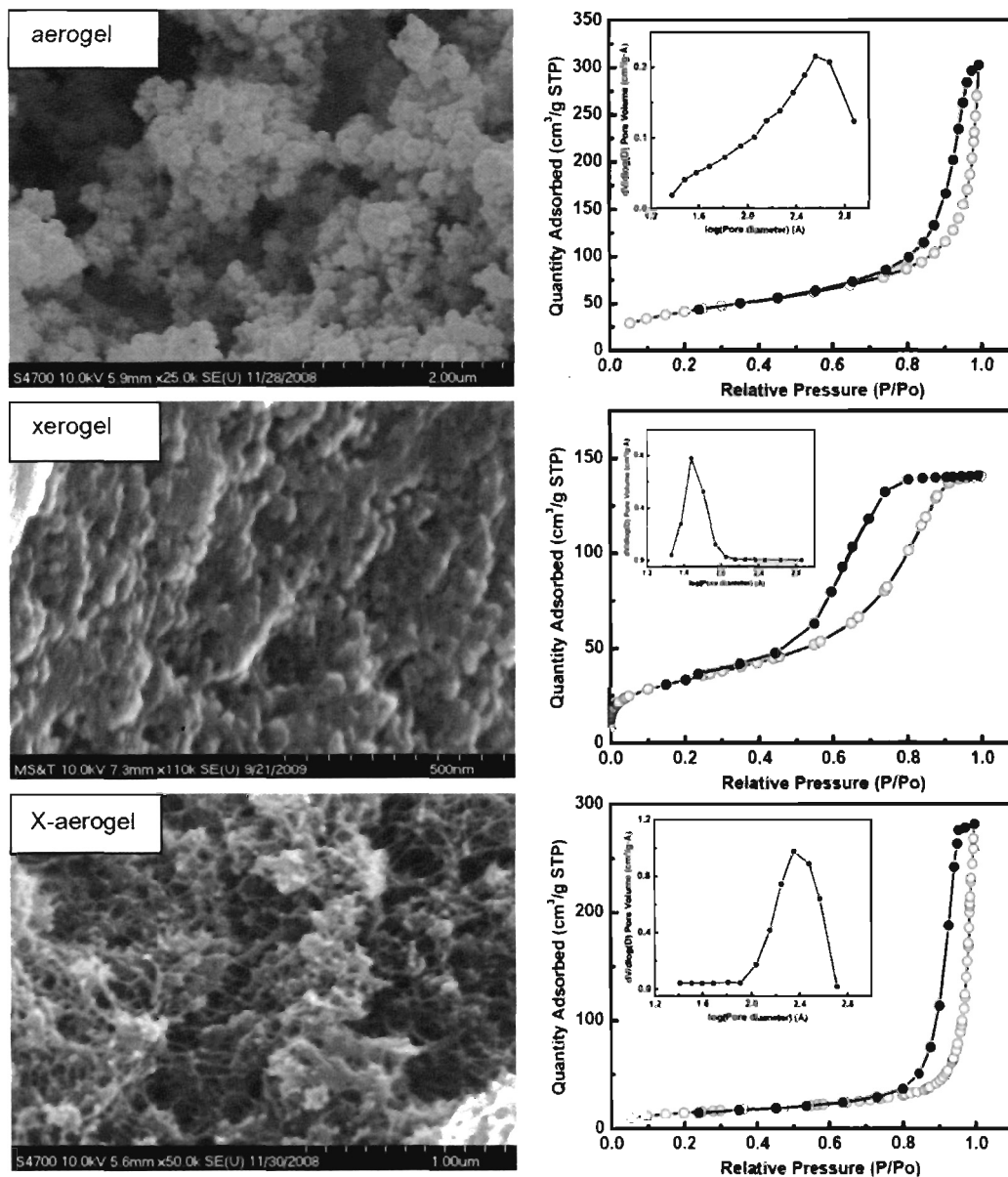
Fig. 5 Representative SEM and N₂ sorption data for the RF-MOx systems exemplified by RF-CoOx in the native aerogel, xerogel and X-aerogel forms. Open circles, adsorption; dark circles, desorption. Insets: BJH-desorption data.

B. RF-HfOx
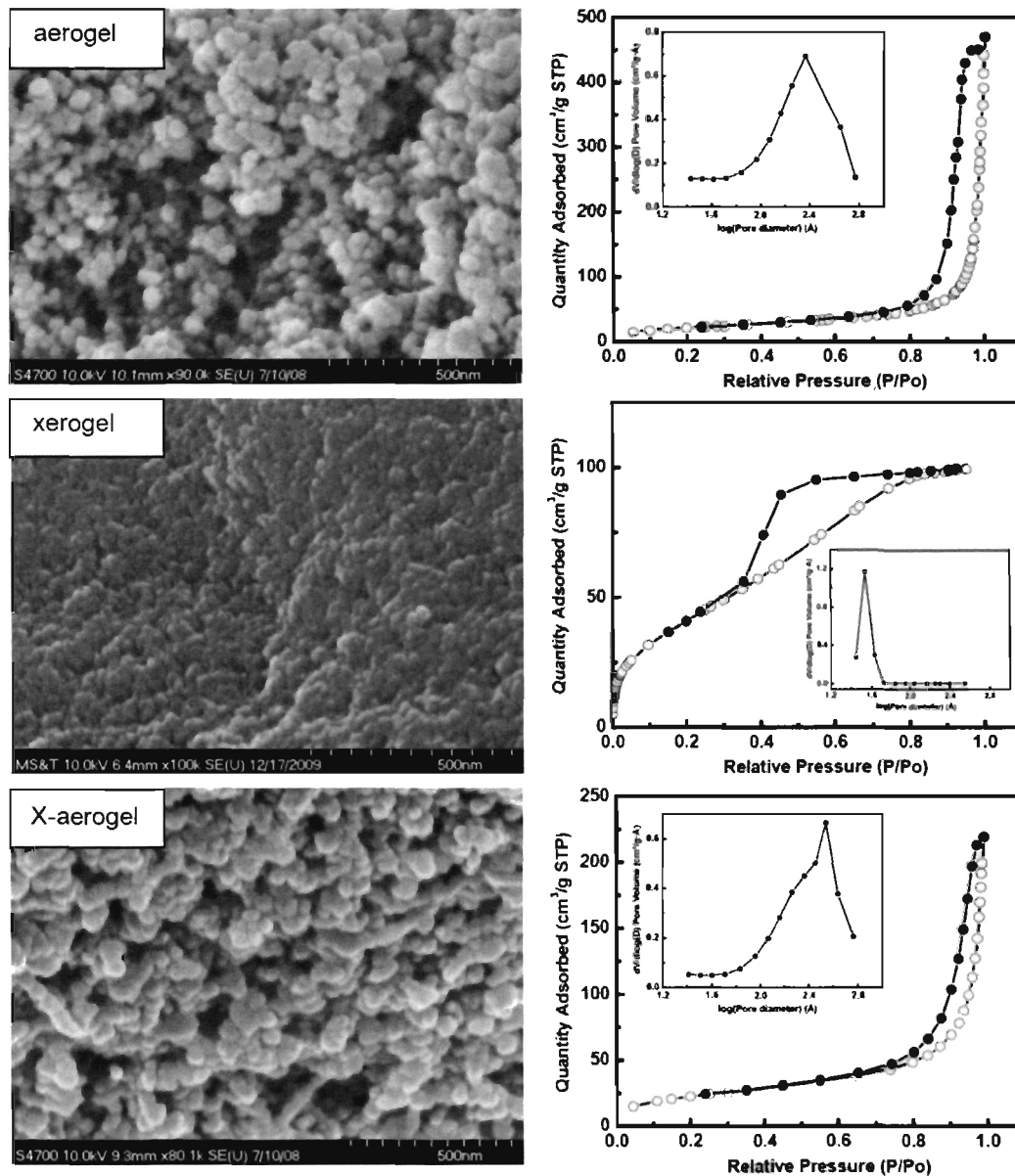
Fig. 5 Representative SEM and N_2 sorption data for the RF-MOx systems exemplified by RF-CoOx in the native aerogel, xerogel and X-aerogel forms. Open circles, adsorption; dark circles, desorption.Insets: BJH-desorption data. (Continued)
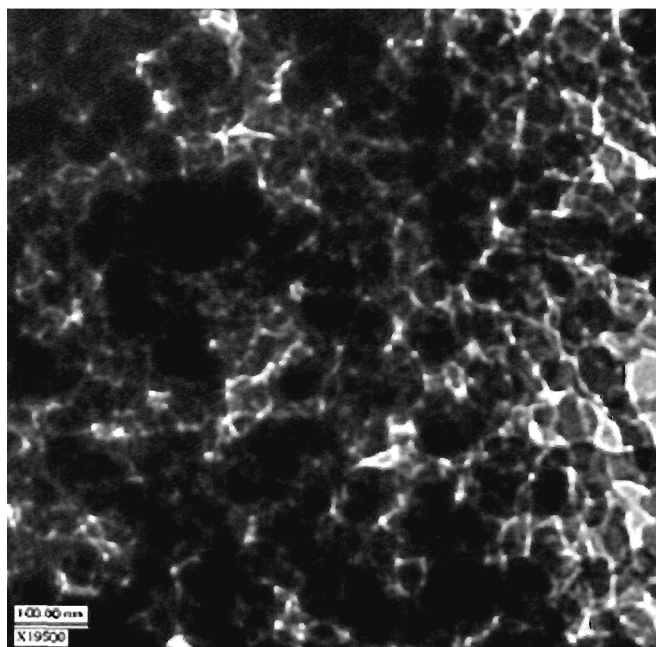
Fig. 6 Bright field TEM of a native-RF-CoOx aerogel (ρ_b=0.082±0.001 g cm^{-3}). Scale bar, 100 nm.
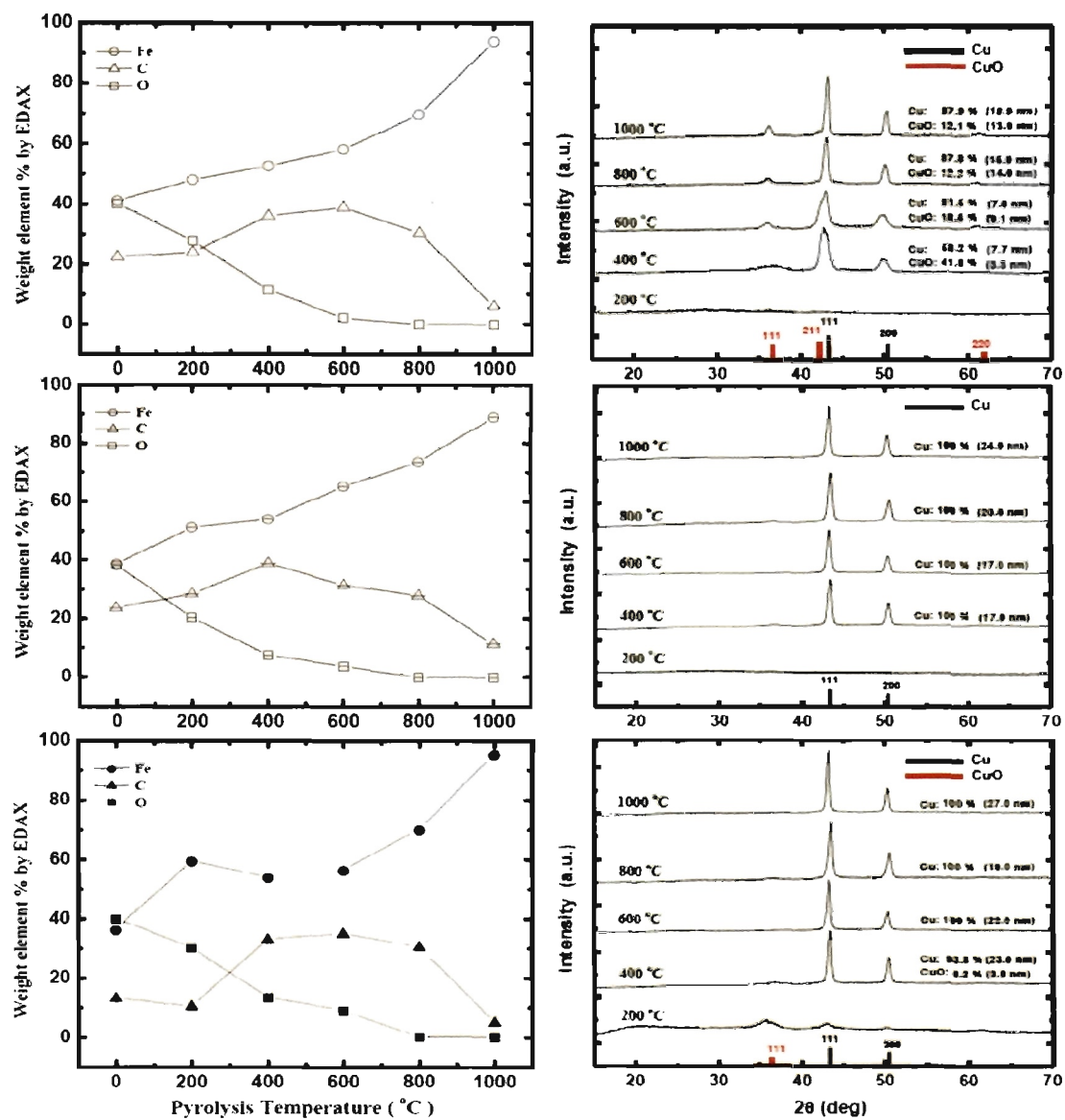
Fig. 7 Representative XRD and EDS data as a function of pyrolysis temperature (Ar) for the smeltable RF-MOx systems exemplified by RF-SnOx in the native aerogel (top), xerogel (middle) and X-aerogel (bottom) forms. For all this systems of this study refer to the ESI†.
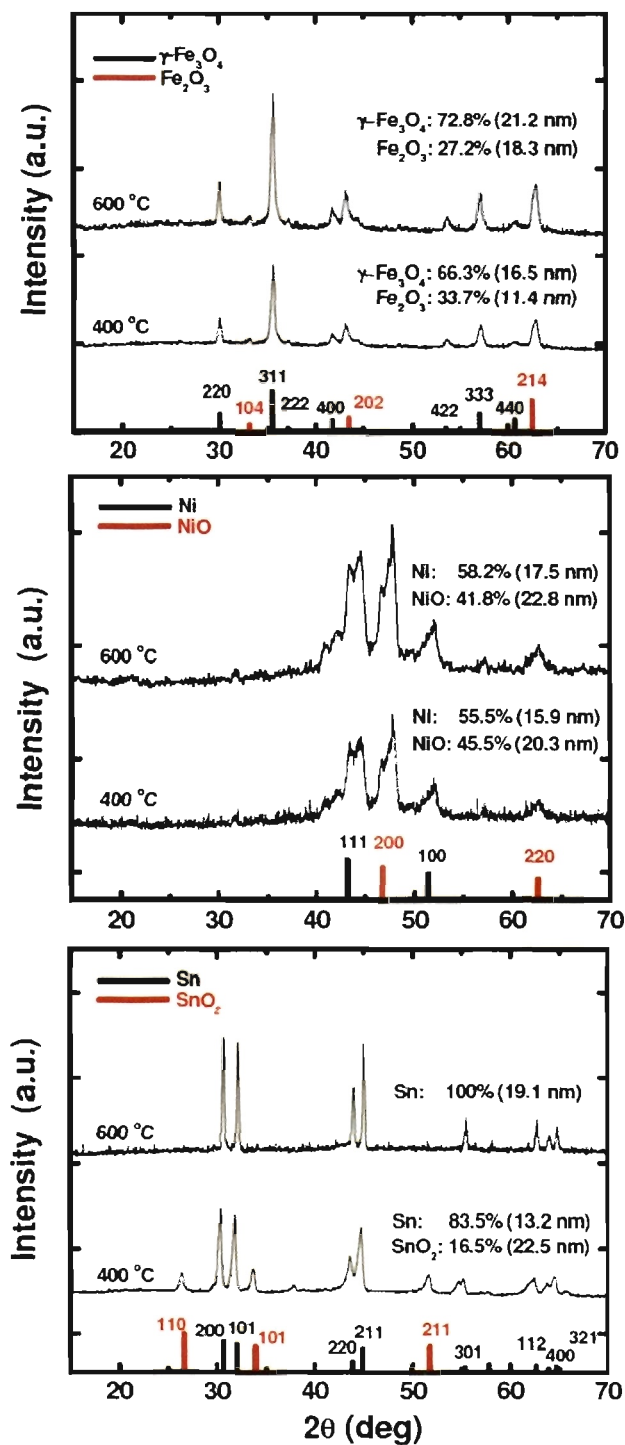
Fig. 8 XRD data after pyrolysis under Ar of X-FeOx, X-NiOx and X-SnOx (no RF) at 400 °C and 600 °C.
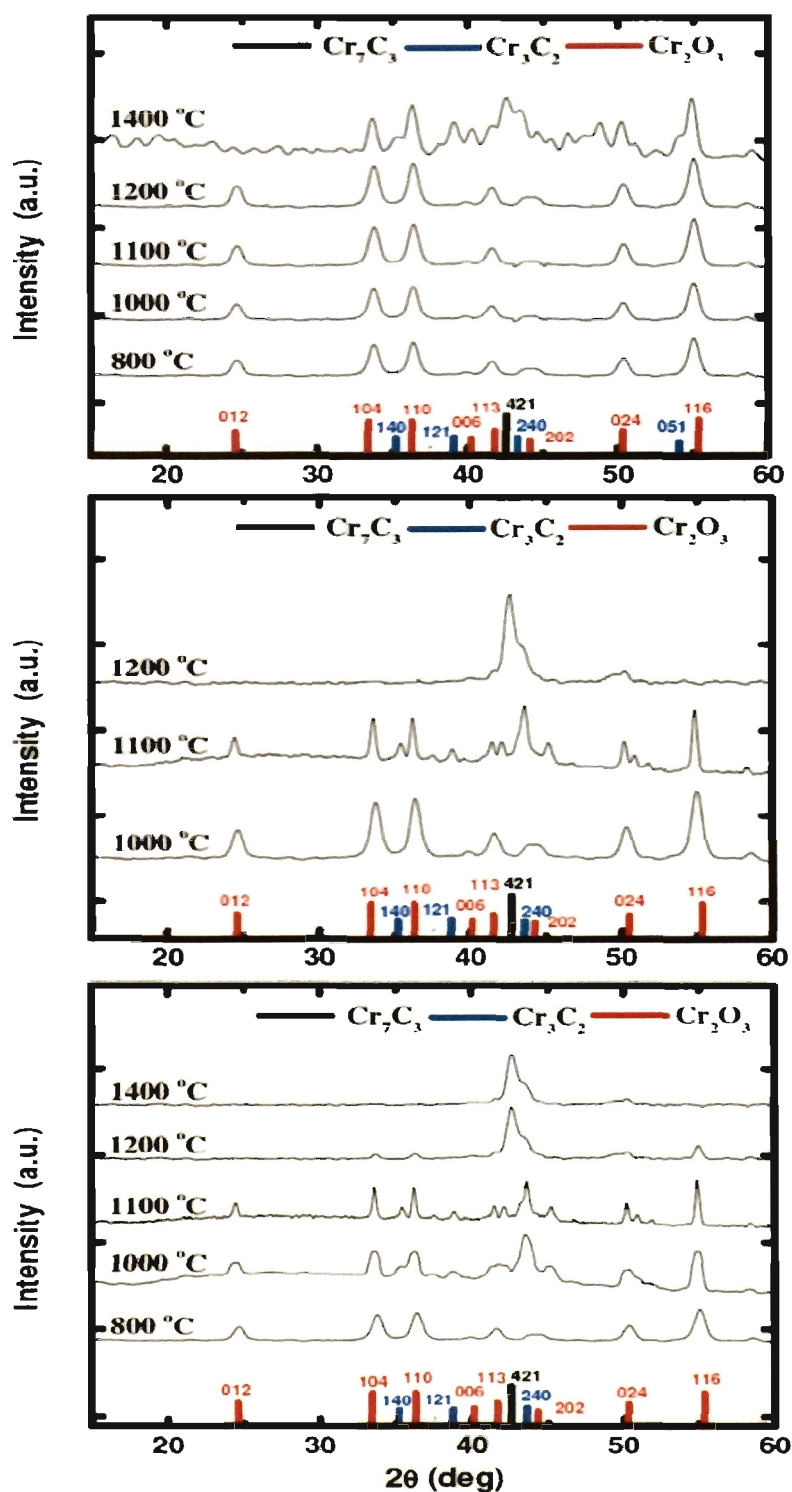
Fig. 9 Representative XRD data as a function of the pyrolysis temperature (under Ar) for the RF-MOx systems convertible to carbides. Case shown RF-CrOx in the native aerogel (top), xerogel (middle) and X-aerogel (bottom) forms. Assignment for Cr_7C_3 from ref. 27.

native RF-CuOx   X-RF-CuOx

RT

200 °C

400 °C

1000 °C
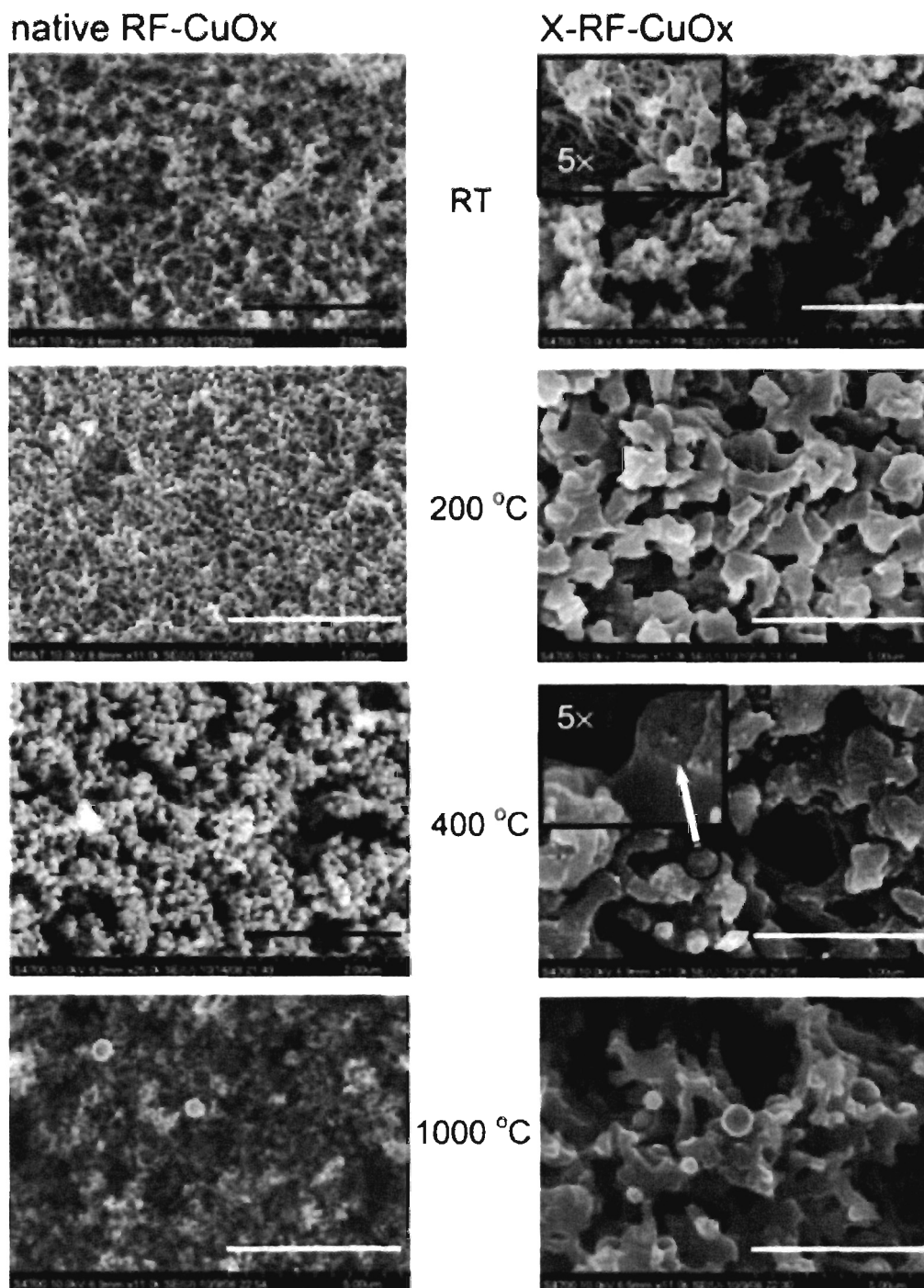
Fig. 10 Typical structural evolution of smeltable RF-MOx. Scale bars:white, 5 μm; black, 2 μm. Arrow points to the xerogel-like structure inside the macroporous wall.[15] For other pertinent materials characterization data refer to the ESI†.

native RF-HfOx   X-RF-HfOx
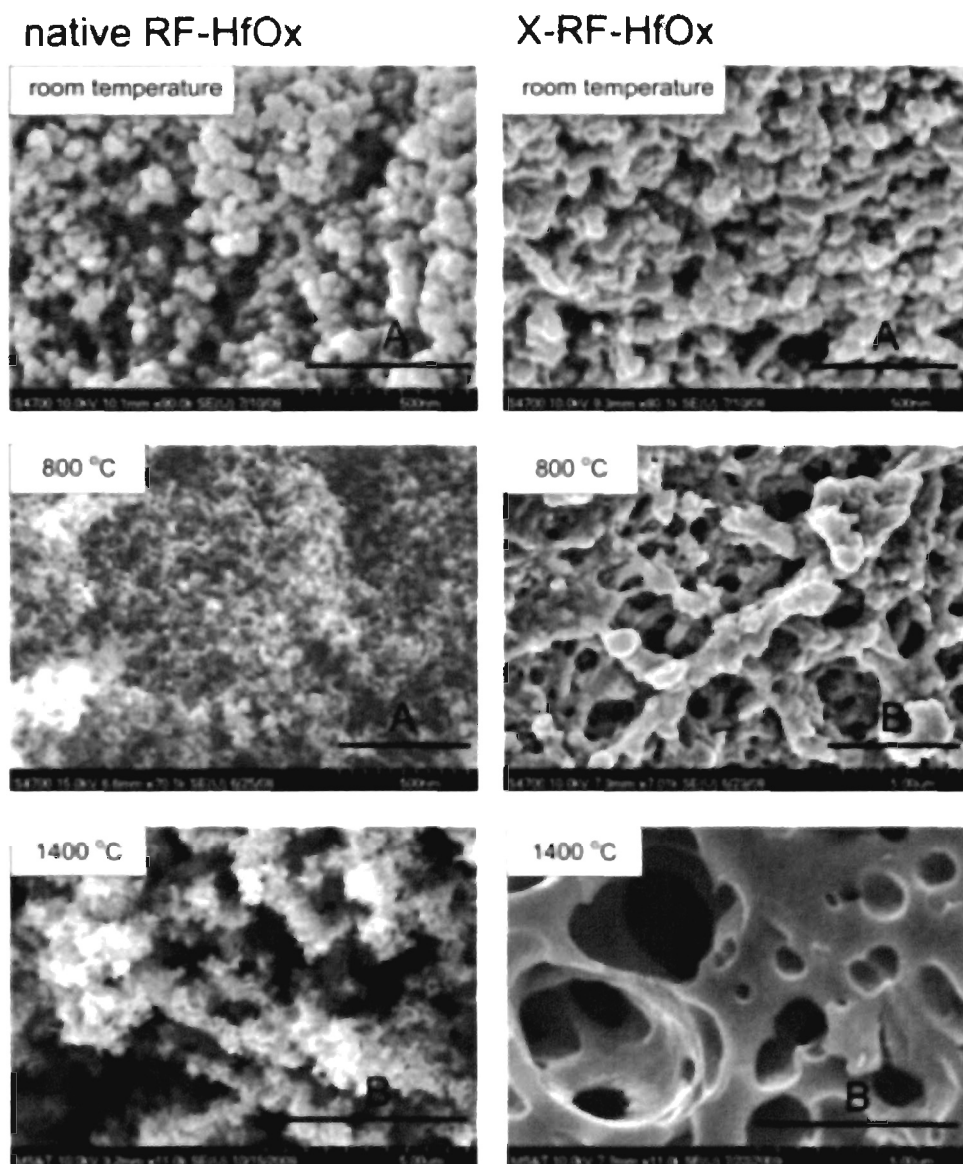
Fig. 11 Structural evolution by SEM upon pyrolysis (Ar, 3 h) of a representative RF-MOx system convertible to carbide. Scale bars: A. 500 nm; B. 5 μm. For other pertinent materials characterization data refer to the ESI†.

7 Supporting Information
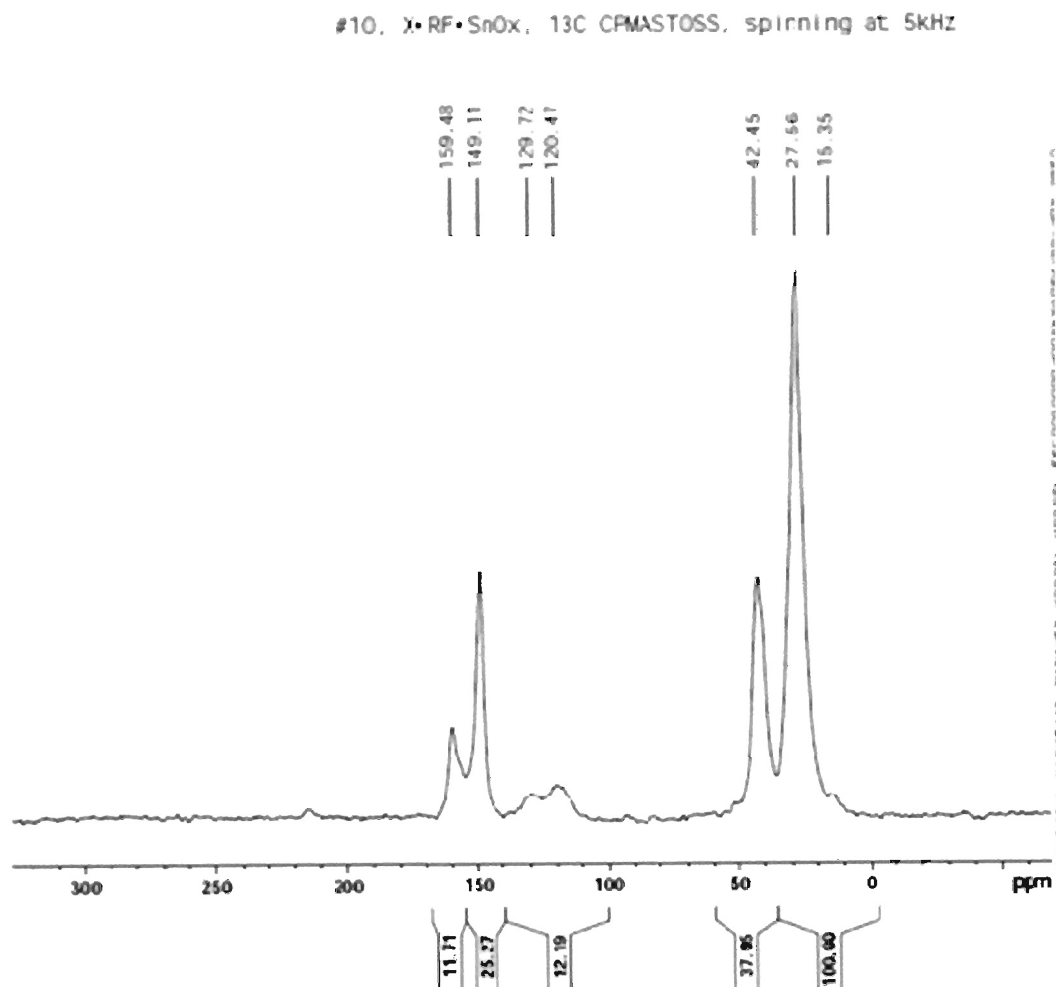
Fig. 1S Solids ^{13}C NMR of representative native and X-RF-SnOx system
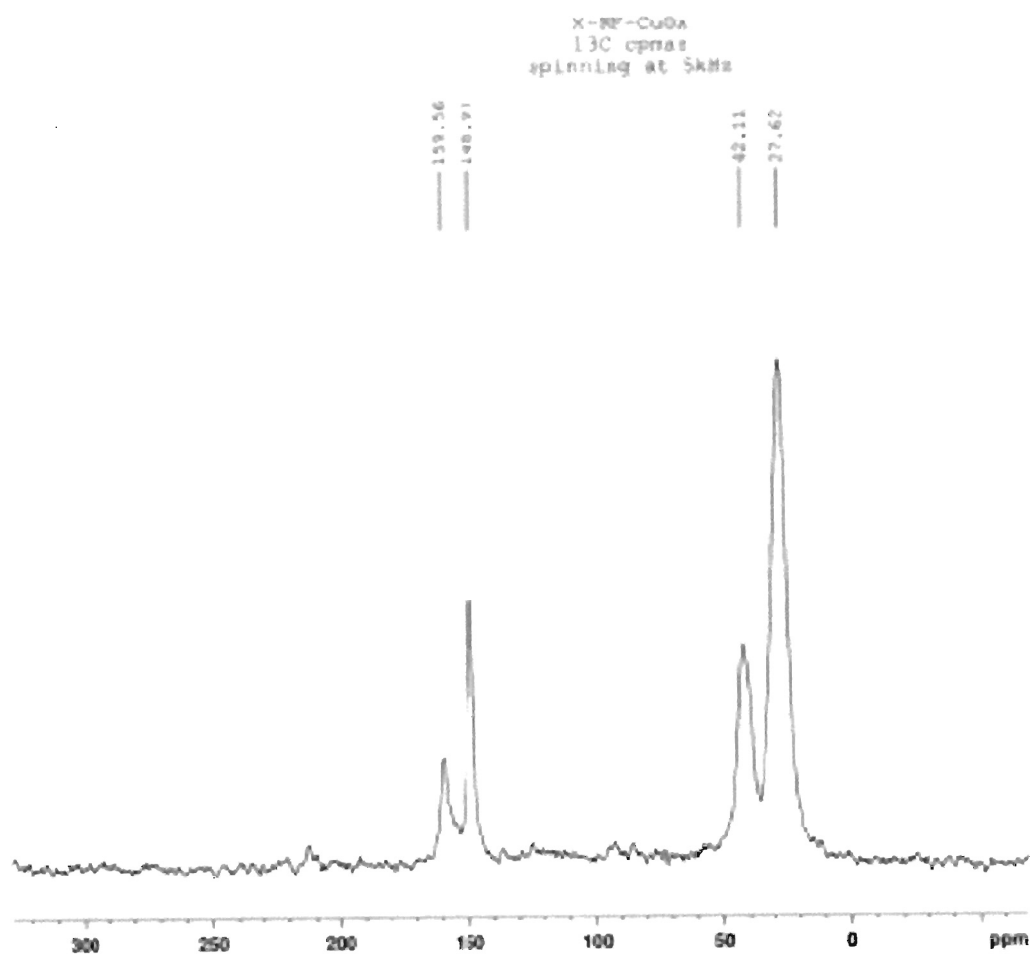
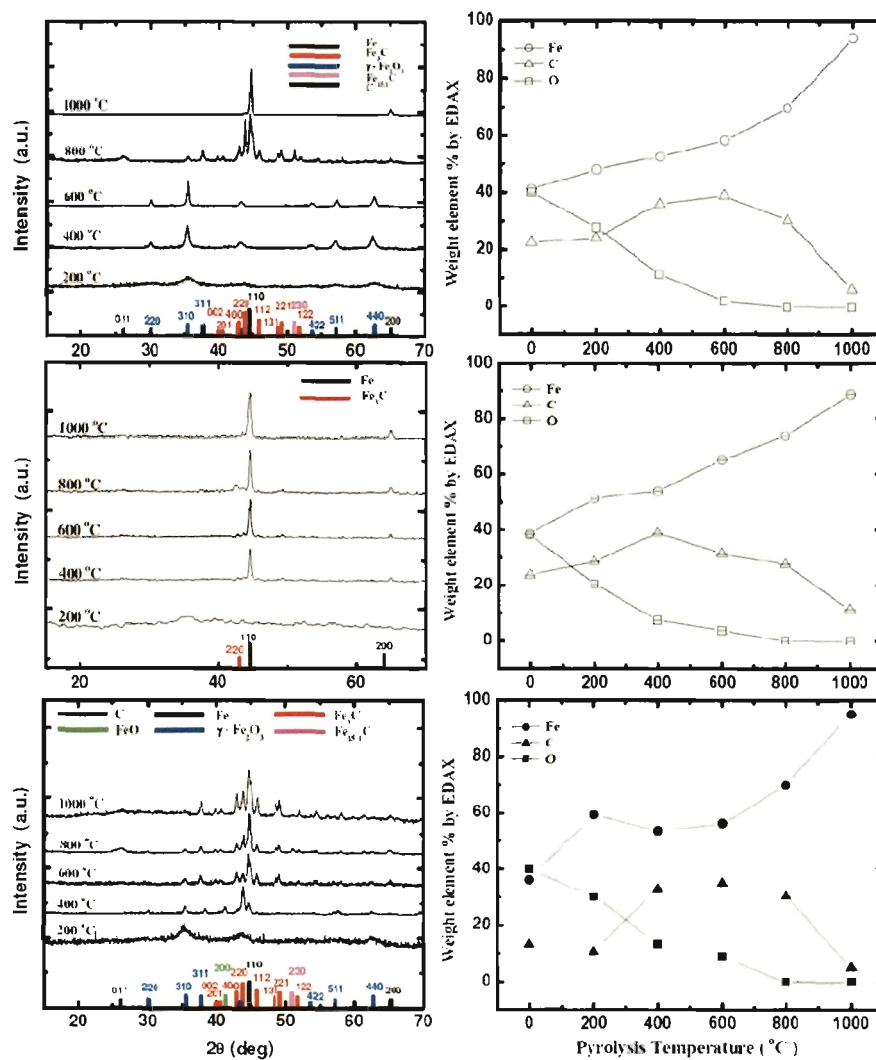**Fig. 2S** Solids ^{13}C NMR of representative native and X-RF-CuOx system
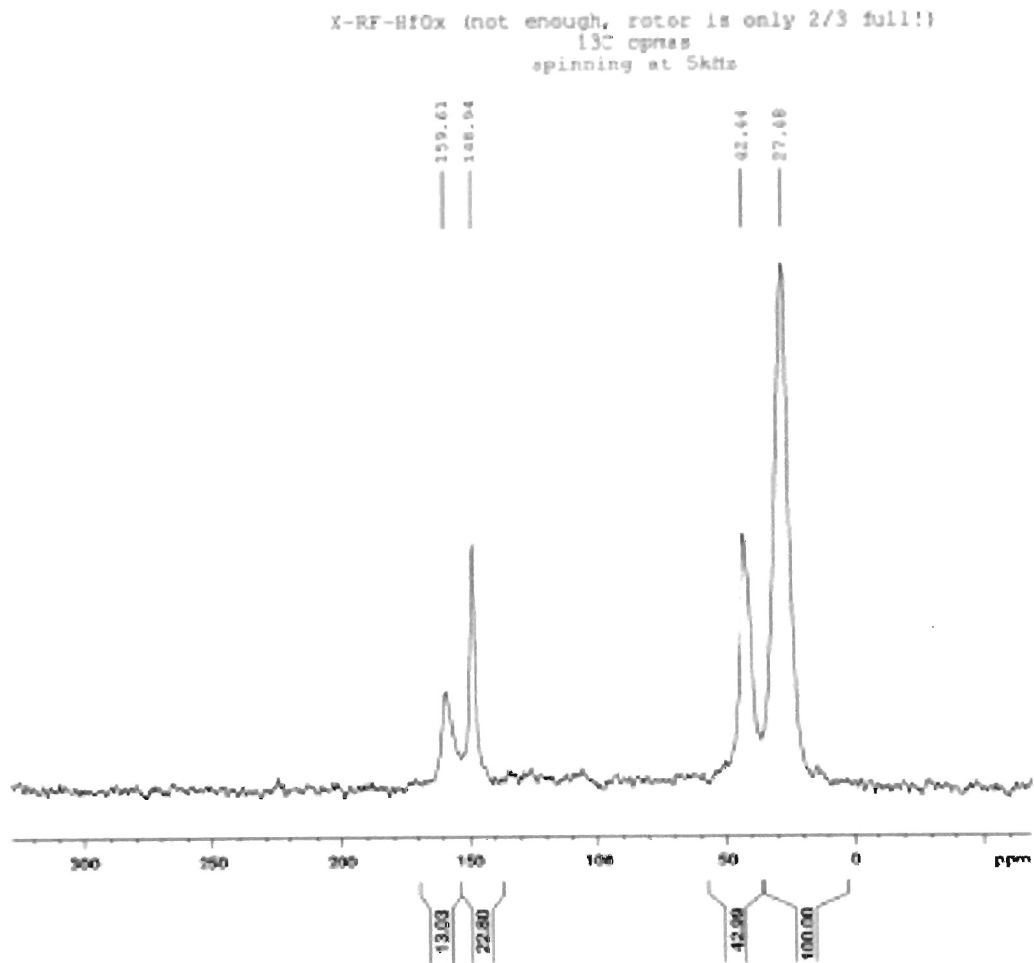
Fig. 3S Solids ^{13}C NMR of representative native and X-RF-HfOx system

Fig. 4S XRD and EDS data as a function of pyrolysis temperature (under Ar) for the smeltable RF-FeOx system in their native aerogel (top), xerogel (middle) and X-aerogel (bottom) forms.
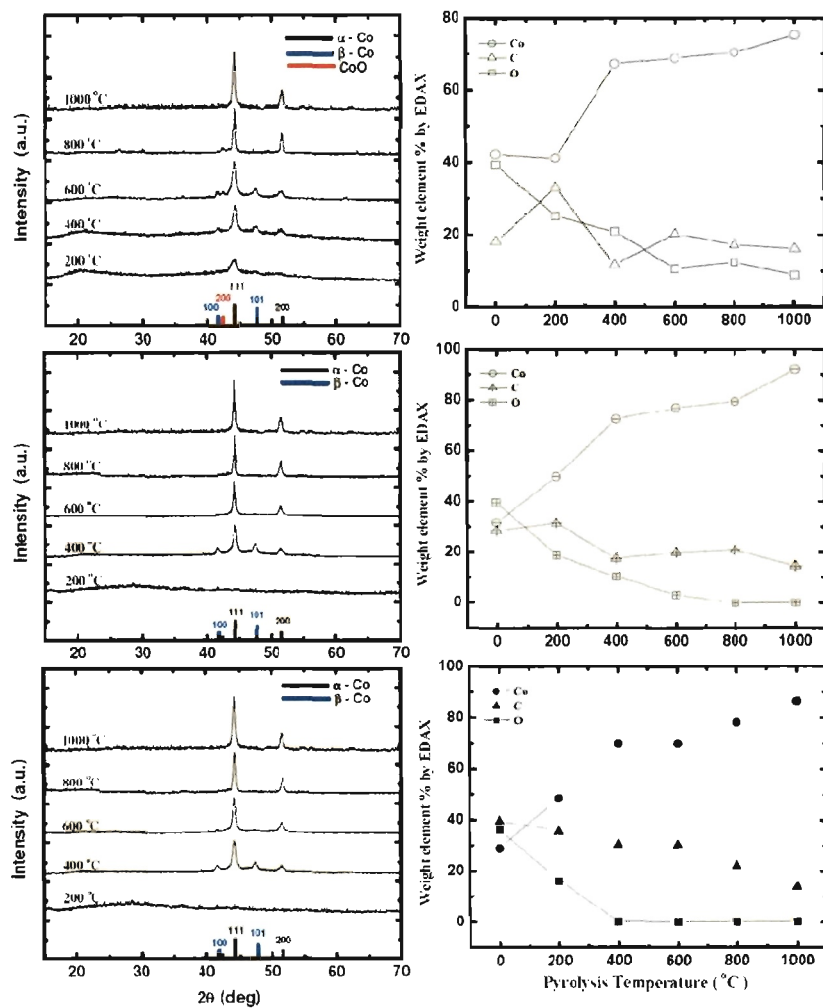
Figure 5S. XRD and EDS data as a function of pyrolysis temperature (under Ar) for the smeltable RF-CoOx system in their native aerogel (top), xerogel (middle) and X-aerogel (bottom) forms.
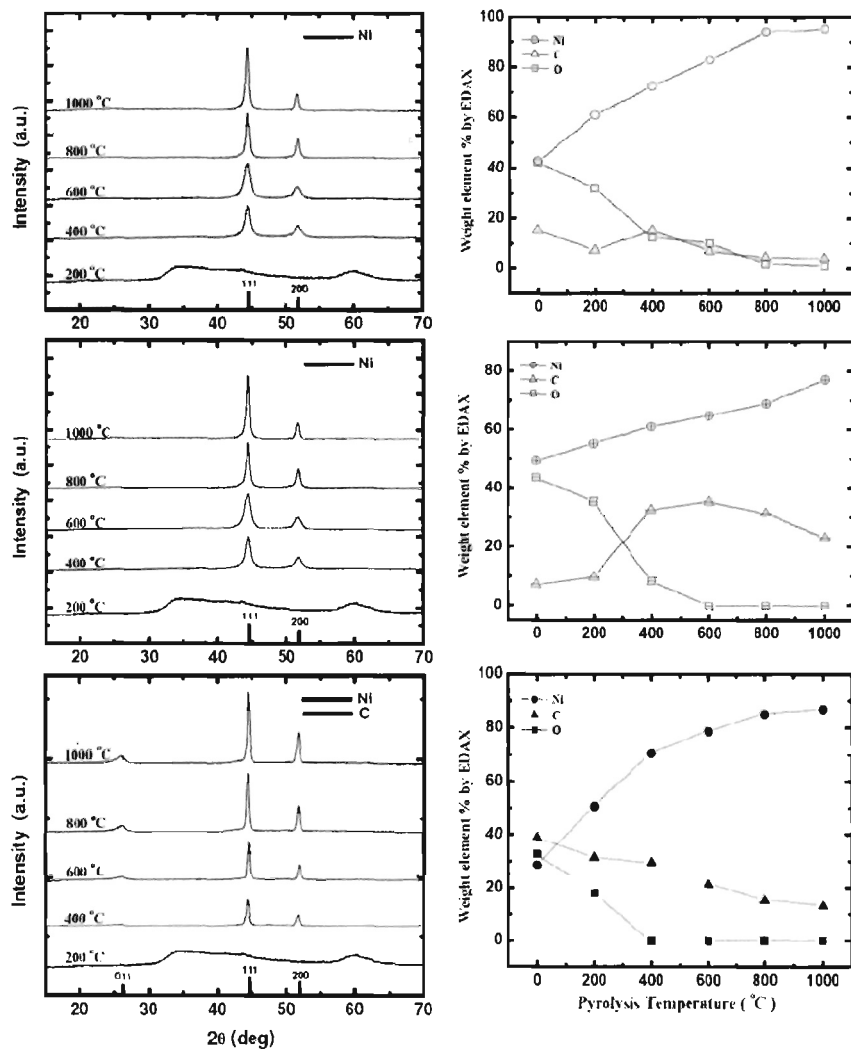
Figure 6S. XRD and EDS data as a function of pyrolysis temperature (under Ar) for the smeltable RF-NiOx system in their native aerogel (top), xerogel (middle) and X-aerogel forms.
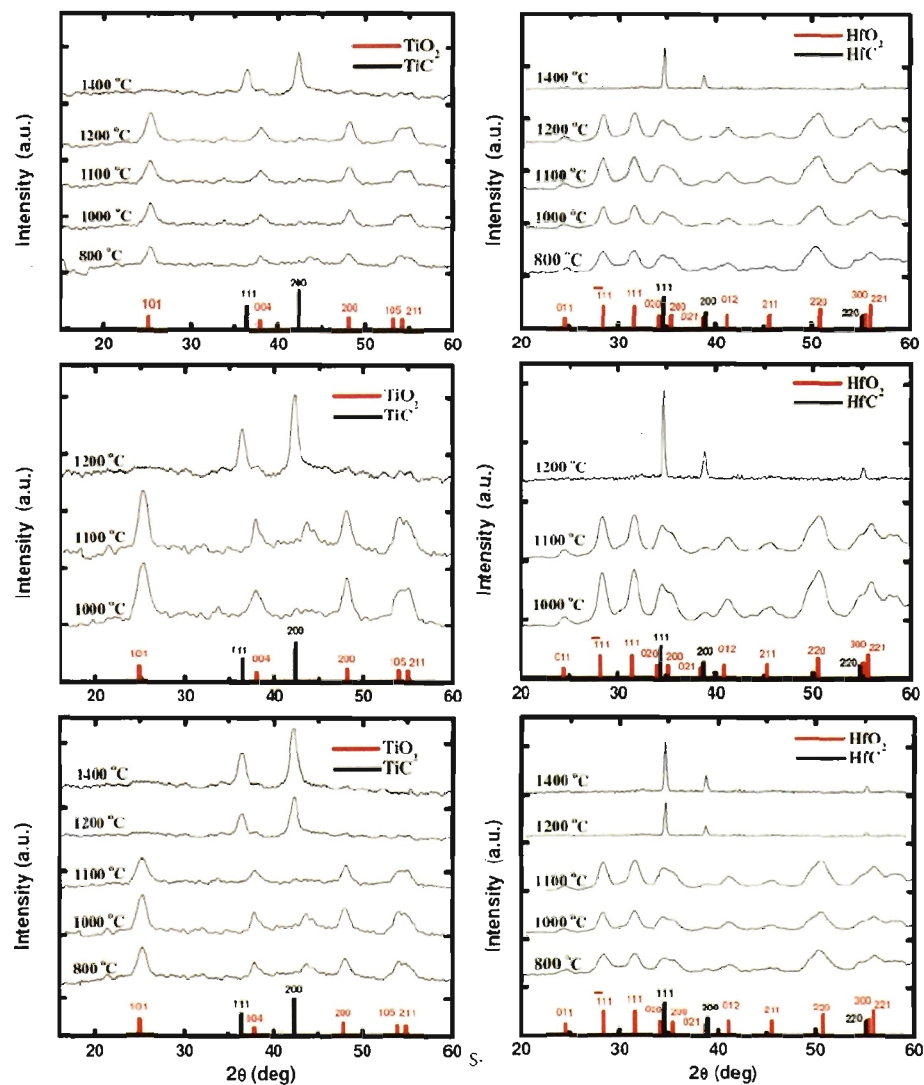
Figure 7S. XRD and EDS data as a function of pyrolysis temperature (under Ar) for the smeltable RF-TiOx system in their native aerogel (top), xerogel (middle) and X-aerogel (bottom) forms.
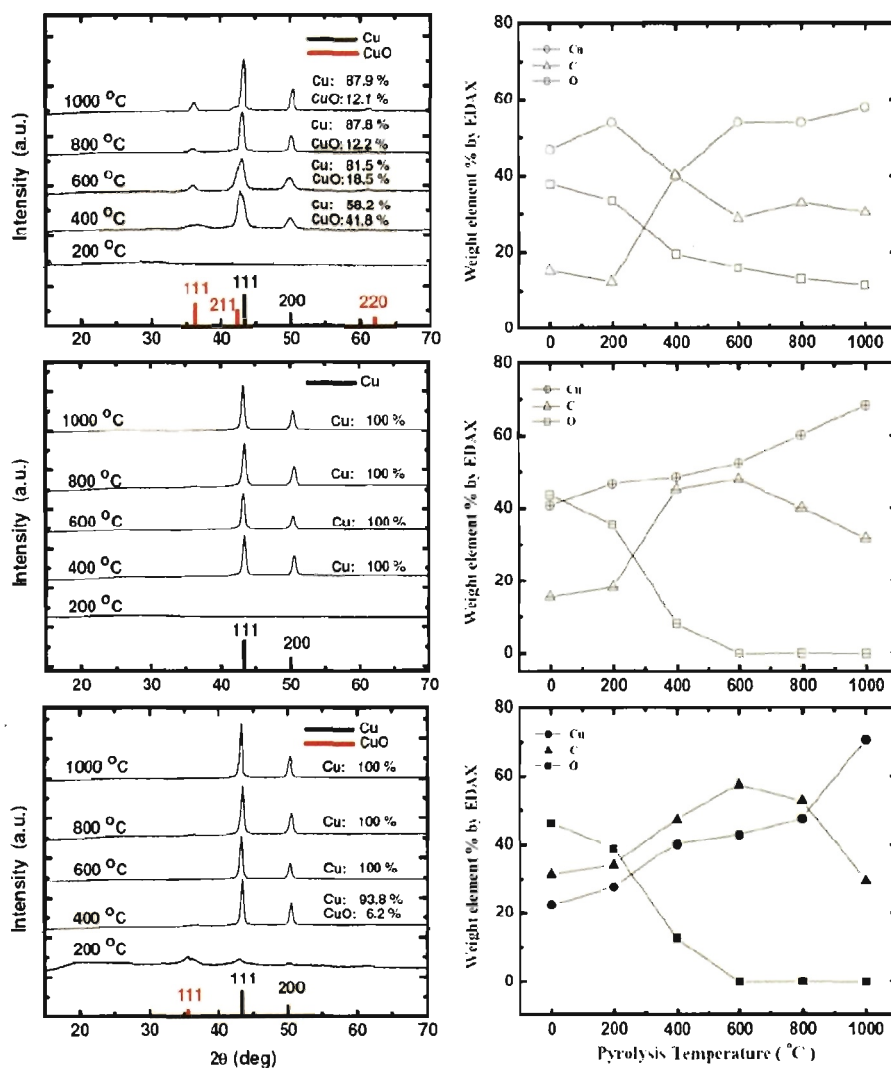
Figure 8S. XRD and EDS data as a function of pyrolysis temperature (under Ar) for the smeltable RF-CuOx system in their native aerogel (top), xerogel (middle) and X-aerogel (bottom) forms.
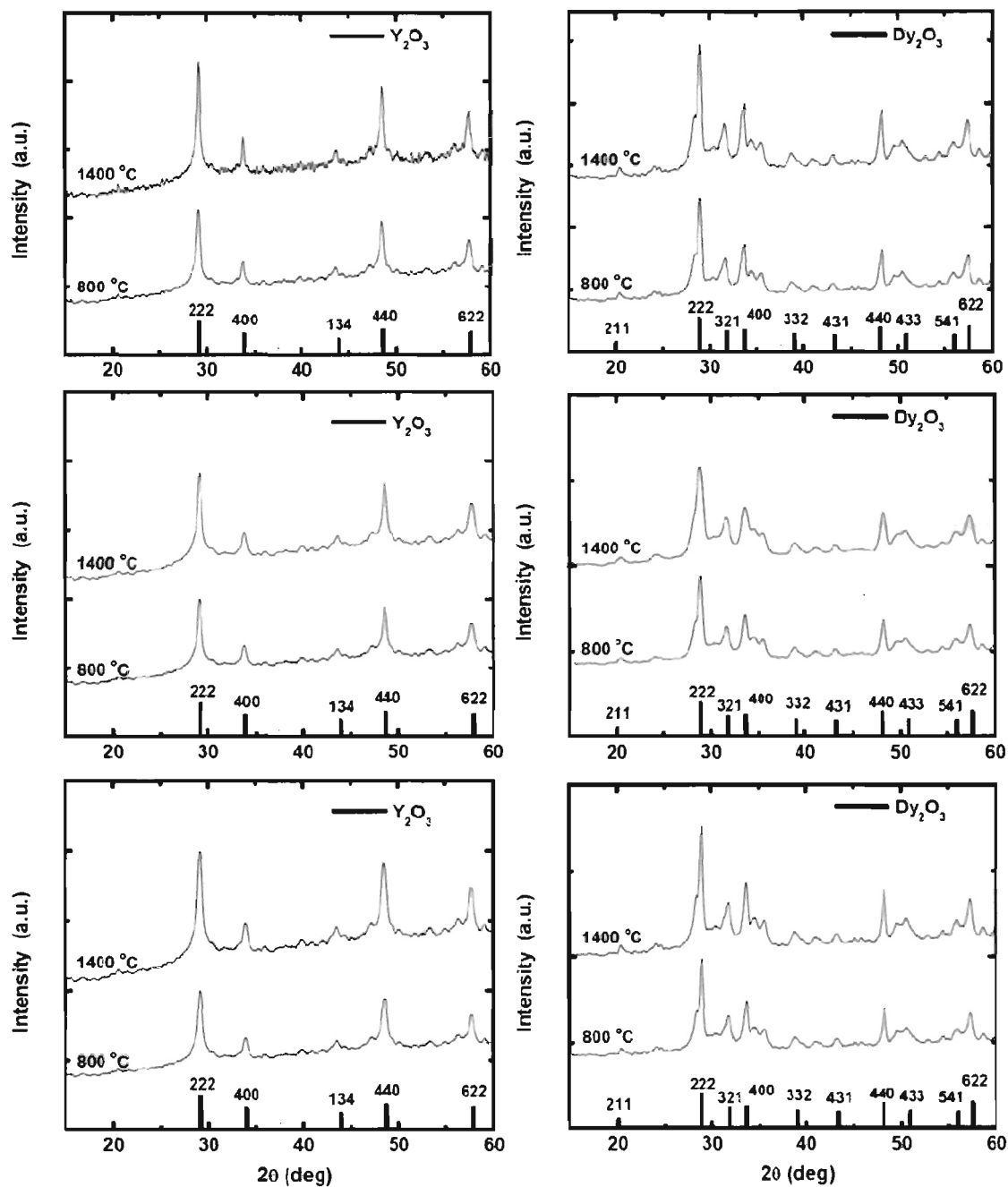
Figure 9S. XRD data as a function of the pyrolysis temperature (under Ar) for RF-YOx and RF-DyOx; Top: native aerogels; Middle: xerogels; Bottom: X-aerogels

VITA

Naveen Chandrasekaran was born on September 12, 1983 in Vriddhachalam, Tamilnadu, India to A. Chandrasekaran and D. B. Hemalatha. He graduated from St. Paul's Matriculation Higher Secondary School in 2000. He received his Bachelors degree in Chemical and Electrochemical Engineering from the Central Electrochemical Research Institute (CECRI) in Karaikudi, India in 2004. Subsequently, he worked for two years on electroplating as Technical Executive in Consolidated Metal Finishing Pvt. Ltd. In 2006 he joined Missouri University of Science and Technology to pursue Ph.D. in Chemistry. During the course of his Ph.D. he has published 12 papers. He is co-inventor in 2 patent publications. He will receive his Ph.D. in chemistry in May 2011.